SLAC-R-924
May 2009

Two Complementary Strategies for New Physics Searches at Lepton Colliders

by

Benjamin Henry Hooberman

B.A. (University of Columbia) 2005
M.A. (University of California, Berkeley) 2008

A dissertation submitted in partial satisfaction of the
requirements for the degree of
Doctor of Philosophy

in

Physics

in the

GRADUATE DIVISION
of the
UNIVERSITY OF CALIFORNIA, BERKELEY

Committee in charge:
Professor Marco Battaglia, Chair
Professor Kam-Biu Luk
Professor Stephen Derenzo

Spring 2009

Work supported in part by US Department of Energy contract DE-AC02-76SF00515

SLAC National Accelerator Laboratory, Menlo Park, Ca 94025

Two Complementary Strategies for

New Physics Searches at Lepton Colliders

Benjamin Henry Hooberman

Abstract

Two Complementary Strategies for

New Physics Searches at Lepton Colliders

by

Benjamin Henry Hooberman

Doctor of Philosophy in Physics

University of California, Berkeley

Professor Marco Battaglia, Chair

In this thesis I present two complementary strategies for probing beyond-the-Standard Model physics using data collected in e^+e^- collisions at lepton colliders. One strategy involves searching for effects at low energy mediated by new particles at the TeV mass scale, at which new physics is expected to manifest. Several new physics scenarios, including Supersymmetry and models with leptoquarks or compositeness, may lead to observable rates for charged lepton-flavor violating processes, which are forbidden in the Standard Model. I present a search for lepton-flavor violating decays of the $\Upsilon(3S)$ using data collected with the *BABAR* detector. This study establishes the 90% confidence level upper limits $BF(\Upsilon(3S) \to e\tau) < 5.0 \times 10^{-6}$ and $BF(\Upsilon(3S) \to \mu\tau) < 4.1 \times 10^{-6}$, which are used to place constraints on new physics contributing to lepton-flavor violation at the TeV mass scale. An alternative strategy is to increase the collision energy above the threshold for new particles and produce them directly. I discuss research and development efforts aimed at producing a

vertex tracker which achieves the physics performance required of a high energy lepton collider. A small-scale vertex tracker prototype is constructed using Silicon sensors of $50\ \mu\mathrm{m}$ thickness and tested using charged particle beams. This tracker achieves the targeted impact parameter resolution of $\sigma_{IP} = (5 \oplus 10\ \mathrm{GeV}/p_T)\ \mu\mathrm{m}$ as well as a longitudinal vertex resolution of $(260 \pm 10)\ \mu\mathrm{m}$, which is consistent with the requirements of a TeV-scale lepton collider. This detector research and development effort must be motivated and directed by simulation studies of physics processes. Investigation of a dark matter-motivated Supersymmetry scenario is presented, in which the dark matter is composed of Supersymmetric neutralinos. In this scenario, studies of the $e^+e^- \to H^0A^0$ production process allow for precise measurements of the properties of the A^0 Supersymmetric Higgs boson, which improve the achievable precision on the neutralino dark matter candidate relic density to 8%. Comparison between this quantity and the dark matter density determined from cosmological observations will further our understanding of dark matter by allowing us to determine if it is of Supersymmetric origin.

Professor Marco Battaglia
Dissertation Committee Chair

Contents

List of Figures

List of Tables

Acknowledgments

I would like to thank the following people for their invaluable help during my graduate career:

My advisor Marco Battaglia, for introducing me to particle physics and for providing excellent guidance and interesting research projects, and for always having an open door.

Yury Kolomensky, for providing excellent guidance for my *BABAR* analysis, and for always taking time to answer my questions.

The members of the LBNL advanced detector group, in particular Devis Contarato, Piero Giubilato, and Lindsay Glesener. I have learned a great deal from collaborating with them. I would like to especially thank Devis for spending a great deal of time teaching me about detectors.

Dave Brown, for help with all things *BABAR*-related, and for taking time to answer my random questions.

Marjorie Shapiro, for her commitment to mentoring graduate students and for providing excellent career advice over the years.

Mark Oreglia, for taking the time to write me a letter of recommendation.

The members of my thesis committee, Kam-Biu Luk and Stephen Derenzo, for providing their time and many useful comments.

The members of my *BABAR* review committee, Mike Roney, Stephen Sekula, and Veronique Ziegler, for their suggestions and guidance while performing the analysis.

My office-mates, in particular Kerstin Tackmann and Tomohiko Tanabe, for their help in learning the ropes of *BABAR*.

My family, for their support, and my friends, without whom life in graduate school would have been considerably less enjoyable.

Chapter 1

Introduction

During the 20^{th} century, our understanding of the fundamental constituents of matter and the forces which mediate their interactions has advanced drastically as a result of several theoretical advances and experimental discoveries occurring over several decades. The culmination of these advances is described by the Standard Model (SM) of particle physics, a quantum field theory (QFT)[1] which describes all of the observed matter particles and the fundamental forces, with the exception of gravity. Although the SM has been verified experimentally with multiple high precision measurements, there is compelling evidence that it is not the final, most general theory of particle physics. In this chapter, the historical development of the SM and its experimental verification are reviewed, along with a discussion of the evidence for physics beyond the SM. I conclude by discussing two complementary strategies for probing this new physics, which is the focus of my thesis.

[1] For further information on quantum field theory, see [1, 2].

1.1 Development of the Standard Model of Particle Physics

The SM in its current form was formulated in the 1970's, but it draws upon concepts dating back to the quantum revolution of the 1920's and 1930's [3], during which a series of theoretical advances led to the establishment of quantum mechanics. The first fully formulated QFT, formulated by Richard Feynman, Julian Schwinger and Sin-Itiro Tomonaga in the 1940's to provide a quantum description of electromagnetism, is called Quantum Electrodynamics (QED) [4]. The particle content of QED consists of two fermionic matter particles, the electron and positron, which interact via exchange of a single gauge boson, the photon. QED has been experimentally verified with extremely high precision and has yielded the single most precise prediction of a measured observable, the magnetic moment of the electron, which agrees with the predicted value at the 10^{-10} level [5]. QED also explains the Lamb shift [6] between the $^2S_{1/2}$ and $^2P_{1/2}$ energy levels of the hydrogen atom, which according to quantum mechanics should be degenerate. Crucial to QED and to QFT in general is the concept of a gauge symmetry[2], which is a symmetry operation which leaves the Lagrangian invariant. The gauge symmetry of QED is the group of rotations in the complex plane, specified by the $U(1)$ gauge group.

Although QED is an extremely successful theory, it is not capable of describing all of the observed forces and elementary particles and must therefore constitute only a part of a more general theory. One such particle is the neutrino, proposed by Wolfgang Pauli in 1930 to preserve energy conservation in nuclear beta decay [7]. It is now known that nuclear beta decay is governed by the weak force, a short-ranged force which manifests only on subatomic size scales. In the 1960's, Sheldon Glashow, Abdus Salam and Steven Weinberg (GSW) successfully unified electro-

[2]For more information on gauge symmetries and groups, see [8].

magnetism with the weak force [9]. The resulting GSW electroweak theory introduces three weak vector bosons, the W^+, W^- and Z^0, which couple to fermions as well as to themselves. The symmetry group of electroweak theory is $SU(2)_L \otimes U(1)_Y$, where L denotes left-handed helicity states and Y denotes a quantum number called hypercharge. This symmetry is spontaneously broken by a scalar Higgs field which acquires a non-zero vacuum expectation value and condenses [10]. This 'Higgs mechanism' results in the weak vector bosons, as well as the fermions, acquiring mass, and breaks the electroweak symmetry group as $SU(2)_L \otimes U(1)_Y \rightarrow U(1)_{EM}$ where EM denotes electromagnetism. This pattern of symmetry breaking maintains the $U(1)$ symmetry of electromagnetism, which is the basis for the observed conservation of electric charge. The first verification of electroweak theory was the discovery of neutral weak current interactions mediated by Z^0 boson exchange by the Gargamelle experiment [11] at the European Organization for Nuclear Research (CERN), leading to widespread acceptance of the theory. Several years later, the weak vector bosons were discovered at the Super Proton Synchrotron ($Sp\bar{p}S$) accelerator [12] at CERN, and their masses agreed extremely well with the SM predictions. Further verification was obtained by precision tests of the theory carried out by the Large Electron Positron (LEP) and Stanford Linear Collider (SLC) [13] collaborations in the 1990's. The final test of electroweak theory involves the search for the Higgs particle, predicted by electroweak theory to manifest as a scalar particle with mass of order 100 GeV/c^2, as well as the investigation of its properties. In particular, the Higgs mechanism predicts that the coupling of the Higgs to fermions g_{Hff} is proportional to the mass of the fermion m_f, while the coupling of the Higgs to the electroweak vector bosons g_{HVV} is proportional to the square of the mass of the vector boson M_V^2 [10]:

$$g_{Hff} = \left(\sqrt{2}G_F\right)^{1/2} m_f \quad \text{and} \quad g_{HVV} = 2\left(\sqrt{2}G_F\right)^{1/2} M_V^2, \tag{1.1}$$

where G_F is Fermi's constant. These relationships can be checked by measuring the branching fractions of the Higgs to pairs of fermions and vector bosons. The search for the Higgs boson constitutes a major part of the physics program to be investigated at the Large Hadron Collider (LHC) [14], which is designed to discover the Higgs particle over the full allowed mass range up to $\sim$1 TeV. LHC data will also be used to measure Higgs branching fractions, but a lepton collider providing e^+e^- collisions at a center-of-mass (CM) energy of several hundred GeV is required to provide precise measurements, for reasons discussed in Chap. 1.4.1.

Electroweak theory, much like its predecessor QED, is extremely successful but does not constitute the full theory of elementary particles and forces. In the 1960's, Murray Gell-Mann and George Zweig proposed that hadrons, particles such as protons and neutrons, are not elementary particles but are composed of subatomic particles called quarks [15]. The original Gell-Mann & Zweig theory involved three types of quarks, which they named up, down, and strange, but was quickly extended by Sheldon Glashow and James Bjorken to contain a fourth 'charm' quark [16]. In the late 1960's deep inelastic scattering experiments performed at the Stanford Linear Accelerator (SLAC) [17] demonstrated that the proton was composed of smaller particles and was therefore not an elementary particle, but the quark model failed to gain widespread acceptance. Several years later Makoto Kobayashi and Toshihide Maskawa proposed the existence of another pair of quarks, now known as bottom and top, in order to explain observations of charge-parity violation [18]. The quark model finally gained widespread acceptance when the charm quark was discovered simultaneously at SLAC [19] and Brookhaven National Laboratory (BNL) [20] in the 1970's. The interactions of these quarks are governed by the theory of quantum chromodynamics (QCD), pioneered by David Gross, David Politzer and Frank Wilczek in the 1970's [21]. Their discovery of

'asymptotic freedom,' the property that quarks become weakly interacting at high energy scales, allowed quantitative predictions to be extracted from QCD using perturbation theory. QCD is based on the $SU(3)$ gauge group and introduces gauge bosons called gluons which mediate a new, 'strong' force. This strong force is responsible for the phenomenon of quark confinement, the binding of combinations of quarks into composite particles called hadrons. Gluons were discovered at the Positron-Electron Tandem Ring Accelerator (PETRA) [22] in the late 1970's, and precise measurements of QCD performed several years later at the LEP collider [23] led to widespread acceptance of QCD.

The remaining particle content of the SM consists of the muon and tau, heavier cousins of the electron, and their corresponding neutrino species. This completes the SM particle content, summarized in Table. 1.1. The electron, muon and tau along with their corresponding neutrino types are collectively referred to as leptons. The quarks and leptons constitute the fermionic matter content of the SM and are arranged in three generations, with the mass of the particles increasing from the first generation to the second and third. The gluon, weak vector bosons and the photon constitute the force-mediating gauge boson content of the SM. These particles and their interactions, governed by electroweak theory and quantum chromodynamics, constitute the Standard Model of particle physics, a quantum field theory based on the gauge group $SU(3) \otimes SU(2)_L \otimes U(1)_Y$. The development of the Standard Model represents the culmination of several decades of theoretical advances and experimental discoveries and is regarded as the crowning achievement of particle physics.

Table 1.1: Elementary particle content of the SM. Spin is denoted by s and charge refers to electric charge. The quoted masses are the 2008 Particle Data Group (PDG) [24] values and the neutrino masses are given for the corresponding mass eigenstate. The masses given for the light u, d, and s quarks are the pole masses which are determined via their radiative corrections, primarily to the electromagnetic coupling constant.

Particle	**Symbol**	**Charge (e)**	**Mass (GeV/c^2)**
quarks (s=1/2)			
up	u	+2/3	$(1.5 - 3.3) \times 10^{-3}$
down	d	-1/3	$(3.5 - 6.0) \times 10^{-3}$
charm	c	+2/3	$1.27^{+0.07}_{-0.11}$
strange	s	-1/3	$(70 - 130) \times 10^{-3}$
top	t	+2/3	171 ± 2.1
bottom	b	-1/3	$4.20^{+0.17}_{-0.07}$
leptons (s=1/2)			
electron	e	-1	0.511×10^{-3}
electron neutrino	ν_e	0	$< 0.46 \times 10^{-6}$
muon	μ	-1	105.7×10^{-3}
muon neutrino	ν_μ	0	$< 0.19 \times 10^{-3}$
tau	τ	-1	1.7768 ± 0.00017
tau neutrino	ν_τ	0	$< 18.2 \times 10^{-3}$
gauge bosons (s=1)			
photon	γ	0	0
$W^\pm$ boson	$W^\pm$	± 1	80.4 ± 0.03
Z^0 boson	Z^0	0	91.2 ± 0.002
gluon	g	0	0
Higgs boson (s=0)			
Higgs	h	0	> 114.4

1.2 Successes of the Standard Model

The SM has been extremely successful in many respects, and experiments performed at colliders up to the $O(10^2)$ GeV energy scale have so far revealed no significant deviations from its predictions. Already mentioned above are several instances in which theoretical considerations led to the predictions of new particles which were later discovered. These include Pauli's neutrino, the electroweak vector bosons, the charm quark, and the bottom and top quarks. The prediction

of the existence of these particles and in many cases precise predictions of their properties such as mass, spin, and electric charge provide compelling evidence for the framework of the SM. A particularly interesting example is the top quark, the heaviest and therefore last elementary particle to be discovered, which was predicted before its discovery in order to complete the third generation of fermions. Measurements performed at LEP and SLC before the discovery of the top quark provided indirect measurements of the top quark mass [13]. These experiments collided electrons and positrons at the CM collision energy $\sqrt{s} = M_Z$, below the threshold for top production. Although top quarks were not directly produced at these colliders, several electroweak observables are altered by radiative corrections involving virtual top quark loops. The magnitudes of these corrections are sensitive to the top quark mass, which can therefore be constrained by precise measurements of these electroweak observables, most importantly the mass of the charged weak vector boson M_W, the leptonic partial width $\Gamma(Z^0 \rightarrow \ell^+\ell^-)$, and the Weinberg mixing angle parameter $\sin^2(\theta_W)$, where $\sin^2(\theta_W)$ determines the ratio between the electric charge e and the weak coupling strength g via $e = g\sin(\theta_W)$. The top quark was later discovered at the Fermilab TeVatron [25], which collides protons and anti-protons at a CM energy of 1.96 TeV, above the threshold for top quark pair production. This allowed for a direct measurement of the top quark mass, which agreed with the previous indirect measurements as shown in Fig. 1.1 (left). These measurements provide a good fit to the SM and are also sensitive to the Higgs mass, which is preferred to be less than about 200 GeV/c^2.

Further compelling evidence for electroweak theory comes from a variety of precise measurements carried out at the LEP and SLC collaborations in the 1990's [13]. These experiments studied the reaction $e^+e^- \rightarrow Z^0 \rightarrow f\bar{f}$, where $f\bar{f}$ denotes a fermion pair. Electroweak theory

has only 3 free non-degenerate parameters, so all electroweak observables depend only on 3 quantities modulo radiative corrections. These parameters can be taken to be the well-measured electric charge e, the Weinberg mixing angle parameter $\sin^2(\theta_W)$, and the mass of the Z^0 boson M_Z. The value of $\sin^2(\theta_W)$ and M_Z have been extracted from multiple measurements performed at LEP and SLC [13]. Once these 3 parameters have been measured, electroweak theory allows for the precise predictions of multiple observables which can be measured and compared with their SM predictions.

An example of these electroweak observables includes the partial widths of the Z^0 to fermions, given at tree-level (without radiative corrections) in the SM by:

$$\Gamma(Z^0 \to f\bar{f}) = C\frac{G_F M_Z^3}{6\sqrt{2\pi}}\left((g_V^f)^2 + (g_A^f)^2\right), \tag{1.2}$$

where G_F is Fermi's constant, M_Z is the mass of the Z^0, C is a color factor equal to 1 for leptons and 3 for quarks, and g_V^f and g_A^f denote the vector and axial couplings of the Z^0 to fermions, respectively. Measurements of the partial width to lepton pairs, hadrons, and the full Z^0 width agree with SM predictions at the 10^{-3} level. Measurement of the invisible width of the Z^0 (the full width minus the sum of the partial widths to all visible final states), divided by the SM prediction for the partial width $\Gamma(Z^0 \to \nu\bar{\nu})$, indicates that the number of neutrino species is equal to 3, in agreement with the 3 generations of the SM.

It is particularly interesting that the LEP/SLC measurements are precise enough to be sensitive to radiative corrections to electroweak observables. This is demonstrated by measurements of the quantities $\Gamma_{\ell\ell} = \Gamma(Z^0 \to \ell^+\ell^-)$ and

$$\sin^2(\theta_{eff}^{lept}) = \frac{1}{4}(1 - \frac{g_V^\ell}{g_A^\ell}). \tag{1.3}$$

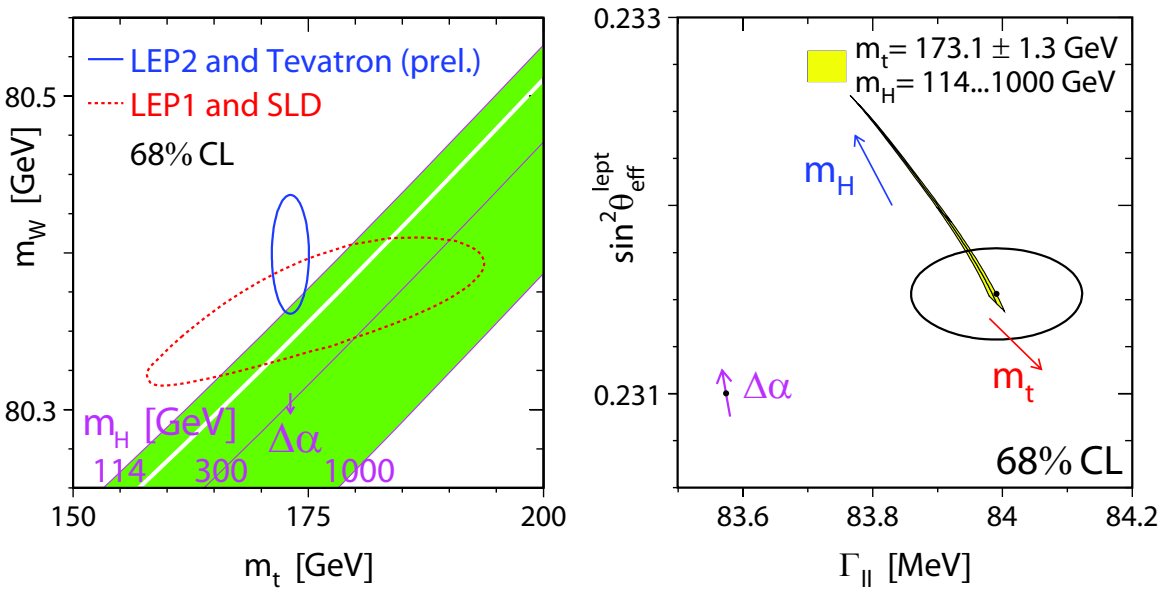

Figure 1.1: Left: comparison of the indirect (dotted red contour) and direct (solid blue contour) measurements of the charged weak vector boson mass m_W and top quark mass m_t with the SM prediction (shaded green diagonal region), which depends on the Higgs mass m_H and fine structure constant α. Right: comparison of the measurements of $\sin^2(\theta^{lept}_{eff})$ and $\Gamma_{\ell\ell} = \Gamma(Z^0 \to \ell^+\ell^-)$ (solid black contour) with the SM prediction with electroweak radiative corrections included (shaded yellow diagonal region), which depends on the Higgs mass and the top quark mass. The point in the lower left-hand corner is the tree-level QED prediction, which depends on α. All contours indicate measurements at 68% confidence level [26].

In Fig. 1.1 (right) the measurements of $\sin^2(\theta^{lept}_{eff})$ vs. $\Gamma_{\ell\ell}$ are compared with the SM predictions. The QED prediction without radiative corrections does not agree with the measured values, while the SM prediction with electroweak radiative correction agrees well. This demonstrates the sensitivity of the LEP/SLC measurements to radiative corrections, which are also sensitive to the Higgs mass and again indicate that a light Higgs is preferred.

Numerous other precise measurements have been carried out at the LEP and SLC experiments. A summary table which compares several of these measurements to their predicted SM values is shown in Fig. 1.2. Both the achieved experimental precision and the agreement with SM predictions are striking. A global fit comparing the SM predictions to all measured electroweak

Figure 1.2: Comparisons of precise measurements of electroweak observables with their SM predictions [26]. The measured value of each observable is denoted $O^{\rm meas}$, its uncertainty is $\sigma^{\rm meas}$, and the value of the observable extracted from a global fit comparing measured electroweak observables to their SM predictions is $O^{\rm fit}$.

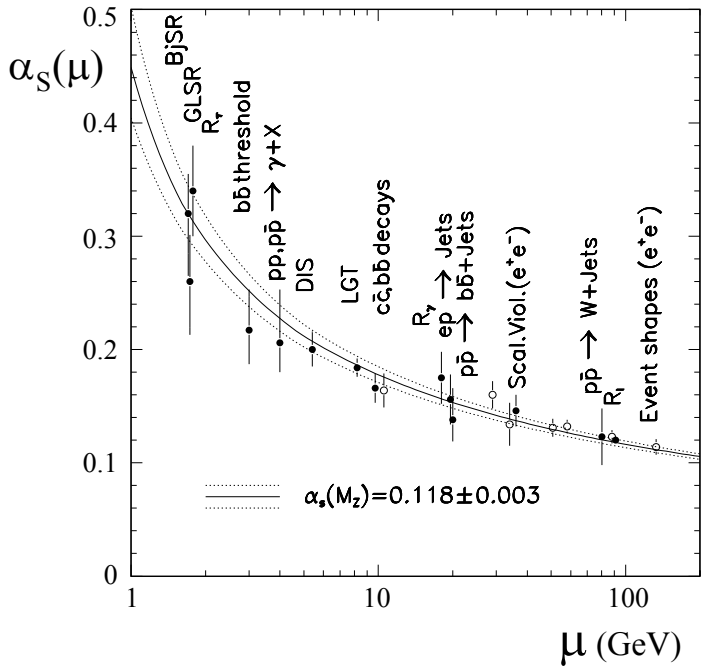

Figure 1.3: Dependence of the strong coupling constant α_S on the energy scale μ [27]. Several measurements are compared with the SM prediction corresponding to $\alpha_S = 0.118 \pm 0.003$ evaluated at the Z^0 mass. The open circles denote measurements based on event shape variables.

observables returns a probability of 4.5%. If one anomalous measurement of the weak mixing angle from the NuTeV experiment [28] at Fermilab is excluded, this probability increases to 27.5% [29].

QCD was first verified by the observation of three-jet events mediated by the process $e^+e^- \rightarrow q\bar{q}g$, which constituted the first experimental observation of the gluon g. The strong coupling constant of the $q\bar{q}g$ vertex is denoted α_S. The SM predicts that this coupling constant depends on the energy scale μ at which it is measured, and allows the energy dependence to be calculated explicitly using a procedure called renormalization group. In Fig. 1.3, the SM prediction for the value of α_S as a function of μ is compared to several experimental measurements, and excellent agreement between the SM prediction and the measurements is obtained. Two qualitative features of the energy dependence of α_S are also notable. First, α_S becomes very small as μ is increased, demonstrating the phenomenon of asymptotic freedom in which quarks become weakly-coupled

at high energy scales. Second, α_S becomes large at an energy scale $\mu \lesssim \Lambda_{QCD} = O(10^2)$ MeV. In this regime the theory becomes non-perturbative and theoretical calculations become much less precise. This highlights an advantage of e^+e^- colliders with respect to hadron colliders, which are dominated by QCD processes and are therefore subject to the theoretical uncertainties intrinsic to non-perturbative QCD.

1.3 Evidence for Physics Beyond the Standard Model

Despite the success of the SM, there is a large body of evidence which indicates that it cannot be the final, most general theory of particle physics. The SM is not capable of explaining why the gravitational force is 32 orders of magnitude weaker than the electroweak force, a discrepancy known as the hierarchy problem [30]. A useful way to understand the magnitude of this discrepancy is to imagine picking up a paper clip with a small magnet. The paper clip accelerates upward, indicating that the electromagnetic force exerted by the magnet is stronger than the gravitational force exerted by the entire planet. An equivalent statement of the problem is the discrepancy between the electroweak energy scale of order 100 GeV and the Planck scale given by $M_P = 1/\sqrt{G_N} = O(10^{19})$ GeV at which gravity becomes strong, where G_N is Newton's gravitational constant. Another intrinsic problem of the SM involves the gauge coupling constants of the electromagnetic, weak and strong forces. It is an experimentally verified prediction of the SM that these coupling constants vary depending on the energy scale at which they are measured, a phenomenon known as running coupling. If these three forces originate from a single 'Grand Unified Theory' (GUT), their coupling constants must all become equal at some high mass scale, resulting in 'gauge coupling unification.' However, the three coupling constants do not converge if their

energy dependence is as predicted by the SM [31].

There are also experimental indications that the SM is not the most general theory of particle physics. The SM predicts that neutrinos should be massless, while recent results from a variety of experiments [32] demonstrate conclusively that neutrinos can oscillate between flavors, requiring them to be massive. Extensions to the minimal SM in which neutrinos are massless are capable of providing mass to neutrinos, but they require the addition of an as yet unobserved right-handed neutrino, which is either very heavy or sterile, meaning that it does not couple to any gauge bosons. Furthermore, observations of the cosmic microwave background (CMB) radiation performed by the Wilkinson Microwave Anisotropy Probe (WMAP) indicate that $\sim 23\%$ of the mass-energy of the universe is composed of dark matter (DM) and $\sim 72\%$ is composed of dark energy (DE) [33]. While the nature of the DM and DE is currently not understood and is the subject of several ongoing experiments, neither can be accounted for in the SM, although extensions to the SM may provide DM candidates as discussed below. This means that the SM is not capable of explaining the existence of $\sim$95% of the content of the universe. Another problem intrinsic to the SM is the predominance of matter over antimmatter in the universe, while both should have been produced in equal amounts in the Big Bang. Although the SM is capable of explaining why there is more matter than antimatter via a mechanism involving charge-parity violation [34], the observed asymmetry is larger by several orders of magnitude than can be accounted for in the SM [24]. These numerous problems intrinsic to the SM provide compelling evidence that it is not the most general theory, motivating the search for a more general theory of which the SM is a low-energy approximation. These theories are known collectively as beyond-the-Standard Model (BSM) theories.

Table 1.2: Elementary particle content of the SM and Minimal Supersymmetric Model (MSSM). The MSSM introduces Supersymmetric partners to each of the SM particles with spin s differing by 1/2. The two MSSM Higgs doublets give mass to the up-type quarks (H_u) and down-type quarks and charged leptons (H_d).

SM	**MSSM**
quarks (s=1/2)	squarks (s=0)
q	$\tilde{q}$
leptons (s=1/2)	sleptons (s=0)
ℓ	$\tilde{\ell}$
gauge bosons (s=1)	gauginos (s=1/2)
$W^{\pm}$	$\tilde{W}^{\pm}$ (wino)
Z^0	$\tilde{Z}^0$ (zino)
γ	$\tilde{\gamma}$ (photino)
g	$\tilde{g}$ (gluino)
Higgs bosons (s=0)	higgsinos (s=1/2)
H_u	$\tilde{H}_u$
H_d	$\tilde{H}_d$

Although many BSM scenarios have been proposed, Supersymmetry[3] (SUSY) emerges as arguably the most well-motivated since it solves a number of the problems intrinsic to the SM. SUSY is a symmetry which relates fermions and bosons. It was discovered independently by three pairs of physicists, Gol'fand and Likhtman [37], Volkov and Akulov [38], and Wess and Zumino [39] in the early 1970's. The mathematical concept of SUSY first arose in early versions of string theory by Ramond [40] and Neveu and Schwarz [41] in 1971. The first realistic extension of the SM to include SUSY is the Minimal Supersymmetric Model (MSSM), introduced by Dimopoulos, Georgi, Raby and Wilczek in 1981 [42, 43]. In the MSSM the number of elementary particles is doubled by introducing for every SM particle a Supersymmetric partner (Superpartner) as summarized in Table 1.2. These Superpartners have the same quantum numbers as their corresponding SM particles, but have opposite spin statistics: SM fermions have bosonic Superpartners, and vice-versa. In addition, two

[3]For concise reviews of Supersymmetry, see [35, 36].

Higgs doublets are required, one to give mass to the up-type quarks and one to give mass to the down-type quarks and charged leptons [44].

In the MSSM, the effects of electroweak symmetry breaking lead to mixing of the Superpartners of the electroweak gauge bosons and Higgs doublets, the electroweak gauginos and higgsinos, respectively. The neutral electroweak gauginos ($\tilde{Z}^0$,$\tilde{\gamma}$) mix with neutral components of the higgsinos to give four neutralino mass eigenstates, denoted χ_i^0, with $i = 1, 2, 3, 4$. The lightest neutralino χ_1^0 is the lightest Supersymmetric particle (LSP) over most of the MSSM parameter space and constitutes a dark matter candidate as discussed below. The charged electroweak gauginos ($\tilde{W}^{\pm}$) mix with charged components of the higgsinos to give two chargino mass eigenstates, denoted $\chi_i^{\pm}$, with $i = 1, 2$. In addition, the two MSSM Higgs doublets mix to give five physical Higgs states: h^0, H^0, A^0, H^+ and H^- [45]. Over much of the MSSM parameter space, the lightest MSSM Higgs h^0 has properties which are similar or indistinguishable from the SM Higgs boson and the other four Higgs bosons are significantly heavier. If SUSY were an exact, unbroken symmetry then all Superpartners would have the same mass as their SM counterparts and would have been observed at particle colliders, but this has not occurred. SUSY must therefore be a broken symmetry, causing the Superparticles to be more massive than their SM partners and elude detection. The search for Supersymmetric particles and Higgs bosons is a major part of the physics program to be investigated at the LHC and at a future e^+e^- collider.

Many of the problems intrinsic to the SM may be solved if SUSY is realized in nature at a mass scale of order 1 TeV. SUSY provides a natural solution to the hierarchy problem [46], the enormous discrepancy between the electroweak scale and the Planck scale. In the SM, the electroweak scale is determined by the Higgs mass, which should therefore be of order 100 GeV/c^2. The

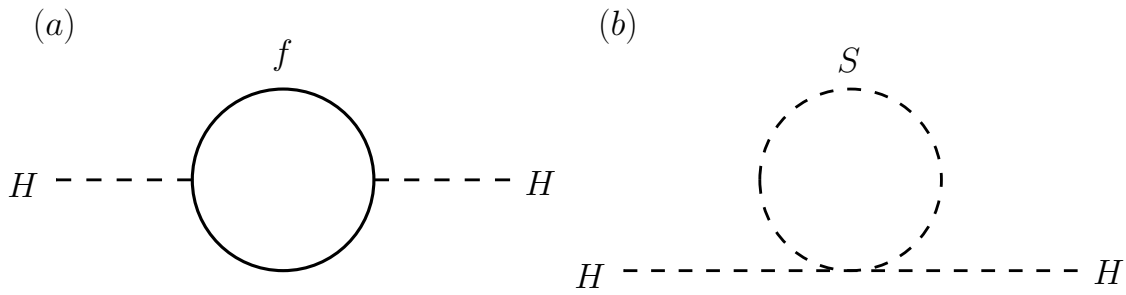

Figure 1.4: One-loop SM (a) and SUSY (b) contributions to the radiative correction of the Higgs squared mass.

physical Higgs squared mass m_H^2 is given by $m_H^2 = m_{H(0)}^2 + \delta m_H^2$ where $m_{H(0)}^2$ is the bare Higgs squared mass and δm_H^2 is the radiative correction to the Higgs squared mass from diagrams involving fermion loops. The one-loop contribution is depicted in Fig. 1.4a and its radiative correction is given by:

$$\delta m_H^2 = \frac{-|\lambda_f|^2}{8\pi^2} \Lambda_{UV}^2, \tag{1.4}$$

where λ_f is the Yukawa coupling of the Higgs to the fermion and Λ_{UV} is the ultraviolet cutoff, the energy scale above which the SM is no longer valid. If the SM were valid all the way up to the Planck scale (it cannot be valid above the Planck scale where gravity becomes strong because the SM does not include gravity), then $\Lambda_{UV} \approx M_P$ and the radiative correction to the Higgs squared mass is of order 10^{33} $(\mathrm{GeV}/c^2)^2$. In order to obtain a Higgs mass of order 100 GeV/c^2, it would be necessary to fine-tune the bare Higgs mass to cancel this correction. Considering that the bare Higgs mass and the radiative correction have completely different origins, this is regarded as an unacceptably miraculous coincidence. This problem is resolved quite naturally by SUSY, which introduces scalar Superpartners to the fermions which contribute additional radiative corrections to the Higgs squared mass. The one-loop contribution is depicted in Fig 1.4b and its radiative correction is given by:

$$\delta m_H^2 = \frac{+\lambda_S}{16\pi^2} \Lambda_{UV}^2, \tag{1.5}$$

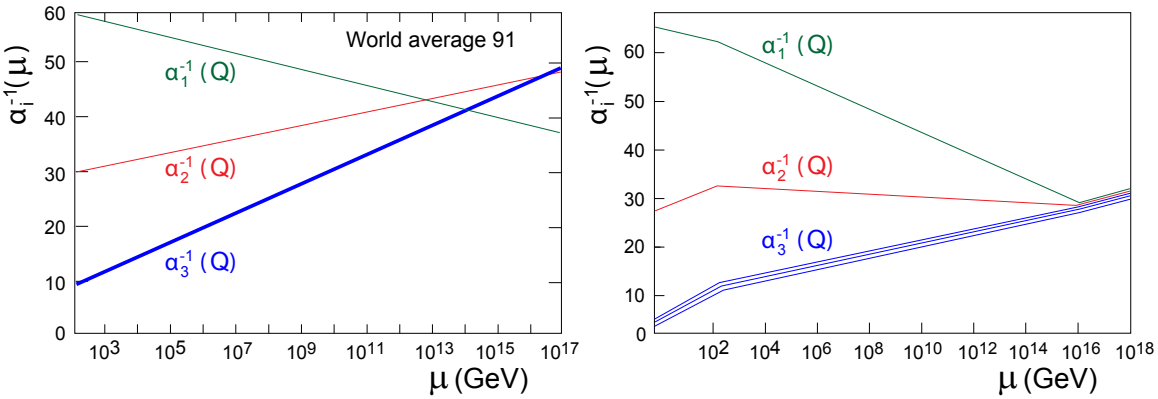

Figure 1.5: The three gauge coupling constants as a function of energy scale μ in the SM as measured at LEP (left), and in the MSSM (right) [31].

where λ_S is the Yukawa coupling of the Higgs to the scalar Superpartners. In SUSY, each fermion is accompanied by two complex scalars, so the negative fermionic radiative corrections will cancel with the positive scalar radiative corrections if $\lambda_S = |\lambda_f|^2$. This relationship is guaranteed to hold in unbroken SUSY and also in so-called 'soft' SUSY-breaking scenarios, which are therefore the focus of theoretical consideration [35]. In this case the radiative corrections proportional to Λ_{UV}^2 cancel and only the following logarithmic dependence on Λ_{UV} remains:

$$\delta m_H^2 = m_{soft}^2 \left(\frac{\lambda}{16\pi^2} \ln(\Lambda_{UV}/m_{soft}) \right). \tag{1.6}$$

Here m_{soft} is the largest SUSY mass scale and λ is a dimensionless coupling of order 1. If we take $\Lambda_{UV} \approx M_P$ then m_{soft} must be at most about 1 TeV in order to avoid the need for fine-tuning of the Higgs mass. This gives the first hint that the relevant mass scale of new physics is at the TeV-scale.

SUSY also provides a solution to the problem of gauge coupling unification [31]. As shown in Fig. 1.5, the addition of SUSY particles at a mass scale of order 1 TeV alters the running of the gauge coupling constants and causes them to converge at the GUT scale, $M_{GUT} = O(10^{16})$ GeV, providing another clue that new physics manifests at the TeV-scale. Another hint

in favor of SUSY involves the Weinberg mixing angle parameter, measured to be $\sin^2(\theta_W) = 0.23149 \pm 0.0002$ [26]. The MSSM predicts that $\sin^2(\theta_W) = 0.2336 \pm 0.0017$ [47], in good agreement with the measured value.

One of the most appealing features of SUSY is that it may explain the origin of DM [48]. For reasons discussed in Chap. 4.1, the experimentally preferred candidate for DM is a weakly-interacting massive particle (WIMP) with mass of order 100 GeV/c^2. Although this gives only an estimate of the WIMP mass, the fact that this estimate points to the same mass scale at which new physics related to electroweak symmetry breaking is expected to manifest provides suggestive evidence that new physics and DM are related. In addition, general considerations allow for further constraints. The WIMP candidate particle must be electrically neutral because otherwise it would couple to the photon and be visible. It also must be stable on the time-scale of the universe because otherwise it would have decayed by now. Remarkably, SUSY introduces a particle with all of these necessary properties. Due to a conserved charge called R-parity which is imposed to forbid the proton from decaying rapidly, the LSP is stable. This occurs for the same reason that the proton is stable, since it cannot decay to a lighter particle while conserving baryon number. Over most of the MSSM parameter space, the LSP is the lightest neutralino χ_1^0. This particle is neutral, stable, and is predicted to have a mass of order 100 GeV/c^2, making it a natural DM candidate. The solution to the hierarchy problem, gauge coupling unification, the correct prediction of the value of $\sin^2(\theta_W)$, and the introduction of a dark matter candidate particle make SUSY an appealing candidate for the BSM theory.

1.4 Probing Physics Beyond the Standard Model

Given that there is compelling evidence for physics beyond the SM, it is necessary to develop strategies to probe this new physics. In this thesis I discuss two complementary strategies which use data collected in e^+e^- collisions at lepton colliders. One strategy, which relies on an indirect method, is to search for effects mediated by new, heavy particles in low energy data by making precise measurements. Alternatively, it is possible to probe new physics by increasing the collision energy and searching for direct production of new particles.

1.4.1 Probing New Physics at Lepton Colliders

As discussed in [49, 50], the general purpose ATLAS and CMS experiments at the LHC will probe Higgs physics and a wide variety of new physics scenarios. The LHC will provide proton-proton collisions up to a CM collision energy $\sqrt{s}$=14 TeV, exploring the $\sim$1 TeV scale at which new physics is expected to manifest. In addition, the cross section for production of new particles in proton-proton collisions is large. If SUSY exists it is very likely to be discovered at the LHC, which is also sensitive to many other new physics scenarios, such as theories with extra dimensions. The LHC is also designed to discover the Higgs particle over the full allowed mass range up to $\sim$1 TeV, so if the Higgs does exist it will be discovered. The data collected at the LHC will allow for numerous measurements of SM observables, in some cases with better precision than has been obtained to date. However, lepton colliders possess several advantages with respect to hadron colliders which in many cases lead to significant improvement in the precision of measurements and the sensitivity to rare processes [51, 52]. At a hadron collider such as the LHC, the interacting particles are quarks and gluons contained inside the proton which carry some

fraction of its momentum. Because the momenta of the interacting particles are not known, the initial state energy and momentum with respect to the lab frame are also not known. At a lepton collider the beam particles are elementary as opposed to composite, so the initial state energy and momentum are known with precision, leading to several advantages. First, selection criteria based on initial state properties are often useful in selecting signal events in data which is dominated by background processes. In the analysis of *BABAR* data discussed in Chap. 2, the primary requirement which selects the signal events is the presence of an electron or muon with energy close to half the initial state energy. Using this requirement, sensitivity to a signal rate which is smaller by three orders of magnitude with respect to the background rate is achieved. The precise knowledge of the initial state energy is also crucial in the investigation of the H^0A^0 production process discussed in Chap. 4, in which the final state consists of four b jets. A constrained kinematic fit algorithm described in Chap. 4.3.2 is performed, which uses the constraint that the sum of the jet energies must be equal to the initial state energy to improve the precision of the jet energy measurements. This leads to significant improvement in the precision of measurements related to the determination of the neutralino DM candidate relic density.

Furthermore, the CM collision energy $\sqrt{s}$ of a lepton collider may be precisely tuned to correspond with the mass of some particle or resonance in order to investigate its properties. An example of this which has been discussed above is the LEP/SLC physics program carried out by tuning the collision energy to correspond to the mass of the Z^0 boson. This property is also crucial in the analysis of *BABAR* data discussed in Chap. 2. In this case, the resonance of interest is an excited state of the $b\bar{b}$ bound system called the $\Upsilon(3S)$. By tuning the collision energy to correspond to the $\Upsilon(3S)$ mass, the *BABAR* detector has recorded $O(10^8)$ $\Upsilon(3S)$ decays in about two months.

This allows for the search for rare and exotic $\Upsilon(3S)$ decays with sensitivity to branching fractions as small as $O(10^{-7} - 10^{-6})$, after including effects from backgrounds and signal efficiencies.

Another advantage of lepton colliders which has been previously discussed is that they are dominated by electroweak processes, as opposed to hadron colliders which are dominated by QCD processes subject to the non-perturbative theory uncertainties discussed in Chap. 1.2. The result of these advantages is that in many cases leptons colliders are capable of measuring observables with higher precision than hadron colliders. Furthermore, there exist several measurements, including both of the analyses presented in this thesis, which can only be performed at lepton colliders.

1.4.2 Indirect Probes of New Physics at Low Energy

Although the new physics is expected to manifest at the TeV-scale, it is possible to probe this new physics indirectly by making precise measurements with data collected at much lower collision energies. Although the new particles are too heavy to be directly produced, they may be produced virtually in loops and lead to observable effects. An example is the indirect measurement of the top quark mass discussed in Chap. 1.2, which was performed at LEP and SLC below the top quark production threshold. My analysis of *BABAR* data also uses an indirect measurement to probe new physics.

In general, processes observed at colliders are dominated by 'tree-level' diagrams, which do not contain loops. In this case, loop diagrams constitute small, higher-order corrections to the tree-level processes, suppressed by powers of a small coupling constant. Corrections mediated by loops containing new, heavy particles are suppressed relative to the SM loop contributions, and therefore lead to very small corrections to the overall rate which are in general not observable. If instead the tree-level diagram is forbidden by some SM symmetry, the SM loop diagram provides

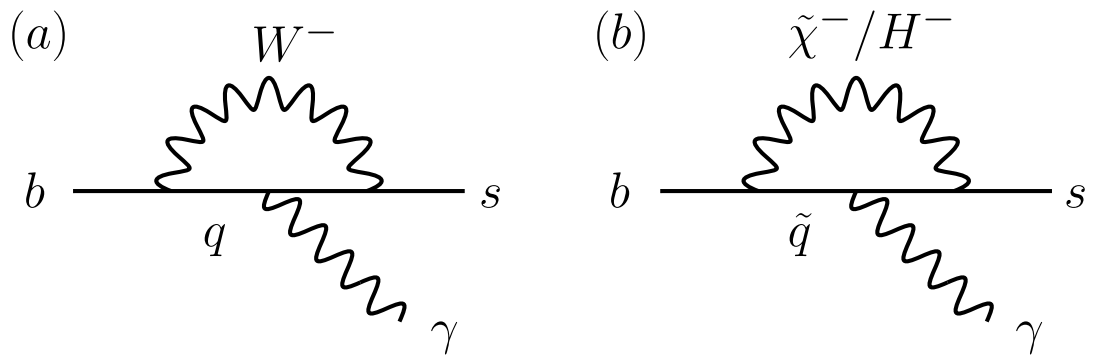

Figure 1.6: (a) SM and (b) SUSY contributions to the $b \to s\gamma$ process.

the dominant contribution. In this case the relative corrections mediated by loops with new particles become enhanced and may be measurable. An example is the $b \to s\gamma$ process, which has been the subject of several measurements and theoretical calculations [53–59]. The tree-level diagram for this process is forbidden in the SM because it involves a forbidden flavor-changing neutral current (FCNC) interaction, so the loop diagram in Fig. 1.6a involving the emission and reabsorption of a virtual $W^{\pm}$ boson provides the dominant contribution in the SM. It is possible however, that new particles such as those predicted by SUSY may contribute additional loop diagrams, shown in Fig. 1.6b, which lead to corrections in the rate of the $b \to s\gamma$ process. It is therefore possible to search for new physics effects by looking for differences between the SM prediction and the observed rate for $b \to s\gamma$. The SM prediction for $BF(b \to s\gamma)$ is of order 10^{-4} and the corrections to this branching fraction mediated by new particles are significantly smaller than this. This implies that extremely precise measurements are required in order to probe new physics using this method, and these measurements must be performed at lepton colliders for reasons discussed in Chap. 1.4.1. To date, no discrepancy between the SM prediction and the observed rate has been found, and this result has been used to exclude regions of the MSSM parameter space [57]. Since the $b \to s\gamma$

process is observable in collisions at $\sqrt{s} = O(10)$ GeV, this provides an example in which new physics at the TeV-scale may be probed using data collected at much lower energies.

In Chapter 2, I present an indirect probe of new physics by searching for decays of the $\Upsilon(3S)$ particle to two charged leptons of unlike flavor in data collected with the *BABAR* detector at a CM energy of 10.35 GeV [60]. This process is strictly forbidden in the minimal SM in which neutrinos are massless due to the symmetry of lepton flavor conservation, and remains unobservable even after the SM is extended to include neutrino masses. However, this decay may be mediated by new particles introduced by several BSM scenarios, and the observation of this process would therefore provide a clear, unambiguous signal of new physics. The previous branching fraction upper limit on this process comes from the CLEO collaboration at CESR and is of order 10^{-5}. In the analysis described in this thesis, sensitivities of order 10^{-6} are obtained and are used to place the best upper limits to date on the branching fractions $BF(\Upsilon(3S) \to e\tau)$ and $BF(\Upsilon(3S) \to \mu\tau)$. These results are then interpreted in terms of constraints on the coupling and mass scale of new physics contributing to lepton-flavor violating $\Upsilon(3S)$ decays at the TeV-scale.

1.4.3 The Need for High Performance Detectors at Future Colliders

Although it is possible to search for new physics with low energy data, the primary strategy is to increase the collision energy above the threshold for new particle production, leading to direct production of these particles. One possible realization of a TeV-scale lepton collider is the proposed International Linear Collider (ILC) [61], which would initially collide electrons and positrons at $\sqrt{s}$=500 GeV and would be upgradeable to 1 TeV. The physics program at the ILC, or in general any TeV-scale lepton collider, would complement that of the LHC by providing precise measurements of the properties of the Higgs boson and precision probes of new physics [51, 52].

However, the currently available detector technology is not sufficient to realize the full physics potential of such a collider. As discussed in Chap. 3.1, the research and development (R&D) effort to produce such a detector is the subject of a world-wide study [62]. In particular, the performance of the vertex tracker (VTX) is required to surpass that of any existing vertex tracker. The VTX is used to distinguish between light quarks and heavy, long-lived particles such as b and c quarks as well as τ leptons, known as flavor tagging. Excellent flavor tagging capability is required in particular to measure the Higgs branching fractions to $b\bar{b}$, $c\bar{c}$, and $\tau^+\tau^-$. This is required to check the relationship in Eq. 1.1 and hence determine if the Higgs mechanism is realized in nature. In addition, heavy fermions provide signatures of several new physics scenarios, such as SUSY with large $\tan\beta$, the ratio of the vacuum expectation values of the two SUSY Higgs doublets. The analysis of H^0A^0 production at a future lepton collider also relies heavily on the flavor tagging performance of the VTX, since the final states contain b quarks and τ leptons.

In Chapter 3 I discuss R&D of advanced Silicon pixel sensors for use in the vertex tracker of a future TeV-scale lepton collider [63, 64]. In order to achieve the required flavor tagging performance, these sensors must be very thin in comparison with conventional Silicon tracking detectors. This is motivated by the need to reduce transverse deflections of particles traversing the Silicon, which occurs as a result of multiple scattering. Conventional hybrid pixel detectors, which consist of separate Silicon sensors and readout electronics chips, are too thick to meet the required flavor tagging performance. Instead, monolithic devices consisting of a single sensor with integrated readout electronics are required. In Chap. 3.3 I discuss R&D efforts aimed at producing thin sensors built in the CMOS monolithic active pixel sensor technology [65]. These thin sensors are then used to produce a small-scale tracker prototype, and the tracking and vertexing performance are assessed

using charged particle beams, as discussed in Chap. 3.4.

1.4.4 Direct Probes of New Physics at High Energy

As mentioned above, a TeV-scale lepton collider with a high performance detector will complement the LHC and allow for detailed investigation of the Higgs mechanism and new physics scenarios with unparalleled precision. In particular, if SUSY is realized in nature and the mass of the lightest SUSY particles are light enough to be produced, such a collider will allow for multiple precise measurements of SUSY observables. In this case SUSY is very likely to be discovered at the LHC, but precise measurements of observables necessary to fully understand the nature of the new physics remain difficult [51, 52]. A high-energy lepton collider would provide precision probes of the new physics discovered at the LHC. Supersymmetric particles can be produced via pair production at a lepton collider in several channels, including:

$$e^+e^- \to \chi_i^0\chi_i^0,\ \ \chi_i^+\chi_i^-,\ \ \tilde{\ell}^+\tilde{\ell}^-,\ \ \tilde{\nu}\tilde{\nu}^*,\ \ \tilde{q}\tilde{q}^*. \tag{1.7}$$

Typical cross sections for these processes are of order $10 - 100$ fb depending on the mass scale of the lightest SUSY particles, leading to $10^3 - 10^4$ SUSY events produced per year assuming an annual integrated luminosity of order 100 fb^{-1}.

One area in which the measurements available at a high energy lepton collider will be particularly useful is understanding the connection between new physics and DM [66, 67]. As discussed in Chap. 4.1, if DM is composed of Supersymmetric particles (usually the lightest neutralino χ_1^0), these particles will be produced at TeV-scale colliders. This will allow for detailed studies of their properties and of the properties of particles which couple to them. Particularly interesting is that these measurements allow for the determination of the neutralino abundance in the universe,

quantified by the neutralino relic density Ω_χ. Comparison between this quantity and the DM relic density as determined from cosmological observations will have striking implications on our understanding of dark matter, by allowing us to determine if it is composed of Supersymmetric particles.

In Chapter 4, simulation studies of a dark-matter motivated SUSY scenario at a future lepton collider are discussed [68]. For this study, a benchmark point is chosen in which the neutralino relic density is determined by the rate of the annihilation process $\chi_1^0\chi_1^0 \to A^0 \to b\bar{b}/\tau^+\tau^-$, where A^0 is the CP-odd SUSY Higgs boson. The rate of this process depends in turn on the properties of the A^0 [66, 67], which are measured by examining the processes $e^+e^- \to H^0A^0 \to b\bar{b}b\bar{b}$ and $e^+e^- \to H^0A^0 \to b\bar{b}\tau^+\tau^-$, where H^0 is the CP-even SUSY Higgs boson. Measurements of the A^0 mass, width and branching fractions are performed and used to constrain the neutralino annihilation rate, which determines Ω_χ . This analysis relies heavily on the excellent performance of the vertex tracker in order to identify the final-state b quarks and τ leptons.

Chapter 2

Search for New Physics in Low Energy e^+e^- Collisions at *BABAR*

2.1 Motivation

As discussed in the previous chapter, there is evidence that physics beyond the SM exists and we expect that it should manifest at the TeV-scale. As discussed in Chap. 1.4, precision measurements of the rate of the $b \to s\gamma$ process produced at a CM collision energy $\sqrt{s} = O(10)$ GeV are sensitive to corrections introduced by new, heavy particles. This is because the tree-level diagram mediating this process is a forbidden flavor changing neutral current interaction, so the loop diagram in Fig. 1.6a is the dominant SM contribution. This results in large suppression of the rate of $b \to s\gamma$, so a small correction due to a loop with new, heavy particles may be observable.

It is also possible for a process to be strictly forbidden to all orders by some SM symmetry. In this case, a precise measurement of the branching fraction is not needed in order to probe

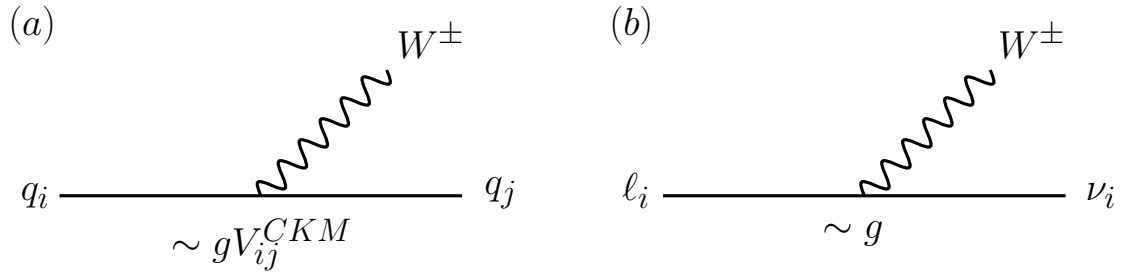

Figure 2.1: (a) A flavor-changing quark transition. The effective coupling between quarks of different flavor is proportional to the product of the weak coupling strength g and an element of the Cabibbo-Kobayashi-Maskawa (CKM) matrix V_{ij}^{CKM}. (b) A flavor-conserving lepton transition. No mixing matrix is present, and the coupling is proportional to g only.

new physics at high mass scales; instead, mere observation of the process is sufficient. A specific example of such a SM symmetry is the conservation of lepton flavor [69]. In the SM, the coupling of fermions to the weak vector bosons is specified by the following Lagrangian [2]:

$$\Delta\mathcal{L} = \frac{-g}{\sqrt{2}} W_{\mu}^{+} (\bar{\nu}_L^i \gamma^{\mu} e_L^i + \bar{u}_L^i \gamma^{\mu} V_{ij}^{CKM} d_L^j) + h.c. \tag{2.1}$$

Here g is the weak coupling strength, W^+ is the positively charged weak vector boson, ν_L, e_L, u_L and d_L are left-handed neutral and charged leptons, up-type and down-type quarks, respectively. The 4-vector of gamma matrices is denoted γ^{μ}, the indices $i, j = 1, 2, 3$ indicate the generation, or flavor, number and $h.c.$ denotes the Hermitian conjugate, which gives the coupling term of the W^- to fermions. Quarks of different flavor are allowed to couple to one another, and these couplings are specified by the elements of a unitary matrix called the Cabibbo-Kobayashi-Maskawa (CKM) matrix V^{CKM} [18]. This term in the Lagrangian leads to diagrams in which a quark changes flavor by absorbing or emitting a $W^{\pm}$ as shown in Fig. 2.1a. Decays of a charged weak vector boson to two quarks of different flavor are also allowed. However, no such mixing matrix is present in the leptonic coupling term, which forbids leptons of different flavor from coupling to one another. Leptons may absorb or emit a $W^{\pm}$ as shown in Fig. 2.1b, but they may not change flavor, and

decays of a $W^{\pm}$ to two leptons of different flavor are also forbidden. Since there is no other term in the SM Lagrangian which couples fermions of different flavor to one another, this leads to the SM prediction that lepton flavor should be conserved.

Lepton flavor conservation is an exact symmetry in the minimal SM, in which neutrinos are massless. The recent discovery that neutrinos are in fact massive and can oscillate between different flavors violates flavor conservation among the neutral leptons, and demonstrates that the minimal SM must be extended. However, the rates for processes involving flavor violation among charged leptons remain unobservably small. This motivates the search for charged lepton-flavor violating (CLFV) processes as probes of new physics scenarios. CLFV decays of the μ and τ leptons have received special attention, and the rates for these processes have been calculated in Supersymmetric scenarios [70, 71]. It is particularly interesting that in regions of the SUSY parameter space which are consistent with cosmological observations including those from WMAP, the rates for the processes $\mu \to e\gamma$ and $\tau \to \mu\gamma$, as well as $\mu \to e$ conversion in the presence of a Titanium nucleus, may be close to the current experimental upper limits. Several experiments have been proposed to improve the sensitivity to these processes, providing promising prospects for new physics discoveries [72].

Another example of a CLFV process is the decay of a neutral particle such as the Υ particle produced at *BABAR* to two charged leptons of different flavor. Such a process is strictly forbidden in the minimal SM as shown in Fig. 2.2a, but the addition of neutrino masses to the SM introduces the diagram shown in Fig. 2.2b, which involves a neutrino oscillation. However, the branching fraction for this process is suppressed by $(\delta(m_\nu)^2/M_W^2)^2 \lesssim 10^{-48}$ [73, 74] and this decay is therefore unobservable, which implies that the observation of CLFV in Υ decays would

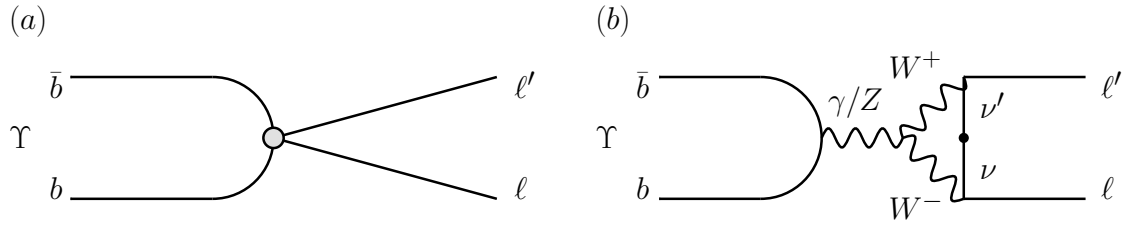

Figure 2.2: (a) Decay of the Υ $b\bar{b}$ bound state to two charged leptons of unlike flavor, which is strictly forbidden in the minimal SM. (b) Decay mediated by a neutrino oscillation, which is introduced by the extension of the SM to include neutrino masses.

provide a clear, unambiguous signal of new physics. Here $\delta(m_\nu)^2$ is the difference between the squared masses of two neutrinos of different flavor and M_W is the mass of the charged weak vector boson. A useful way to understand why this suppression factor is so large is that neutrinos oscillate over long distance scales such as several kilometers, but the diagram in Fig. 2.2b requires that the neutrino oscillate over the length scale corresponding to the $W^\pm$ lifetime $\sim 10^{-15}$ m.

In this analysis, documented in [60], I search for decays of the Υ $b\bar{b}$ bound state to two charged leptons of different flavor in data produced at the PEP-II collider and collected with the *BABAR* detector. The Υ particle has energy levels denoted $\Upsilon(nS)$, where $n = 1, 2, 3, 4....$ For reasons discussed in Chap. 2.5, I search for lepton-flavor violating decays of the narrow $\Upsilon(3S)$ resonance as opposed to the $\Upsilon(4S)$, which constitutes the bulk of the data collected at *BABAR*. Although the $\Upsilon(3S) \to \ell\ell'$ process, in which ℓ and ℓ' denote charged leptons of unlike flavor, is unobservable in the SM, there are several BSM scenarios in which the rate for this process may be sizable [75, 76], including Supersymmetry or other exotic scenarios as shown in Fig. 2.3. Any interaction which mediates this decay may be parameterized as a generic four-fermion $b\bar{b}\ell\ell'$ contact interaction shown in Fig. 2.3f, using effective field theory. In Chap. 2.13, limits are derived on the effective coupling constant $\alpha_{\ell\ell'}$ and mass scale $\Lambda_{\ell\ell'}$ of such an interaction, and sensitivity to new physics at the TeV-scale is achieved.

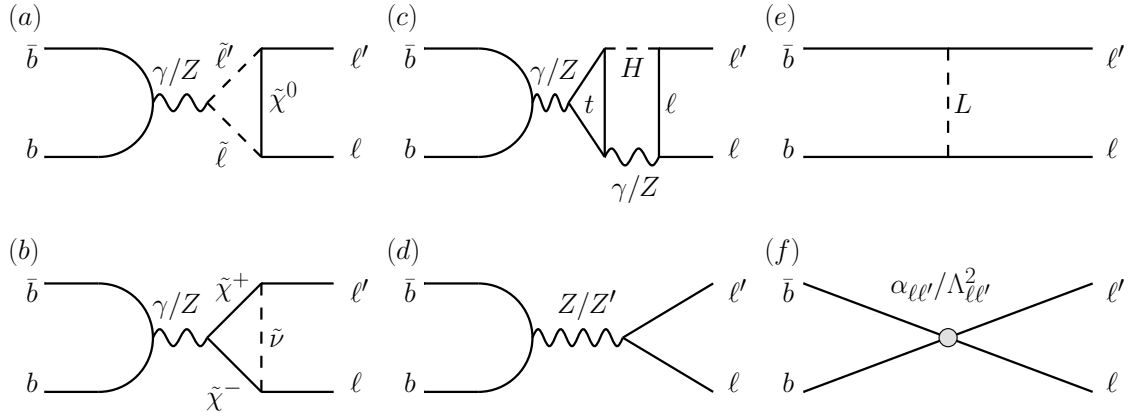

Figure 2.3: BSM processes mediating lepton-flavor violating decays of the Υ $b\bar{b}$ bound state to two charged leptons of different flavor. Processes (a) and (b) are mediated by loops containing Supersymmetric particles. Process (c) is mediated by a SUSY Higgs doublet H and process (d) is mediated by an anomalous Z or heavy cousin of the Z denoted Z'; these particles may couple to charged leptons of different flavor. Process (e) is mediated by the exchange of a leptoquark L, a particle postulated in Grand Unified Theories which couples to both quarks and leptons. Process (f) depicts a generic 4-fermion contact interaction with coupling constant $\alpha_{\ell\ell'}$ and mass scale $\Lambda_{\ell\ell'}$.

The rest of this chapter is organized as follows. In Chap. 2.2, prior constraints on lepton-flavor violating Υ decays are discussed. In Chap. 2.3 and Chap. 2.4 the principal components of the PEP-II collider and *BABAR* detector are reviewed, respectively. In Chap. 2.5 the production of Υ particles at PEP-II is reviewed and the motivation for searching for CLFV in $\Upsilon(3S)$ decays is presented. In Chap. 2.6 the data and simulated event samples used in this analysis are presented. In Chap. 2.7 the signal signatures and backgrounds are reviewed, and the selection procedure for isolating the signal events is presented in Chap. 2.8. The fit procedure is presented in Chap. 2.9 and validation studies of this procedure are presented in Chap. 2.10. In Chap. 2.11 the determination of systematic uncertainties is presented. Results are given in Chap. 2.12 and the interpretation in terms of constraints on new physics is presented in Chap. 2.13. A selection of results from other searches for CLFV are presented in Chap. 2.14.

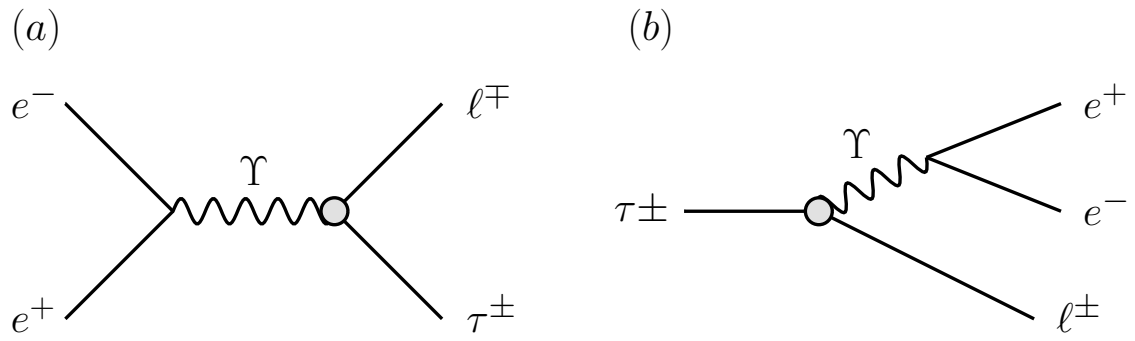

Figure 2.4: (a) Diagram mediating the process $e^+e^- \to \Upsilon \to \ell^\mp\tau^\pm$ and (b) diagram mediating the process $\tau^\pm \to e^+e^-\ell^\pm$ via virtual exchange of an Υ.

2.2 Prior Constraints on Lepton-Flavor Violating Υ Decays

There has been considerable interest in searches for CLFV in decays of several particles including μ and τ leptons as well as B and K mesons, and the lack of observation of these decays has been used to place constraints on new physics scenarios [77–86]. However, CLFV in the Υ sector remains relatively unexplored. The only experimental constraints on CLFV Υ decays come from the CLEO experiment [87], which placed the 95% confidence level upper limit $BF(\Upsilon(3S) \to \mu\tau) < 2.03 \times 10^{-5}$ based on 5.9×10^6 collected $\Upsilon(3S)$ decays. In this analysis the achieved sensitivity to $BF(\Upsilon(3S) \to \mu\tau)$ is greater by a factor of several, due to the larger data sample, sophisticated multivariate algorithms used for particle identification, and the inclusion of an additional hadronic decay mode of the τ. I also place the first upper limit on $BF(\Upsilon(3S) \to e\tau)$.

Theoretical constraints on the Υ CLFV decay branching fractions can be derived using an argument based on unitarity considerations [88]. As shown in Fig. 2.4, the diagram mediating the process $e^+e^- \to \Upsilon \to \ell\tau$ is related to the diagram mediating $\tau \to e^+e^-\ell$ via reordering of input and output lines (here and in the following $\ell = e, \mu$). If the Υ couples to $\ell\tau$, then by exchange it

must contribute to the decay $\tau^- \to e^+e^-\ell^-$. This allows the following relation to be derived:

$$BF(\Upsilon(nS) \to \ell\tau) \leq \frac{BF(\tau \to e^+e^-\ell)}{BF(\tau^- \to \ell^-\nu_\tau\bar{\nu}_\ell)} \frac{\Gamma(W \to \ell\nu)^2}{\Gamma(\Upsilon(nS))\Gamma(\Upsilon(nS) \to \ell^+\ell^-)} \left(\frac{M_{\Upsilon(nS)}}{M_W}\right)^6. \quad (2.2)$$

The current experimental upper limits $BF(\tau^- \to e^+e^-e^-) < 3.6\times10^{-8}$ and $BF(\tau^- \to e^+e^-\mu^-) < 2.7\times10^{-8}$ from the Belle collaboration [89] imply $BF(\Upsilon(3S) \to e\tau) \leq 5.6\times10^{-3}$ and $BF(\Upsilon(3S) \to \mu\tau) \leq 4.2 \times 10^{-3}$. Branching fractions of this magnitude would result in $O(10^5)$ lepton-flavor violating $\Upsilon(3S)$ decays in the data sample and would be easily observable, although the upper limit from the CLEO collaboration constrains $BF(\Upsilon(3S) \to \mu\tau)$ to be less than the theoretically allowed upper limit. A similar relation between $e^+e^- \to \Upsilon \to e\mu$ and $\mu^- \to e^+e^-e^-$ can be derived:

$$BF(\Upsilon(nS) \to e\mu) \leq \frac{BF(\mu \to e^+e^-e)}{BF(\mu^- \to e^-\nu_\mu\bar{\nu_e})} \frac{\Gamma(W \to \ell\nu)^2}{\Gamma(\Upsilon(nS))\Gamma(\Upsilon(nS) \to \ell^+\ell^-)} \left(\frac{M_{\Upsilon(nS)}}{M_W}\right)^6. \quad (2.3)$$

In this case, the experimental upper limit $BF(\mu^+ \to e^+e^-e^+) < 10^{-12}$ from the SINDRUM collaboration [77] implies $BF(\Upsilon(nS) \to e\mu) < 2.7 \times 10^{-8}$. Since the data sample consists of $O(10^8)$ collected $\Upsilon(3S)$ decays, this process is unlikely to be observed and I therefore restrict my search to $\Upsilon(3S) \to \ell\tau$.

2.3 The PEP-II Collider

The data used in this analysis were collected with the *BABAR* detector at the PEP-II collider [90] at the Stanford Linear Accelerator (SLAC). Before the end of operations in early 2008, PEP-II nominally collided 9.0 GeV electrons with 3.1 GeV positrons at a CM energy equal to the $\Upsilon(4S)$ mass. The $\Upsilon(4S)$ is above the threshold for B meson pair production and decays almost exclusively to B^0B^0 or B^+B^-. This facilitates the primary physics mission of *BABAR*, the search for CP violation in the decay of B mesons. The energy asymmetry between the electrons and positrons

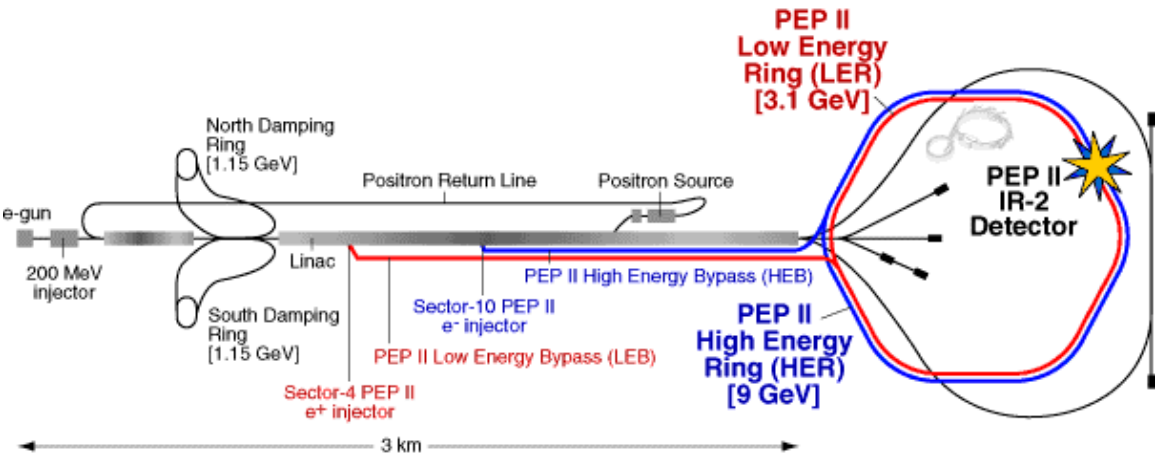

Figure 2.5: Layout and principle components of SLAC and the PEP-II collider.

causes the Υ system to be boosted with $\beta\gamma$=0.56 with respect to the lab frame. In order to produce $\Upsilon(3S)$ mesons, the electron beam energy is reduced to 8.6 GeV. The concept of an asymmetric-energy B factory was first proposed by Piermaria Oddone of LBNL in 1989 [91] and has since been adopted by the Belle experiment at the KEK collider [92] in Japan.

There are several performance requirements which drove the design of the PEP-II collider. The design luminosity is to reliably achieve a peak value of $3 \times 10^{33}\text{cm}^{-2}\text{s}^{-1}$, and upgrades have increased this value by a factor of 3-4. The collider must be capable of storing high currents of order 1-2 A with excellent stability and colliding the beams with a CM energy of order 10 GeV. Acceptable detector background levels must also be maintained. These requirements are met by the SLAC accelerator and PEP-II collider, depicted in Fig. 2.5. SLAC produces and accelerates electrons and positrons using linear accelerators (linacs) based on the radio-frequency (RF) cavity technology. Electrons are accelerated to 9.0 GeV and injected into the high energy PEP-II storage ring. Positrons are produced by colliding electrons on a Tungsten target, producing bremsstrahlung photons which convert to electron-positron pairs. The positrons are collected, accelerated to 3.1

Table 2.1: PEP-II beam parameters for the design specifications [93], typical operating conditions during the collection of $\Upsilon(4S)$ data used in this analysis, and typical operating conditions during the $\Upsilon(3S)$ data collection period. The high-energy ring (HER) stores the electrons, the low-energy ring (LER) stores the positrons.

Quantity	**Design**	**$\Upsilon(4S)$ Typical**	**$\Upsilon(3S)$ Typical**
Energy HER/LER (GeV)	9.0 / 3.1	9.0 / 3.1	8.6 / 3.1
Current HER/LER (A)	0.75 / 2.15	0.9-1.9 / 1.3-2.6	0.9-1.8 / 1.3-2.4
# of bunches	1658	1722	1722
Bunch Spacing (ns)	4.2	4.2	4.2
Luminosity (10^{33}cm^{-2}s^{-1})	3	4.4-10.4	4.5-10.1
Luminosity (pb^{-1}/day)	135	267-619	333-658

GeV, and injected into the low energy PEP-II storage ring. The electrons and positrons circulate in opposite directions multiple times before colliding at the interaction region. The PEP-II beam parameters are summarized in Table 2.1, and the integrated luminosity delivered by the PEP-II collider and recorded with the *BABAR* detector is shown in Fig. 2.6.

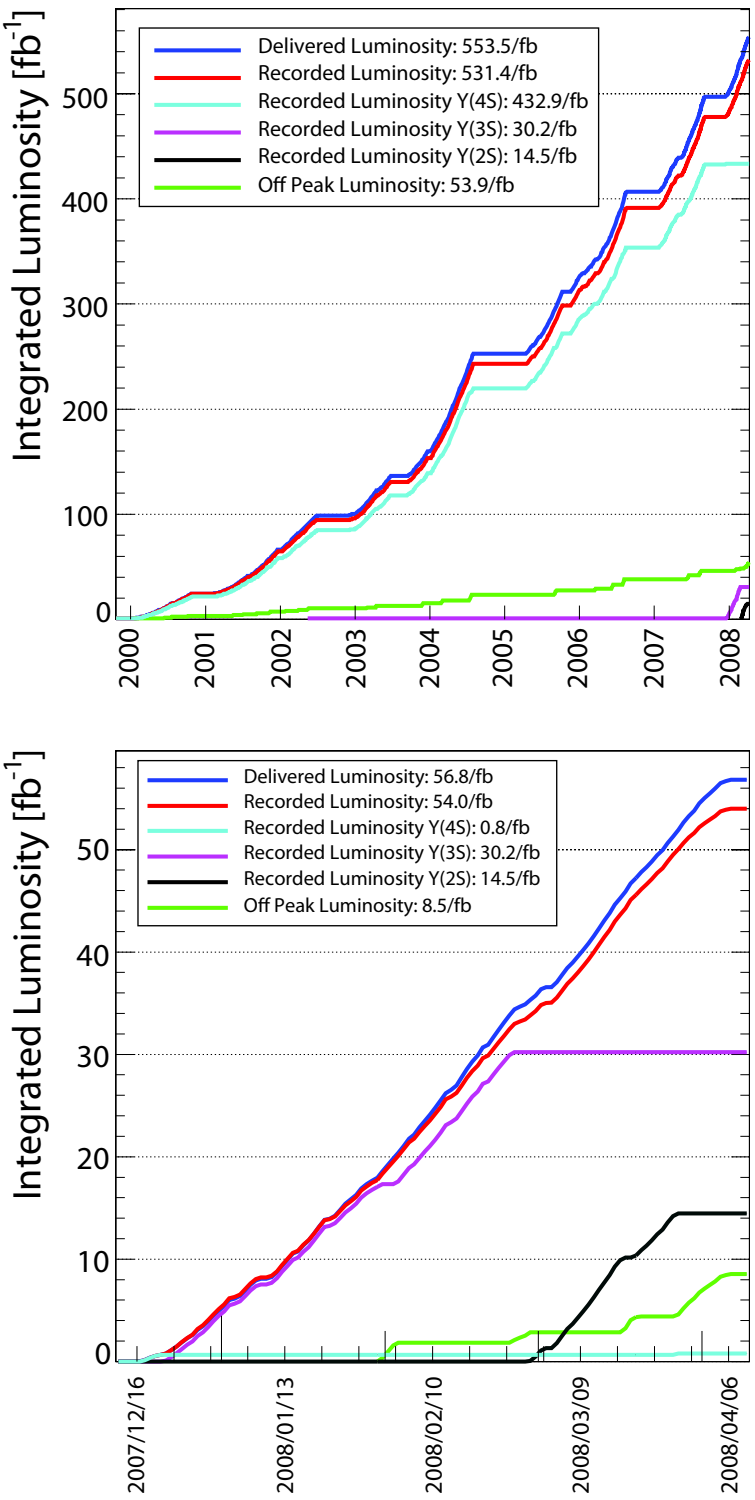

Figure 2.6: The total integrated luminosity delivered by the PEP-II collider and recorded with the *BABAR* detector (top) and the integrated luminosity during the $\Upsilon(2S)$ and $\Upsilon(3S)$ data collection periods (bottom).

2.4 The *BABAR* Detector

The *BABAR* detector, described in detail in [94], is designed to satisfy several performance requirements. These include maximum coverage extending to small angles with respect to the beamline, excellent photon energy and angular measurements as well as reconstruction efficiency, very good track momentum and vertex resolution. The detector is also driven by the need for efficient and pure particle identification. Particularly important are the identification of electrons and muons with low misidentification rates for charged hadrons, as well as charged hadron identification over a wide momentum range. The detector systems must also be capable of withstanding large radiation doses and high backgrounds.

These requirements are met by the *BABAR* detector, which is situated at the PEP-II interaction region. The detector is offset from the primary interaction point and asymmetric to maximize the acceptance for decay products from the boosted Υ system. Extrapolation of particle tracks to their production points as well as the measurement of low-momentum particles is provided by a multilayer silicon vertex tracker (SVT). The precise measurements of particle momenta are provided by the drift chamber (DCH), which consists of a gas-filled chamber with wires oriented roughly parallel to the beamline. A ring-imaging Cherenkov detector (DIRC) outside of the DCH is used to identify charged hadrons. An electromagnetic calorimeter (EMC) composed of an array of Cesium-Iodide scintillating crystals located outside the DCH provides measurements of electromagnetic showers. These detector systems are mounted inside a superconducting solenoidal magnet which provides a magnetic field of 1.5 T. The flux of the magnetic field is returned by a layer of steel located outside the solenoid, which is interleaved with particle sensors for the identification of muons and neutral hadrons. A simulated $e^+e^- \rightarrow \mu^+\mu^-$ event reconstructed with the *BABAR* detector is shown in

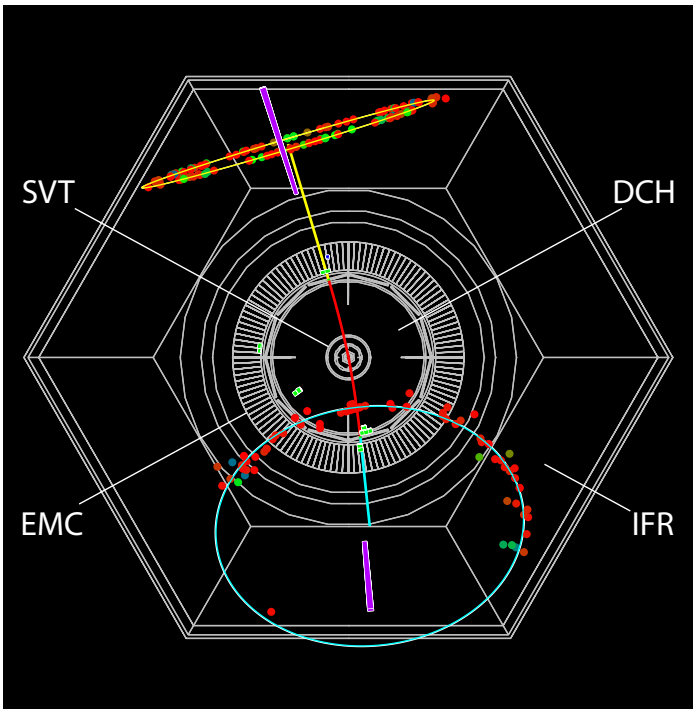

Figure 2.7: A simulated $e^+e^- \rightarrow \mu^+\mu^-$ event reconstructed with the *BABAR* detector, projected in the plane orthogonal to the beam axis. The silicon vertex tracker (SVT), drift chamber (DCH), electromagnetic calorimeter (EMC) and instrumented flux return (IFR) are indicated. The red lines in the SVT and DCH are tracks, and the clusters of shaded green cells in the EMC indicate energy depositions. The shaded purple cells in the IFR indicate activity in the muon system, and the ellipses are projections of the Cherenkov rings imaged with the DIRC.

Fig. 2.7, and the detailed layout and componenets of the detector are displayed in Fig. 2.8.

The primary physics requirements for this analysis include excellent track momentum resolution for measuring the high momentum electrons and muons produced in the signal $\Upsilon(3S) \rightarrow \ell\tau$ decays, which is provided by the DCH tracking detector. Precise measurements of photon energy and position is required to identify neutral pions decaying to photon pairs; these measurements are provided by the EMC. Identification of charged leptons and pions is also critical and is performed using information from all of the detector subsystems except for the DIRC.

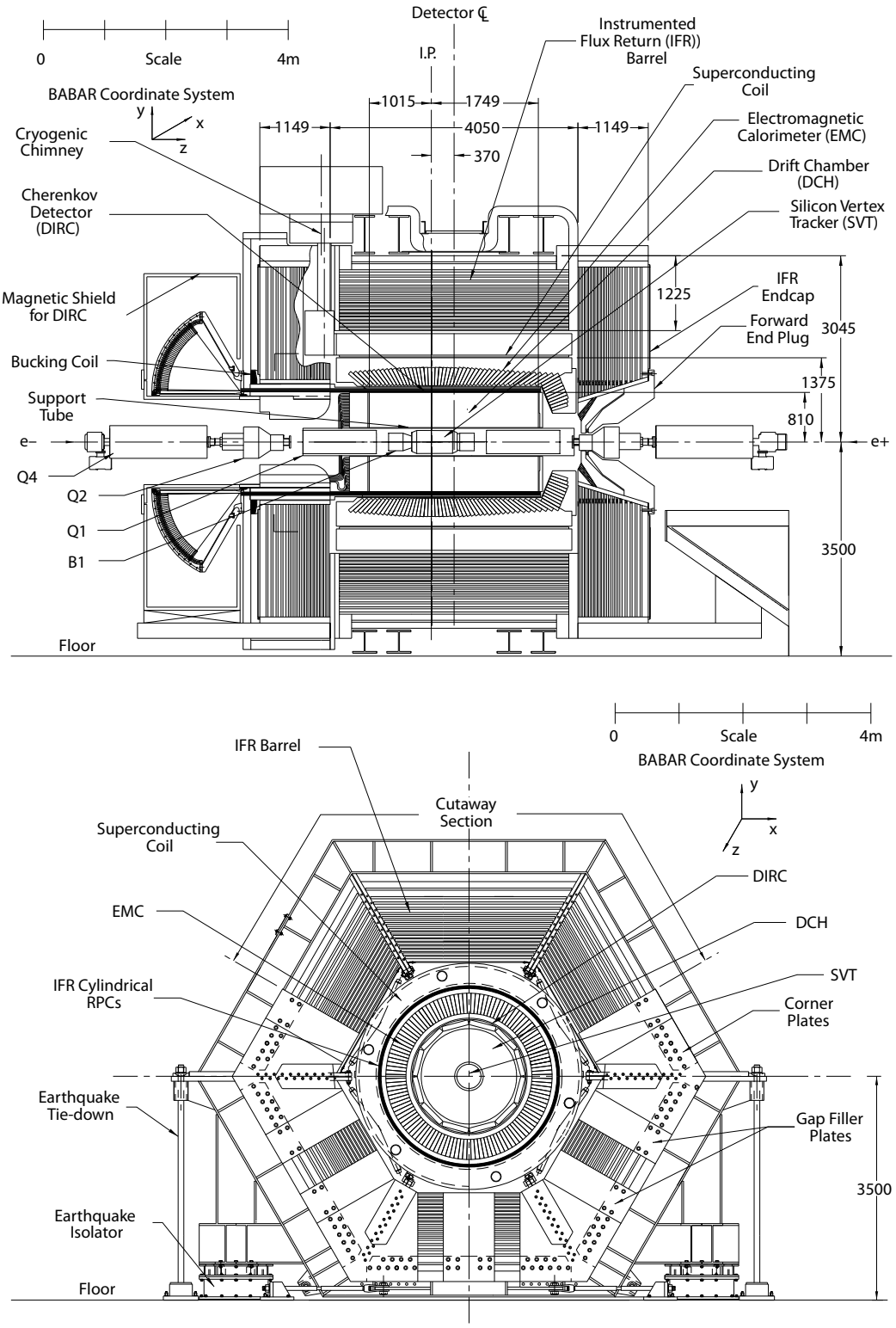

Figure 2.8: Layout of the *BABAR* detector projected along the beam axis (top) and projected in the plane orthogonal to the beam axis (bottom) [94].

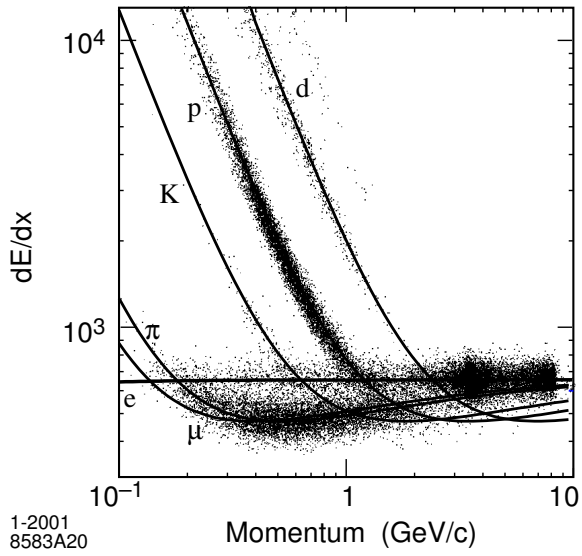

Figure 2.9: The specific ionization dE/dx as measured by the *BABAR* drift chamber, as a function of particle momentum [94]. The solid lines indicate the prediction from the Bethe-Bloch equation [24] for electrons (e), muons (μ), charged pions (π), charged kaons (K), protons (p), and deuterons (d).

2.4.1 Detector Subsystems

The SVT is the innermost detector and consists of five concentric cylindrical layers centered around the beam line, each composed of double-sided Silicon microstrip sensors. The primary function of the SVT is the precise extrapolation of particle tracks to their production points, necessary for the precise vertex resolution required by *BABAR*. This is performed using the inner three SVT layers, which are situated at small radii as close as possible to the beampipe. The outer two layers are situated at larger radii, and provide measurements of low momentum particles. These two layers also serve to match tracks from the SVT with those from the DCH, and to provide angular information for these tracks. The SVT also provides a measurement of the energy deposited by a charged particle per unit length, known as specific ionization and denoted dE/dx, which is used for particle identification as shown in Fig. 2.9.

The DCH is located outside the SVT and constitutes the primary tracking detector of

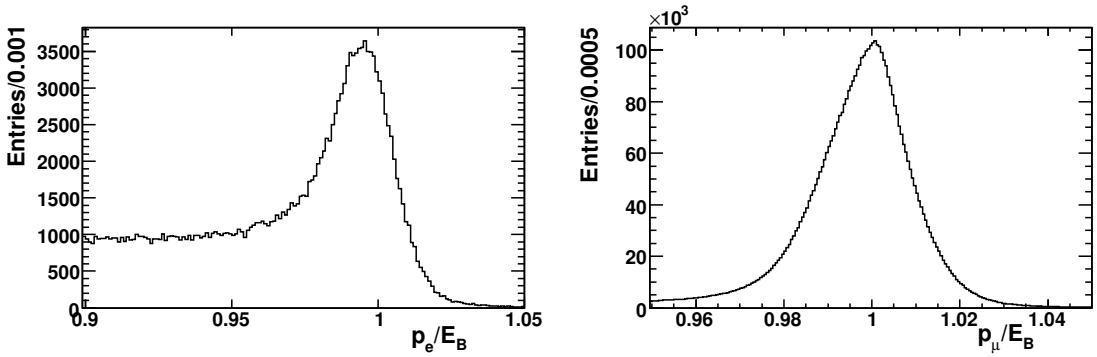

Figure 2.10: Distributions of the beam energy-normalized electron (muon) CM momentum in selected Bhabha (μ-pair) events in $\Upsilon(3S)$ data. The low-energy tail is from initial and final state radiation, as well as additional backgrounds which produce final states consisting of an electron-positron pair in the Bhabha sample. The Gaussian width of the peak in the Bhabha sample is $\sim$0.01. The peak in the μ-pair sample is highly non-Gaussian; the RMS of the distribution is also $\sim$0.01.

BABAR. It consists of a helium-based gas-filled chamber with wires oriented roughly parallel to the beamline. The wires are organized in 40 concentric cylindrical layers which each consist of thousands of hexagonal cells. The primary function of the DCH is to precisely measure the momentum of charged particles, which follow helical trajectories due to the axial magnetic field oriented parallel to the beamline. The transverse track momentum is inversely proportional to the radius of curvature, which is measured in the DCH by fitting a helix to the trail of energy depositions from charged particles. Wires placed at small angles with respect to the beamline provide angular information which, in combination with the angular information from the SVT, allows the longitudinal momentum to be determined. As mentioned above, excellent momentum resolution is required of the DCH. The typical relative uncertainty for high momentum charged leptons is $\sim$1% as shown in Fig. 2.10, which shows the reconstructed lepton momentum from Bhabha and μ-pair events in $\Upsilon(3S)$ data. The DCH also measures the charged particle specific ionization, and is used to match tracks to energy depositions in the EMC, known as clusters.

The DIRC consists of rectangular bars of synthetic fused silica located outside the DCH.

Charged particles traversing these bars emit Cherenkov light, which is transported to an array of photomultiplier tubes (PMTs) via total internal reflection. The PMT array is located along the back wall of a water tank and is used to reconstruct the Cherenkov rings using position and timing information. This allows for the Cherenkov angle to be measured, which is related to the particle velocity. This information, in combination with the measurement of the particle momentum obtained from the DCH, allows the particle mass to be determined, hence identifying the particle type. The DIRC is used primarily for discriminating between high momentum charged pions and kaons which are not considered in this analysis, so the DIRC does not provide significant information relevant to particle identification.

The EMC is composed of a highly granular array of Cesium-Iodide scintillating crystals read out individually by pairs of Silicon PIN diodes. The EMC is divided in two sections, a barrel located outside the DIRC bars and a forward endcap. The primary function of the EMC is to identify and precisely measure the energy and position of electrons and photons. Excellent photon energy and angular resolution is required for reconstructing the invariant mass of neutral pions that decay to photon pairs. The energy resolution of the EMC can be expressed as [94]:

$$\frac{\sigma(E)}{E} = \frac{(2.32 \pm 0.30)\ \%}{\sqrt[4]{E}} \oplus (1.85 \pm 0.12)\ \% \tag{2.4}$$

in which E is measured in GeV. The typical invariant mass resolution for $\pi^0 \to \gamma\gamma$ decays provided by the EMC is $\sim$9 MeV/c^2 as shown in Fig. 2.11. This resolution provides good suppression of combinatoric photon pair backgrounds. The fraction of the particle energy deposited in the calorimeter, as well as the shape of the shower, is used for particle identification. This information is especially important for the identification of electrons and photons, which deposit all or most of their energy in the EMC and result in short, narrow showers. Hadrons deposit a fraction of their

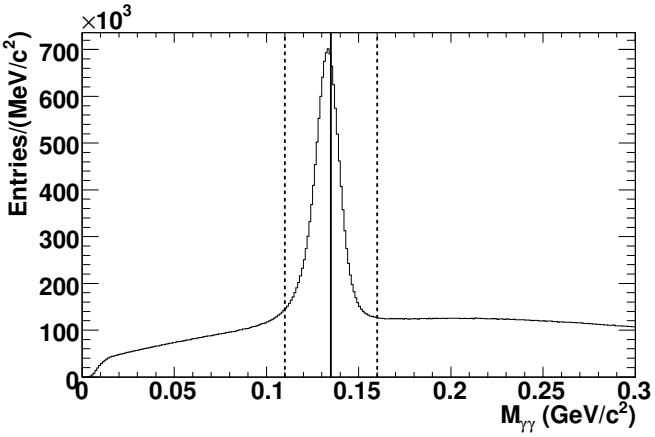

Figure 2.11: Distribution of the invariant mass of photon pairs in $\Upsilon(3S)$ data. The distribution consists of a peak from $\pi^0 \to \gamma\gamma$ decays plus a smooth combinatoric background. Photon pairs which lie between the dashed lines are selected as π^0 candidates, and the solid line shows the true mass of the π^0, 0.135 GeV/c^2 [24]. The Gaussian width of the π^0 peak is $\sim$9 MeV/c^2.

energy and result in wider, scattered showers, while muons do not shower and deposit only a small fraction of their energy in the EMC.

Outside of the EMC is a superconducting solenoid, which generates a 1.5 T magnetic field oriented parallel to the beamline. The instrumented flux return (IFR) functions as the the return yoke for the magnetic flux. It is comprised of layers of steel interleaved with limited streamer tubes which detect ionizing radiation. The IFR is divided into a barrel section situated outside of the solenoid and two endcaps. Most particles are absorbed before they reach the IFR, but muons, neutral hadrons, and some high momentum charged pions reach the IFR and are detected. The IFR is used primarily to identify muons, which penetrate several or all of the layers, and is also used for the detection of energy clusters deposited by neutral hadrons.

2.4.2 Particle Identification

Particle identification (PID) is performed using sophisticated multivariate algorithms [95] that use measurements from all of the detector sub-systems, including but not limited to E/p and

shower profile from the EMC, the specific ionization dE/dx from the SVT and DCH, and the penetration depth in the IFR muon system. The most important information relevant to selecting the charged particles used in this analysis is that electrons deposit all or most of their energy in the EMC, while muons deposit a fraction of their energy in the EMC and penetrate deeply into the IFR muon system. Charged pions deposit a fraction of their energy and do not penetrate deeply into the IFR, and the specific ionization provides an additional important discriminant.

An electron selector and muon veto, combined with the requirement that the particle falls within the angular acceptance of the EMC, are used to identify electrons. A muon selector and electron veto are used to identify muons, while a charged pion selector, electron veto and muon veto are used to select charged pions. Efficiencies for the particle selectors used in this analysis are displayed in Fig. 2.12. Charged lepton misidentification rates are crucial because they determine the selection efficiencies for Bhabha and μ-pair backgrounds. The probability for a muon to pass the electron selection criteria is $O(10^{-5})$. The probability for an electron to pass the muon selection criteria, plus the additional requirement that the particle traverses at least 4 layers of the IFR muon system, is $O(10^{-6})$. The probability for an electron or muon to pass the charged pion selection criteria is $O(10^{-1})$. Photons are required to deposit at least 50 MeV in the EMC and have a transverse shower profile consistent with that expected from an electromagnetic shower. A pair of photons with invariant mass 0.11 GeV/c^2 $< M_{\gamma\gamma} <$0.16 GeV/c^2 is selected as a neutral pion candidate.

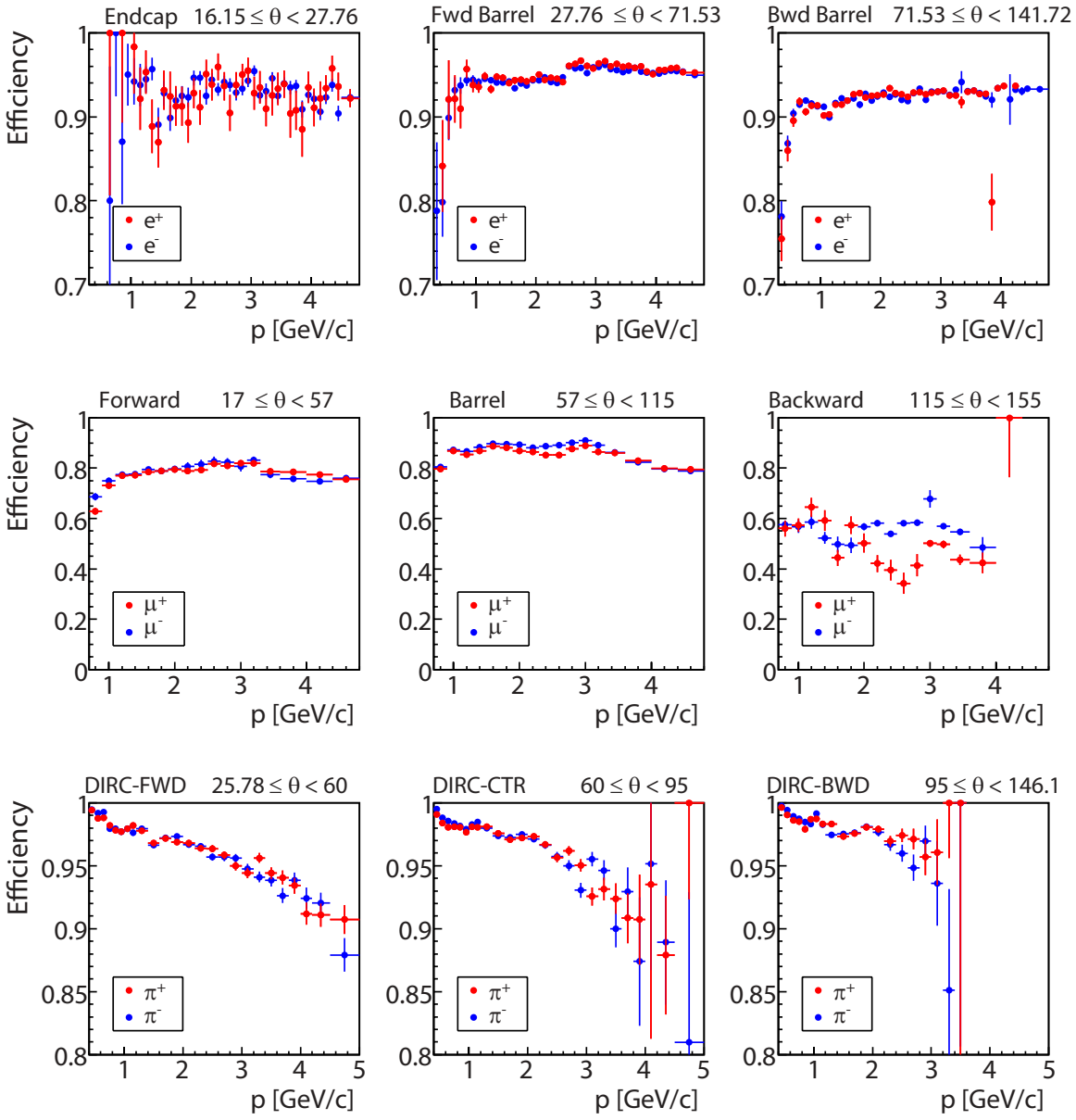

Figure 2.12: Efficiencies for the electron (top), muon (middle), and charged pion (bottom) selectors used in this analysis as a function of the particle momentum. The plots are divided into three bins of the polar angle θ measured in degrees and defined with respect to the e^+ beam axis, which correspond to sections of the ECAL for electrons, IFR for muons, and DIRC for charged pions.

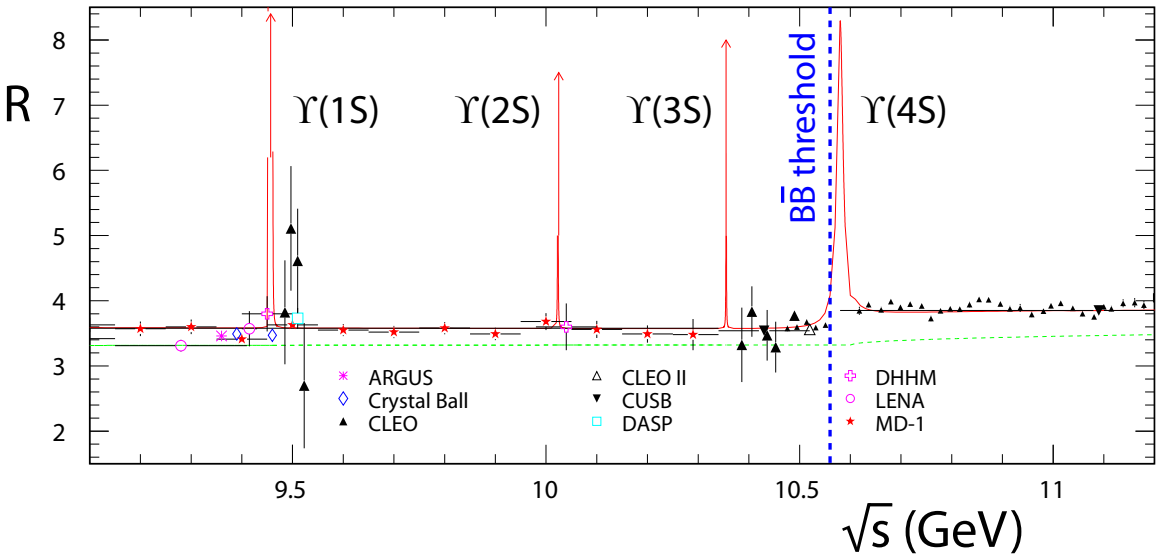

Figure 2.13: The ratio R $= \sigma(e^+e^- \rightarrow \text{hadrons})/\sigma(e^+e^- \rightarrow \mu^+\mu^-)$ as a function of collision energy $\sqrt{s}$ in the neighborhood of the Υ resonances [96].

2.5 Υ Production at *BABAR*

The Υ particle is a bound state of a b and $\bar{b}$ quark with quantum numbers $J^{PC} = 1^{++}$. Much like the energy levels of hydrogen, the Υ particle has energy levels nS with $n = 1, 2, 3, 4, 5....$ As shown by the Υ mass spectrum in Fig. 2.13, the $\Upsilon(4S)$ is above the threshold for $B\bar{B}$ meson production. The $\Upsilon(4S)$ decays almost exclusively to B meson pairs, allowing for the study of CP violation in the B meson system. The decay $\Upsilon(4S) \rightarrow B^0\bar{B}^0/B^+B^-$ is mediated by the strong force and occurs very rapidly. Thus, by the time-energy uncertainty principle the energy of the $\Upsilon(4S)$ cannot be known with precision. The result is that the width of the $\Upsilon(4S)$ is larger by a factor of order 10^3 with respect to the narrow $\Upsilon(1S)$, $\Upsilon(2S)$ and $\Upsilon(3S)$ resonances below the $B\bar{B}$ threshold, which can only decay via $b\bar{b}$ annihilation to a virtual photon or Z^0. From 2000-2008, 465×10^6 $\Upsilon(4S)$ decays corresponding to an integrated luminosity of 432.9 fb^{-1} were collected with the *BABAR* detector.

Because the widths of the narrow resonances are much smaller than that of the $\Upsilon(4S)$, the branching fractions for rare Υ decays are increased, leading to dramatic enhancement in the sensitivity to rare and exotic decays. For this reason, at the end of PEP-II operations in early 2008 data samples of 122×10^6 $\Upsilon(3S)$ decays (30.2 fb^{-1}), and 99×10^6 $\Upsilon(2S)$ decays (14.5 fb^{-1}), were collected. These samples provide an excellent laboratory to search for rare and exotic processes not accessible in $\Upsilon(4S)$ decays [97–100]. These include decays to several previously unobserved states predicted to occur in the SM, such as the $b\bar{b}$ ground state η_b, which was recently discovered in the *BABAR* $\Upsilon(3S)$ data sample [101]. The SM prediction that the photon and Z^0 boson couple equally to electron, muon and tau leptons, known as lepton universality, may be tested with precision, and violation of this prediction would provide a clear signal of new physics. The data collected at the narrow resonances also allows for the search for lepton flavor violation, the subject of the analysis presented in this thesis. This analysis is based on the $\Upsilon(3S)$ data sample and will be extended to include the $\Upsilon(2S)$ data sample.

2.6 Data and Simulated Events

As discussed in Chap. 2.1, I search for the decays $\Upsilon(3S) \rightarrow e\tau$ and $\Upsilon(3S) \rightarrow \mu\tau$. The data used for this search consists of $(116.7 \pm 1.2) \times 10^6$ $\Upsilon(3S)$ decays corresponding to an integrated luminosity of 27.5 fb^{-1}. Data collected at the $\Upsilon(4S)$ corresponding to 77.7 fb^{-1} and data collected 30 MeV below the $\Upsilon(3S)$ resonance (off-peak data) corresponding to 2.6 fb^{-1} constitute data control samples which are not expected to contain signal events. An additional data sample collected at the $\Upsilon(3S)$ corresponding to 1.2 fb^{-1}, for which the limit from the CLEO collaboration implies that less than 5 signal events should be present per channel, is also used as a data control

sample which is not included in the 27.5 fb^{-1} sample. These control samples are used to validate the analysis procedure by verifying that signals yields consistent with zero are obtained.

Simulated events are also produced and analyzed in order to optimize the selection and fitting procedure and to compare to data. The background to my events is dominated by continuum QED processes, with an additional contribution from resonant $\Upsilon(3S) \to \tau^+\tau^-$ production. The KK2F generator [102] is used to produce μ-pair and τ-pair events while taking into account the effects of initial state radiation. The BHWIDE generator [103] is used to produce Bhabha events, also taking into account initial state radiation. The EvtGen generator [104] is used to produce generic $\Upsilon(3S)$ decays as well as 1.55×10^5 signal $\Upsilon(3S) \to e\tau$ and $\Upsilon(3S) \to \mu\tau$ decays. The efficiency for $q\bar{q}$ events ($q = u, d, s, c$) and for two-photon processes to pass selection is found to be negligible, so these processes are not included. The simulated μ-pair, τ-pair and generic $\Upsilon(3S)$ samples correspond to roughly twice the number of events in the $\Upsilon(3S)$ data, while the Bhabha sample, which constitutes a small background to my events, corresponds to roughly half the number of events. PHOTOS [105] is used to simulate radiative corrections, and GEANT-4 [106] is used to simulate the interactions of particles traversing the *BABAR* detector.

2.7 Signal Signatures and Backgrounds

The signature for the signal $\Upsilon(3S) \to \ell\tau$ processes consists of a primary lepton, an electron or muon, with momentum close to the beam energy, and a τ decay in the opposite hemisphere (here and in the following momentum refers to CM momentum). I require that the τ decays to a single charged particle, either a lepton or charged pion, plus possible additional neutral pions and that the τ daughter track is of opposite charge to the primary lepton. If the τ decays leptoni-

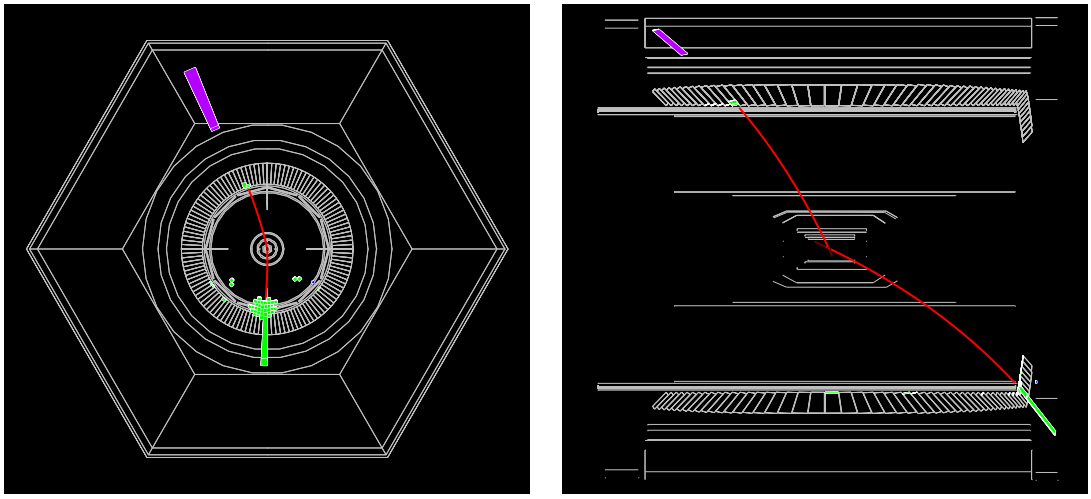

Figure 2.14: A simulated $\Upsilon(3S) \to e^+\tau^-, \tau^- \to \mu^-\bar{\nu}_\mu\nu_\tau$ event (leptonic $e\tau$ channel) reconstructed with the *BABAR* detector, projected in the plane orthogonal to the beam axis (left) and projected along the beam axis (right). The red lines in the inner detector indicate tracks, the clusters of green cells in the EMC indicate energy depositions, and the purple cells in the IFR indicate activity in the muon system. The primary e^+ is the downward-traveling track, the other is the μ^- τ-daughter.

cally, I require that the primary lepton and τ-daughter lepton are of different flavor. If the τ decays hadronically, I require one or two additional neutral pions from this decay. Thus I define four signal channels (here and in the following charge conjugate final states are implied):

- leptonic $e\tau$ channel: $\Upsilon(3S) \to e^+\tau^-, \tau^- \to \mu^-\nu_\tau\bar{\nu}_\mu$
- hadronic $e\tau$ channel: $\Upsilon(3S) \to e^+\tau^-$,$\tau^- \to \pi^-\pi^0\nu_\tau/\pi^-\pi^0\pi^0\nu_\tau$
- leptonic $\mu\tau$ channel: $\Upsilon(3S) \to \mu^+\tau^-, \tau^- \to e^-\nu_\tau\bar{\nu}_e$
- hadronic $\mu\tau$ channel: $\Upsilon(3S) \to \mu^+\tau^-$,$\tau^- \to \pi^-\pi^0\nu_\tau/\pi^-\pi^0\pi^0\nu_\tau$

A sample event display of the leptonic $e\tau$ process is shown in Fig. 2.14. The $\Upsilon(3S) \to \ell^+\tau^-$, $\tau^- \to \pi^-\nu_\tau$, $\Upsilon(3S) \to e^+\tau^-, \tau^- \to e^-\nu_\tau\bar{\nu}_e$ and $\Upsilon(3S) \to \mu^+\tau^-, \tau^- \to \mu^-\nu_\tau\bar{\nu}_\mu$ decay channels are omitted due to strong contamination from Bhabha and μ-pair events.

The distribution of the discriminant variable $x = p_1/E_B$, the primary lepton momentum normalized to the beam energy $E_B = \sqrt{s}/2$, is shown in Fig. 2.15 for simulated events only. The

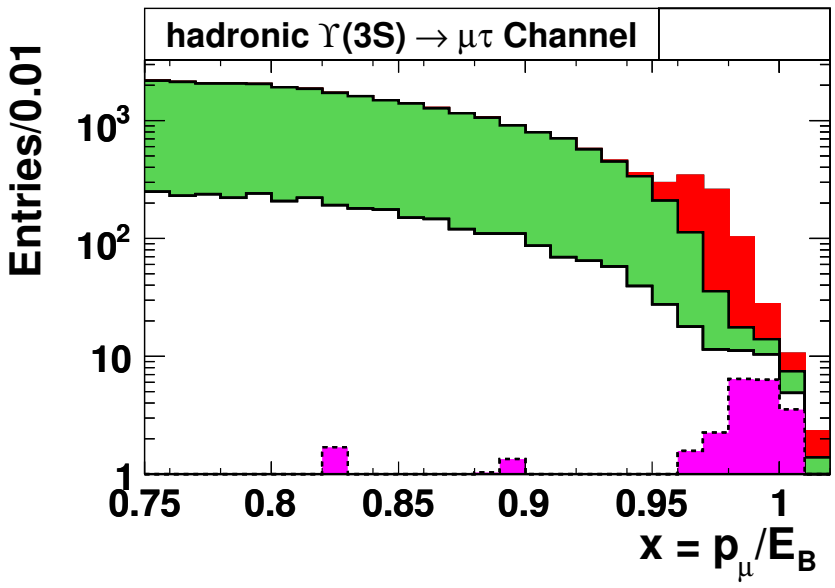

Figure 2.15: Beam energy-normalized primary lepton momentum distribution for selected simulated events in the hadronic $\mu\tau$ channel. The green histogram with the solid outline is continuum τ-pair production and the unshaded histogram with the solid outline is resonant $\Upsilon(3S) \to \tau^+\tau^-$ production. The magenta histogram with the dotted outline is μ-pair production and the red histogram with no outline is signal $\Upsilon(3S) \to \mu\tau$ production with the branching fraction for this decay set to 10^{-4}.

main source of background to my events comes from τ-pair production, which is dominated by continuum production but has a contribution from resonant $\Upsilon(3S) \to \tau^+\tau^-$ production as well. This constitutes an irreducible background since it decays to the same final state as the signal process. The kinematic difference between this background and the signal process is that the primary lepton from $\Upsilon(3S) \to \ell\tau$ production is monoenergetic, since its energy is constrained by the kinematics of the two-body decay, while the τ daughter lepton momentum follows the Michel spectrum. There is also a background contribution to the $\Upsilon(3S) \to e\tau$ search from Bhabha events in which one of the electrons is misidentified, and to the $\Upsilon(3S) \to \mu\tau$ search from μ-pair events in which one of the muons is misidentified or decays in flight, or an electron is generated in a material interaction. The x distributions of these reducible backgrounds have a peak near $x = 1$, which is $\sim 2.5 - 3\sigma$ above

the signal peak, where σ denotes the lepton momentum resolution, and the signal and reducible background peaks can therefore be individually resolved. The strategy used in the analysis is to perform a maximum likelihood fit to the x distributions for the four signal channels to extract the signal yields.

2.8 Selection

The selection strategy is to select events with the correct particle types, while maximizing the signal efficiency and rejecting as much of the reducible backgrounds as possible. Then I fit for the number of events containing an electron or muon with momentum close to the beam energy, which are identified as signal events. A preliminary unblinded analysis is performed using the 1.2 fb^{-1} $\Upsilon(3S)$ data sample in order to ensure agreement between data and simulation and to validate the analysis method. A blinded analysis is then performed using the full $\Upsilon(3S)$ data sample in which events satisfying $0.95 < x < 1.00$ are excluded. The blinding criterion rejects more than 99% of observable $\Upsilon(3S) \to \ell\tau$ decays. The event selection proceeds in two steps, a preselection for all four signal channels followed by a channel-specific selection.

2.8.1 Event Preselection

To pass preselection the event must have two tracks of opposite charge, both consistent with originating from the primary interaction point, with opening angle greater than 90° in the CM frame. The event must satisfy requirements designed to select $e^+e^- \to \tau^+\tau^-$ events, which are very efficient for my signal. The distributions of kinematic variables used to select signal events are displayed in App. A. I require that $\cos(\theta^{lab}_{miss})$ <0.9 and $\cos(\theta^{CM}_{miss})$ >-0.9, where θ^{lab}_{miss} (θ^{CM}_{miss})

is the polar angle of the missing momentum vector in the lab (CM) frame. These requirements suppress events in which particles are lost because they travel along the beam direction and also suppress Bhabha, μ-pair and two-photon processes. I require that $M_{VIS}/\sqrt{s}$ <0.95, where M_{VIS} is the mass of the 4-vector obtained by adding up the 4-vectors of the two tracks plus those of any additional neutral particles in the event; this requirement also suppresses Bhabha and μ-pair backgrounds. Finally, I require $(\vec{p}_1 + \vec{p}_2)_\perp/(\sqrt{s} - |\vec{p}_1| - |\vec{p}_2|)$ >0.2, where $\vec{p}_1$ and $\vec{p}_2$ are the CM momentum vectors of the two tracks. The requirement on this kinematic variable is effective at suppressing two-photon processes as well as suppressing beam-gas interactions, in which a particle from the beam undergoes small-angle scattering after interacting with residual gas particles in the beam-pipe.

2.8.2 Channel-Specific Selection

The channel-specific selection consists of requirements on the identified particle types and their momenta, which are used to classify events into one of the four signal channels. Additional kinematic selection criteria aimed at further suppressing the Bhabha and μ-pair backgrounds are then applied. The channel-specific selection is summarized in Table 2.2. A summary of signal efficiencies, number of simulated background events, and number of data events passing selection for each of the four signal channels in the 27.5 fb^{-1} $\Upsilon(3S)$ data sample is displayed in Table 2.3. The signal efficiencies include the relevant τ branching fractions which are taken from the 2008 Particle Data Group (PDG) [24] and are equal to $BF(\tau^- \to e^-\bar{\nu}_e\nu_\tau) = (17.85 \pm 0.05)$ %, $BF(\tau^- \to \mu^-\bar{\nu}_\mu\nu_\tau) = (17.36 \pm 0.05)$ %, and $BF(\tau^- \to \pi^-\pi^0\nu_\tau/\pi^-\pi^0\pi^0\nu_\tau) = (34.79 \pm 0.16)$ %. After including all selection requirements the signal efficiencies are 4-6%, simulated τ-pair background efficiencies are $(6 - 10) \times 10^{-4}$, and the number of simulated and data events passing selection in

Table 2.2: Channel-specific selection for the four signal channels [60]. The subscript 1 refers to the primary lepton which is the electron (muon) for the $e\tau$ ($\mu\tau$) channels; the subscript 2 refers to the τ-daughter track. The CM momentum and transverse momentum are denoted p and p_T, respectively. The difference between the azimuthal angles of the two tracks in the CM frame is $\Delta\phi^{CM}$ and the number of layers of the IFR muon system penetrated by the τ-daughter is N_{IFR2}. The invariant mass of the $\pi^{\pm}\pi^0$ system is denoted M($\pi^{\pm}\pi^0$). If there are two neutral pions in the event, the π^0 giving the $\pi^{\pm}\pi^0$ mass closest to m_ρ=0.77 GeV/c^2 is chosen. The requirement on M($\pi^{\pm}\pi^0\pi^0$) is included only if there are two neutral pions in the event. Empty table entries indicate that no requirement is used for the given channel.

Quantity	**leptonic $e\tau$**	**hadronic $e\tau$**	**leptonic $\mu\tau$**	**hadronic $\mu\tau$**
Particles	1e, 1μ	1e, 1$\pi^{\pm}$, 1 or 2 π^0's	1e, 1μ	1μ, 1$\pi^{\pm}$, 1 or 2 π^0's
p_1/E_B	$p_e/E_B > 0.75$	$p_e/E_B > 0.75$	$p_\mu/E_B > 0.75$	$p_\mu/E_B > 0.75$
p_{T2}/E_B		>0.05		
p_2/E_B		<0.8		<0.8
$\Delta\phi^{CM}$			<172°	
N_{IFR2}	>3			
M($\pi^{\pm}\pi^0$)		0.4-1.1 GeV/c^2		0.4-1.1 GeV/c^2
M($\pi^{\pm}\pi^0\pi^0$)		0.6-1.5 GeV/c^2		0.6-1.5 GeV/c^2

Table 2.3: Summary of selection for 27.5 fb^{-1} of $\Upsilon(3S)$ data and simulated events [60]. Shown are the simulated signal efficiencies, number of simulated background events, and number of data events passing selection in the four signal channels. The signal efficiencies include the τ branching fractions. All errors are statistical only and the errors in the τ branching fractions are included in the signal efficiency uncertainties. Systematic effects leading to potential discrepancies between the number of data and simulated events passing selection are discussed in Chap. 2.11.

Quantity	**leptonic $e\tau$**	**hadronic $e\tau$**	**leptonic $\mu\tau$**	**hadronic $\mu\tau$**
ϵ_{SIG} (%)	4.72±0.05	4.94±0.06	4.16±0.05	6.21±0.06
N_{BKG}	19896±102	21539±103	20976±102	29464±122
N_{DATA}	19658	21586	20946	28765

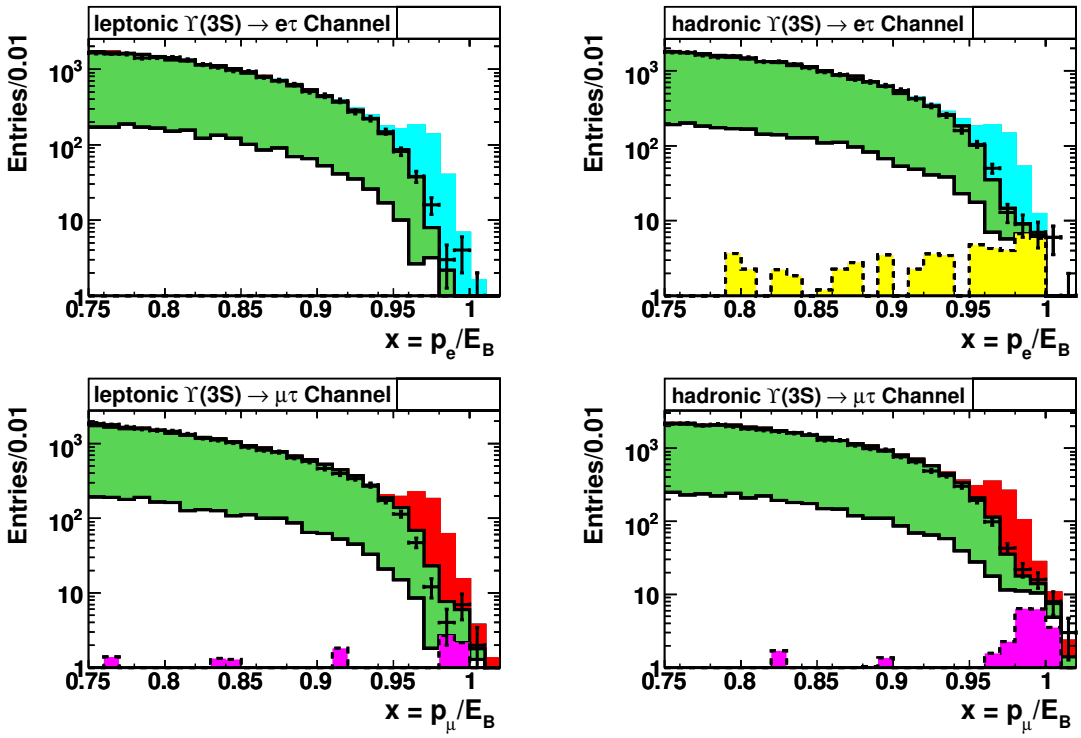

Figure 2.16: Comparison of the beam energy-normalized primary lepton momentum distributions for selected data (points with statistical error bars) and simulated events (histograms) in the four signal channels [60]. The shaded green histogram with the solid outline is continuum τ-pair production and the unshaded histogram with the solid outline is resonant τ-pair production. For the $e\tau$ channels, the yellow histogram with the dotted outline is Bhabha events and the light blue histogram with no outline is signal $\Upsilon(3S) \to e\tau$ production. For the $\mu\tau$ channels, the magenta histogram with the dotted outline is μ-pair events and the red histogram with no outline is signal $\Upsilon(3S) \to \mu\tau$ production. The signal decay branching fraction has been set to $BF(\Upsilon(3S) \to \ell\tau) = 10^{-4}$.

each channel is $(2 - 3) \times 10^4$, depending on the signal channel. A comparison between the x distributions of selected data and simulated events is shown in Fig. 2.16, which shows good agreement between data and simulation.

Due to the combination of particle identification selectors and vetoes used in this analysis, it is in general not possible for a single event to pass selection for more than one signal channel. The exception is that it is possible for a τ-pair event decaying to a final state containing an electron

and a muon with p_e/E_B, $p_\mu/E_B > 0.75$ to pass selection for both the leptonic $e\tau$ and leptonic $\mu\tau$ signal channels. The probability for an event passing selection for one of the leptonic channels to pass selection for the other leptonic channel is determined to be 2%, in which case the event is included in both leptonic signal channels.

2.9 Maximum Likelihood Fit Procedure

A maximum likelihood fit procedure is performed using the discriminant variable x, the primary lepton momentum normalized to the beam energy, for the four signal channels individually. Probability density functions (PDFs) for signal (Chap. 2.9.2), Bhabha/μ-pair background (Chap. 2.9.3) and τ-pair background (Chap. 2.9.4) are determined for each of the channels. The PDF is a function which is normalized to unit area, and gives the probability for the outcome of a single measurement of x to lie between a and b according to:

$$\text{Prob}(a < x < b) = \int_a^b PDF(x, \theta)dx, \tag{2.5}$$

in which $\theta = (\theta_1, ..., \theta_n)$ denotes a set of one or more parameters whose values are unknown. The likelihood function L is given by evaluating the PDF with a set of N statistically independent measurements x_i, and viewing it as a function of the unknown parameters θ according to $L(\theta) = PDF(x, \theta)$. The likelihood function is given by [24]:

$$L(\theta) = \prod_i^N PDF(x_i, \theta). \tag{2.6}$$

The maximum likelihood method is to determine the estimators $\hat{\theta}$ which maximize the likelihood function. In general it is easier to work with the logarithm of the likelihood function $\log L$, which

is maximized for the same set of parameters. This is achieved by solving the likelihood equations:

$$\left.\frac{\partial(\log L(\theta))}{\partial\theta_i}\right|_{\hat{\theta}_i} = 0, \quad i = 1, ..., n. \tag{2.7}$$

In this analysis an extended, unbinned maximum likelihood fit is performed. A global PDF consisting of the sum of the PDFs for the three event types (signal, Bhabha/μ-pair background and τ-pair background) is fitted to the x distributions with the yields of each component floated and extracted by the fit. In this case the likelihood function is given by [107]:

$$L(\theta) = \exp\left(-\sum_k n_k\right)\prod_i^N\left(\sum_j n_j\ PDF_j(x_i,\theta)\right). \tag{2.8}$$

The indices j and k indicate the three event types, n_j and n_k are the yields, and PDF_j is the PDF for event type j. The unknown parameters extracted by the fit are the yields for the three event types as well as the τ-pair background shape parameters c_2 and c_3 (discussed in Chap. 2.9.4). The signal yield extracted by the fit N_{SIG} is related to the branching fraction BF according to $BF = N_{SIG}/(\epsilon_{SIG} \times N_{\Upsilon(3S)})$, where ϵ_{SIG} is the signal efficiency and $N_{\Upsilon(3S)}$ is the number of collected $\Upsilon(3S)$ decays.

2.9.1 Special Functions

In the following discussion of the determination of PDFs, two special functions are used: the Argus distribution [108], and a modified Crystal Ball function [109], hereafter referred to as a double Crystal Ball function. The Argus distribution is given by:

$$\text{Argus}(x) = x\sqrt{1-\left(\frac{x}{c}\right)^2}\,e^{-\chi\left(1-\left(\frac{x}{c}\right)^2\right)} \quad (x > 0). \tag{2.9}$$

The parameter c determines the endpoint of the Argus distribution, while χ determines the curvature, as shown in Fig. 2.17.

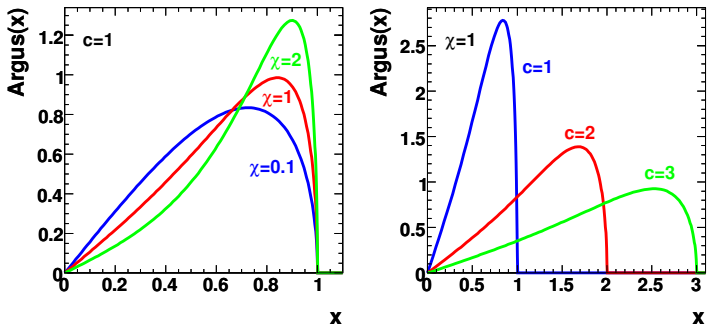

Figure 2.17: Plots of the Argus distribution. Left: the endpoint parameter c is fixed while the curvature parameter χ is varied. Right: χ is fixed and c is varied.

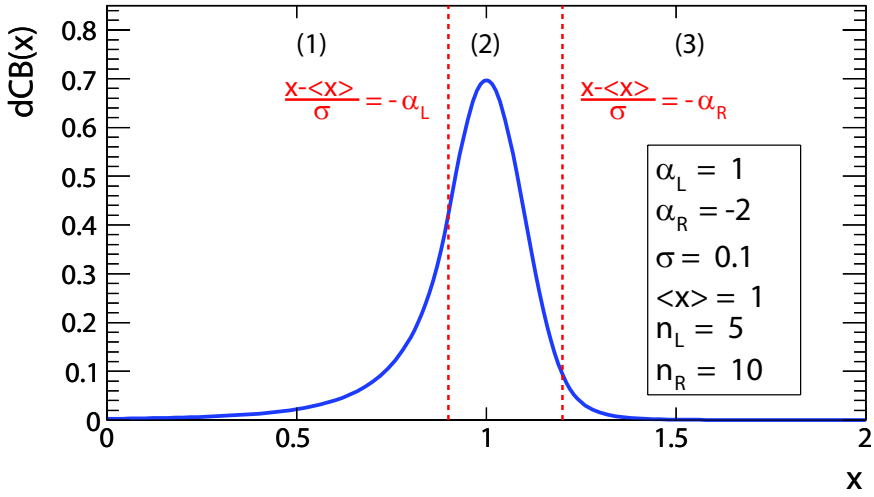

Figure 2.18: Plot of the double Crystal Ball function. The three regions are indicated and separated with vertical dashed lines.

The double Crystal Ball function consists of a Gaussian core with inverse power law tails to the left and right of the core as shown in Fig. 2.18. The function is given by:

$$\mathrm{dCB}(x) = \begin{cases} A_L \left(B_L - \frac{x-<x>}{\sigma}\right)^{-n_L} & \left(\frac{x-<x>}{\sigma} \leq -\alpha_L\right) \\ \exp\left(-\frac{(x-<x>)^2}{2\sigma^2}\right) & \left(-\alpha_L < \frac{x-<x>}{\sigma} < -\alpha_R\right) \\ A_R \left(B_R - \frac{x-<x>}{\sigma}\right)^{-n_R} & \left(\frac{x-<x>}{\sigma} \geq -\alpha_R\right) \end{cases} \tag{2.10}$$

where:

$$A_{L,R} = \left(\frac{n_{L,R}}{|\alpha_{L,R}|}\right)^{n_{L,R}} e^{-\frac{|\alpha_{L,R}|^2}{2}} \quad \text{and} \quad B_{L,R} = \frac{n_{L,R}}{|\alpha_{L,R}|} - |\alpha_{L,R}|. \tag{2.11}$$

The mean and width of the Gaussian core are given by $< x >$ and σ, respectively. The parameter $\alpha_{L(R)}$ determines how far to the left (right) of $< x >$ the Gaussian core extends, while $n_{L(R)}$ is the index of the inverse power law tail to the left (right) of the core.

2.9.2 Signal $\Upsilon(3S) \to \ell\tau$ Fit Procedure

For $\Upsilon(3S) \to \ell\tau$ decays the x distribution is peaked at $x = 0.97$ because some of the collision energy is carried away by the τ mass. The distribution has a width of about 0.01 due to the detector momentum resolution and a radiative tail, which is more pronounced for the $e\tau$ than for the $\mu\tau$ channels. The resulting x distribution is well-described by a double Crystal Ball function. The shape of this function is extracted from fits to the simulated $\Upsilon(3S) \to \ell\tau$ x distributions, for which the same selection is applied as for data. The fit results for the four signal channels are shown in Fig. 2.19.

2.9.3 Bhabha/μ-pair Background Fit Procedure

For the $\Upsilon(3S) \to e\tau$ channels, Bhabha events in which the softer electron is misidentified as a muon or charged pion contribute to the background. For the $\Upsilon(3S) \to \mu\tau$ channels, μ-pair events in which the softer muon is misidentified as an electron or charged pion or decays in flight, or an electron is generated in a material interaction contribute to the background. The x distributions for these Bhabha and μ-pair events consist of a threshold component which truncates near $x = 1$ and a peaking component near $x = 1$. The threshold component is modeled by an Argus distribution and the peaking component is modeled by a Gaussian. A PDF consisting of the sum of these two components is fitted to the x distributions of simulated Bhabha and μ-pair events, which extracts the PDF shape.

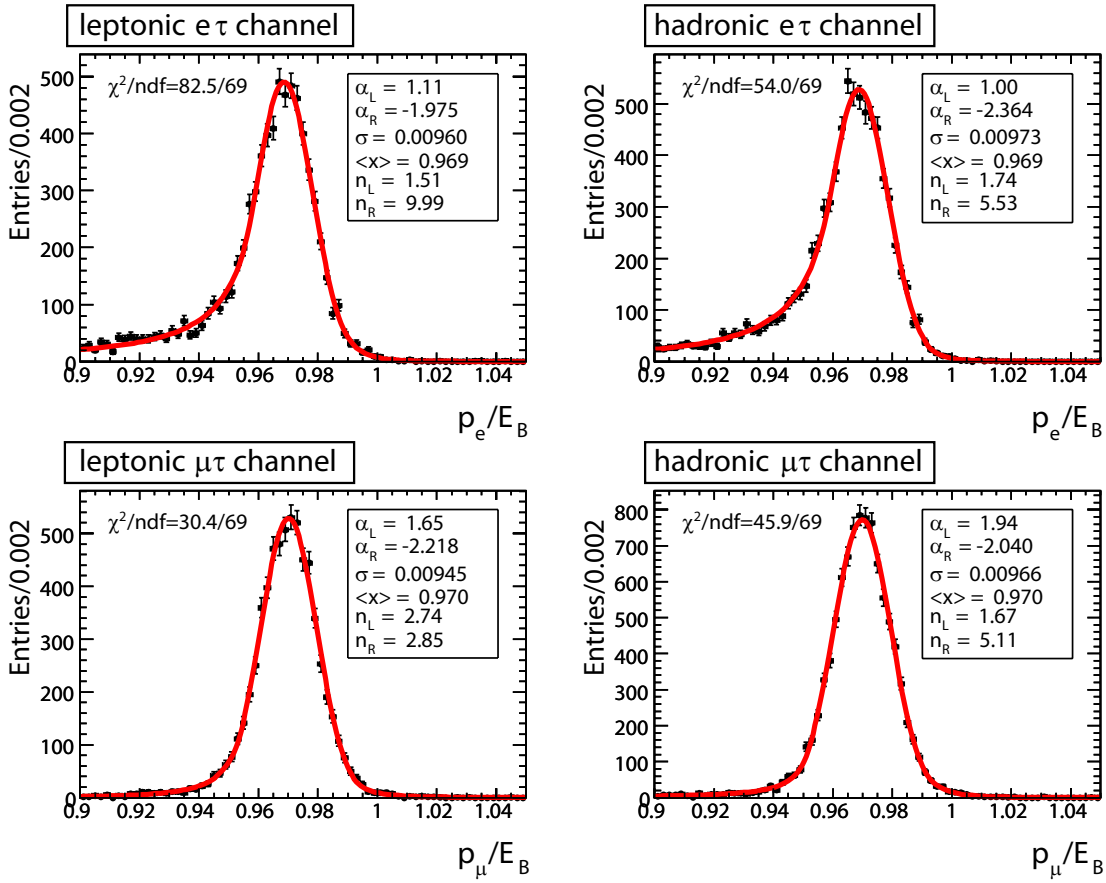

Figure 2.19: Fit results for the simulated signal $\Upsilon(3S) \to \ell\tau$ events. The PDF is a double Crystal Ball function. The mean and width parameters of the PDF are $< x >$ and σ, respectively. The parameters $\alpha_{L(R)}$ and $n_{L(R)}$ are the tail parameters to the left (right) of the Gaussian core.

For all signal channels except the hadronic $\mu\tau$ channel, the number of simulated events passing selection is very low and the extracted PDF shape parameters have large statistical uncertainties. For the $e\tau$ channels, the efficiency for Bhabha events can be increased by requiring that the τ-daughter is identified as an electron instead of a muon (charged pion) for the leptonic (hadronic) signal channels. For the leptonic $\mu\tau$ channel, the efficiency for μ-pair events can be increased by relaxing the requirement $\Delta\phi^{CM} < 172°$, where $\Delta\phi^{CM}$ is the difference between the two track azimuthal angles in the CM as shown in Fig. A.2. To ensure that this does not result in a bias of the x distribution, the correlation coefficient between $\Delta\phi^{CM}$ and x is computed in the region

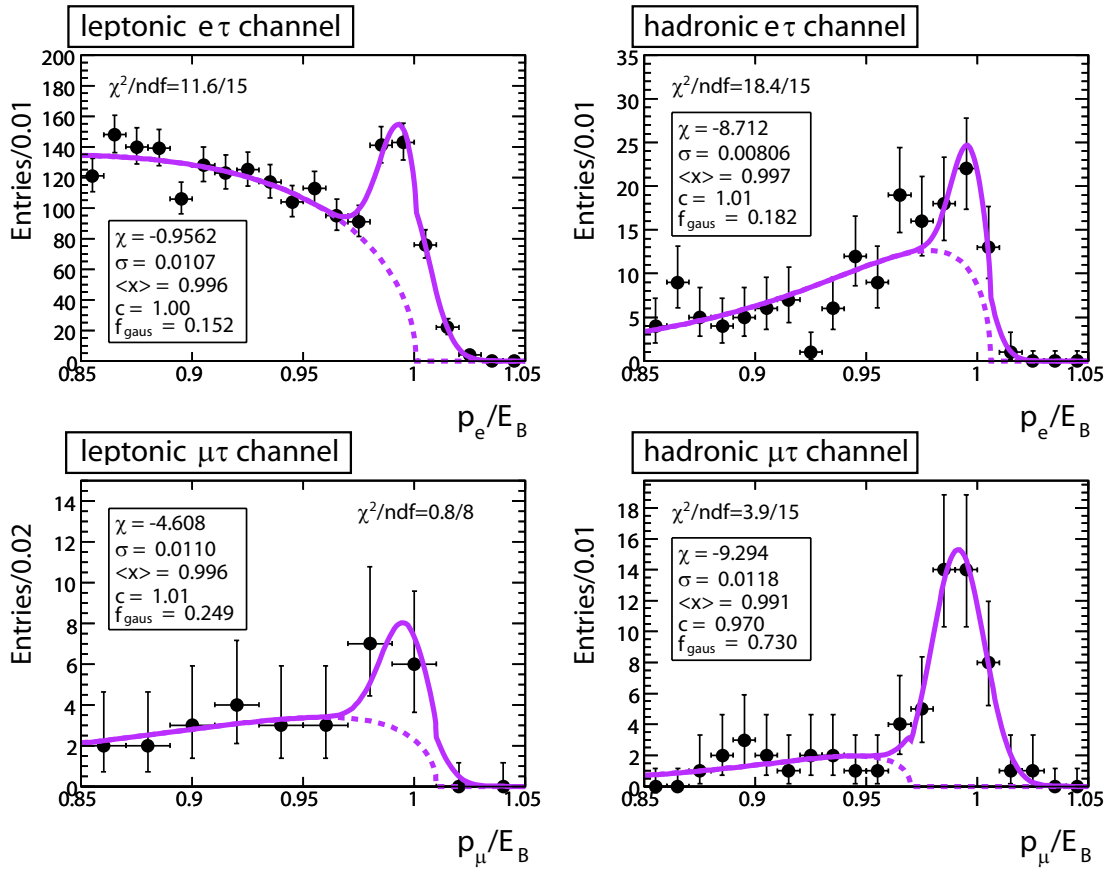

Figure 2.20: Fit results for the simulated Bhabha ($e\tau$ channels) and μ-pair ($\mu\tau$ channels) background events. The PDF is the sum of an Argus component (dotted line) plus a Gaussian component. The mean and width of the Gaussian are $< x >$ and σ, respectively. The Argus curvature and endpoint are χ and c, respectively. The Gaussian fraction of the PDF is $\mathrm{f_{gaus}}$.

$170^\circ < \Delta\phi^{CM} < 180^\circ$, $0.95 < p_1/E_B < 1.05$ and is determined to be 0.0019. By varying the requirement on $\Delta\phi^{CM}$ and performing fits to the corresponding x distributions, it is found that the mean and width of the Gaussian, as well as the Argus endpoint parameter, are constant within statistical errors. The Argus curvature, as well as the Gaussian fraction of the global PDF, do vary significantly and these parameters are therefore extracted from a fit to the x distribution for which the nominal requirement $\Delta\phi^{CM} < 172^\circ$ is included. The fit results for the Bhabha and μ-pair backgrounds are displayed in Fig. 2.20.

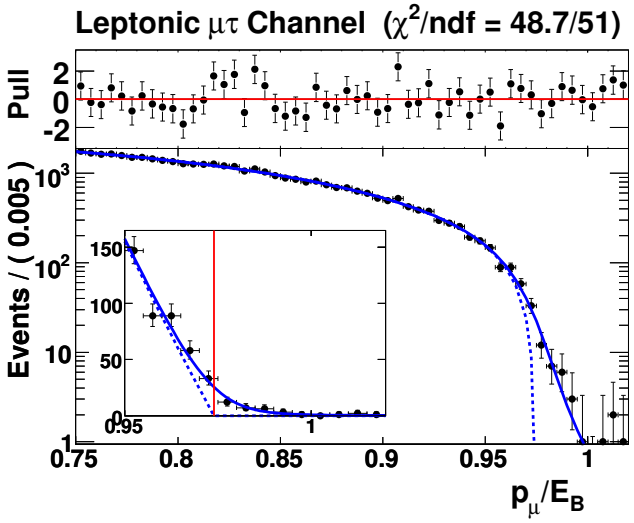

Figure 2.21: Fit of the τ-pair background PDF to simulated events only. The dashed blue line is the polynomial and the solid blue line is the polynomial convoluted with the detector resolution function. The inset shows a close-up of the region 0.95$<x<$1.02 and the vertical red line indicates the value of x_{MAX}.

2.9.4 τ-pair Background Fit Procedure

The main background for all signal channels consists of τ-pair events, which constitute an irreducible background decaying to the same final state as the signal process. The τ-pair x distribution is a smooth function which approaches zero as $x \rightarrow x_{MAX}$, where $x_{MAX} \approx 0.97$ is the effective kinematic endpoint for the lepton momentum in the decay $\tau^- \rightarrow \ell^- \bar{\nu}_\ell \nu_\tau$, boosted into the $\Upsilon(3S)$ rest-frame. Due to the detector momentum resolution the high energy tail of this x distribution extends past the kinematic endpoint in the region where the signal peaks, as shown in Fig. 2.21. It is therefore necessary to characterize the τ-pair background x distribution as accurately as possible in order to maximize the signal sensitivity. To do so, I describe the distribution by the convolution of a polynomial and a detector resolution function. The polynomial is given by:

$$\text{poly}(x) = (1 - x/x_{MAX}) + c_2(1 - x/x_{MAX})^2 + c_3(1 - x/x_{MAX})^3, \qquad (2.12)$$

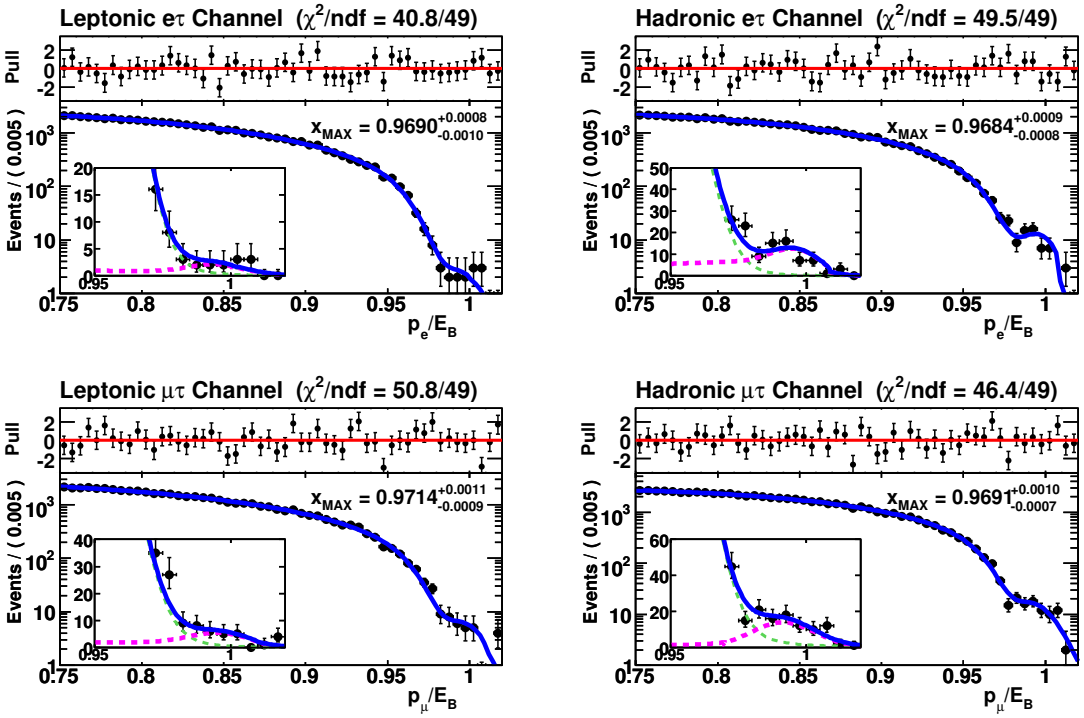

Figure 2.22: Fit results for the 77.7 fb^{-1} $\Upsilon(4S)$ data sample for the four signal channels [60]. The thin green dashed line is the τ-pair background PDF, the thick magenta dashed line is the peaking background PDF, and the solid blue line is the sum of these components. The inset shows a close-up of the region 0.95$<$ x $<$1.02. The extracted value of x_{MAX} is shown along with its statistical errors.

where the parameters c_2 and c_3 determine the shape of the polynomial, which vanishes at $x = x_{MAX}$. In order to characterize the τ-pair background, it is necessary to determine x_{MAX} as well as the detector lepton momentum resolution function. The polynomial shape parameters are not strongly correlated with the signal yield and are therefore floated in the fit to the $\Upsilon(3S)$ data sample. The derivation of the detector lepton momentum resolution function is discussed in detail in App. B.1. The resolution function is found to be well-described by a double Crystal Ball function, whose shape is extracted from simulated τ-pair events. The accurate determination of x_{MAX} is extremely important because it is strongly anti-correlated with the signal yield. To extract x_{MAX}, fits are performed to the $\Upsilon(4S)$ data sample as shown in Fig. 2.22, which is not expected to contain

Table 2.4: Summary of results of the fits to data control samples. Displayed are the extracted signal yields and their statistical errors for each control sample and signal channel.

Channel	25.9 fb^{-1} $\Upsilon(4S)$ Data	2.6 fb^{-1} $\Upsilon(3S)$ Off-Peak Data	1.2 fb^{-1} $\Upsilon(3S)$ Data
leptonic eτ	2.1±8.8	0.1±2.2	-2.2±1.7
hadronic eτ	18±13	6.7±5.3	-0.3±2.3
leptonic $\mu\tau$	15±9.6	-1.9±2.7	2.9±3.1
hadronic $\mu\tau$	5.7±12	-4.6±3.3	-7.7±2.6

signal events. A global PDF consisting of the sum of the τ-pair and peaking background PDFs is fitted to the x distributions for each signal channel with the kinematic endpoint parameter x_{MAX} floated and extracted by the fit. The results show excellent goodness of fit and result in uncertainties of order 10^{-3} in x_{MAX}.

2.10 Fit Validation Studies

The fit procedure is validated by performing fits to data control samples in which no signal is expected, in order to ensure that a signal yield consistent with zero is obtained. Three control samples are used: $\Upsilon(4S)$ data (25.9 fb^{-1}), $\Upsilon(3S)$ off-peak data collected 30 MeV below the $\Upsilon(3S)$ resonance (2.6 fb^{-1}), and $\Upsilon(3S)$ data (1.2 fb^{-1}). Results are summarized in Table 2.4, which demonstrate that signal yields consistent with zero within $\pm 1.6\sigma$ are obtained for all control samples and signal channels except for a discrepancy in the hadronic $\mu\tau$ channel in the 1.2 fb^{-1} $\Upsilon(3S)$ control sample. This discrepancy is discussed in Chap. 2.10.3.

2.10.1 Fit to 25.9 fb^{-1} $\Upsilon(4S)$ Data Control Sample

The full $\Upsilon(4S)$ data sample is split into a 51.8 fb^{-1} *control* sample and a 25.9 fb^{-1} *fit* sample. The τ-pair background shape is extracted from the fit to the *control* sample, in which the

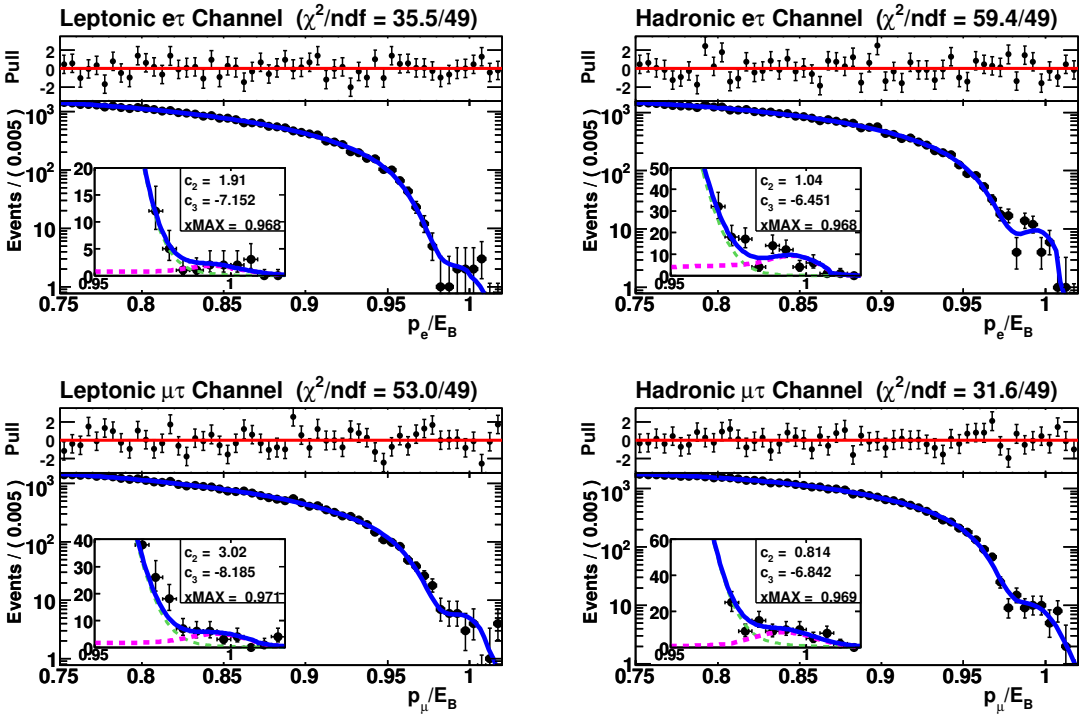

Figure 2.23: Fit results for the 51.8 fb^{-1} $\Upsilon(4S)$ data *control* sample for the four signal channels. The thin green dashed line is the τ-pair background PDF, the thick magenta dashed line is the peaking background PDF, and the solid blue line is the sum of these components. The inset shows a close-up of the region $0.95< x <1.02$. The extracted τ-pair background parameters and their statistical errors are displayed.

τ-pair and peaking background yields are floated but the signal yield is fixed to zero, as shown in Fig. 2.23. The fit procedure is repeated using the *fit* sample, in which the τ-pair background shape is fixed using the results from the *control* sample while the signal, τ-pair and Bhabha/μ-pair background yields are floated as shown in Fig. 2.24. Signal yields consistent with zero within $\pm 1.6\sigma$ are obtained for all four channels.

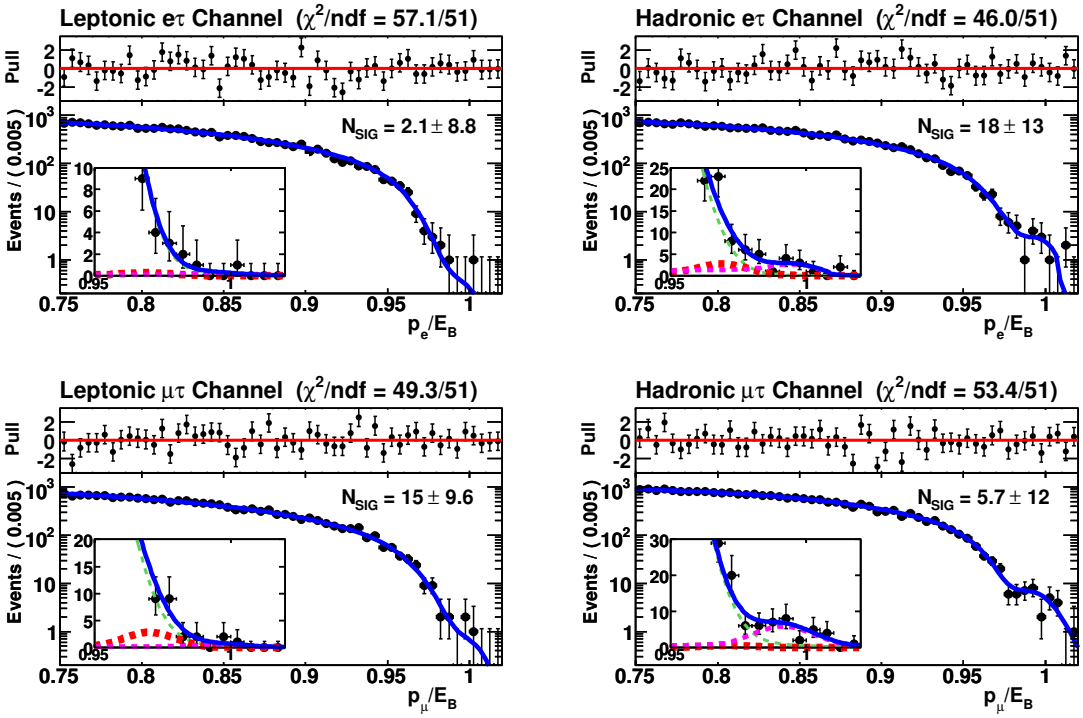

Figure 2.24: Fit results for the 25.9 fb^{-1} $\Upsilon(4S)$ data *fit* sample for the four signal channels. The thin green dashed line is the τ-pair background PDF, the medium magenta dashed line is the peaking background PDF, the thick red dashed line is the signal PDF, and the solid blue line is the sum of these components. The inset shows a close-up of the region 0.95$<$ x $<$1.02. The extracted signal yield N_{SIG} and statistical uncertainty are displayed.

2.10.2 Fit to 2.6 fb^{-1} $\Upsilon(3S)$ Off-Resonance Data Control Sample

The τ-pair background polynomial shape and endpoint are fixed to the values extracted from the full $\Upsilon(4S)$ sample. This is motivated by the fact that resonant τ-pair background events are not present in either the $\Upsilon(4S)$ or $\Upsilon(3S)$ off-peak data, so the background shapes should be consistent. Since x_{MAX} is extracted from fits to $\Upsilon(4S)$ data, correction for differences in momentum resolution between $\Upsilon(3S)$ and $\Upsilon(4S)$ data must be applied as discussed in App. B.2. The signal yield, τ-pair and peaking background yields are floated in the fits, and the extracted signal yields are all consistent with zero within $\pm 1.4\sigma$, as shown in Fig. 2.25.

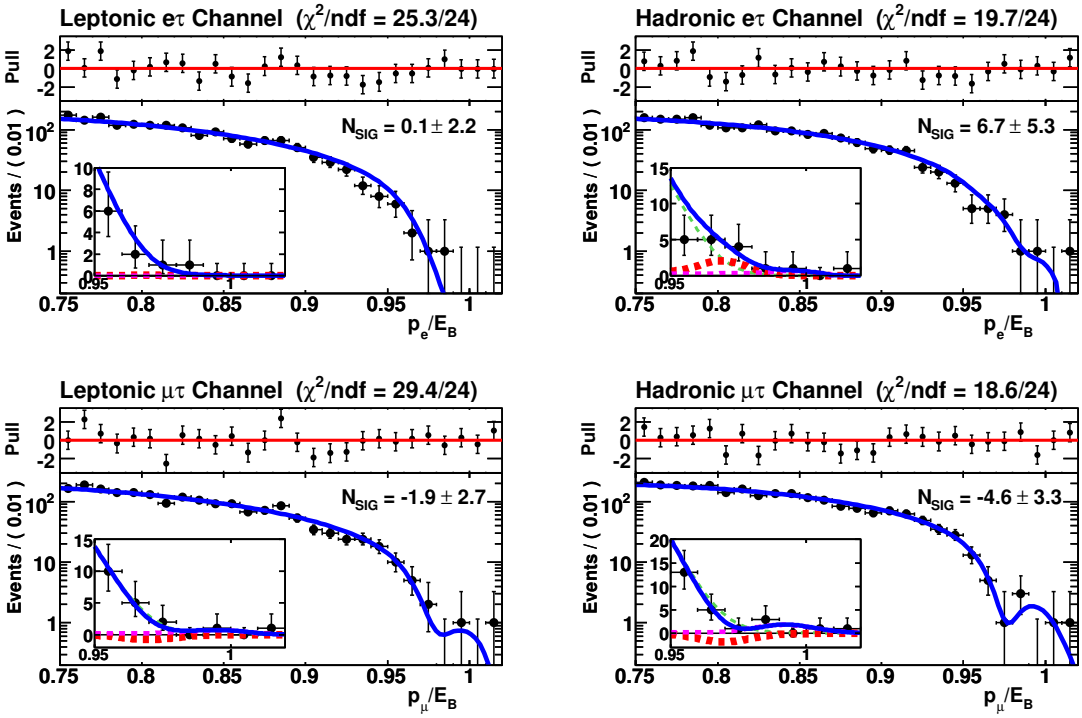

Figure 2.25: Fit results for the 2.6 fb^{-1} Υ(3S) off-peak data sample for the four signal channels. The thin green dashed line is the τ-pair background PDF, the medium magenta dashed line is the peaking background PDF, the thick red dashed line is the signal PDF, and the solid blue line is the sum of these components. The inset shows a close-up of the region 0.95$<$ x $<$1.02. The extracted signal yield N_{SIG} and statistical uncertainty are displayed.

2.10.3 Fit to 1.2 fb^{-1} $\Upsilon(3S)$ Data Control Sample

The τ-pair background endpoint parameter x_{MAX} is fixed to the value extracted from the full $\Upsilon(4S)$ data sample, while the polynomial shape parameters c_2 and c_3 are floated in the fit, since the τ-pair background shape is different from the $\Upsilon(4S)$ data sample due to the presence of resonant τ-pair production. Correction for differences in momentum resolution between $\Upsilon(3S)$ and $\Upsilon(4S)$ data is applied as discussed in App. B.2. The signal yield, τ-pair and peaking background yields are floated in the fits. For all channels except for the hadronic $\mu\tau$ channel, the extracted signal yields are consistent with zero within $\pm 1.3\sigma$, as shown in Fig. 2.26. For the hadronic $\mu\tau$ channel, a large

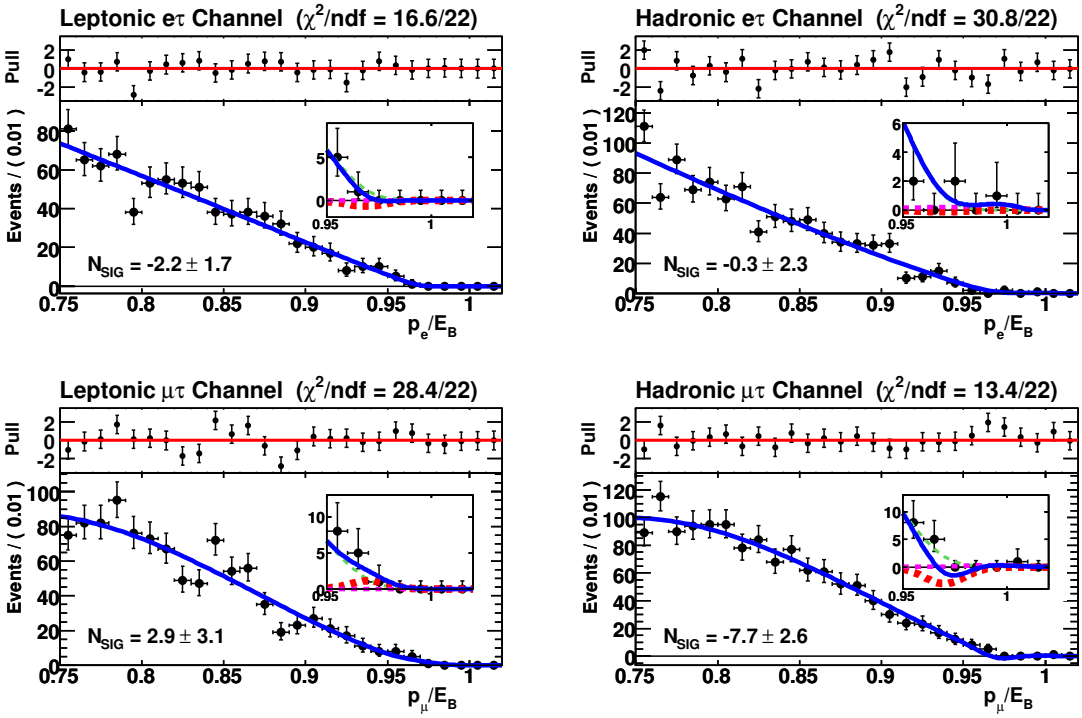

Figure 2.26: Fit results for the 1.2 fb^{-1} $\Upsilon(3S)$ data sample for the four signal channels. The thin green dashed line is the τ-pair background PDF, the medium magenta dashed line is the peaking background PDF, the thick red dashed line is the signal PDF, and the solid blue line is the sum of these components. The inset shows a close-up of the region 0.95$<$ x $<$1.02. The extracted signal yield N_{SIG} and statistical uncertainty are displayed.

negative signal yield is extracted. This occurs because there are no events in the signal region to prevent the PDF from becoming negative in that region. As described below, this scenario is not likely to occur in the fit to the full $\Upsilon(3S)$ data sample.

As discussed in detail in App. C, a large number of simulated pseudo-experiments are performed to further validate the fit procedure. This study confirms that the fit converges, that there is no significant bias in the extracted signal yield, and that the calculated signal yield uncertainties are accurate. This study also demonstrates that the scenario described above in which the PDF becomes negative in the signal region does not occur in 1000 simulated samples corresponding to

Table 2.5: Summary of systematic uncertainties in the signal yield N_{SIG}, signal efficiency ϵ_{SIG} and number of collected $\Upsilon(3S)$ decays $N_{\Upsilon(3S)}$ [60]. The uncertainties in the signal efficiencies and number of $\Upsilon(3S)$ decays include both statistical and systematic effects. Also shown is the uncertainty due to potential bias in the fit procedure.

Quantity	**leptonic $e\tau$**	**hadronic $e\tau$**	**leptonic $\mu\tau$**	**hadronic $\mu\tau$**
N_{SIG}	5.8 events	8.2 events	6.7 events	11.5 events
ϵ_{SIG}	1.8%	3.0%	1.9%	2.8%
$N_{\Upsilon(3S)}$	1.0%	1.0%	1.0%	1.0%
Fit Bias	1.6 events	1.3 events	0.8 events	1.3 events

the full $\Upsilon(3S)$ data sample, roughly 20 times larger than the sample used in the fit to 1.2 fb^{-1} $\Upsilon(3S)$ data.

2.11 Determination of Systematic Uncertainties

The decay branching fractions are determined using the extracted signal yield N_{SIG}, the signal efficiency ϵ_{SIG} determined from simulated events, and the number of collected $\Upsilon(3S)$ decays $N_{\Upsilon(3S)}$. The uncertainties in these quantities are summarized in Table 2.5. There is also a systematic uncertainty arising from potential bias in the fit procedure.

2.11.1 Signal Selection Efficiency

The signal efficiency is determined using simulated events, so there is a systematic uncertainty arising from any potential discrepancies between data and simulated events. To assess this uncertainty, the relative difference between the yields for data and simulated events is determined using τ-pair control samples from a portion of the sideband of the x distribution defined by $0.8 < x < 0.9$. Due to a large discrepancy between the selection efficiencies for high momentum muons, efficiency correction is applied to the $\mu\tau$ channels. This is accomplished by comparing the

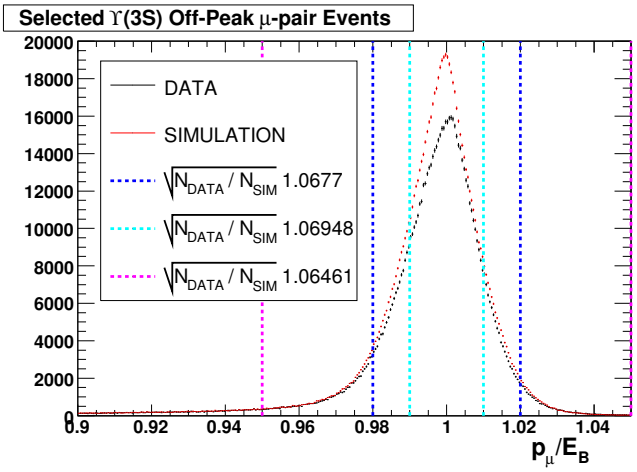

Figure 2.27: Yields for data and simulated events for the μ-pair control sample. Since the control sample requires two identified muons, the error in the muon selection efficiency is the square root of the ratio of data to simulated event yields $\sqrt{\mathrm{N_{DATA}/N_{SIM}}}$. This quantity is evaluated over three regions of p_μ/E_B. The correction factor is determined using the yield ratio over the range $0.98 < x < 1.02$, and the uncertainty is taken to be the larger of the differences between this yield ratio and the yield ratios for the other two ranges.

yields for data and simulated events for a μ-pair control sample as shown in Fig. 2.27. This procedure determines that the simulated event muon selection efficiency is significantly higher than the corresponding efficiency for data, and a correction factor of 1/1.0677 with an uncertainty of 0.3% is applied to the simulated events. There is also a (5.8 ± 1.4) % discrepancy in the yields of data and simulated events for the hadronic $e\tau$ channel, due to a discrepancy in the efficiency of software triggers used to select events for high-level processing. Therefore the simulated event yield is scaled to match the data yield in the region $0.8 < x < 0.9$, and an uncertainty of half the correction (3%) is assessed as the signal efficiency uncertainty for this channel. For the remaining channels, the procedure results in signal efficiency uncertainties of 2-3% depending on the signal channel, due to the uncertainties in the particle identification, tracking, trigger and kinematic selection efficiencies. After efficiency correction is applied, a comparison of data and simulated event x distributions is

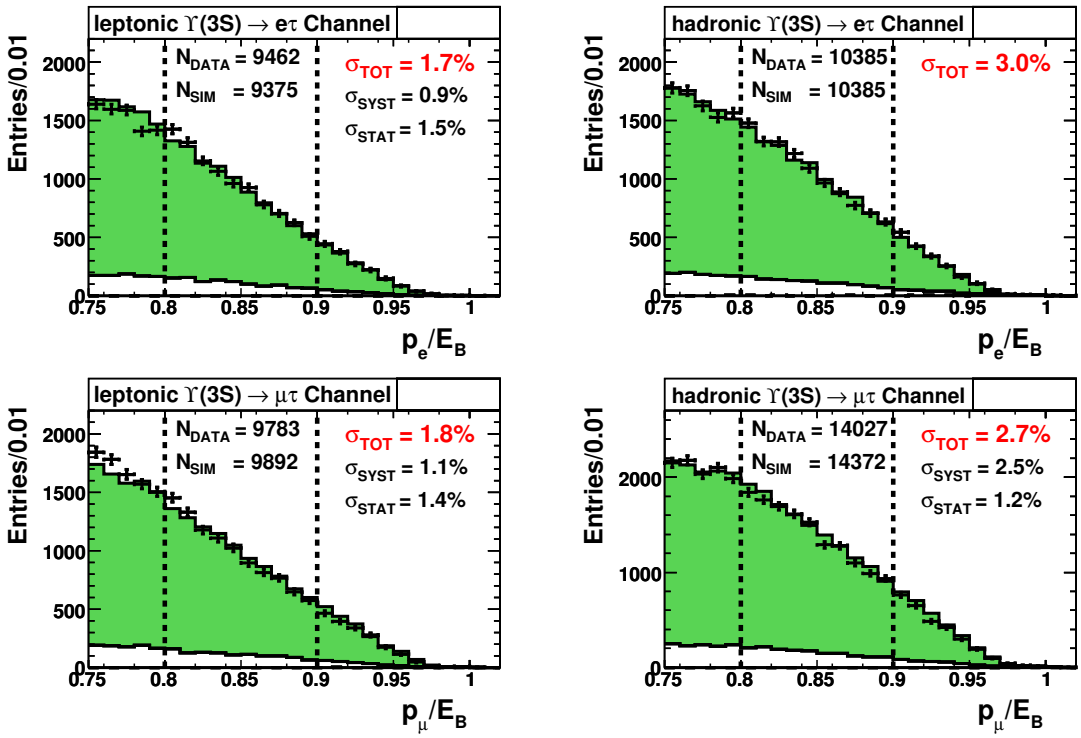

Figure 2.28: Comparison of the x distributions between data and simulated events after efficiency correction is applied. $\mathrm{N_{DATA}}$ and $\mathrm{N_{SIM}}$ denote the data and simulated event yields in the range $0.8 < x < 0.9$. For the hadronic $e\tau$ channel, the simulated event yield has been scaled to match the data yield, and half the correction factor is assessed as the uncertainty in the signal efficiency. For all other channels the uncertainty is assessed by comparing the data and simulated event yields in this range, where $\sigma_{SYST} = |\mathrm{N_{DATA}} - \mathrm{N_{SIM}}|/\mathrm{N_{DATA}}$, $\sigma_{STAT} = \sqrt{1/\mathrm{N_{DATA}} + 1/\mathrm{N_{SIM}}}$ and $\sigma_{TOT} = \sigma_{SYST} \oplus \sigma_{STAT}$.

shown in Fig. 2.28, in which the uncertainties for each channel are displayed.

Uncertainties in the τ branching fractions as well as the statistical uncertainties in the signal selection efficiency must also be taken into account. The signal selection efficiency can be expressed as $\epsilon_{SIG} = \frac{N_{PASS}}{N_{GEN}} = \frac{N_{PASS}}{BF \times N_{GEN}} BF$, where N_{PASS} and N_{GEN} are the number of events passing selection and the number of generated events, respectively, and BF denotes the relevant τ branching fraction. I use the 2008 PDG values [24] for the τ decay branching fractions and their uncertainties, which are stated in Chap. 2.8.2. The statistical uncertainty in the quantity

Table 2.6: Summary of systematic uncertainties in the signal efficiency due to discrepancies between data and simulation, the errors in the τ branching fractions, statistical uncertainties, and the error in the muon selection efficiency (for the $\mu\tau$ channels only).

Quantity	**leptonic $e\tau$**	**hadronic $e\tau$**	**leptonic $\mu\tau$**	**hadronic $\mu\tau$**
Data vs. Simulation ($\times 10^{-2}$)	1.7	3.0	1.8	2.7
τ BFs ($\times 10^{-3}$)	2.9	4.6	2.8	4.6
Statistical ($\times 10^{-3}$)	2.8	1.6	2.6	1.7
$\sigma(\epsilon_\mu)$ ($\times 10^{-3}$)			3.0	3.0
Total ($\times 10^{-2}$)	**1.8**	**3.0**	**1.9**	**2.8**

$\epsilon_{SEL} = \frac{N_{PASS}}{BF \times N_{GEN}}$ is given by $\sqrt{(\epsilon_{SEL}(1-\epsilon_{SEL}))/(BF \times N_{GEN})}$. The uncertainties due to discrepancies between data and simulated events, uncertainties in the τ branching fractions, statistical uncertainties, and the errors in the muon selection efficiency (for the $\mu\tau$ channels only) are added in quadrature to give the total signal selection efficiency uncertainties, as summarized in Table 2.6.

2.11.2 Signal Yield

The dominant contribution to the systematic uncertainty in the decay branching fractions comes from the uncertainty in the extracted signal yields, which is due to uncertainties in the PDF shapes. To assess these uncertainties each PDF shape parameter p_i is varied by its uncertainty and the resulting change in signal yield δ_i=ΔN_{SIG} is determined. The total systematic uncertainty in the signal yield is given by $\delta_{TOT} = \sqrt{\vec{\delta}^T C \vec{\delta}}$, where $\vec{\delta} =< \delta_1 \cdots \delta_N >$ and C is the parameter correlation matrix, giving a systematic uncertainty in the signal yield of 6-12 events depending on the signal channel. The total number of PDF parameters consists of 6 parameters for the signal double Crystal Ball function, 5 parameters for the peaking background Argus plus Gaussian PDF, 6 parameters for the double Crystal Ball detector resolution function, the τ-pair kinematic endpoint x_{MAX}, the shift and scale factors accounting for potential discrepancies in momentum resolution

Table 2.7: Summary of systematic uncertainties due to the PDF shape uncertainties. Displayed is the uncertainty in the signal yield obtained by varying all parameters in a given category. The lepton momentum resolution is denoted by $\sigma(p_\ell)$. The total signal yield uncertainty is the quadrature sum of the uncertainties for each of the six categories.

Category	**leptonic $e\tau$**	**hadronic $e\tau$**	**leptonic $\mu\tau$**	**hadronic $\mu\tau$**
Bhabha/μ-pair PDF	0.3	4.4	3.6	6.5
Signal PDF	1.2	0.2	0.2	0.4
Detector Resolution Function	2.4	2.5	2.0	3.7
τ-pair Endpoint	4.9	6.2	5.1	8.5
$\Upsilon(3S)$ vs. $\Upsilon(4S)$ $\sigma(p_\ell)$	1.3	1.8	1.2	2.0
$\Upsilon(3S)$ data vs. simulation $\sigma(p_\ell)$	0.7	0.5	0.9	0.7
TOTAL	**5.8**	**8.2**	**6.7**	**11.5**

between the $\Upsilon(3S)$ and $\Upsilon(4S)$ data samples as discussed in App. B.2, and the shift and scale factors accounting for potential discrepancies between the momentum resolution in $\Upsilon(3S)$ data and simulated events as discussed in App. B.3, resulting in 22 total parameters. The uncertainty in the signal PDF, peaking background PDF, and detector resolution parameters are determined according to their statistical uncertainties extracted by fits to the simulated events and their correlation matrices are taken into account. The uncertainty in x_{MAX} is taken to be the statistical error in the fit to the full $\Upsilon(4S)$ data sample. The uncertainties in the momentum resolution shift and scale parameters between $\Upsilon(4S)$ and $\Upsilon(3S)$ data are taken as half the correction factors determined in App. B.2. The detector momentum resolution function is shifted and scaled by the values determined in App. B.3 by comparing $\Upsilon(3S)$ data and simulated events, in order to assess the uncertainties due to potential discrepancies between the resolution in data and simulation. The signal yield uncertainties resulting from the uncertainties in these PDF shape parameters are displayed in Table 2.7.

2.11.3 Number of Collected $\Upsilon(3S)$ Decays

The number of collected $\Upsilon(3S)$ decays in the data sample is determined to be $N_{\Upsilon(3S)} = (116.7 \pm 1.2) \times 10^6$ by counting the number of multihadron events in the data. This leads to a 1% systematic uncertainty, which is dominated by the uncertainty in the selection efficiency for multihadron events.

2.11.4 Fit Bias

To assess the potential bias in the fit procedure, the study described in detail in App. C using a large number of simulated pseudo-experiments is performed. A large number of simulated background x distributions are generated from the background PDFs, and a Poisson-smeared yield of simulated signal events is added. The mean of the Poisson distribution of the signal yield is set to the extracted signal yield for those channels in which a positive signal yield is extracted; otherwise it is set to zero. The fit is performed multiple times and the deviation from zero in the distribution of extracted minus generated signal yield is taken as the uncertainty due to the fit bias, yielding uncertainties of about 1-2 events for each of the four signal channels, as shown in Fig. 2.29.

2.12 Maximum Likelihood Fit Results and Extraction of Branching Fraction Upper Limits

The maximum likelihood fit results for the full $\Upsilon(3S)$ data sample are summarized in Table 2.8 and displayed in Fig. 2.30. After including the systematic uncertainties in the PDF shapes and those from the fit bias, the extracted signal yields are all consistent with zero within $\pm 2.1\sigma$. The 90% confidence level upper limits, most probable values, and errors on the signal decay branching

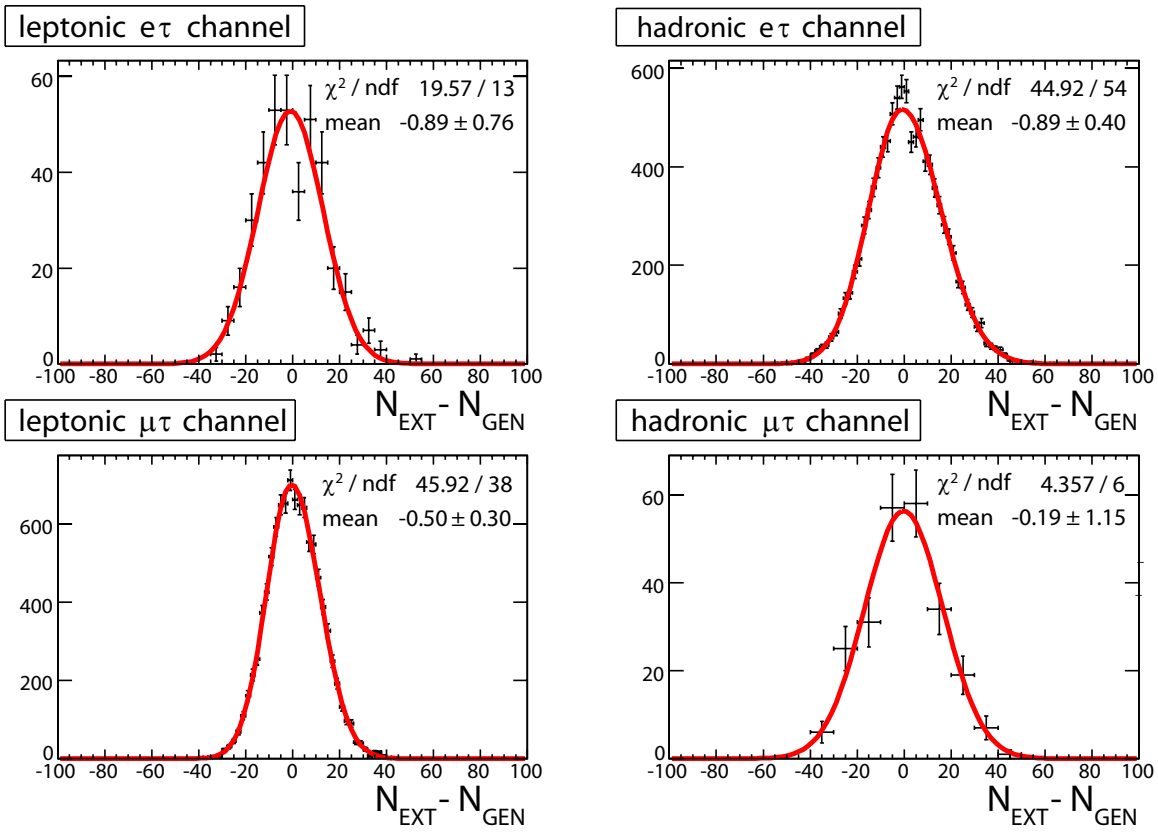

Figure 2.29: Results of the study of bias in the fit procedure using a large number of simulated pseudo-experiments. Plotted is the distribution of extracted signal yield $\mathrm{N_{EXT}}$ minus generated yield $\mathrm{N_{GEN}}$ for the four signal channels. The uncertainty due to the fit bias is taken to be the absolute value of the mean plus the error in the mean of the fit function, which is a Gaussian for the leptonic $e\tau$ channel and hadronic $\mu\tau$ channel, and a bifurcated Gaussian for the other two channels.

fractions are measured by determining the dependence of the likelihood function L on the branching fractions. For each signal channel individually, the relevant branching fraction ($BF(\Upsilon(3S) \to e\tau)$ for the $e\tau$ channels and $BF(\Upsilon(3S) \to \mu\tau)$ for the $\mu\tau$ channels) is scanned in small increments, and the maximum likelihood fit is performed with the signal yield fixed to the corresponding value given by $N_{SIG} = \epsilon_{SIG} \times N_{\Upsilon(3S)} \times BF$. The resulting distributions of the negative log likelihood as a function of branching fraction are well-described by 5^{th}-order polynomial functions as shown in Fig. 2.31. The maximum likelihood estimator $\hat{\theta}$ is the value of the unknown parameter θ, in this

case the signal decay branching fraction, which minimizes the negative log likelihood. Next, the following quantities are evaluated [24]:

$$\chi^2_{stat}(\theta) = -2\log L(\theta)/L_0 \tag{2.13}$$

$$\chi^2_{syst}(\theta) = \frac{(\theta - \hat{\theta})^2}{2\sigma^2_{syst}}. \tag{2.14}$$

Here the subscripts $stat$ and $syst$ indicate that only statistical and systematic uncertainties are incorporated, L_0 is the minimum value of the negative log likelihood, and it is assumed that the systematic errors are Gaussian distributed with uncertainty σ_{syst}. The systematic errors have additive contributions $\sigma^{(A)}_{syst}$ which do not scale with the branching fraction, and multiplicative contributions $\Delta^{(M)}_{stat}$ which are proportional to the branching fraction. Since the systematic uncertainties are being incorporated for each signal channel individually, only the systematic errors which are uncorrelated between the signal channels are taken into account at this step. The additive contributions include the uncertainties due to the PDF shapes and the fit bias, while the multiplicative contribution is due to the signal efficiency uncertainty. The total systematic uncertainty is the sum in quadrature of these contributions:

$$\sigma^2_{syst} = \left(\sigma^{(A)}_{syst}\right)^2 + \theta^2 \left(\Delta^{(M)}_{stat}\right)^2. \tag{2.15}$$

The statistical and systematic χ^2 values add according to:

$$\frac{1}{\chi^2_{tot}(\theta)} = \frac{1}{\chi^2_{stat}(\theta)} + \frac{1}{\chi^2_{syst}(\theta)}, \tag{2.16}$$

and the distributions of $\chi^2_{stat}(\theta)$ and $\chi^2_{tot}(\theta)$ are displayed for each channel in Fig. 2.32.

The next step is to combine the results of the two $\Upsilon(3S) \to e\tau$ and the two $\Upsilon(3S) \to \mu\tau$ channels, which is performed by adding their distributions of $\chi^2_{tot}(\theta)$. The systematic uncertainties due to the number of collected $\Upsilon(3S)$ decays, as well as the uncertainty in the muon selection

efficiency (for the $\mu\tau$ channels only) are then incorporated using the same procedure as above. The most probable values of the branching fractions are the values which minimize $\chi^2_{tot}(\theta)$. The negative and positive errors in the branching fractions are determined by finding $\pm\Delta(\theta)$ such that $\Delta\chi^2_{tot}(\theta)$=1. In order to extract the branching fraction upper limits, the likelihood is determined according to:

$$L(\theta) = e^{-\chi^2_{tot}(\theta)/2}, \tag{2.17}$$

as shown in Fig. 2.33. The 90% confidence level upper limit UL is determined by solving:

$$\int_0^{UL} L(\theta)\, d(\theta) / \int_0^{\infty} L(\theta)\, d(\theta) = 90\%, \tag{2.18}$$

which is equivalent to a Bayesian upper limit extraction in which the prior is taken to be the step function given by:

$$\mathrm{SF}(BF, 0) = \begin{cases} 0 & (BF < 0) \\ 1 & (BF > 0) \end{cases} \tag{2.19}$$

The results of the likelihood scan are summarized in Table 2.9.

Table 2.8: Summary of the fit results for the four signal channels of the $\Upsilon(3S)$ data sample [60]. Shown are the extracted signal yield N_{SIG}, the extracted Bhabha/μ-pair background yield N_{PKBKG}, and the extracted τ-pair background yield N_{BKG}. The first error is the parabolic statistical error, the second error (displayed only for the signal yield) is the systematic error from the PDF shape uncertainties and the fit bias.

Yield	**leptonic $e\tau$**	**hadronic $e\tau$**	**leptonic $\mu\tau$**	**hadronic $\mu\tau$**
N_{SIG}	$21 \pm 12 \pm 6$	$-1 \pm 14 \pm 8$	$-16 \pm 9 \pm 7$	$42 \pm 17 \pm 12$
N_{PKBKG}	25 ± 15	63 ± 16	35 ± 13	57 ± 12
N_{BKG}	19611 ± 141	21523 ± 147	20923 ± 145	28661 ± 170

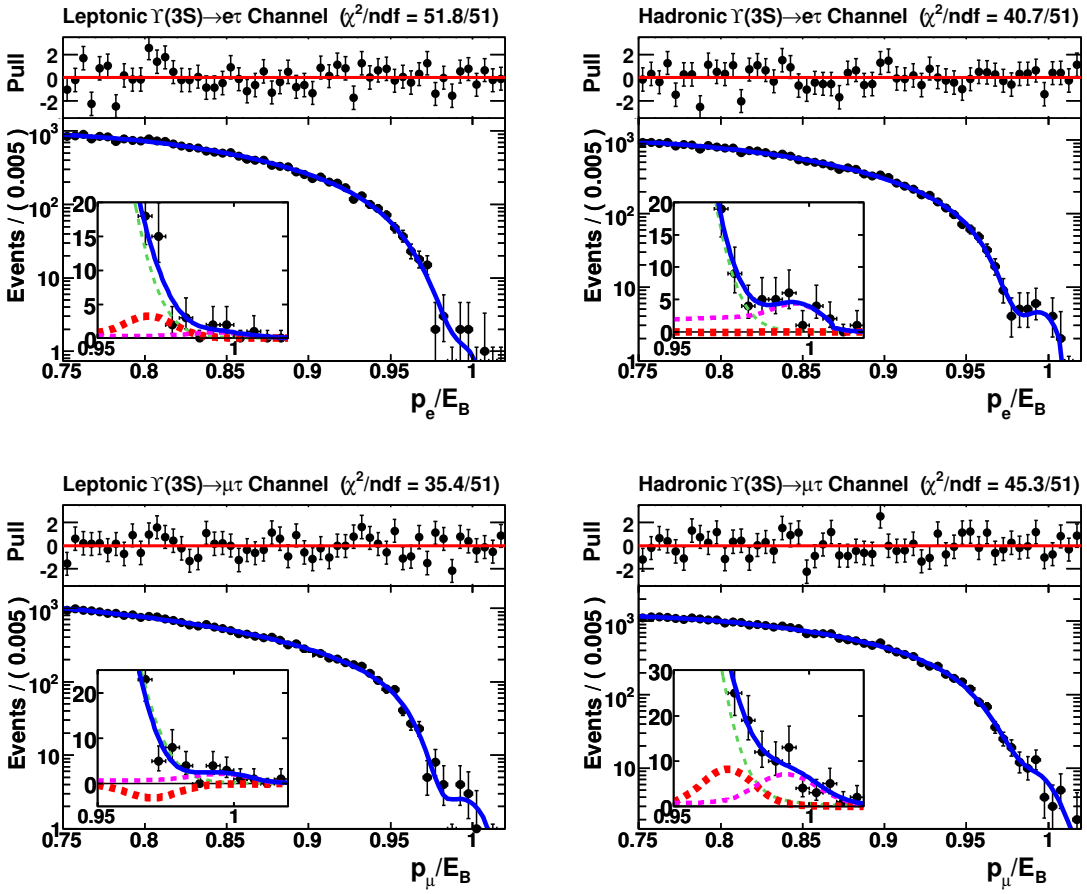

Figure 2.30: Fit results for the 27.5 fb^{-1} Υ(3S) data sample for the four signal channels [60]. The thin green dashed line is the τ-pair background PDF, the medium magenta dashed line is the peaking background PDF, the thick red dashed line is the signal PDF, and the solid blue line is the sum of these components. The inset shows a close-up of the region $0.95< x <1.02$.

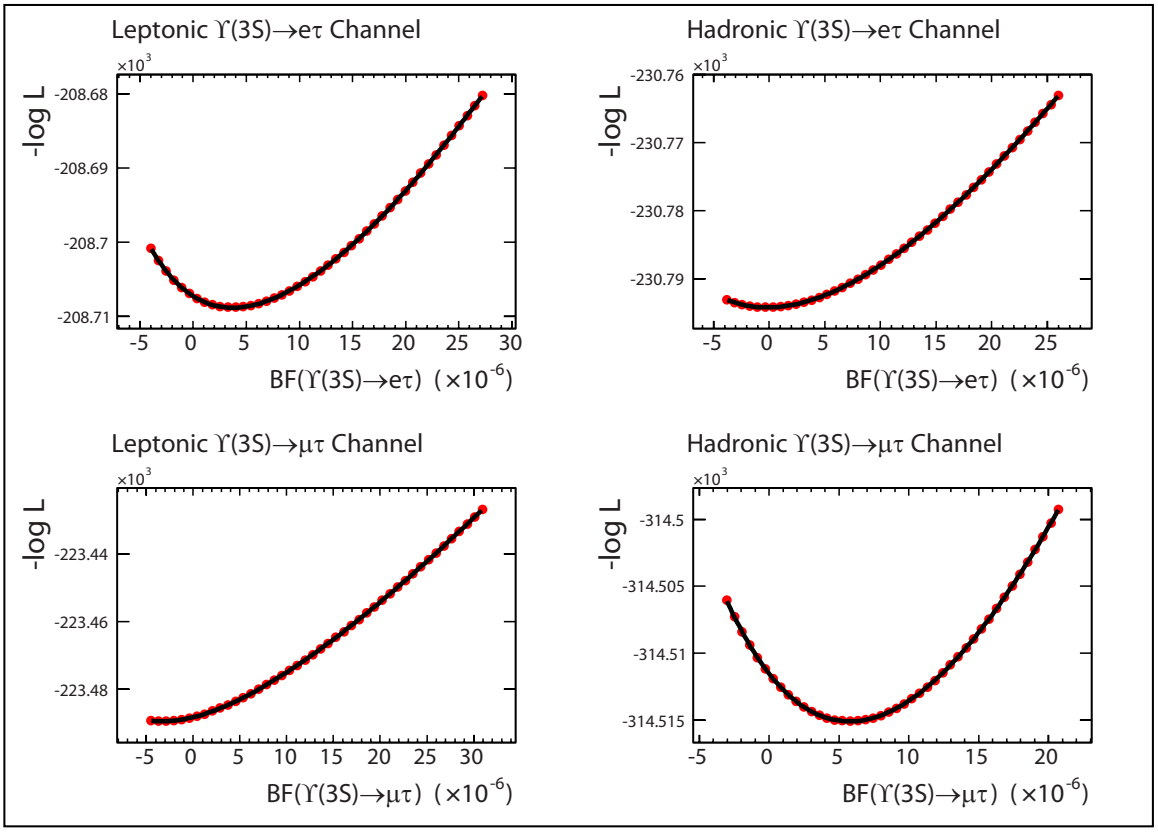

Figure 2.31: Negative log likelihood as a function of the branching fractions $BF(\Upsilon(3S) \rightarrow e\tau)$ and $BF(\Upsilon(3S) \rightarrow e\tau)$. The red circles indicate the results of the maximum likelihood fits and the black curve is a 5^{th}-order polynomial fit to the results.

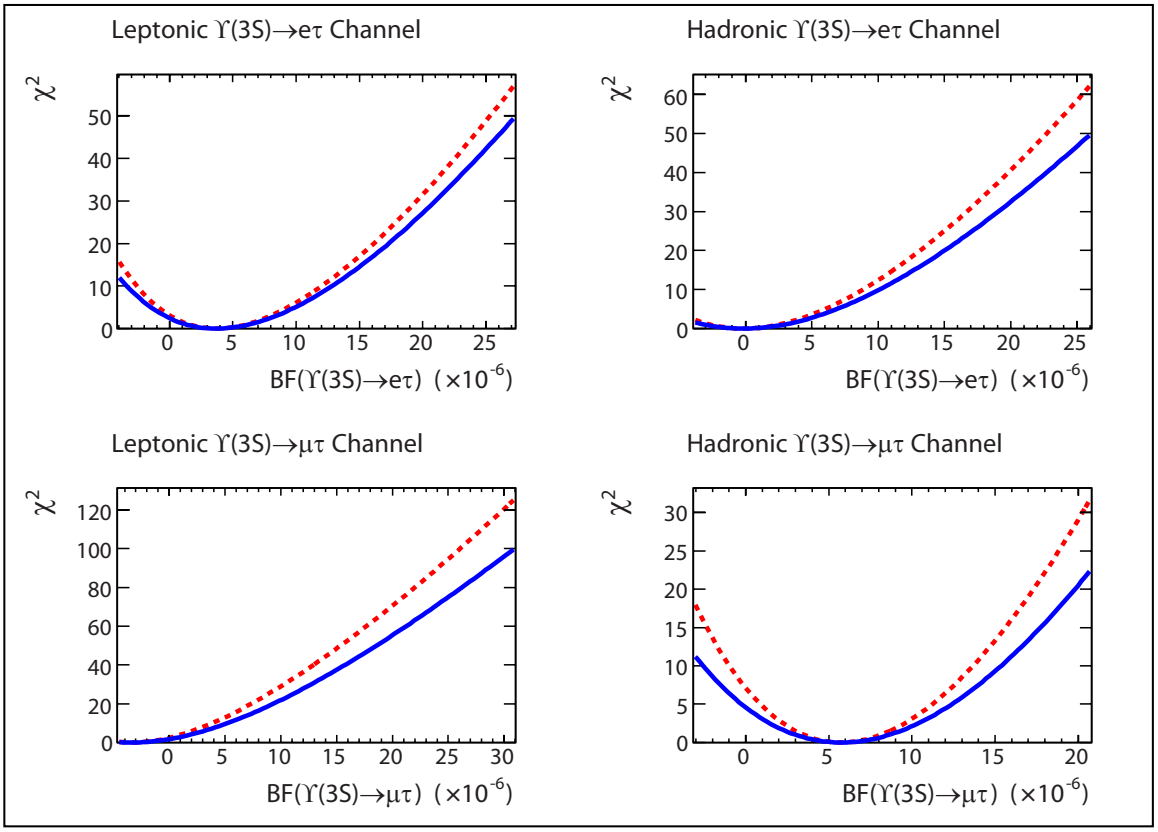

Figure 2.32: The quantity χ^2 as a function of the branching fractions $BF(\Upsilon(3S) \rightarrow e\tau)$ and $BF(\Upsilon(3S) \rightarrow e\tau)$. The dashed red curve incorporates statiscal uncertainties only, the solid blue curve also incorporates systematic uncertainties.

Table 2.9: Summary of the results of the likelihood scan [60]. Displayed are the 90% confidence level upper limits, most probable values, and negative and positive asymmetric errors.

	UL	MPV	σ_-	σ_+
$BF(\Upsilon(3S) \to e\tau)$ ($\times 10^{-6}$)	<5.0	2.2	-1.8	+1.9
$BF(\Upsilon(3S) \to \mu\tau)$ ($\times 10^{-6}$)	<4.1	1.2	-1.9	+1.9

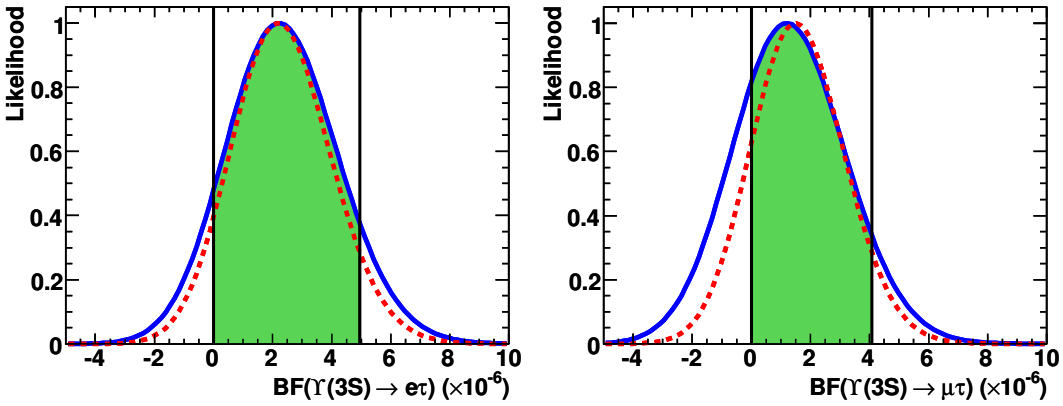

Figure 2.33: Likelihood as a function of the branching fractions $BF(\Upsilon(3S) \to e\tau)$ (left) and $BF(\Upsilon(3S) \to \mu\tau)$ (right) [60]. The dotted red curve includes statistical uncertainties only, the solid blue curve includes systematic uncertainties as well. The shaded green regions bounded by the vertical lines indicate 90% of the area under the physical ($BF > 0$) regions of the likelihood curves.

2.13 Constraints on New Physics

The search for the charged lepton-flavor violating decays $\Upsilon(3S) \to e\tau$ and $\Upsilon(3S) \to \mu\tau$ finds no evidence for a signal. The observed signal yields are used to place the following 90% confidence level upper limits on the decay branching fractions: $BF(\Upsilon(3S) \to e\tau) < 5.0 \times 10^{-6}$ and $BF(\Upsilon(3S) \to \mu\tau) < 4.1 \times 10^{-6}$. These results represent the first upper limit on $BF(\Upsilon(3S) \to e\tau)$ and a factor of better than 4 improvement in $BF(\Upsilon(3S) \to \mu\tau)$.

The derived branching fraction upper limits can be used to place constraints on new

physics parameters using effective field theory. The decay $\Upsilon(3S) \rightarrow \ell\tau$ can be parameterized as an effective 4-fermion $b\bar{b}\ell\tau$ contact interaction with coupling constant $\alpha_{\ell\tau}$ and mass scale $\Lambda_{\ell\tau}$ as shown in Fig. 2.3f. In [110, 111], the following relation between the lepton-flavor violating and dilepton branching fractions is derived:

$$\frac{\alpha_{\ell\tau}^2}{\Lambda_{\ell\tau}^4} = \frac{BF(\Upsilon(3S) \rightarrow \ell\tau)}{BF(\Upsilon(3S) \rightarrow \ell^+\ell^-)} \frac{2q_b^2\alpha^2}{(M_{\Upsilon(3S)})^4} \quad (\ell = e, \mu) \tag{2.20}$$

The quantity $\alpha_{\ell\tau}^2/\Lambda_{\ell\tau}^4$ is proportional $BF(\Upsilon(3S) \rightarrow \ell\tau)$, so the derived upper limit on $BF(\Upsilon(3S) \rightarrow \ell\tau)$ translates to an upper limit on $\alpha_{\ell\tau}^2/\Lambda_{\ell\tau}^4$. I use $\alpha = \alpha(M_{\Upsilon(3S)}) = 1/132.1$ and evaluate $BF(\Upsilon(3S) \rightarrow \ell^+\ell^-) = (0.218 \pm 0.15)$ %, using the average of the 2008 PDG values [24] $BF(\Upsilon(3S) \rightarrow e^+e^-) = (2.18 \pm 0.20)$ % and $BF(\Upsilon(3S) \rightarrow \mu^+\mu^-) = (2.18 \pm 0.21)$ %. The likelihood scan as a function of $BF(\Upsilon(3S) \rightarrow \ell\tau)$ described Chap. 2.12 is modified to give the likelihood as a function of the quantity $\alpha_{\ell\tau}^2/\Lambda_{\ell\tau}^4$ as shown in Fig. 2.34 (top), while taking into account the 7% uncertainty in the dilepton branching fraction of the $\Upsilon(3S)$. Using the same method of integrating the likelihood function, the following 90% confidence level upper limits are derived: $\alpha_{e\tau}^2/\Lambda_{e\tau}^4 < 0.256$ TeV^{-4} and $\alpha_{\mu\tau}^2/\Lambda_{\mu\tau}^4 < 0.212$ TeV^{-4}. These limits translate to an exclusion region in the $\Lambda_{\ell\tau}$ vs. $\alpha_{\ell\tau}$ plane, as shown in Fig. 2.34 (bottom). Assuming strong coupling ($\alpha_{e\tau} = \alpha_{\mu\tau} = 1$), these results correspond to the 90% confidence level lower limits $\Lambda_{e\tau} >$1.41 TeV and $\Lambda_{\mu\tau} >$1.47 TeV on the mass scale of BSM physics contributing to CLFV $\Upsilon(3S)$ decays. The corresponding 95% confidence level lower limits are $\Lambda_{e\tau} >$1.36 TeV and $\Lambda_{\mu\tau} >$1.42 TeV.

2.14 Other Lepton Flavor Violation Searches

Although flavor violation among charged leptons is unobservable in the SM, it is a general feature of several new physics scenarios, including SUSY and theories with extra dimensions, that

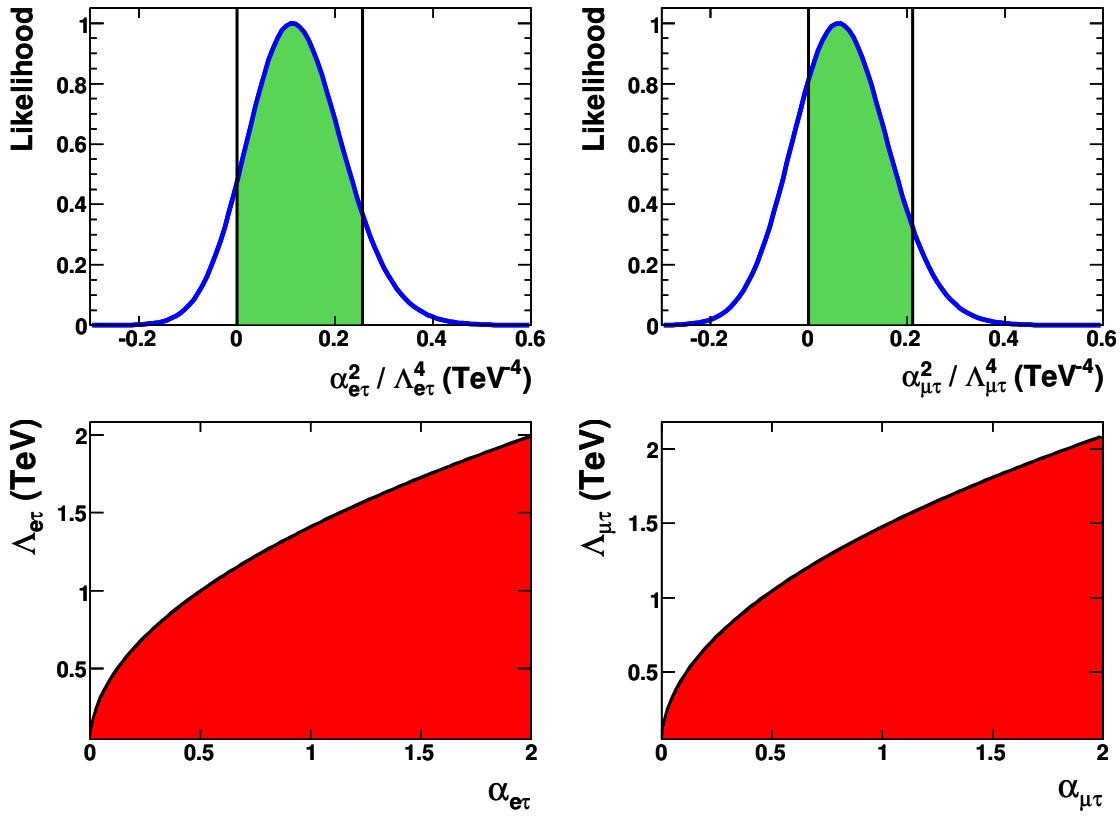

Figure 2.34: Likelihood as a function of the quantity $\alpha^2_{\ell\tau}/\Lambda^4_{\ell\tau}$ (top two plots), with all systematic uncertainties included. The shaded green regions bounded by the vertical lines indicate 90% of the area under the physical regions of the likelihood curves. Two-dimensional exclusion regions in the $\Lambda_{\ell\tau}$ vs. $\alpha_{\ell\tau}$ plane (bottom two plots). The shaded red regions are excluded at 90% confidence level.

additional sources of LFV are introduced [72]. This new physics may be observable in the decays of many particles, and searches have been performed for LFV in μ, τ, π, K, D, B, $W^{\pm}$ and Z^0 decays. Although no signal has been observed to date, the results have been used to place constraints on new physics at extremely high energy scales.

The best sensitivity to LFV branching fractions has been achieved in μ decay searches. These results come from dedicated experiments which take advantage of muon beams with extremely high fluxes and hence achieve extremely large statistical samples. The muons are brought

Table 2.10: Summary of selected results of searches for LFV μ and τ processes [72].

Mode	**90% CL Upper Limit**	**Experiment**	**Reference**
$\mu^+ \to e^+e^+e^-$	1×10^{-12}	SINDRUM I	[77]
$\mu^+ \to e^+\gamma$	1.2×10^{-11}	MEGA	[78]
$\mu^-\mathrm{Ti} \to e^-\mathrm{Ti}$	6.1×10^{-13}	SINDRUM II	[79]
$\tau^- \to e^-\gamma$	11×10^{-8}	*BABAR*	[80]
$\tau^- \to \mu^-\gamma$	6.8×10^{-8}	*BABAR*	[81]
$\tau^- \to \ell^-\ell^+\ell^-$	$(2-4) \times 10^{-8}$	Belle	[89]
$\tau^- \to e^-\pi^0$	8.0×10^{-8}	Belle	[82]
$\tau^- \to \mu^-\pi^0$	11×10^{-8}	*BABAR*	[83]

to rest after striking a target inside a detector, which measures the μ decay products. Using this method, searches for $\mu \to e\gamma$, $\mu \to eee$, and $\mu \to e$ conversion in the presence of a nucleus have been performed. The current upper limits on these processes are summarized in Table 2.10, and are of order $10^{-11} - 10^{-13}$. These results have been used to place limits on the mass scale of new physics contributing to LFV μ decays of order $100 - 1000$ TeV, as shown in Fig. 2.35. However, these mass scale constraints are derived using the assumption of strong coupling, which is not necessarily valid. If the flavor-violating couplings of charged leptons are determined by a mixing matrix in analogy with the neutrino mixing matrix, the elements of this matrix are unknown. It is therefore possible that the flavor-violating coupling between the first two generations is smaller than couplings of the first or second to the third generation. In addition, if the new physics is in the Higgs sector, coupling between the light electrons and muons would be substantially suppressed with respect to couplings of the electron, and especially the muon, to the tau. In either case the assumption of strong coupling could be grossly violated, resulting in substantial reduction of the constraints on the new physics mass scale. The implication is that the interpretation of upper limits

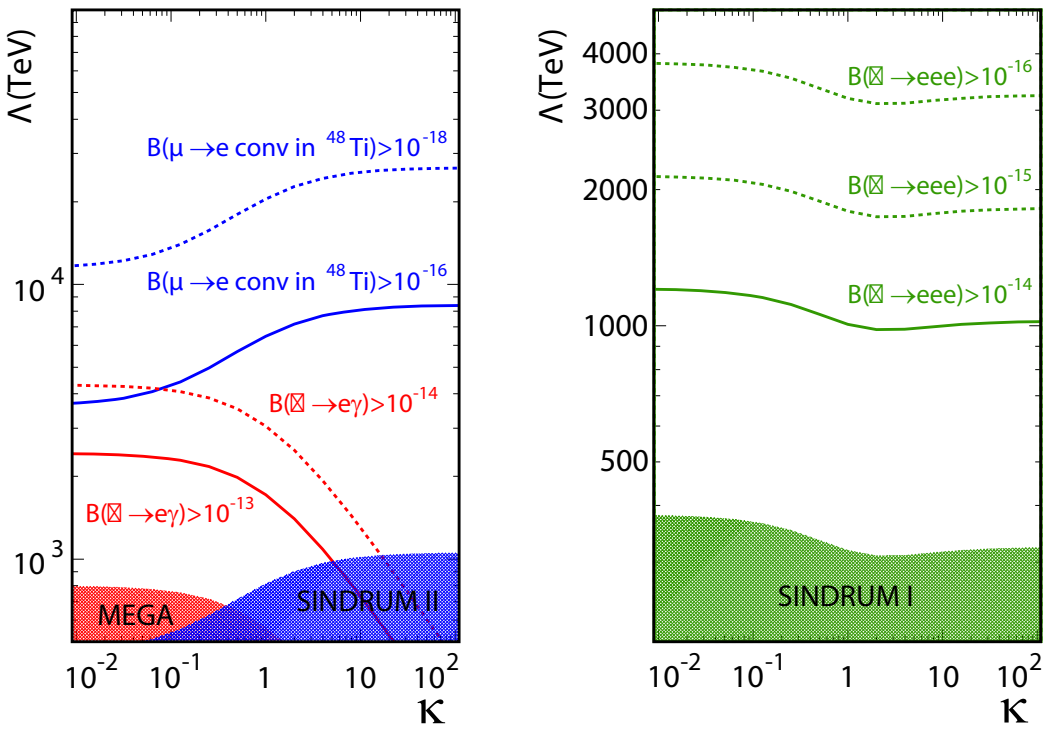

Figure 2.35: Constraints on the mass scale of new physics from LFV μ decay searches [112]. The parameter κ determines the relative rates for various LFV μ processes. If $\kappa << 1$ the $\mu \to e\gamma$ and $\mu \to eee$ processes are enhanced, while if $\kappa >> 1$ the $\mu \to e$ conversion process is enhanced. The shaded regions are excluded by the indicated experiments, while the solid and dotted curves indicate the targeted sensitivity reach of future experiments.

on LFV μ processes in terms of constraints on new physics is highly model-dependent.

Searches for LFV τ decays have also been carried out at the B-factories, *BABAR* and Belle. These experiments have searched for several LFV τ decays, which are summarized in Table 2.10. Although not as sensitive as the upper limits on LFV μ processes, these searches have obtained sensitivities to branching fractions of order 10^{-8}. The $\tau \to \ell\ell\ell$ process is of particular interest since the upper limit can be compared to the LFV Υ branching fraction upper limits using Eq. 2.2. If the $\tau \to \ell\ell\ell$ process were mediated solely by virtual Υ exchange as shown in Fig. 2.4, the upper limit $BF(\Upsilon(3S) \to \ell\tau) < (4.1 - 5.0) \times 10^{-6}$ would translate to $BF(\tau \to \ell\ell\ell) < (2.6 - 3.2) \times 10^{-11}$, significantly better than the current upper limit for this process. However, since the relative

contribution of virtual Υ exchange to the $\tau \to \ell\ell\ell$ process is not known, it is not possible to compare $BF(\Upsilon(3S) \to \ell\tau)$ and $BF(\tau \to \ell\ell\ell)$ in a model-independent way.

The conclusion of these considerations is that LFV may manifest in the decays of many particles, and the relative rates for these processes are highly model-dependent. Therefore it is important to search for LFV in as many decay channels as possible and compare results. If a signal is observed, this comparison will aid in ellucidating the nature of the new physics contributing to LFV, while null results may be used to constrain new physics scenarios.

Chapter 3

Research and Development of Advanced Sensors for the Vertex Tracker at a Future Lepton Collider

3.1 Motivation

Although precise measurements at low energy can be used to probe the TeV-scale, the primary strategy for new physics searches is to probe this mass regime by direct production of new particles at higher collision energies. This requires the construction of a collider capable of attaining TeV-scale CM energies, as well as a detector capable of reconstructing events accurately enough to realize the full physics potential of such a collider. The LHC will provide proton-proton collisions up to $\sqrt{s} = 14$ TeV, the highest collision energies achieved to date. This large CM energy and the large cross section for production of new states make the LHC a discovery machine, capable

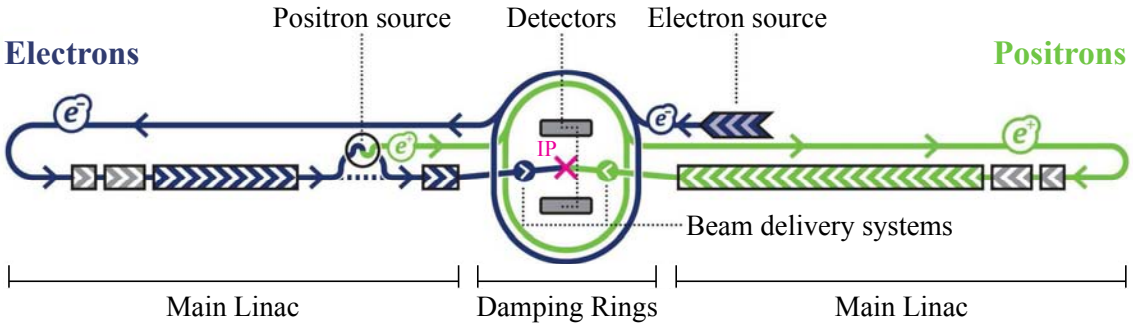

Figure 3.1: Layout and primary components of the proposed ILC. Electrons are produced, circulated in damping rings to minimize their emittance, and injected into a linear accelerator (linac). Positrons are produced by colliding some of these electrons on a target, resulting in bremsstrahlung photons which convert to electron-positron pairs in the presence of the target nuclei. The positrons are collected, circulated in damping rings and injected into a linac. Collisions take place at a single interaction point (IP), with two detectors which are alternately placed at the IP. Image from B. Barish.

of probing a wide variety of new physics scenarios and of searching for the Higgs boson over the full anticipated mass range up to ∼1 TeV [49, 50]. However, in order to provide precision probes of the discoveries made at the LHC, an e^+e^- collider operating at CM energies of order 1 TeV is required [51, 52]. The proposed ILC [61], depicted in Fig. 3.1, would initially provide e^+e^- collisions at a tunable CM energy up to 500 GeV and would be upgradeable to 1 TeV. As discussed in Chap. 1.4.1, the precise measurements available in e^+e^- collisions are made possible by several advantages of lepton colliders with respect to hadron colliders. Since the particles undergoing collision are elementary particles, the initial state energy and momentum with respect to the lab frame are known. The CM collision energy of a lepton collider is adjustable, which allows the energy of a lepton collider to be tuned to the mass of some particle or resonance in order to investigate its properties. Since e^+e^- processes are subject to fewer theoretical uncertainties and backgrounds arising from non-perturbative QCD effects, the measurements at a lepton collider allow for more precise determinations of observables including masses, couplings and spins. Furthermore, there

are classes of new physics scenarios which the LHC data alone may not be able to distinguish[1]. A lepton collider such as the ILC is therefore likely required to take full advantage of the discoveries made at the LHC, allowing for a more complete understanding of BSM physics [51, 52]. A notable example of the complementarity between lepton and hadron colliders is the agreement between the indirect and direct top quark mass measurements, discussed in Chap. 1.2.

The physics at a TeV-scale lepton collider will include precise measurements of the Higgs properties if its mass is light and precision probes of BSM physics. This program places extremely stringent demands on the detector, surpassing the performance of any existing detector in several respects. The effort to construct such a detector is the subject of a world-wide study, which has the goal of developing sensor technologies and detector designs of sufficient performance to fully realize the physics program [62]. In particular, precise measurements of the properties of the Higgs boson require excellent detector performance. If the Higgs is heavy ($M_h \gtrsim 140\ GeV$), it will decay predominantly to pairs of electroweak bosons, W^+W^- and Z^0Z^0. These electroweak bosons decay predominantly to quark pairs, leading to pairs of jets (dijets). In order to measure the Higgs branching fractions $BF(h \to W^+W^-)$ and $BF(h \to Z^0Z^0)$, it is necessary to distinguish between dijets resulting from $W^\pm$ decays and those from Z^0 decays, which is performed by measuring the dijet mass. In order to achieve sufficient dijet mass resolution to distinguish between $W^\pm$ and Z^0 dijets, the calorimetry must provide excellent jet energy resolution. The required jet energy resolution is given by $\sigma(E_j)/E_j = 0.3/\sqrt{E_j}$, where E_j is the jet energy measured in GeV. This is significantly better than the best jet energy resolution that has been obtained to date at the ALEPH experiment at LEP, which achieved $\sigma(E_j)/E_j = 0.59/\sqrt{E_j} \oplus 0.6/E_j$ [113].

[1] A notable example includes Supersymmetry and a theory with extra dimensions known as the Unified Extra Dimensions model. Both models produce signatures consisting of jets, isolated leptons, and missing transverse energy and are therefore difficult to disentangle using only LHC data [114].

An important physics requirement driving the momentum resolution of the tracking detectors is the precise measurement of the Higgs mass independent of its decay mode. This can be performed by searching for the Higgsstrahlung process $e^+e^- \to hZ^0$, $Z^0 \to \ell^+\ell^-$, in which the Z^0 decays to a pair of electrons or muons. By precisely measuring the momenta of the leptons from the Z^0 decay, the Higgs mass can be measured by determining the mass recoiling against the lepton pair since $\sqrt{s}$ is known. The recoil mass resolution depends strongly on the track momentum resolution, for which the ILC target is $\sigma(1/p_T) = 5 \times 10^{-5}$ GeV^{-1}, where $1/p_T$ is the inverse of the track transverse momentum measured in GeV^{-1}. This is an order of magnitude more precise than the best track momentum resolutions that have been obtained to date of $\sigma(1/p_T) = 6 \times 10^{-4}$ (GeV/c)$^{-1}$ [113] and $\sigma(1/p_T) = 6 \times 10^{-4} \oplus 0.015/p_T$ (GeV/c)$^{-1}$ [115], achieved at the ALEPH and DELPHI experiments at LEP, respectively.

In this chapter, research and development (R&D) of Silicon sensors for the vertex tracker (VTX) at a TeV-scale lepton collider is presented. The performance of the VTX is driven in large part by the requirement to accurately measure branching fractions of the Higgs, necessary for probing the Higgs mechanism as discussed in Chap. 1.1. The VTX is the innermost detector and consists of multiple concentric barrels of Silicon pixel detectors surrounding the beam-pipe as shown in Fig. 3.2 (left). The function of the VTX is the precise extrapolation of charged particle tracks to their production points, which allows for the identification of heavy, long-lived particles such as b and c quarks and τ leptons. These particles travel a measurable distance before decaying and result in secondary decay vertices which are displaced from the primary interaction point. The precise track extrapolation provided by the VTX allows identification of these displaced vertices as shown in Fig. 3.2 (right). Tracks originating from displaced vertices, when extrapolated back toward their

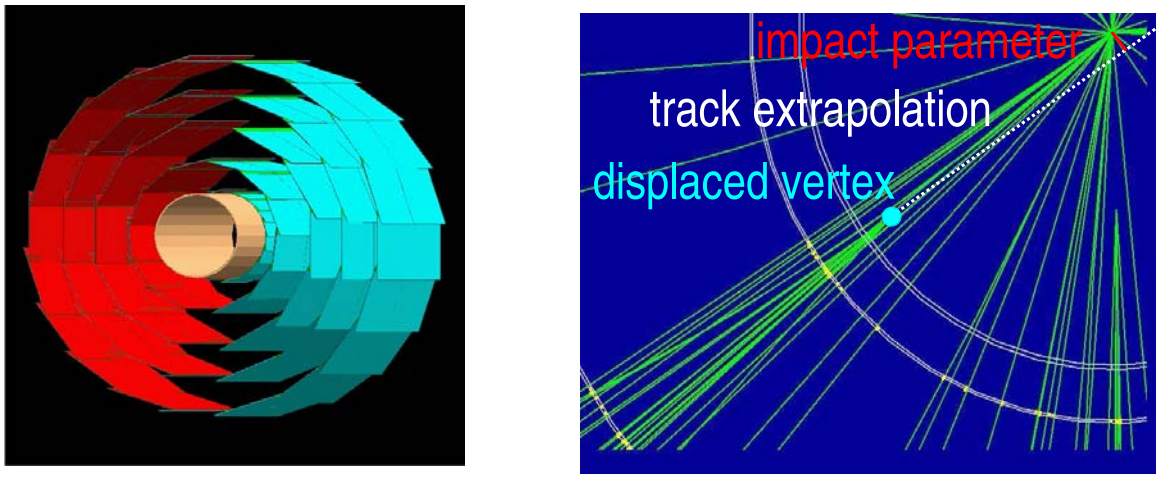

Figure 3.2: Left: proposed layout of the ILC VTX. Five concentric barrels of Silicon sensors surround the beam-pipe, which is the innermost cylinder. Right: event display zoomed in on the VTX and projected in the plane orthogonal to the beam axis. The white circular arcs are layers of the VTX and the straight green lines are charged tracks. The displaced vertex, extrapolation of a track associated to the secondary vertex toward the primary interaction point, and impact parameter of this track are indicated.

production point, have a larger distance of closest approach to the primary interaction point (called the impact parameter) than do tracks originating from the primary vertex. The efficiency of the VTX to identify heavy, long-lived particles via their displaced vertices, known as flavor tagging capability, depends on the impact parameter resolution σ_{IP}, which is the primary figure of merit of the VTX detector. If the Higgs is light ($M_h \lesssim 140$ GeV/c^2), it will decay to pairs of b and c quarks, τ leptons, as well as pairs of photons and gluons. The ability to identify and measure the branching fractions for the Higgs decays $h \to \tau^+\tau^-$, $h \to c\bar{c}$, and $h \to b\bar{b}$ requires excellent flavor tagging performance. Heavy particles also provide signatures of many new physics scenarios, including SUSY with large $\tan\beta$, the ratio of the vacuum expectation values of the two SUSY Higgs doublets. In addition, excellent flavor tagging performance is required for the analysis of pair production of heavy Higgs bosons in an extended model such as SUSY, which is the subject

of the analysis presented in Chap. 4. In this study final states consisting of 4 b jets and 2 b jets + 2 τ jets are considered. In order to isolate the 4 b jet signal from the multijet backgrounds which have a production cross section $O(10^4)$ larger than the signal process, it is necessary to identify all four b jets. The signal efficiency for this channel is therefore proportional to the 4^{th} power of the b identification efficiency. Excellent τ tagging ability is also required to isolate the 2 b jet + 2 τ jet final state.

The impact parameter resolution is due to two effects whose contributions add in quadrature, and can be expressed as $\sigma_{IP} = (a \oplus b/p_T\sqrt{\sin\theta})\ \mu\text{m}$, where p_T is the transverse momentum in GeV and θ is the track polar angle with respect to the beam axis. The constant term a depends on the finite spatial resolution of the Silicon sensors and the radial distances of the Silicon barrels. The contribution from this term is minimized by using sensors with excellent spatial resolution and placing the innermost VTX layer as close as possible to the primary interaction point. The second term proportional to $1/p_T\sqrt{\sin\theta}$ is due to multiple scattering. As a charged particle traverses a material, it undergoes deflections resulting from small-angle scatters. These deflections are due primarily to Coulomb interactions with the nuclei of the material. The RMS deflection angle of a particle traversing a material of thickness X is given by [24]:

$$\theta_{RMS} = \frac{13.6\text{MeV}}{\beta cp} z \sqrt{\frac{X}{X_0}} \left(1 + 0.038 \log \frac{X}{X_0}\right), \tag{3.1}$$

where the momentum, velocity, and charge of the particle are denoted p, βc, and z. The radiation length of the material is X_0 and the quantity X/X_0 is known as the material budget. In order to minimize the deflection angle it is necessary to minimize the thickness of the sensors used in the VTX. At high p_T the constant term provides the dominant contribution to σ_{IP}, while at low p_T the multiple scattering term dominates. Even at $\sqrt{s} = 0.5 - 1.0$ TeV, most of the particles in a hadronic

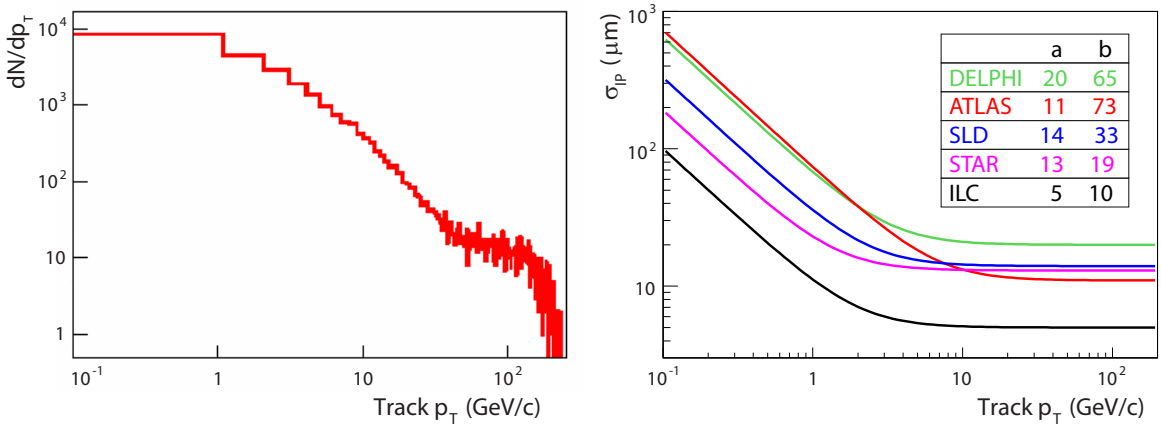

Figure 3.3: Left: distribution of transverse momentum for particles produced in the process $e^+e^- \rightarrow hZ^0 \rightarrow b\bar{b}\ell^+\ell^-$ at $\sqrt{s} = 500$ GeV. Image from M. Battaglia. Right: comparison of the achieved impact parameter resolutions for several existing experiments [115–117] and the targeted performance for the STAR heavy flavor tracker [118] and the ILC VTX [62]. The impact parameter resolution at normal incidence is given by $\sigma_{IP} = (a \oplus b/p_T)\ \mu\text{m}$ with p_T measured in GeV.

jet have transverse momenta less than a few GeV/c as shown in Fig. 3.3 (left), due to the large particle multiplicities. In this regime the multiple scattering term dominates as shown in Fig. 3.3 (right), in which the achieved impact parameter resolutions at several experiments are compared to the targeted ILC performance. Thin sensors are therefore required in order to minimize σ_{IP} for particles in hadronic jets.

The targeted impact parameter resolution for the ILC VTX is $\sigma_{IP} = (5 \oplus 10/p_T\sqrt{\sin\theta})\ \mu\text{m}$. Using this impact parameter resolution, the achievable b tagging performance is displayed in Fig. 3.4, and surpasses that of any existing experiment. The targeted ILC resolution is also significantly better than the best resolution achieved to date, that of the VXD3 detector of the SLAC Large Detector experiment which achieved $\sigma_{IP} = (14 \oplus 33/p_T\sqrt{\sin\theta})\ \mu\text{m}$ [117]. In Table 3.1, the performance of the calorimetry, tracking, and vertex detectors is compared between the DELPHI, *BABAR*, and ATLAS detectors, and the targeted performance for the ILC detector. In terms of jet energy resolution,

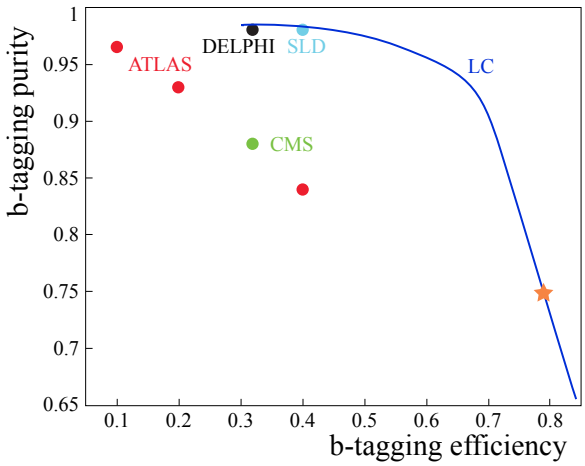

Figure 3.4: The b tagging performance envisioned for a future lepton collider (solid line), assuming an impact parameter resolution of $\sigma_{IP} = (5 \oplus 10/p_T\sqrt{\sin\theta})$ μm. Reference points from various other experiments (solid circles) are included for comparison. The working point chosen for the analysis of H^0A^0 production is indicated by the star. Image from M. Battaglia.

track momentum resolution, and impact parameter resolution, the detector performance required by a TeV-scale lepton collider substantially surpasses all detectors built to date.

The ILC impact parameter resolution requirement translates to a requirement for sensor modules not exceeding $X/X_0 = 0.1\%$ ($\sim$ 100 μm) including support and cabling, and the sensor thickness therefore cannot exceed $40 - 50$ μm. This constitutes one of the primary performance drivers dictating the choice of detector type for the ILC VTX and requires the development of novel sensor technologies. In this chapter I describe R&D of Silicon sensors for the vertex tracker at a future lepton collider. The goal of this work is to demonstrate the feasibility of designing and constructing a vertex tracker which satisfies the ILC performance specifications. In Chap. 3.2 I provide a brief introduction to Silicon tracking detectors. In Chap. 3.3 I review R&D efforts aimed at developing thin, high performance sensors using the CMOS pixel sensor technology. In Chap. 3.4 I discuss the development and performance of a small-scale vertex tracker prototype built using multiple planes of thinned CMOS sensors, and I present the conclusions of this work in Chap. 3.5.

Table 3.1: Comparison of the performances of the DELPHI, ATLAS and BABAR detectors and the targeted performance for the ILC detector [62, 115, 116, 119]. The calorimetry figure of merit (FOM) is the jet energy resolution $\sigma(E_j)/E_j$, the tracker FOM is the resolution of the inverse transverse momentum $\sigma(1/p_T)$, and the vertex tracker FOM is the impact parameter resolution σ_{IP}. All values of energy E and transverse momentum p_T are expressed in GeV and GeV/c, respectively. No jet energy resolution is quoted for BABAR because jet formation does not occur at $\sqrt{s} = M_\Upsilon$.

Detector FOM	**DELPHI**	**BABAR**	**ATLAS**	**ILC (target)**
$\sigma(E_j)/E_j$	$\frac{0.84}{\sqrt{E}}$		$\frac{0.48}{\sqrt{E}} \oplus 0.018$	$\frac{0.3}{\sqrt{E}}$
$\sigma(1/p_T)$	$6 \times 10^{-4} \oplus \frac{0.015}{p_T}$	$0.14\% \oplus \frac{0.21\%}{p_T}$	$3.6 \times 10^{-4} \oplus \frac{0.013}{p_T\sqrt{\sin\theta}}$	5×10^{-5}
σ_{IP} (μm)	$20 \oplus \frac{65}{p_T\sqrt{\sin\theta}}$	$15 \oplus \frac{50}{p_T\sqrt{\sin\theta}}$	$11 \oplus \frac{73}{p_T\sqrt{\sin\theta}}$	$5 \oplus \frac{10}{p_T\sqrt{\sin\theta}}$

3.2 Introduction to Silicon Detectors

Several requirements drive the choice of sensor technology for use in vertex tracking detectors. The sensors must have excellent spatial resolution in order to precisely extrapolate particle tracks, they must be thin in order to reduce multiple scattering, and they must be capable of fast readout. In addition, the placement of these sensors at small radii close to the beam results in large particle fluxes. The sensors must therefore be capable of withstanding high radiation doses, and they must be highly granular to facilitate pattern recognition in the environment of high hit density. These requirements may be met a particular class of Silicon tracking detectors called monolithic pixel sensors.

Silicon tracking detectors play a major role in all current and foreseen high energy physics experiments, and excellent reviews of these devices are available in [120, 121]. The most basic Silicon detector consists of a layer of Silicon sandwiched between two electrodes with an applied voltage as shown in Fig. 3.5. Ionizing radiation incident on the sensor excites electrons from the valence band to the conduction band, leaving 'holes' in their place. These electrons and holes drift

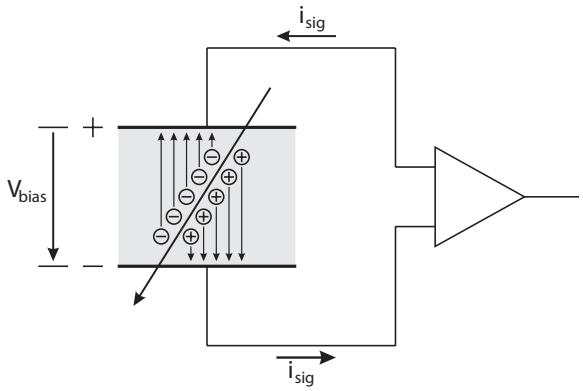

Figure 3.5: A simple Silicon sensor composed of a Silicon layer sandwiched between two electrodes with an applied voltage [120].

in opposite directions along the applied electric field lines and induce a current, which is amplified and read out.

Although this simple example demonstrates the basic principle of charge generation and collection in Silicon detectors, such a device is not of practical use. The reason is that in pure Silicon, there is a large density of free charge carriers, resulting from the promotion of electrons to the conduction band via thermal excitation. As a result, a large current flows through the Silicon as a result of the applied voltage, even in the absence of incident radiation. The charge generated by ionizing radiation, typically of order 10,000 electron-hole pairs per centimeter of Silicon traversed, would therefore be undetectable in the presence of this large current. Practical devices therefore require the use of impure Silicon, which is achieved using a process called doping.

Pure Silicon consists of a crystal lattice in which the atoms are interconnected via four covalent bonds. In p-doped Silicon, some of the Silicon atoms are replaced by atoms with one fewer valence electron. These atoms capture an electron from the valence band, thus contributing a hole in its place which acts as a positive free charge carrier. In n-doped Silicon the dopant has an additional

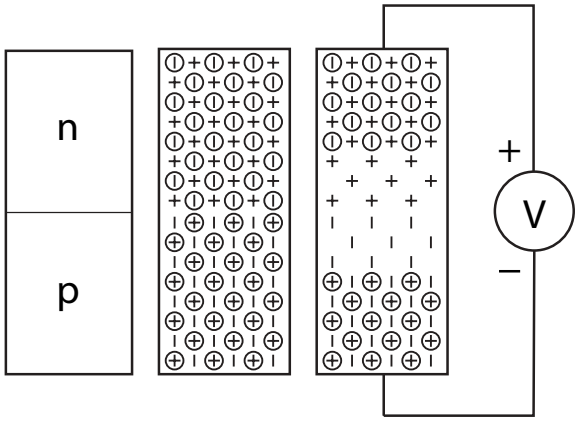

Figure 3.6: Schematic of a p-n junction [120]. P-type and n-type Silicon are placed in contact (left). The net charge of the mobile electrons and holes (circled) is balanced by the charges of the nuclei (middle). The p-n junction is reversely biased by applying the positive node to the n-side and negative node to the p-side (right).

valence electron and contributes an electron to the conduction band. In both cases the net charge of the doped Silicon is zero, since the additional mobile charges are balanced by the charges of the nuclei. Modern devices use both p-doped and n-doped Silicon, sandwiched together to form a p-n junction. An external potential is applied to the device with the positive node attached to the n-side and negative node to the p-side, as shown in Fig. 3.6. This configuration is called a reversely biased p-n junction, and forms the basis of modern Silicon detectors. The applied voltage draws the free charge away from the junction, resulting in a depletion region in which the net charge is non-zero and therefore an electric field is present. The width of the depletion region grows as the voltage is increased, and the entire device can be depleted by applying a sufficient voltage. In a fully-depleted device, the free charge carriers are removed but the electric field is still present. However, a small leakage current flows through the device even in the absence of incident radiation, due to a sparse population of electrons promoted to the conduction band via thermal excitation. Charge generated by ionizing radiation drifts along the electric field lines, and results in a detectable modulation of

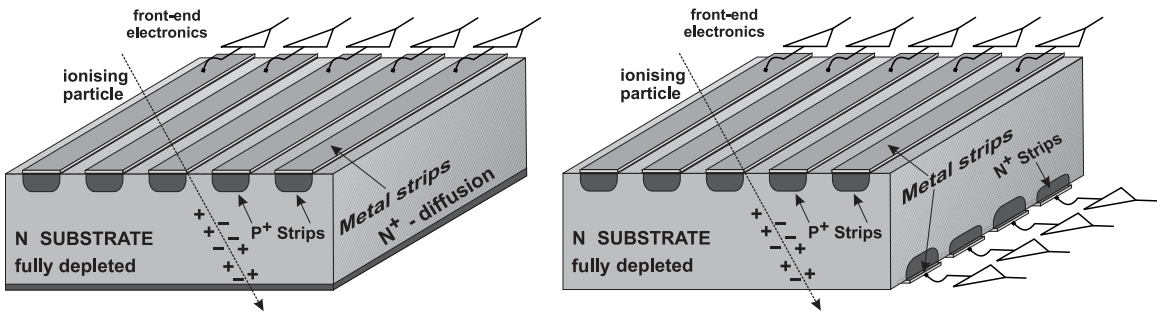

Figure 3.7: Layout of single-sided (left) and double-sided (right) Silicon microstrip detectors [122].

the current flowing through the circuit.

3.2.1 Silicon Microstrip and Hybrid Pixel Detectors

The oldest and simplest realization of Silicon tracking detectors are called microstrip detectors. These devices consist of a thin, highly-doped layer of p^+-type Silicon on a high resistivity (low doping concentration) n-type Silicon substrate[2], with a thin, highly doped n^+-type layer forming the backplane. Position information can be obtained by segmenting the p^+ Silicon and its corresponding electrode into strips. The signal on each strip can be read out from the side of the device, providing 1-dimensional position information as shown in Fig. 3.7 (left). Such devices are called single-sided microstrip detectors. To provide 2-dimensional information, the n^+-type Silicon and its corresponding electrode are also segmented into strips oriented at an angle with respect to the p^+ strips as shown in Fig. 3.7 (right), resulting in double-sided microstrip detectors. Silicon microstrip detectors have been implemented in numerous high energy physics experiments, including the LEP experiments as well as the two general purpose experiments at the LHC, ATLAS [116] and CMS [123]. However, microstrip detectors are not suitable for environments of extremely high hit

[2]Devices consisting of a thin layer of n^+ type Silicon on a p-type substrate are also used.

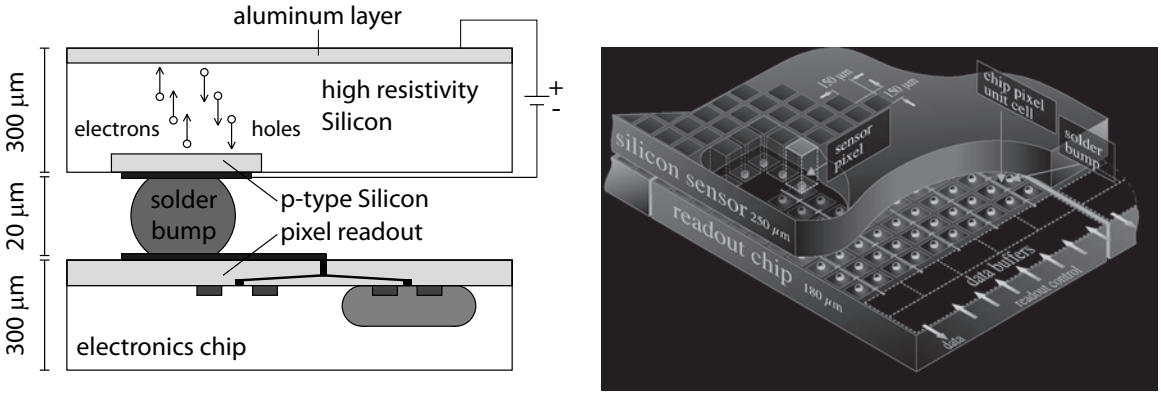

Figure 3.8: Schematic side-view of a hybrid pixel sensor (left) and diagram of the hybrid pixel sensors used at the CMS experiment (right) [124].

density, such as near the beam-pipe where the vertex tracking detectors are placed. This is because high particle fluxes result in ambiguities in the position of the particle hits, due to the projective strip geometry. To solve this problem, the sensor must be finely segmented in two-dimensions, resulting in an array of pixels. However, in such devices the signal on each pixel cannot be read out from the side of the sensor as in microstrip detectors. Therefore a separate electronics readout chip is used, which consists of an array of readout circuits corresponding to the sensor pixels. This chip is placed on top of the sensor, and the pixels and their corresponding readout circuits are electrically connected via small balls of solder called bump bonds. This device is called a hybrid pixel detector, depicted in Fig. 3.8. Hybrid pixel detectors were first used at the WA94 [125] and DELPHI experiments at CERN, and have been adopted by the ATLAS and CMS experiments, in the environments of high hit density near the beam-pipe. Although the technology has been very successful, hybrid pixel detectors are also not suitable for application in the vertex tracker at a TeV-scale lepton collider. The primary reason is that the readout chip introduces additional material budget which exceeds the requirements at a future lepton collider. In addition, the pixels cannot be made smaller

than the size of the bump bonds and readout circuits and the spatial resolution is therefore limited. It is therefore necessary to consider alternative Silicon detector technologies.

3.2.2 Alternative Silicon Detector Technologies

A variety of Silicon detector technologies have been proposed to overcome the obstacles discussed above. The oldest such technology is the charge-coupled device (CCD); the application of CCDs in vertex trackers is discussed in [126]. CCDs are pixel sensors realized on a high-resistivity, partially depleted substrate. To read out the signals, the charge on each pixel is shifted laterally across the detector by applying a sequence of bias voltages to an array of electrodes on top of the pixels. The charge is transferred to an output electrode connected to an amplifier, so that the readout electronics can be placed next to the sensor. CCDs have been used successfully in vertex tracking detectors for several experiments, including the VXD3 detector at SLD, which has achieved the best impact parameter resolution to date [117]. However, CCDs have several important drawbacks which limit their applicability for a future lepton collider. First, the devices typically cannot withstand large radiation doses. This is because radiation causes defects in the Silicon which trap charge as it moves across the detector, resulting in loss of signal. CCDs must also be cooled, which requires additional material which contributes to multiple scattering.

One promising technology for the vertex tracking detector at a future lepton collider is the DEPFET[3] [127] device. This technology offers a high-resistivity, fully depleted device with integrated in-pixel amplification. Furthermore, these devices may be thinned to achieve the material budget constraints at a future lepton collider. The DEPFET device consists of an array of transistors, with an n-doped implant buried beneath each transistor. Charge generated by ionizing particles

[3]DEpleted P-channel Field Effect Transistor

collects on the buried implant and modifies the gate voltage, modulating the current flowing through the transistor. A custom chip placed next to the sensor is used for the readout of the pixels. One drawback of this process is that it relies on a proprietary process currently available only at the Max Planck Institute in Munich, Germany, which originally proposed and developed the technology.

3.2.3 CMOS Monolithic Active Pixel Sensors

Another promising technology, which is used for the studies described in this thesis, is the CMOS[4] monolithic active pixel sensor (MAPS). CMOS pixel sensors were first developed in the 1990's as an alternative imaging device to CCDs [128]. This technology adapted the existing CMOS manufacturing process, originally developed in the 1960's. Since then the CMOS process has undergone decades of industry-driven R&D for use in various digital logic devices, including microprocessors, RAM and storage memory. CMOS sensors for tracking applications were first adapted in 2001 [65], and have undergone significant R&D efforts performed in large part at IPHC[5] in Strasbourg, France. These studies demonstrate that CMOS sensors are capable of achieving low noise, adequate readout speed, excellent spatial resolution and adequate tolerance to radiation [122, 129, 130]. These devices are currently undergoing R&D for application in the heavy flavor tracker upgrade of the STAR experiment [118] at the Relativistic Heavy Ion Collider, which will use thin CMOS sensors and a detector geometry similar to that envisioned for the ILC VTX.

The crucial advantage of CMOS MAPS is that the readout electronics and sensitive volume are integrated on a single substrate, resulting in monolithic devices. This allows amplification and signal processing electronics to be embedded in the individual pixels. A diagram of a CMOS

[4]Complementary Metal Oxide Semiconductor.
[5]Institut Pluridisciplinaire Hubert Curien

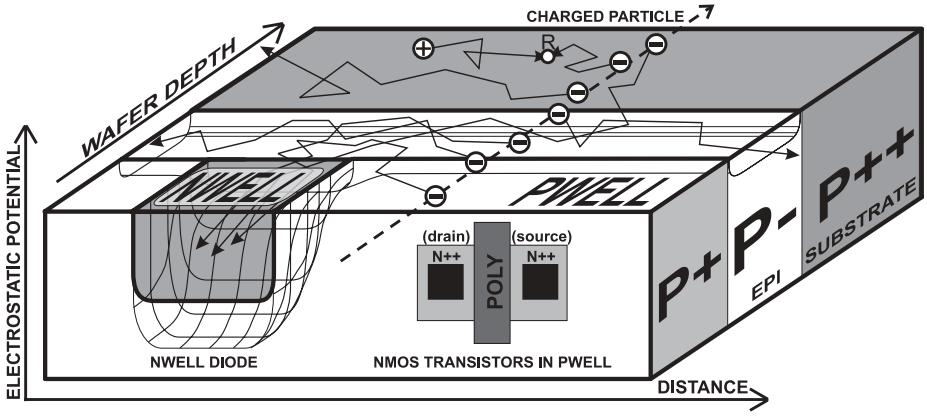

Figure 3.9: Layout of a CMOS monolithic active pixel sensor [122]. The readout electronics and the sensitive epitaxial layer (epi-layer) are integrated on the same Silicon substrate. The figure is not to scale.

MAPS is shown in Fig. 3.9. A 300-500 μm thick layer of low-resistivity bulk Silicon functions as the substrate and provides rigidity and mechanical support. A 10-20 μm thick layer of epitaxial p-type Silicon (epi-layer) with lower doping concentration is grown on top of the bulk Silicon. The full sensor and epi-layer thickness are determined by the CMOS manufacturing process. The epi-layer functions as the sensitive volume of the detector. It contains an array of n-doped implants which form potential wells for electrons and act as charge collection diodes, surrounded by p^+-doped implants which form potential barriers and are used to integrate the in-pixel electronics. Due to the manufacturing process, the maximum achievable depletion voltage is limited to a few volts. The detector is therefore mostly undepleted, with the exception of a shallow depletion zone of order $\sim$1 μm near the charge collection diode. Electrons generated by ionizing radiation diffuse thermally throughout the epi-layer, in contrast to drifting along electric field lines as in depleted detectors. Electrons which approach the boundaries with the p-doped Silicon are reflected by the potential barriers, and they are collected on the diodes if they reach the shallow depletion zone

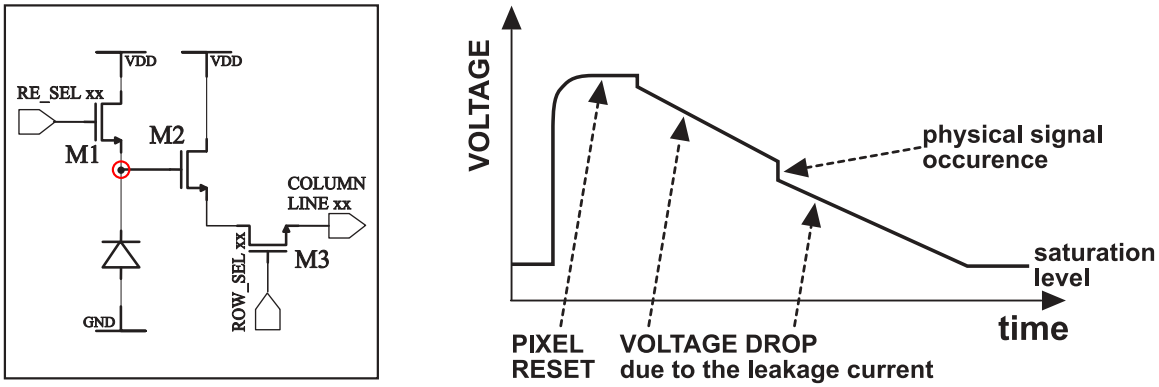

Figure 3.10: The 3-T circuit architecture (left) and the voltage at the charge collection node (red circle) as a function of time (right). The reset transistor (M1), source follower transistor (M2), and row select transistor (M3) are indicated. Images from G. Deptuch.

before recombining.

The baseline readout electronics for each pixel is formed by three NMOS transistors (3-T) embedded in the p^+-doped implants. The 3-T circuit architecture is depicted in Fig. 3.10 (left) and the voltage at the charge collection node as a function of time is shown in Fig. 3.10 (right). The readout cycle consists of the following sequence. First, the reset transistor is opened, which draws the voltage at the charge collection node to the bias voltage VDD. After the reset, leakage current flows through the diode, hence lowering the voltage at the charge collection node. Additional charge generated by ionizing radiation which reaches the depletion zone results in a sharp voltage drop. The source-follower transistor buffers the voltage signal to the pixel output. The signal is read out from the pixel by opening the row select transistor. Next the reset is issued again, and the cycle repeats. The full pixel array is read out serially by applying the proper voltage sequence to the row and column selection switches. A network of metal traces embedded in the passivation oxide on top of the sensor delivers the bias voltages and clock signals and reads out the signals from the pixels.

The drawbacks of the CMOS pixel technology stem from the limited depletion voltage

that can be applied to the sensitive volume. This results in longer charge collection times and a reduction of the total collected charge with respect to a depleted detector of the same thickness. In addition, CMOS sensors cannot withstand the extremely high annual radiation doses of order 10^{14} neutrons/cm^2 which are expected at the innermost layer of the LHC vertex tracker. Such doses result in defects in the Silicon which decrease the charge carrier lifetime and result in signal loss. However, these problems are not prohibitive for application in the vertex tracker at a future lepton collider. The achievable charge collection time is of order 100 ns. This is sufficient to provide the required time resolution, since the beam structure foreseen for the ILC will provide intervals of 185-1000 ns between bunch crossings [61]. Although the collected charge is reduced, CMOS sensors can achieve extremely low noise, and sensors with signal-to-noise (S/N) ratios in excess of 30 have been produced [130]. Although currently available CMOS sensors are not capable of withstanding the radiation dose in an environment such as the LHC, they are capable of withstanding the substantially smaller doses at a high energy lepton collider. This annual dose is expected to be of order 10^{10} neutrons/cm^2 at the innermost vertex tracker layer. The CMOS pixel technology also offers several advantages with respect to other detector technologies. Decades of industry-driven R&D have resulted in a production process capable of achieving low-noise devices with small feature size and low power dissipation, which are cheap and widely available via standardized commercial processes. CMOS pixel sensors also have the potential for sophisticated in-pixel functionality, and for on-chip data processing such as analog-to-digital conversion (ADC) by placing ADCs at the periphery of the chip. Most importantly, the monolithic structure removes the need for additional readout electronics chips. Furthermore, since the charge generation is confined primarily to a thin 10-20 μm epi-layer, the devices can be thinned to meet the material budget constraints. These

numerous advantages motivate the R&D effort to produce CMOS sensors capable of meeting the physics requirements at a future lepton collider.

3.3 Backthinning Studies

Because the sensitive layer of a CMOS MAPS device is 10-20 μm thick, it is in principle possible to produce thin sensors by removing most of the supporting bulk Silicon, a process known as backthinning, without affecting the sensor performance. Previous studies [131, 132] have yielded some successful results by thinning full Silicon wafers, but they have also reported problems in charge collection due to the thinning process. We carry out a research program in order to demonstrate the feasibility of producing thin CMOS sensors without degrading their performance by characterizing individual sensors before and after backthinning and comparing results [63]. The Mimosa-V chip produced at IPHC Strasbourg in the 0.6 μm AMS-OPTO process, described in detail in [133, 134], is chosen for this study. This chip is chosen because the large reticle size of 17 mm $\times$ 19 mm allows individual diced sensors to undergo the backthinning processes. The chip features four independent sectors, each consisting of an array of 510$\times$512 pixels. The epi-layer is 14 μm thick, the full wafer is 550 μm thick, and the center-to-center distance between adjacent pixels, known as the pixel pitch, is 17 μm. The experimental test setup is shown in Fig. 3.11. The chip is attached to a mezzanine card, which is mounted on a custom readout board. The readout board features four 14 bit ADCs which simultaneously digitize the signals from the four sectors, and a Field-Programmable Gate Array (FPGA) which generates the clock signals and collects the data from the ADCs. To study the effect of backthinning on the sensor performance, an individual chip is first attached to the mezzanine card using a removable glue. After the characterization procedure

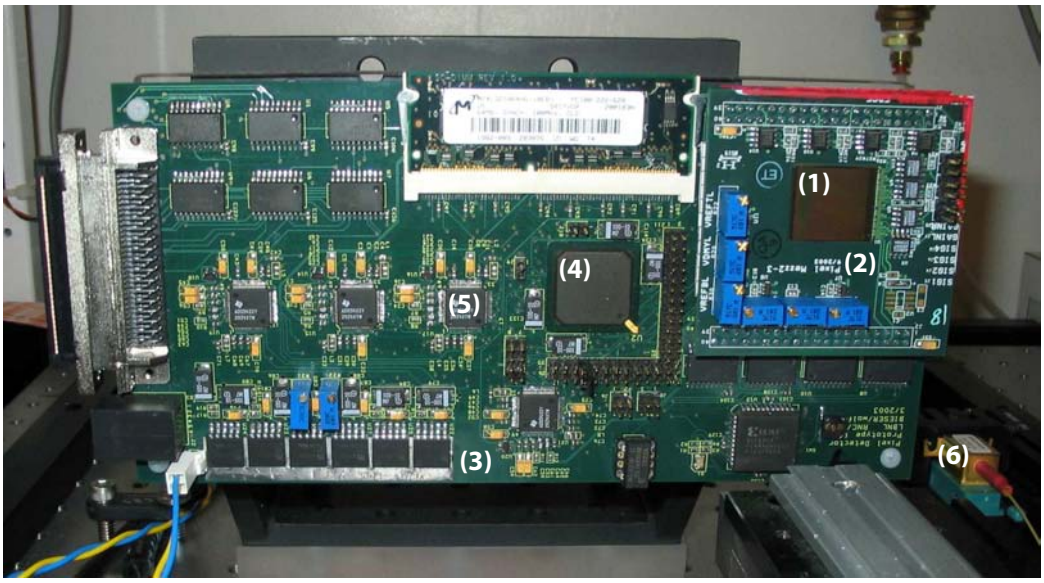

Figure 3.11: Experimental test setup for the CMOS pixel sensors. The sensor (1) is mounted to the mezzanine card (2) which is installed on the custom readout board (3). The readout card features a FPGA (4) and four ADCs (5). The laser diode (6) is also indicated.

described in Chap. 3.3.1 is performed, the chip is removed from the mezzanine card by removing the wire bonds and then placing it in a heated solvent bath which removes the glue. The chip is then sent to Aptek Industries [135], where it undergoes the backthinning process. The chip is mounted to stainless steel grinding plates using hot wax and backthinning is performed using a wet grind process, followed by a polishing procedure. As will be demonstrated below, this procedure can achieve sensor thicknesses of $\sim$40-50 μm without degrading the sensor performance. After backthinning, the chip is permanently mounted on the mezzanine card and the characterization procedure is repeated. Comparison of the results before and after backthinning allows us to determine the effect of backthinning on the sensor performance.

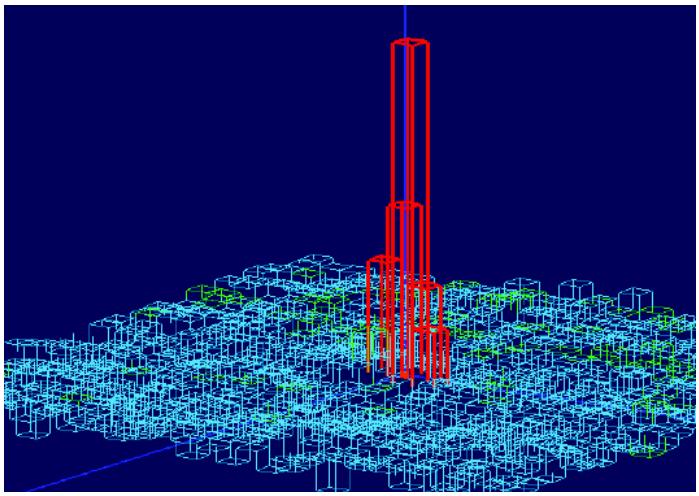

Figure 3.12: A cluster reconstructed with a CMOS pixel sensor. The signal value is represented as the height of the column corresponding to each pixel. The tall red columns are pixels associated to the cluster, the remaining pixels fluctuate due to the detector noise.

3.3.1 Sensor Characterization Procedure

The characterization procedure consists of testing with a radioactive source, lasers of various wavelength, and a 1.5 GeV e^- beam. The first step is the measurement of the detector gain using a radioactive source. In our setup, the voltages at the pixel outputs are amplified and digitized using ADCs, and the signal on each pixel is thus measured in units of ADC counts. In order to measure the charge collected on the pixels, the charge corresponding to an ADC count must therefore be measured. This is performed using a radioactive ^{55}Fe source which emits 5.9 keV X-rays. If the X-ray deposits its energy in the shallow depletion region near the charge collection diode, the full charge corresponding to 1640 electrons is collected by the readout diode. This value is calculated by dividing 5.9 keV by 3.6 eV, the average energy required to produce an electron-hole pair in Silicon. If the X-ray deposits its energy elsewhere, only a fraction of the total energy is collected and is spread among several neighboring pixels. This results in either a single pixel or a group of contiguous pixels with large signal values, known as a cluster and depicted in Fig. 3.12.

To measure the energy deposited by ionizing radiation, a cluster search is performed by scanning the detector for pixels with S/N values exceeding a given threshold. These pixels are designated as cluster 'seeds', and the neighboring pixels are tested for addition to the cluster by requiring that they exceed a second, lower S/N threshold. The sum of the signal values of the pixels associated to the cluster is known as the cluster pulse height, and measures the total collected charge generated by the ionizing radiation. The distribution of pulse heights resulting from reconstructing a large numbers of clusters induced by the radioactive source has a peak resulting from the X-rays whose energy is fully collected, as shown in Fig. 3.13 (top). A Gaussian is fitted to this peak, and the mean of the Gaussian gives the number of ADC counts corresponding to 5.9 keV. By dividing 1640 electrons by this value, the ADC count calibration is determined, yielding typical values of 6-8 electrons per ADC count.

The next step is the characterization of the sensors using lasers of various wavelength. Here we make use of the fact that the penetration depth for photons in Silicon is strongly dependent on wavelength. We use an 850 nm laser which has a penetration depth of about 20 μm and a 1060 nm laser which has a penetration depth of about 1 mm. By measuring the collected charge generated by these lasers, it is possible to probe charge generation confined primarily to the epi-layer using the 850 nm laser and charge generation throughout the full wafer thickness using the 1060 nm laser. The setup consists of a laser diode pig-tailed to a 6 μm optical fiber terminated on an aspheric lens doublet, providing a collimated beam with a nearly Gaussian profile which is incident on the sensor. The data is analyzed by selecting a fixed 25×25 pixel matrix centered on the beam maximum and determining the average pulse height over several hundred events. The resulting cluster pulse height distributions are shown in Fig. 3.13 (middle).

An important figure of merit for Silicon tracking detectors is the amount of charge generated by a charged particle traversing the sensor, since this is directly related to the track reconstruction efficiency of the full tracking detector. The Bethe-Block equation [24] determines the energy deposited per unit length by a charged particle in a material, known as specific ionization and denoted by dE/dx, as a function of the particle momentum p (see Fig. 2.9). The dE/dx vs. p curve has a minimum near 1 GeV/c which depends on the particle type. A particle with a momentum in the neighborhood of this minimum is known as a minimum ionizing particle (MIP). It is convenient to define the sensor figure of merit as the collected charge induced by a MIP, since this determines the minimum amount of charge that will be generated by a charged particle traversing the sensor. The collected charged induced by MIPs is studied at the Advanced Light Source (ALS) [136] facility at LBNL. A 1.5 GeV e^- beam is extracted from the booster ring and strikes the sensor under test. The readout cycle consists of a reset followed by a period of integration time, during which leakage current flows through the diode. The voltage signal on each pixel is sampled three times in intervals of 84 ms, called frames, after the reset. The readout sequence is synchronized with the 1 Hz booster extraction cycle and the beam strikes the sensor just before the second frame. The empty frames are used to measure the noise and the voltage drop on each pixel between frames induced by the leakage current, known as the pedestal values. For each pixel, the signal in the first frame is subtracted from the signal in the second frame to remove the signal base level. The pedestal values of each pixel are then subtracted to isolate the signal generated by the incident electrons. The distribution of cluster pulse height follows the Landau distribution, which describes the stochastic process of energy loss of a particle as it undergoes multiple interactions while traversing a layer of material. The resulting cluster S/N distributions are shown in Fig. 3.13 (bottom). The amount of charge corresponding to

Table 3.2: Summary of results of the backthinning of 2 CMOS sensors thinned to 50 μm and 39 μm [63]. Displayed are the relative changes after backthinning in the mean noise, mean of a Gaussian fitted to the 5.9 keV X-ray peak of a radioactive ^{55}Fe source, mean collected charge induced by the two lasers, and the most probable value of a Landau function fitted to the collected charge distribution from the 1.5 GeV e$^-$ ALS test beam. All figures are expressed in percent values and given in terms of mean$\pm$RMS for the four sectors of a single chip.

Thickness (μm)	**Noise**	**^{55}Fe**	**850 nm**	**1060 nm**	**1.5 GeV e^-**
50	+3$\pm$7	-7$\pm$8	-16$\pm$6	-16$\pm$10	-9$\pm$7
39	+8$\pm$13	+2$\pm$2	-10$\pm$6	+130$\pm$42	+2$\pm$4

the most probable value of a Landau function fitted to the data provides the desired figure of merit, the charge induced by a MIP.

3.3.2 Backthinning Results

The results of the comparison of sensor performance before and after backthinning for two chips, one thinned to 50 μm and one to 39 μm, are summarized in Table 3.2 and displayed in Fig. 3.13. Data from the radioactive ^{55}Fe source and 1.5 GeV e^- beam indicate that neither the ADC count calibration nor the response to minimum ionizing particles is significantly affected by the backthinning process. The detector noise also does not change significantly after backthinning. The laser output has been monitored using a Silicon photodiode and is found to be stable to about 10%. Results from the 850 nm laser therefore show that no significant change in the charge generation and collection in the epi-layer is caused by the backthinning process. However, a large increase in the collected charge induced by the 1060 nm laser is observed for the chip thinned to 39 μm. This may be due to changes in the optical properties of the back-plane due to backthinning, but this does not alter the sensor response to charged particles. We therefore conclude that no significant performance degradation is observed after backthinning CMOS pixel sensors to 50 μm and 39μm, which meets the ILC material budget requirements.

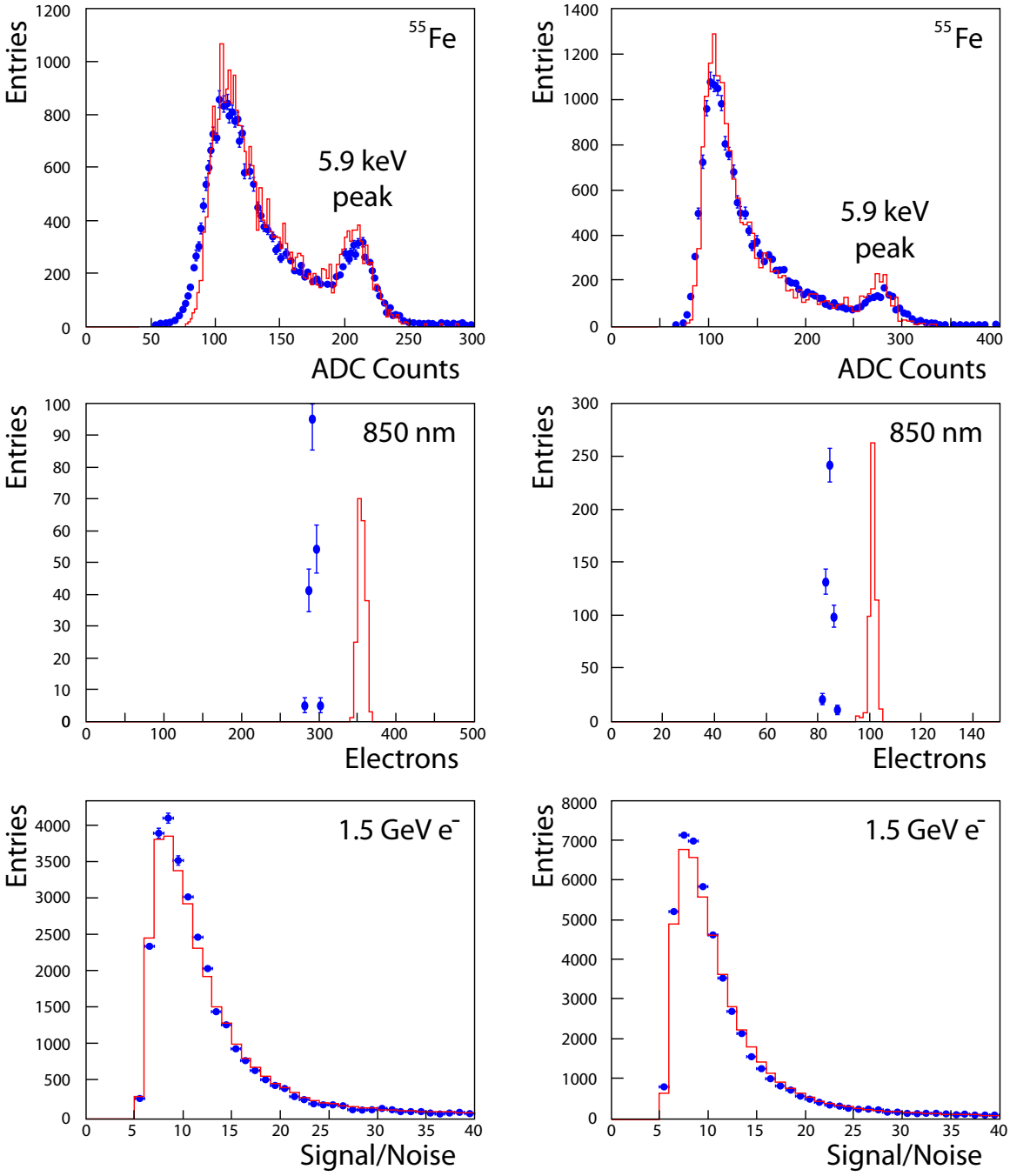

Figure 3.13: Comparison of the performance of CMOS pixel sensors thinned to 50 μm (left) and 39 μm (right) before and after backthinning [63]. The performance before thinning is indicated by the solid red histogram, the performance after thinning is indicated by blue points with error bars. Displayed are the cluster pulse height distributions from the radioactive ^{55}Fe source (top), from the 850 nm laser (middle), and the S/N distributions from the 1.5 GeV e$^-$ beam (bottom).

3.4 A Small-Scale Vertex Tracker Prototype

After demonstrating that the performance of CMOS pixel sensors is not affected by thinning them to meet the ILC material budget requirements, it must be demonstrated that these sensors are capable of providing the tracking and vertexing performance required by the ILC physics program. For this purpose we have constructed a small-scale vertex tracker prototype called the T966 pixel telescope, which consists of multiple planes of thinned CMOS sensors. The detailed setup and performance of this pixel telescope are documented in [64]. Although extensive studies have been carried out [62] in order to determine the required specifications for the tracking and vertexing performance of the ILC VTX, it is essential to validate these studies with real data collected in realistic operating conditions and hit occupancy levels. To accomplish this, the performance of the T966 pixel telescope is studied using a proton beam at the Fermilab Meson Test Beam Facility (MTBF) and an electron beam at the LBNL Advanced Light Source.

3.4.1 Setup and Readout

The T966 telescope was deployed at the MTBF in Summer 2007, which provides a 120 GeV proton beam extracted from the Main Injector of the TeVatron and attenuated through a pinhole collimator. The telescope consists of four planes of thinned CMOS sensors spaced 15 mm apart as shown in Fig. 3.14. This geometry is similar to that envisioned for the ILC VTX, which will consist of 5 or 6 layers spaced 11 mm apart located at radii from 15 to 60 mm. In addition to the four telescope layers, remotely-controlled mechanical stages allow an additional 'detector under test' (DUT) to be placed 20 mm downstream from the telescope, and a Copper target to be placed 30 mm upstream. This target is used for studying the vertexing performance by reconstructing ver-

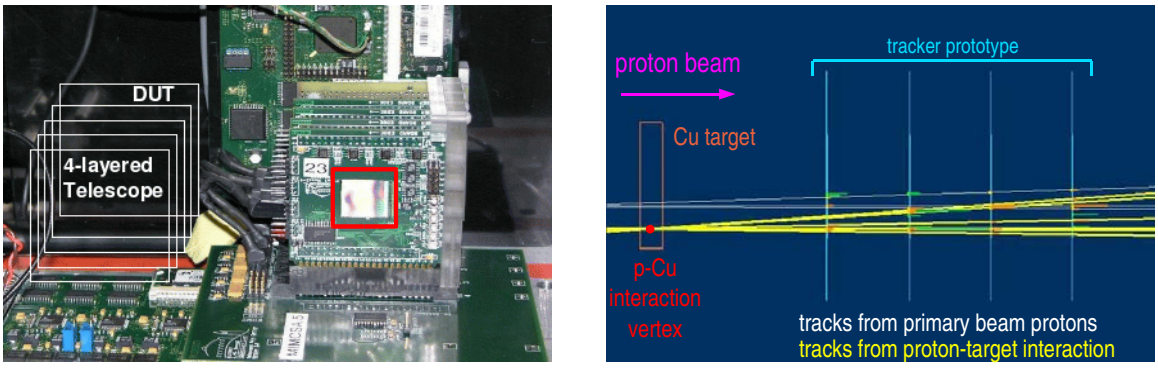

Figure 3.14: Left: photograph showing the layout of the small-scale vertex tracker prototype. Shown are the four layers of the tracker and the detector under test (DUT), mounted on the carrier board. A thinned CMOS sensor is indicated by the red square. Right: event display of the tracker prototype at the 120 GeV proton beam at the Fermilab MTBF. A six-track vertex resulting from a proton-Copper interaction is displayed [64].

tices formed by interactions between the incident protons and the target. The telescope is composed of Mimosa-V chips thinned to (50±7) μm by Aptek Industries. Each chip is glued to PC boards mounted to a carrier board and held fixed with precision mechanics. The carrier board is interfaced to the same custom readout board used for the backthinning studies discussed in Chap. 3.3. This assembly is mounted inside an optical enclosure, installed and aligned with the beam-line so that the protons traverse the four telescope planes at normal incidence. The system is cooled to approximately 20°C by flowing cold air through the enclosure. Finger scintillators mounted just in front of the enclosure provide the trigger and define a fiducial area of approximately 1 cm^2 corresponding to the detector surface. The readout cycle consists of a reset followed by two frames of one sector of each sensor. The data is processed online by a control PC using a dedicated LabView program which subtracts the pixel signals in the first frame from the second to remove the base levels, performs pedestal subtraction, noise computation and cluster identification and records the addresses and pulse heights of the identified clusters. The data is then converted into the Linear Collider

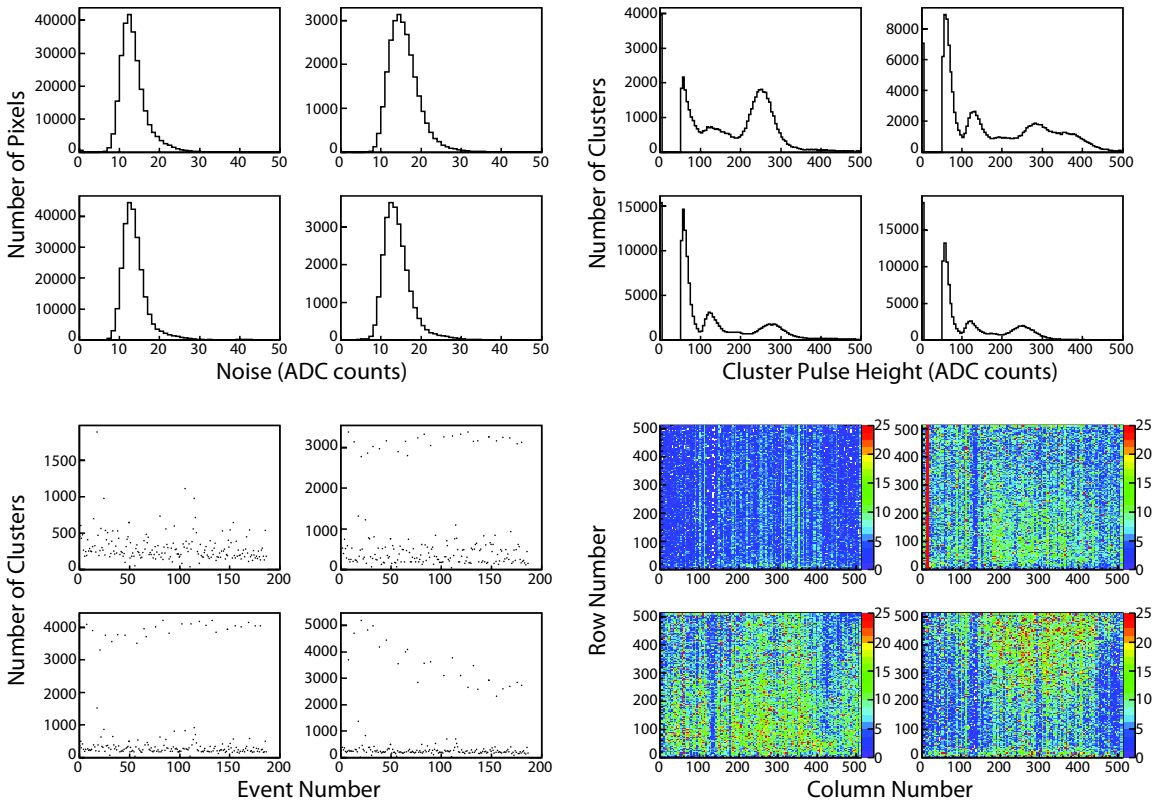

Figure 3.15: Screen display of the online-monitoring software for the tracker prototype. Displayed are the noise distributions, cluster pulse height distributions, number of clusters per event, and the coordinates of the clusters for the four detector planes of the tracker. The structures at large pulse height values are due to noisy pixels and lines which are removed in the offline analysis.

Input Output (LCIO) [137] format for offline analysis, which is performed using the LCIO-based C++ Marlin framework [138] discussed below. The proton beam intensity varied from an average hit density of 0.07 up to 0.7 hits/mm^2 with local densities up to 5 hits/mm^2. For comparison, the average hit density is expected to be in the range 0.2-1.0 hits/mm^2 for e^+e^- collisions at 500 GeV with local hit densities up to 5 hits/mm^2. In order to provide online monitoring of the tracking detectors, I contributed a custom C++ based program. A screen display of this software is shown in Fig. 3.15. The sparsified data consisting of the addresses and pulse heights of the clusters is written to ASCII files, and this data is copied event by event to a temporary buffer. The online monitoring

program reads this buffer and calculates the number of reconstructed clusters in each event, their pulse heights and 2-dimensional coordinates, and the noise values of the pixels in the detector, and displays this information in histograms. This information is useful in determining that the detectors are functioning as expected as well as ensuring that the proton beam is striking the detectors.

3.4.2 Simulation and Reconstruction

Simulation of the T966 telescope is performed with the GEANT-4 software [106], which generates particle impact points in the sensors and the resulting energy depositions in the sensitive volume, while accounting for surrounding material. This simulated data is stored in the LCIO format, the same format used to store data, and passed to a Marlin module which performs CMOS pixel simulation. The Marlin framework is used to analyze both the simulated events and data collected with the tracker, facilitating the comparison of data and simulation. Individual software modules perform the dedicated tasks of cluster searching, hit reconstruction, pattern recognition and track fitting, and vertexing.

Hits are reconstructed on each detector as clusters with pulse heights exceeding a threshold S/N ratio. The selected clusters have an average pixel multiplicity of 2.35 and S/N ratio of 10.3, in good agreement with simulation as shown in Fig. 3.16. The position of the particle hit is taken to be the center of gravity of the charge on the pixels associated to the cluster. Simulation predicts that the spatial resolution of a single detector, known as the single point resolution, is (1.7$\pm$0.02) μm for a cluster S/N value of 20, in excellent agreement with the measured value of 1.7 μm obtained while operating the detector cold as reported in [133]. This excellent spatial resolution is achieved by interpolating the charge collected on several pixels.

The hit positions are adjusted to a common reference system defined by the position and

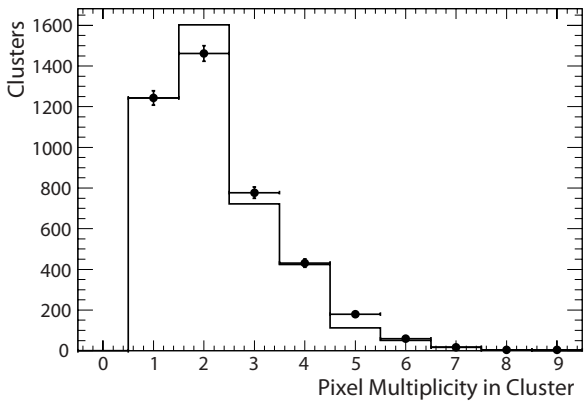

Figure 3.16: Comparison between tracker data (points with error bars) and simulation (histogram) of the pixel multiplicity in reconstructed clusters [64].

orientation of the layer 1 detector. The origin of the reference frame is the center of the layer 1 sensor, while the orientation is specified by three axes pointing along the vertical and horizontal directions of the sensor plane and one orthogonal to the plane. To adjust the hit positions on the other detectors, the relative translational offsets with respect to the origin (Δx, Δy, Δz) and rotational offsets with respect to the three axes defined by the layer 1 orientation ($\Delta\theta_x$, $\Delta\theta_y$, $\Delta\theta_z$) must be determined, giving 6 alignment parameters per detector plane. This is performed using a track-based alignment procedure performed using a large sample of well-isolated tracks. The alignment parameters of each detector plane are adjusted while minimizing the sum of the squared distances between each track hit and the track position extrapolated to the plane of the given hit for all tracks. I wrote software which stores and reads these alignment parameters from a database using the Linear Collider Conditions Database (LCCD) [139] toolkit, a LCIO-based C++ framework which offers full database functionality and straightforward implementation. These alignment parameters are stored in LCIO files and are read from the database at run-time. Due to mechanical fluctuations resulting from thermal variations from day to night, the alignment procedure is repeated for each

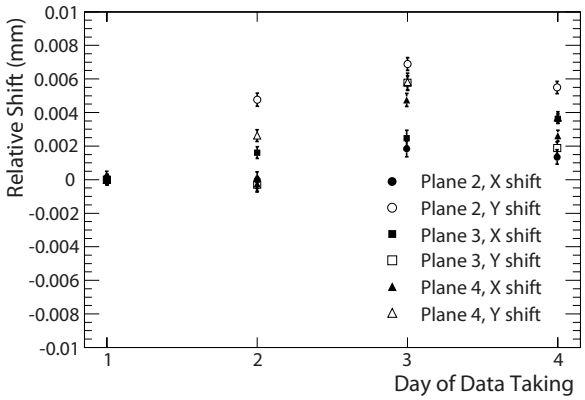

Figure 3.17: The tracker alignment parameters for four days of data collection [64].

day of data taking and variations of 6-7 μm are observed, as shown in Fig. 3.17. This variation is consistent with the measured stability of the mechanical mounting.

3.4.3 Tracking Procedure and Results

Particle tracks are reconstructed from the identified hits using a straight track model. Hit pairs on separate detector layers are used to form a track candidate provided that the extrapolated track slope does not exceed a threshold value, which eliminates lower momentum particles resulting from interactions upstream from the tracker and combinatoric backgrounds. Hits on the remaining planes are tested for compatibility with the extrapolated track, which is then refitted using all associated hits. Remaining hits which are not associated to a track are used for a second pass pattern recognition. This tracking procedure has been validated using simulated events, in which the track density is matched to that in data. This procedure predicts that the fraction of correctly assigned hits to tracks with at least three hits is 0.93 ± 0.01. The single point resolution is measured using tracks with four associated hits, by examining the distribution of the distances on each plane between the track-associated hit and the track extrapolation on that plane. This procedure yields single point

resolutions of (2.85±0.04) μm and (2.29±0.18) μm using tracks with average cluster S/N values of 10 and 15, respectively, in good agreement with the result from simulation of (2.90±0.02) μm and (2.08±0.02) μm.

The impact parameter resolution of the pixel telescope is studied using tracks with associated hits on layers 2, 3 and 4. The distance between the track extrapolated to layer 1 and the closest hit, called the residual, is measured for a large sample of tracks. Because the spacing between layers 1 and 2 is 15 mm, the same distance envisioned between the interaction point and the innermost layer of the ILC VTX, this procedure provides a realistic determination of the extrapolation resolution achievable at the ILC. The resulting residual distribution has a Gaussian width of (5.7±0.1) μm, while simulation predicts (5.6±0.1) μm, as shown in Fig. 3.18 (left). This width is the quadrature sum of the extrapolation resolution and the single point resolution of the layer 1 detector. To determine the extrapolation resolution the single point resolution is taken from simulation and subtracted in quadrature from the width of the residual distribution, yielding $\sigma_{extr} = (4.9 \pm 0.1)\ \mu m$ and $\sigma_{extr} = (4.2 \pm 0.3)\ \mu m$ for average cluster S/N values of 10 and 15, respectively. The T966 telescope was also tested with the 1.5 GeV e^- beam at the LBNL ALS, where an extrapolation resolution of $\sigma_{extr} = (8.5 \pm 0.4)\ \mu m$ was obtained [63]. These results are displayed in Fig. 3.18 (right) along with the targeted performance for the ILC VTX. This data demonstrate that the extrapolation resolution required by the ILC physics program has been achieved with a small-scale, standalone vertex tracker prototype composed of thin CMOS pixel sensors operated under realistic conditions with airflow cooling.

To study the dependence of the extrapolation resolution on the detector S/N, we vary the cluster pulse height S/N threshold, and plot the width of the residual distribution as a function of

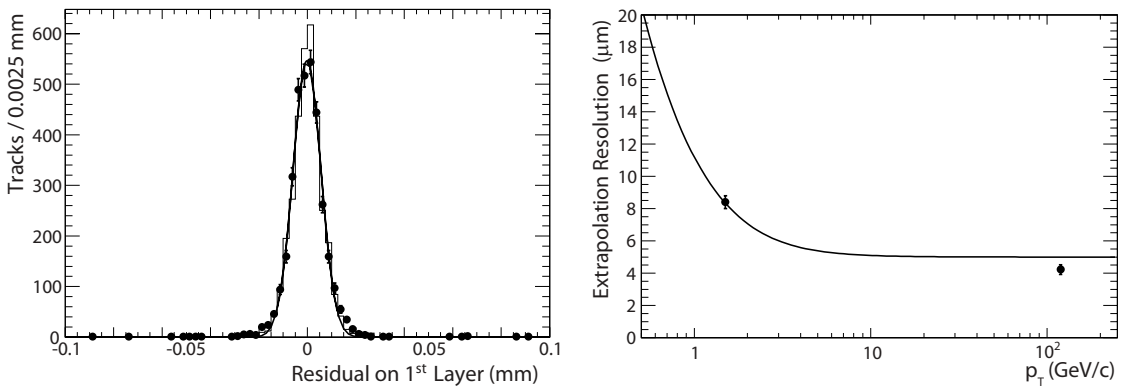

Figure 3.18: Left: The distribution of residuals on the layer 1 detector for data collected at the 120 GeV proton beam. Data is shown as points with error bars and simulation as the solid histogram. The extracted width of a Gaussian fitted to the data is (5.7±0.1) μm. Right: measurements of the impact parameter resolution at the 1.5 GeV electron beam and the 120 GeV proton beam (points with error bars) compared to the targeted ILC resolution of $\sigma_{IP} = (5 \oplus 10/p_T)\ \mu$m [64].

the average cluster pulse height S/N. As shown in Fig. 3.19 for data and simulation, the width of the residual distribution decreases from $(5.9 \pm 0.1)\ \mu$m to $(4.6 \pm 0.3)\ \mu$m as the average cluster pulse height S/N increases from 9.6 to 15.2. For comparison, the best S/N values achieved by CMOS pixel sensors to date exceeds 30 [130, 140].

Another experimental challenge for the ILC VTX is to perform tracking in an environment of high track- and hit-density. As mentioned above, one of the primary functions of the ILC VTX is to identify tracks resulting from the decay of a meson containing a b quark. These decays result in multiple charged tracks which are collimated, since the b quark is highly boosted due to the large CM collision energy. The result is a large track- and hit-density in the core of a hadronic b jet, and it is important to ensure that the tracking performance of the VTX does not degrade significantly in this environment. We study the dependence of the tracking performance on the hit density by measuring the fraction F of tracks with residuals greater than 2.5σ from zero as the hit density is varied. The hit density is quantified by the 'distance-of-closest hit' d_{ch}, which is defined for each track as the smallest distance between any hit not associated to the track on planes 2, 3, or 4 and the track

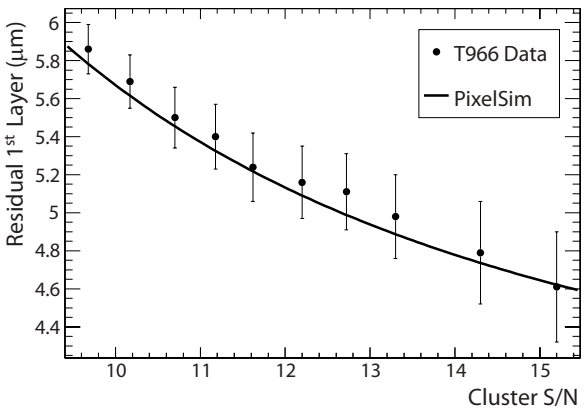

Figure 3.19: The width of the layer 1 residual distribution as a function of the average pulse height S/N of the clusters used to reconstruct the tracks. Data is shown as points with error bars and simulation as a solid line [64].

extrapolated to that plane. The most probable value of d_{ch} in the pixel telescope data is 0.19 mm, while in the core of a b jet in the $e^+e^- \rightarrow hZ^0, h \rightarrow b\bar{b}$ process at 500 GeV this value is estimated to be 0.4 mm. The fraction F is 0.04, 0.05 and 0.085 for d_{ch} >100 μm, 75 μm< d_{ch} <100 μm, and d_{ch} <75 μm, respectively, which is consistent with simulation and provides a measure of the rate of outliers in the pattern recognition for high hit occupancy environments. This demonstrates that the tracking performance does not degrade significantly in an environment of extremely high hit-density.

3.4.4 Vertexing Procedure and Results

Vertexing studies are performed by placing a 4 mm thick Copper target 30 mm upstream from the first layer of the pixel telescope. Protons that interact with the Copper target result in secondary particles, leading to multiple inclined tracks. These tracks are used both for alignment purposes and to study the vertexing capability of the telescope. For this study the cluster S/N threshold is reduced and the track slope requirement is relaxed in order to retain the inclined tracks. Vertices

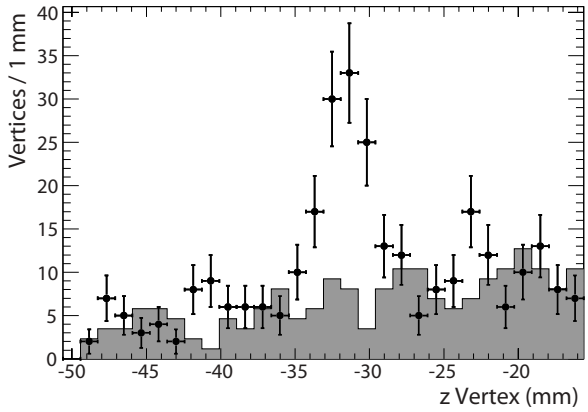

Figure 3.20: Distribution of the longitudinal coordinate of the reconstructed vertices in data with the target in place (black points with error bars) and in a data control sample in which the target has been removed (shaded histogram) [64].

are fitted using the VT [141] Kalman filter vertex fit algorithm developed for HERA-B [142] and LHCb [143], which has been ported into a dedicated Marlin module. First, the tracking procedure is performed and the resulting track collections are used to search for seed vertices. The requirements for a seed vertex are two tracks consistent with originating from the same interaction point, which must satisfy minimum hit multiplicity and minimum slope requirements to remove combinatoric backgrounds as well as tracks resulting from protons that did not interact with the target. The remaining tracks are then tested for compatibility with the seed vertex. My contribution to this part of the analysis was to extend the vertex search algorithm to include a second-pass pattern recognition.

The fitted vertex is considered as a track hit, and pairs of hits on the telescope planes that are not associated to a track are used to form additional track candidates. The vertex is then refitted using all associated tracks. The distribution of the coordinate of the reconstructed vertices along the beam-axis z shows a clear peak at the target location in addition to a flat distribution due to combinatoric backgrounds as shown in Fig. 3.20. This analysis is applied both to simulated events and to a data control sample in which the target has been removed, which is used to estimate the combinatoric backgrounds. The distribution of the vertex z coordinates is shown for data with and without the

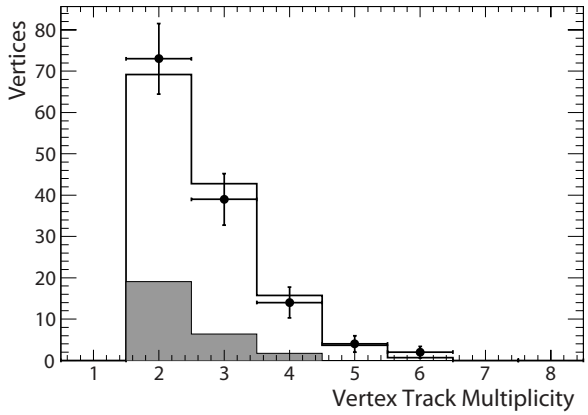

Figure 3.21: Vertex track multiplicity for simulation (unshaded histogram) and data (points with error bars). The shaded histogram shows the contribution from combinatorial backgrounds, determined by taking data without the target [64].

Copper target, which demonstrates that the data control sample is consistent with the sidebands of the data target sample. In Fig. 3.21 the vertex track multiplicity for data and the simulation is compared and excellent agreement is obtained. The average track multiplicity in the data is 2.74±0.09, after subtracting off the contribution from the combinatorial backgrounds as determined by taking data without the target. This value is in excellent agreement with the simulation, which predicts an average track multiplicity of 2.73±0.04.

The resolution of the vertex position along the particle line of flight z, known as the longitudinal vertex resolution, is determined from the VT algorithm to be (260±10) μm for vertices 32 mm from the closest telescope detector plane. This value is validated using simulated events in which a proton beam strikes the target, the resulting inclined tracks are reconstructed using the same algorithm as for the data, and the position of the secondary vertex is determined using the VT algorithm. The resulting pull distribution of the longitudinal vertex coordinate z (the difference between the reconstructed and simulated z coordinates of the simulated secondary vertices, normalized to the (260±10) μm measurement uncertainty determined from data), has a Gaussian width of 1.03±0.05, confirming the accuracy of the resolution determined from the data. This resolution is compared to

the expected longitudinal vertex resolution for the full ILC detector using GEANT-based simulation software discussed in detail in Chap. 4.2.2. I have simulated a sample of b jets in the energy range 100-150 GeV which are reconstructed using a model of the full ILC detector, in which the primary interaction point is 15 mm from the first sensitive layer. The LCFIVertex software package, discussed in Chap. 4.3.3, is used to reconstruct the secondary vertices in the b jet, and the longitudinal vertex resolution, reweighted by the vertex track multiplicity to match that of the pixel telescope, is determined to be (170$\pm$20) μm. This value is consistent with the resolution obtained from the tracker data, taking into account that the distance between the interaction point and the first sensitive layer, as well the inter-plane spacing and number of detector layers, are different from the ILC VTX.

3.5 Conclusions

The effort to design and construct a detector capable of meeting the strict performance requirements necessary to fully realize the physics potential of a TeV-scale lepton collider constitutes an extreme experimental challenge. We have demonstrated the feasibility of producing thin CMOS monolithic active pixel sensors which meet the ILC material budget constraints and used them to construct a small-scale vertex tracker prototype. Tracking studies performed with charged particle beams demonstrate that the impact parameter resolution required by the ILC physics program is achievable with a vertex tracker based on thinned CMOS MAPS. The tracker prototype is also used to reconstruct vertices from interactions of a proton beam on a Copper target, and a longitudinal vertex resolution consistent with that expected for the full ILC detector is obtained.

Chapter 4

Investigation of a Dark Matter-Motivated Supersymmetry Scenario at a Future Lepton Collider

4.1 Motivation

The primary strategy for searching for new physics is to directly produce new particles by building accelerators capable of achieving large collision energies. This approach is motivated by indications that Higgs production and BSM physics may be within reach of a lepton collider operating at $\sqrt{s} = 0.5 - 1$ TeV. Constraints on the Higgs mass have been derived from data collected at LEP operating at $\sqrt{s} = 130 - 209$ GeV (LEP2), and the lack of observation of the Higgs has been used to place the 95% confidence level lower limit $M_h > 114.4$ GeV/c^2 [144]. In addition, just as precise measurements of electroweak observables obtained at LEP operating at $\sqrt{s} = M_Z$

are indirectly sensitive to the top quark mass as discussed in Chap. 1.2, these measurements are also indirectly sensitive to the Higgs mass [145]. Electroweak data from the LEP2 experiments has been used to indirectly measure the Higgs mass as $M_h = 129^{+74}_{-49}$ GeV/c^2, giving the 95% confidence level upper limit $M_h < 285$ GeV/c^2 [13]. The proposed ILC would initially achieve a maximum collision energy of 500 GeV and would produce the Higgs directly via the Higgsstrahlung process provided that $M_h \lesssim 400$ GeV/c^2, above the indirect limit from LEP2. This fact provides one of the primary motivations for building a TeV-scale lepton collider.

In addition, a TeV-scale lepton collider may also produce new particles, and in particular SUSY particles. If SUSY is to solve the hierarchy and gauge coupling unification problems, the SUSY mass scale must satisfy $M_{SUSY} \lesssim 1$ TeV. As discussed below, the neutralino DM candidate particle is expected to have a mass of order 100 GeV/c^2. In addition, constraints on the mass of the lightest observable SUSY particle can be derived from the measurement of the anomalous magnetic moment of the muon, which is sensitive to corrections mediated by loop diagrams involving SUSY particles. If SUSY is to explain the observed 2.6σ deviation between the SM prediction and the measured value given by $\alpha_\mu^{exp} - \alpha_\mu^{SM} = (43 \pm 16) \times 10^{-10}$ [146], the lightest observable SUSY particle is required to have a mass in the range $m \lesssim$ 400-500 GeV/c^2 [51]. Although LHC data will be necessary to conclusively determine the SUSY mass scale, these considerations provide good reasons to be optimistic that SUSY might be within reach of a TeV-scale lepton collider.

In order to motivate and direct the detector R&D effort for a future lepton collider, it is necessary to perform detailed simulation studies of physics processes. This is necessary both to assess the performance and sensitivity of the detector and to optimize its design. Because it is not known which physics lies beyond the SM, it is necessary to choose multiple well-defined BSM

scenarios and points in the parameter space of these scenarios, known as benchmark points, for detailed study. These studies serve to ensure that the detector will be capable of making measurements with the required precision regardless of which benchmark point is realized in nature. In this analysis, which is documented in [68], a SUSY benchmark point is investigated which is motivated by cosmological observations of DM. A study of this scenario using a parametric detector simulation has been performed in [147], but in this study I use full simulation and reconstruction with a realistic, detailed detector model. At this benchmark point, the SUSY DM candidate is the lightest neutralino χ_1^0 and the neutralino relic density is determined by the rate of the annihilation process $\chi_1^0\chi_1^0 \rightarrow A^0 \rightarrow b\bar{b}/\tau^+\tau^-$. This rate depends on the properties of the A^0 CP-odd SUSY Higgs bosons, which are investigated by examining the $e^+e^- \rightarrow H^0A^0 \rightarrow b\bar{b}b\bar{b}$ and $e^+e^- \rightarrow H^0A^0 \rightarrow b\bar{b}\tau^+\tau^-$ processes. In order to identify these processes above large multijet backgrounds, a vertex tracker capable of realizing the b and τ tagging performance discussed in Chap. 3.1 is required. The goal of this analysis is to determine the achievable precision of measurements of the A^0 properties, which are used to constrain the neutralino DM candidate relic density. To do so I use a suite of software packages which generate physics events resulting from e^+e^- collisions inside the detector, simulate the detector response to the particles produced in the event, and reconstruct the resulting events using the simulated detector data.

4.1.1 Cosmological Evidence and Constraints on Dark Matter

During the 20^{th} century, compelling evidence of the existence of DM has been gathered [148]. The first evidence of DM came in the 1930's from Fritz Zwicky's observations of the Coma galaxy cluster [149]. By observing the motion of galaxies in the cluster and applying the virial theorem, Zwicky obtained an estimate of the total mass of the cluster. This estimate was larger by

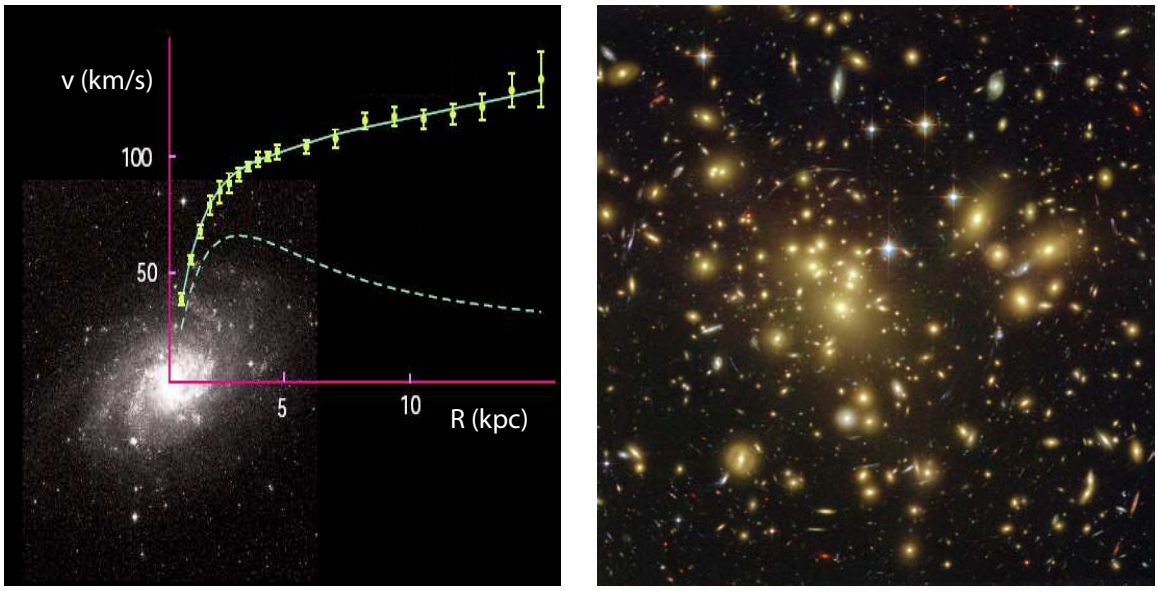

Figure 4.1: Left: velocity-of-rotation curve of the M33 galaxy [150]. The radial velocity is plotted as a function of the distance from the center of the galaxy, measured in kiloparsecs (1 kpc=3.26×10^3 light years). The data is represented as points with error bars and is fit with the solid line. The dotted line represents the expected velocity-of-rotation curve if only luminous mass were present in the galaxy. Right: Hubble image of the galaxy cluster Abell 1689 [151]. The cluster is composed of numerous galaxies, visible as yellow clumps. The red and blue circular arcs are distant galaxies whose light has been distorted by the massive cluster.

two orders of magnitude with respect to the expected mass based on the number of galaxies and the luminosity of the cluster. This provided evidence that most of the mass in the cluster was non-luminous, or dark. The most conclusive evidence for the existence of DM comes from observations of galactic velocity-of-rotation curves, such as that of the spiral galaxy M33 [150], shown in Fig. 4.1 (left). The dependence of the radial velocity of stars on their distance from the galactic center deviates significantly from that expected by the observed distribution of luminous matter, indicating the presence of a large amount of unseen mass. This result has been corroborated by multiple observations of galaxies whose velocity-of-rotation curves show the same discrepancy [152].

Further evidence for the existence of DM comes from observations of the phenomenon

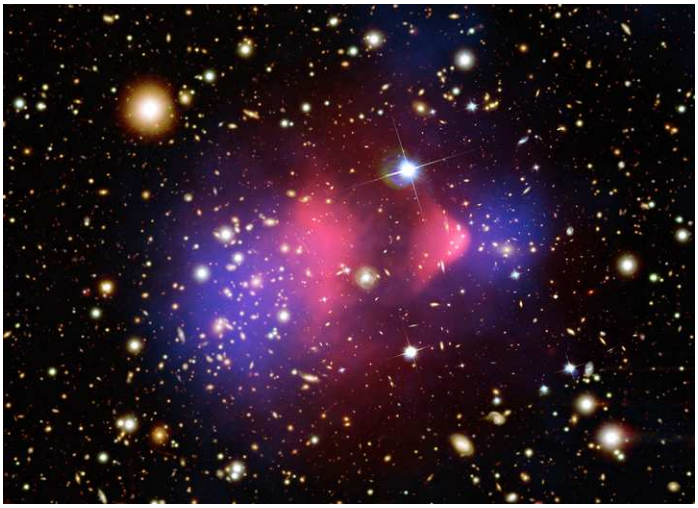

Figure 4.2: Composite image of the bullet cluster [153]. The two pink clumps near the center of the image indicate luminous matter primarily in the form of hot gas. The two blue clumps on either side indicate the mass distribution determined using weak gravitational lensing data.

of gravitational lensing [154], in which a massive celestial object acts as a lens by causing light to bend in the presence of its gravitational field. An example of this phenomenon is the observation of the galaxy cluster Abell 1689 [151], imaged by the Hubble Space Telescope and shown in Fig. 4.1 (right). The massive galaxy cluster in the foreground causes bending of the light emitted by galaxies in the background, which pass through the 'gravitational lens' en route to Earth. The amount of light bending can be used to estimate the amount of mass in the Abell 1689 cluster, which far exceeds the amount of luminous mass. This result has been corroborated with multiple observations of gravitational lensing effects which indicate the presence of large amounts of unseen mass.

In addition, a particularly striking piece of evidence comes from the observation of the bullet cluster [153] as shown in Fig. 4.2. This cluster was formed as two galaxy clusters collided and passed through one another. The luminous mass is composed primarily of hot gas that emits X-rays which are detected by the Chandra observatory [155]. Gravitational lensing data is used to determine the distribution of the total mass in the cluster, which is spatially separated from the

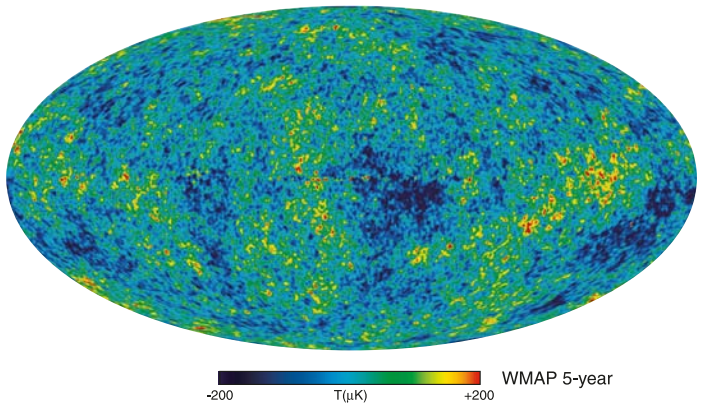

Figure 4.3: Full sky image of the CMB temperature map from the WMAP experiment [33].

luminous matter and indicates that most of the mass in the cluster is dark. These results have led to near-unanimous consensus in the scientific community of the existence of DM.

The most precise measurements of DM come from observations of the leftover radiation from the Big Bang, known as the cosmic microwave background (CMB). The Cosmic Background Explorer (COBE) experiment [156] was the first to measure the minute temperature fluctuations of the CMB. These measurements, in combination with those performed by several subsequent experiments including WMAP [33], have yielded extensive information related to cosmological parameters and in particular the DM relic density. The recently launched Planck satellite [157] will further refine these measurements. According to the Standard Model of cosmology, dark matter in the early universe provided gravitational 'seeds,' leading to clumping of luminous matter. The resulting matter distribution in the early universe is reflected in the pattern of temperature fluctuations of the CMB photons, due to redshifting in the presence of the gravitational fields generated by these clumps of matter. By accurately mapping out the spatial temperature distribution of the CMB as shown in Fig. 4.3, WMAP has provided an extremely precise measurement of the amount

of DM in the universe, quantified by the dark matter relic density $\Omega_{DM}h^2 = 0.110 \pm 0.006$ [33]. Here $\Omega_{DM} = \rho_{DM}/\rho_C$, where ρ_{DM} is the dark matter mass density and ρ_C is the critical closure density of the universe. If the total mass-energy density in the universe ρ_{tot} exceeds ρ_C then the universe will eventually stop expanding and begin to collapse, eventually resulting in a 'Big Crunch.' If $\rho_{tot} < \rho_C$, the universe will continue to expand forever. The dimensionless quantity h is defined by $H_0 = 100h$ (km/s)/Mpc and is equal to 0.72±0.03 [33], where H_0 is the Hubble constant. For comparison, the density of luminous baryonic matter is $\Omega_B h^2 = 0.023 \pm 0.0006$ [33], which demonstrates that DM constitutes ∼83% of the matter in the universe. Further constraints on DM can be derived by general considerations as discussed in Chap. 1.3. DM must be neutral, since otherwise it would have been observed via its electromagnetic interactions. It also must be stable on the timescale of the age of the universe, since otherwise it would have decayed by now.

Although there has been significant progress in the exploration of DM, there is still a great deal that is not understood about it. Most importantly, it is not known what DM is composed of. Several candidates have been proposed for the DM, which fall primarily into two categories: Massive Compact Halo Objects (MACHOs), dark celestial objects such as black holes, neutron stars, white or brown dwarf stars, and Weakly-Interacting Massive Particles (WIMPs), elementary particles which interact via the weak interaction. MACHO searches have been performed by monitoring the light from distant stars and searching for intervening objects which obscure the starlight. These searches show that MACHOs cannot compose more than a small fraction of the observed DM relic density [158]. Hot dark matter WIMPs, consisting of light particles such as neutrinos, are ruled out because they would travel with relativistic velocities beginning in the early universe. This would result in smearing of the distribution of luminous mass, in contradiction with observations of matter

clumping in the universe. Observations of the CMB by WMAP imply $\Omega_\nu h^2 < 0.014$ at 95% confidence level [33], and neutrinos therefore cannot constitute more than a small fraction of the DM. This leaves cold WIMPs as the experimentally preferred explanation of dark matter. Assuming that cold WIMPs were produced thermally in the early universe and are left over from near complete annihilation, the current WIMP density Ω_χ is given to within $\sim 10\%$ by [159]:

$$\Omega_\chi h^2 = \frac{s_0}{\rho_C/h^2}\sqrt{\frac{45}{\pi g_*}}\frac{x_f}{M_P}\frac{1}{\langle\sigma_{ann}v\rangle} \approx \frac{0.1 \text{ pb c}}{\langle\sigma_{ann}v\rangle}. \tag{4.1}$$

Here s_0 is the entropy density of the universe, g_* is the number of relativistic degrees of freedom when the WIMP is no longer in thermal equilibrium, and $x_f \approx 25$. The WIMP annihilation cross section is σ_{ann}, v is the relative velocity of the WIMPs in the CM system, and the brackets denote the thermal average of the product of these two quantities. If the WIMP density is equated with the measured DM density $\Omega_{DM} = 0.23$, the result $\langle\sigma_{ann}v\rangle \approx 0.9$ pb c is obtained. This translates to an estimate of the WIMP mass using the relation $\langle\sigma_{ann}v\rangle = \pi\alpha^2/8M_\chi^2$, which leads to $M_\chi = O(10^2)$ GeV/c^2 assuming a weak-scale coupling constant α [66]. Although this argument gives only an estimate of the WIMP mass, this estimate points to the same mass scale at which new physics related to electroweak symmetry breaking is expected to manifest. This provides suggestive evidence that new physics and DM are related.

4.1.2 New Physics and Dark Matter

There are many theories of the DM candidate, but none can be incorporated within the SM, providing convincing evidence of the existence of BSM physics. This is supported by the fact that there are several BSM scenarios, including SUSY and some theories with extra dimensions, which introduce a neutral, stable, weakly-interacting massive particle which would be a natural DM

candidate. If this scenario is correct, then WIMP DM is likely to be produced at the next generation of particle colliders operating at the TeV-scale. No single measurement can determine the identity of the DM; instead, it is only with the multiple measurements available at satellites, particle colliders, and direct DM searches, leading to an understanding of the BSM scenario which incorporates the DM candidate, that this question can be resolved [66]. This provides an integral role for colliders in the quest to understand DM.

As discussed in Chap. 1.3, SUSY solves many of the problems intrinsic to the SM. SUSY explains the origin of the sixteen order-of-magnitude discrepancy between the Higgs mass and the Planck mass, known as the hierarchy problem, by regulating the quadratic divergences in radiative corrections to the Higgs mass. SUSY also causes the three gauge coupling constants to unify at a mass scale near the Planck mass, which is necessary if these forces originate from a Grand Unified Theory (GUT). Most relevant to the discussion of DM however is the fact that R-parity conservation implies that the lightest Supersymmetric particle (LSP) is stable, providing a natural dark matter candidate particle. R-parity is defined by $R = (-1)^{3(B-L)+2s}$, where B is baryon number, L is lepton number and s is spin. All SM particles have $R = +1$, while SUSY particles have $R = -1$. R-parity conservation is imposed because without it, the proton would decay at a rapid rate, in contradiction with observation. As discussed in Chap. 1.3, the Minimal Supersymmetric Model (MSSM) describes the simplest way to extend the SM to include SUSY. In most regions of the MSSM parameter space, the LSP is the lightest neutralino χ_1^0 which is neutral, stable, and is predicted to have a mass of order 100 GeV/c^2. This particle therefore possesses all of the necessary characteristics of the dark matter candidate. If this scenario is correct, the χ_1^0 particle will be produced and studied at the next generation of TeV-scale colliders. Of particular interest is the fact that

this data can be used to predict the neutralino relic density $\Omega_\chi h^2$. Although the χ_1^0 cannot decay due to R-parity conservation, it can undergo annihilation with another SUSY particle. Assuming that neutralinos were produced thermally in the early universe and that their number density n_χ has decreased over time due to annihilation processes, n_χ as a function of time is given by [159]:

$$\frac{dn_\chi}{dt} = -3H_0 n_\chi - \langle \sigma_{ann} v \rangle (n_\chi^2 - n_{eq}^2), \tag{4.2}$$

where n_{eq} is the neutralino number density in thermal equilibrium. The first term on the right hand side of the equation is due to the dilution which results from the expansion of the universe, while the second term accounts for the change in number density due to annihilation processes. The Boltzmann equation allows n_{eq} to be determined, and the velocity distribution is determined by the Maxwell distribution. The only remaining unknown in Eq. 4.2 is the neutralino annihilation cross section σ_{ann}, which is determined by the mass and couplings of the χ_1^0 and of the particles which interact with it. By measuring these properties at TeV-scale colliders and determining σ_{ann}, it is possible to determine the present value of n_χ and hence determine $\Omega_\chi h^2$. Comparison between the neutralino relic density predicted from collider data and the measured dark matter relic density from CMB observations may allow us to determine is DM is composed of SUSY particles. Agreement between these two quantities would constitute a major achievement and breakthrough in our understanding of DM.

The physics processes which determine σ_{ann} and in turn $\Omega_\chi h^2$ depend on which point in the MSSM parameter space is realized in nature. Because the MSSM contains over 100 free parameters, it is convenient to work within the context of the specific model known as mSUGRA, which is defined by only 5 free parameters: m_0, $m_{1/2}$, A, $\tan\beta$, and sign(μ). It is assumed that all SUSY particle masses are determined by m_0 and $m_{1/2}$, the scalar and fermion mass parameters at

the GUT scale, which are evolved down to the TeV-scale via the renormalization group method to give the spectrum of physical masses. A is a trilinear coupling term, $\tan\beta$ is the ratio of the vacuum expectation values of the two Higgs doublets, and sign(μ) is the sign of the higgsino mass parameter. This reduced parameter space provides a convenient framework for defining benchmark points for detailed study. In Fig. 4.4 (left), the two-dimensional m_0 vs. $m_{1/2}$ slice of the mSUGRA parameter space is displayed. In the bulk region at low m_0 and $m_{1/2}$, the dominant physics mechanism contributing to $\Omega_\chi h^2$ is the annihilation process $\chi_1^0\chi_1^0 \rightarrow \ell\ell$, which proceeds through t-channel exchange of a slepton $\tilde{\ell}$ as shown in Fig. 4.5a. In this region the predicted value of $\Omega_\chi h^2$ agrees with the result from WMAP, but this region is disfavored because it tends to give a Higgs mass which is too light and part of the region is ruled out by measurements of the $b \rightarrow s\gamma$ process [57]. As m_0 and/or $m_{1/2}$ is increased the sparticle masses increase, and in particular the slepton mass increases and causes the rate of $\chi_1^0\chi_1^0 \rightarrow \ell\ell$ to decrease. This decrease in annihilation rate causes $\Omega_\chi h^2$ to exceed the observed relic density unless an additional mechanism contributes to the neutralino annihilation rate. In this analysis we consider the LCC-4 benchmark point defined in [66] in the rapid annihilation funnel region displayed in Fig. 4.4 (left). LCC-4 is defined by m_0=380 GeV, $m_{1/2}$=420 GeV, A=0, $\tan\beta$=53, sign(μ)=+1 and M_{top}=178 GeV, giving $M_{\chi_1^0}$=169.1 GeV and M_{A^0}=419.4 GeV. At this benchmark point $\Omega_\chi h^2$ is determined by the s-channel annihilation processes $\chi_1^0\chi_1^0 \rightarrow A^0 \rightarrow b\bar{b}/\tau^+\tau^-$ as shown in Fig. 4.5b, leading to $\Omega_\chi h^2$=0.108 computed using the microMEGAS 2.0 [160] software, in agreement with the relic density measurement from WMAP. This scenario will be first investigated at the LHC, but the achievable precision on $\Omega_\chi h^2$ is extremely limited, of order 400% [66]. An e^+e^- collider operating at $\sqrt{s}$ =1 TeV is necessary to achieve a measurement of $\Omega_\chi h^2$ with precision approaching that from the WMAP experiment. At LCC-4, $\Omega_\chi h^2$ depends strongly on the

A^0 mass as as shown in Fig. 4.4 (right). For $M_{A^0} = 2M_\chi$ the annihilation rate becomes maximal and $\Omega_\chi h^2 \to 0$, but agreement with the observed relic density can be obtained if M_{A^0} is close to but not equal to $2M_{\chi_1^0}$. Because the slope of $\Omega_\chi h^2$ vs. M_{A^0} is steep, a $\sim$10% measurement of $\Omega_\chi h^2$ requires a $\sim$0.5% measurement of M_{A^0}. Measurements of the A^0 width and decay branching ratios provide additional information relevant to the determination of $\Omega_\chi h^2$. In this analysis, I determine the achievable precision on the A^0 mass, width and decay branching fractions at a 1 TeV e^+e^- collider by studying the $e^+e^- \to H^0A^0 \to b\bar{b}b\bar{b}$ and $e^+e^- \to H^0A^0 \to b\bar{b}\tau^+\tau^-$ processes. The sensitivity of this analysis depends crucially on the ability to tag b and τ jets to isolate signal events from the large multi-quark jet backgrounds, and the jet-flavor tagging performance of the vertex tracker is therefore critical. I also determine the improvement in the achievable precision on $\Omega_\chi h^2$ provided by these measurements of the properties of the A^0.

The rest of this chapter is organized as follows. In Chap. 4.2, I review the simulation and reconstruction process used in the analysis. In Chap. 4.3, I review several software tools key to this analysis. The analysis of the $e^+e^- \to H^0A^0 \to b\bar{b}b\bar{b}$ process is presented in Chap. 4.4 and the analysis of the $e^+e^- \to H^0A^0 \to b\bar{b}\tau^+\tau^-$ process is presented in Chap. 4.5. Constraints on the neutralino relic density are presented in Chap. 4.6, and the conclusions of this work are presented in Chap. 4.7.

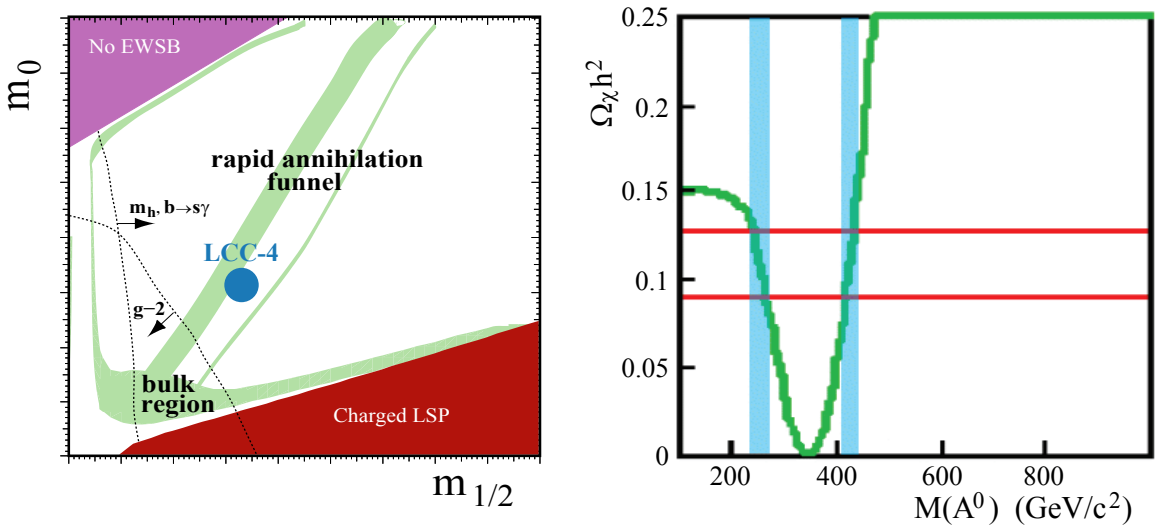

Figure 4.4: Left: two-dimensional m_0 vs. $m_{1/2}$ slice of the mSUGRA parameter space [67]. The pink shaded region at large m_0 is excluded because electroweak symmetry breaking does not occur in this region, while the brown shaded region at large $m_{1/2}$ is excluded because it leads to a charged LSP. The remaining light green shaded region is compatible with the DM relic density as measured by WMAP. The arrows and dotted lines indicate the regions preferred by the exclusion limit on the Higgs mass m_h, measurements of the $b \to s\gamma$ process, and the anomalous magnetic moment of the muon $g-2$. The LCC-4 benchmark point in the rapid annihilation funnel region, as well as the bulk region, are indicated. Right: dependence of $\Omega_\chi h^2$ on M_{A^0}. The horizontal red lines indicate the $\pm 1\sigma$ limit on $\Omega_\chi h^2$ as measured by WMAP and the vertical blue shaded regions indicate the regions of M_{A^0} compatible with the observed $\Omega_\chi h^2$.

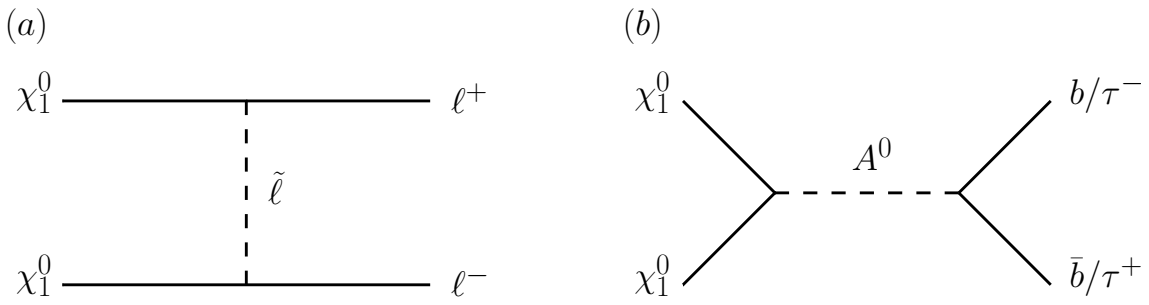

Figure 4.5: Neutralino annihilation processes which contribute to $\Omega_\chi h^2$. (a) Pair annihilation to a lepton pair via t-channel exchange of a slepton. This process dominates in the bulk region at low m_0 and $m_{1/2}$. (b) Pair annihilation to $b\bar{b}$ or $\tau^+\tau^-$ via s-channel exchange of the A^0 SUSY Higgs boson. This process dominates at LCC-4 in the rapid annihilation funnel region.

4.2 Analysis of Simulated Physics Events

Analysis of simulated physics events proceeds according to the following procedure:

- **Generation** of e^+e^- collisions occurring inside the detector and of the decay products resulting from the collision,
- **Simulation** of the interactions between the final-state particles and the detector, and determination of the detector response,
- **Reconstruction** of physics objects such as tracks and clusters using the simulated detector data, as well as higher-order reconstruction including particle reconstruction, jet clustering, and jet-flavor tagging,
- **Analysis** of the reconstructed physics objects to extract the desired observables.

4.2.1 Generation

The first step of the process is to generate physics events resulting from an e^+e^- collision, which is performed using the Pythia 6.205 [161] software, taking into account beamstrahlung effects [162]. The input required by Pythia includes the physics processes to be examined and the values of the mSUGRA parameters, which are used by the Isasugra 7.69 [163] software to determine the physical mass spectrum. Also required are the beam properties, including the 1 TeV CM energy. The physics processes of interest include the signal process $e^+e^- \to H^0A^0$, which has a production cross section $\sigma = 1.4$ fb and relevant branching fractions $BF(H^0 \to b\bar{b}) = BF(A^0 \to b\bar{b}) = 0.87$ and $BF(H^0 \to \tau^+\tau^-) = BF(A^0 \to \tau^+\tau^-) = 0.13$. Also included are the SM background processes, $e^+e^- \to W^+W^-, Z^0Z^0, t\bar{t}$, and inclusive $b\bar{b}b\bar{b}$ production. These have production cross sections computed using CompHep 4.4.0 [164] of 0.17 pb, 3.0 pb, 0.19 pb, 0.63 fb, respectively, where the contribution to inclusive $b\bar{b}b\bar{b}$ production from the Z^0Z^0 channel has been subtracted off. I choose the mSUGRA parameters corresponding to the LCC-4 benchmark point and assume that the collider is operated for 5 years at a luminosity of $4 \times 10^{34}\text{cm}^{-2}\text{s}^{-1}$, yielding 2 ab^{-1} of

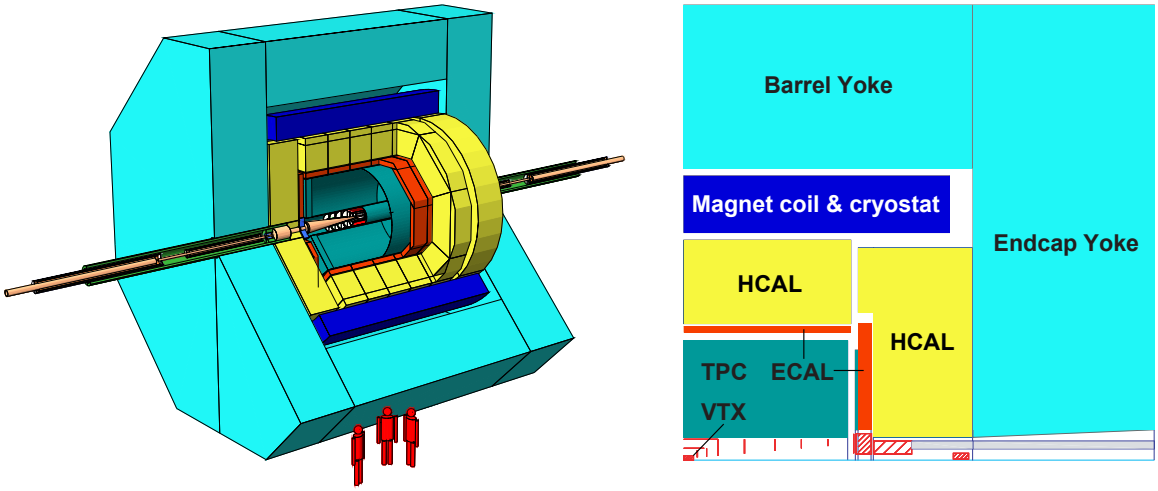

Figure 4.6: Simulated full view (left) and 1/4 view (right) of the Large Detector Concept, one of the four proposed detectors for the ILC [62]. The detector components are discussed in Chap. 4.2.2.

data (taking 1 yr=10^7sec). The output of Pythia is a list of events, with each event consisting of a list of particle types and their 4-vectors corresponding to each particle produced in the collision, as well as information which specifies the decay chain. These events are stored in the standardized stdhep [165] file format and passed as input to the simulation software discussed below.

4.2.2 Simulation

Next, the interactions between the final-state particles generated by Pythia and the detector are simulated using Mokka 06-03 [166], an ILC-specific implementation of GEANT-4, the same simulation software used to simulate events for single sensors and the vertex tracker prototype discussed in Chap. 3.4. The input required by Mokka includes the stdhep file produced by Pythia, as well as a realistic, detailed model of the full detector. In this study we adopt the proposed Large Detector Concept (LDC) described in detail in [167] and depicted in Fig. 4.6. The LDC is based on a large volume Time Projection Chamber (TPC) which provides continuous charged

particle tracking, surrounded by a Silicon-Tungsten electromagnetic calorimeter (ECAL) which is finely segmented both transversely and longitudinally to allow 3-D shower reconstruction. A five-layer Silicon pixel vertex detector (VTX) provides precise extrapolation of charged particle tracks to their production points and is surrounded by two layers of Silicon strip detectors (SIT) to facilitate track matching between the VTX and TPC. The ECAL is surrounded by a highly granular iron-scintillator hadronic calorimeter (HCAL) which measures the energy of neutral hadrons. The HCAL is in turn surrounded by a Superconducting coil providing a 4 T magnetic field. The flux of the Superconducting coil is returned by a large iron return yoke located outside of the coil, which is instrumented with multiple layers of resistive plate chambers for the identification of muons. This detector design is optimized for excellent jet energy resolution using the particle flow algorithm (PFA), discussed in Chap. 4.3.1, and also provides excellent angular resolution, necessary for the accurate measurement of dijet invariant masses as required in this analysis. The VTX is optimized for excellent impact parameter resolution, necessary for the high performance b and τ tagging which is used to isolate signal events from the large multi-quark jet backgrounds. The GEANT-4 softwares determines the energy deposited by the final state particles in the detector and simulates the detector response to these energy depositions. Effects such as ionization processes, multiple scattering, bremsstrahlung, Compton scattering and the photoelectric effect are included in this simulation. The resulting simulated detector data is stored in the LCIO persistency framework and passed as input to the reconstruction software discussed below.

4.2.3 Reconstruction

Reconstruction of physics objects is performed using the LCIO-based C++ Marlin framework. This is the same framework used to analyze both simulated and real data from single sensors

and the pixel telescope. The excellent agreement obtained between simulation and data from single sensors and the pixel telescope using GEANT-4 simulation and Marlin reconstruction validates the software framework and allows us to extend it to study the full LDC detector. Using as input the LCIO file provided by Mokka, physics objects are reconstructed in a modular framework which proceeds from low-level to high-level physics objects. Pattern recognition and track fitting are performed using two methods, using MC truth information ('truth patrec') and using full pattern recognition and tracking ('full patrec') with the FullLDCTracking [168] package, and the performances of these two approaches are compared. Reconstruction of clusters resulting from energy depositions in the calorimeter and matching of these clusters to tracks is performed by the Pandora v02-00 software [169], which implements the PFA discussed in Chap. 4.3.1 and reconstructs the final-state particles. Clustering of these reconstructed particles into jets is performed using the Durham algorithm [170] and the jet energy resolution is improved using a constrained kinematic fit algorithm discussed in Chap. 4.3.2. Jet-flavor tagging is performed using the LCFIVertex package [171] discussed in Chap. 4.3.3, and a custom τ identification algorithm discussed in Chap. 4.3.4 is used to analyze the $e^+e^- \rightarrow H^0A^0 \rightarrow b\bar{b}\tau^+\tau^-$ process. The quantitative properties of the reconstructed particles and jets are stored in the ntuple data structure and analyzed using ROOT.

4.2.4 Analysis

ROOT is used to analyze the ntuples produced by Marlin. This analysis includes the selection criteria, fit procedure, and extraction of the desired physics observables: the mass, width and decay branching fractions of the A^0, as well the achievable uncertainties in these quantities.

4.3 Software Tools

4.3.1 Particle Flow Algorithm and Jet Energy Resolution

Precise measurement of the A^0 mass requires excellent jet energy resolution exceeding that of any existing detector, which may be achieved at a future lepton collider using a PFA [172]. The PFA improves the jet energy resolution by using the optimal detector subsystems to separately measure the components of a hadronic jet. The momenta of charged particles, which carry the largest fraction of the jet energy, are measured using the TPC, whose resolution exceeds that of either calorimeter by 1-2 orders of magnitude. Photon energies are measured using the ECAL, while neutral hadrons are measured using the HCAL, the detector subsystem with the poorest energy resolution. In order to perform this algorithm the calorimeters must be capable of 3-D shower reconstruction and must therefore have fine longitudinal and transverse segmentation, which is necessary in order to separate charged and neutral clusters and to match charged clusters to their corresponding tracks. This feature is implemented in the LDC calorimetry, and I have studied the achievable jet energy resolution using the PFA provided by Pandora v02-00 [169]. I have simulated a sample of single b jets with energies ranging from 10 to 210 GeV, over the polar angle range $0.4 < \theta < \pi/2$ and find $\sigma(E_j)/E_j = (0.34 \pm 0.02)/\sqrt{E} \oplus (0.015 \pm 0.005)$, which is consistent with the required jet energy resolution.

4.3.2 The Constrained Kinematic Fit Algorithm

The required precision on the A^0 mass constitutes an experimental challenge because the jet energy resolution for signal events is of order 3-5%, b-jets contain numerous particles which may be lost or assigned to the wrong jet, and energy may be lost due to neutrino production in

semileptonic B decays. To improve the dijet mass resolution, a constrained kinematic fit algorithm is applied. I have implemented the PUFITC [173] algorithm developed for the DELPHI experiment in a dedicated Marlin module. The algorithm adjusts the measured jet momenta according to:

$$\vec{p_F} = e^a \vec{p_M} + b\vec{p_b} + c\vec{p_c}, \tag{4.3}$$

where $\vec{p_F}$ is the fitted momentum, $\vec{p_M}$ is the measured momentum, $\vec{p_b}$ and $\vec{p_c}$ are two unit vectors transverse to each other and to $\vec{p_M}$ and a, b, and c are free parameters in the fit. The fitted momenta must satisfy a set of constraints while minimizing the fit χ^2 given by:

$$\chi^2 = \sum_i (a_i - a_0)^2/\sigma_a^2 + b_i^2/\sigma_b^2 + c_i/\sigma_c^2, \tag{4.4}$$

where the index i runs over the number of jets in the event, a_0 is the expected energy loss parameter, σ_a is the energy spread parameter and σ_b and σ_c are the transverse momentum spread parameters. I impose the following constraints: $p_x = p_y = 0$, and $E \pm p_z = \sqrt{s}$, where the last condition accounts for initial state radiation directed along the beam axis z. The dijet masses for selected signal H^0A^0 events have a Gaussian resolution of 23 GeV/c^2 using 'truth patrec' and 27 GeV/c^2 using 'full patrec' before the constrained kinematic fit applied. These resolutions improve to 13.7 GeV/c^2 and 13.8 GeV/c^2 after applying the kinematic fit algorithm.

4.3.3 b-tagging with the LCFIVertex Package

The total background production cross section is larger than that of the signal by a factor of order 10^4, but the background rejection factors achieved using kinematic selection alone (discussed in Chap. 4.4 and Chap. 4.5) are of order 10-100. This implies that the identification of jets containing b quarks, known as b-tagging, is crucial in order to achieve the required signal-to-background ratio.

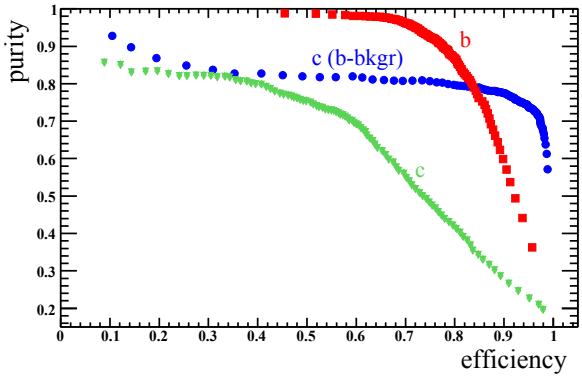

Figure 4.7: Performance plot of flavor tagging of jets from Z^0 decays with the LCFIVertex Package [62]. The purity vs. efficiency curves are plotted for b quarks (red squares), c quarks (green triangles), and c quarks with b quark background only (blue circles). The latter is relevant for the measurement of Higgs branching fractions.

In this analysis b-tagging is performed using the LCFIVertex package [171], which uses track and vertex information fed into a neural network to distinguish between b, c, and light quark ($q = u, d, s$) jets. The b tagging procedure has been discussed in Chap. 3.1, which describes how the VTX identifies tracks with large impact parameters and associates these tracks to a secondary vertex. This approach alone is not sufficient to distinguish between b and c jets, which both contain secondary vertices, so a more sophisticated algorithm is required. Jets from b decays differ from jets from c decays in several ways, including: the secondary vertex mass tends to be larger because $m_b > m_c$, the fraction of the jet energy associated to the secondary vertex tends to be larger, and the number of tracks associated to the secondary vertex tends to be larger. These variables, along with several additional discriminant variables, are fed into a neural network which outputs a discriminant variable P_b which is peaked at 1 for b jets and 0 for jets of other flavor. By requiring $P_b > P_b^{cut}$ a sample of b jets is selected from a sample of hadronic jets. As the value of P_b^{cut} is increased, the purity of the b jet sample increases but the selection efficiency decreases. The achievable purity and efficiency for a sample of b jets, c jets, and c jets in the presence of only b jet backgrounds selected

by the LCFIVertex software is shown in Fig. 4.7. The b tagging performance of the LCFIVertex software is comparable to the targeted performance depicted in Fig. 3.4.

4.3.4 The τ-Identification Algorithm

In order to measure the branching fraction $BF(A^0 \rightarrow \tau^+\tau^-)$, it is necessary to identify τ leptons, which are difficult to distinguish from light quark jets. The signature of a τ lepton is 1 or 3 charged particles plus possible additional neutral particles, which is similar to the signature of a light quark jet. In order to distinguish τ jets from q jets I have implemented a simplified version of the τ identification algorithm developed for CMS [174]. Jets from τ decays differ from jets from q decays in several ways, including: the invariant mass of the tracks associated to the secondary vertex in a τ jet tends to be larger because $m_\tau > m_q$, a τ jet tends to contain a charged particle with a large impact parameter due to the long lifetime of the τ, and τ jets tend to be more collimated. The first two of these properties are quantified by taking the invariant mass of tracks associated to the secondary vertex and the impact parameter of the track with the greatest transverse momentum, while the third is quantified by the variable $P_{ISOL} = \sum_{\Delta R<0.40} E_T - \sum_{\Delta R<0.13} E_T$. Here, $\Delta R = \sqrt{(\Delta\eta)^2 + (\Delta\phi)^2}$ denotes the angular deviation from the jet axis, defined by summing the momentum vectors of all the particles in the jet, and E_T is the transverse energy deposited in the region defined by the summation range. The variable P_{ISOL} therefore measures the transverse energy deposited in an annulus centered around the jet axis, which tends to be smaller for τ jets than for q jets because they are more collimated. Using these three variables, a discriminant variable P_τ is calculated, which peaks at 1 for τ jets and 0 for q jets, as shown in Fig. 4.8 (left). By requiring $P_\tau > P_\tau^{cut}$ and varying the value of P_τ^{cut} the efficiency for τ and q jets is displayed in Fig. 4.8 (right).

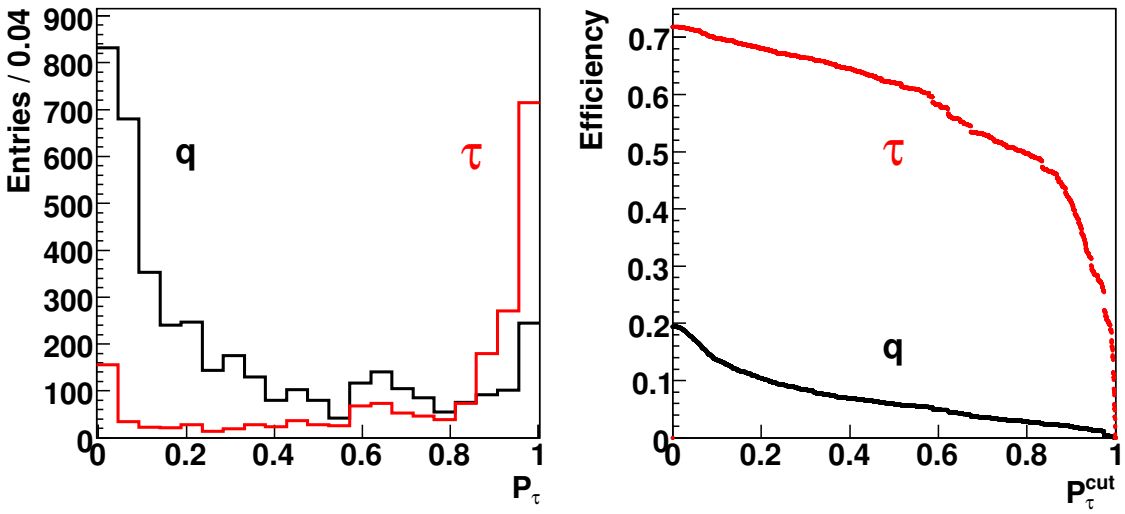

Figure 4.8: For both diagrams, red is τ jets and black is $q = u, d, s$ jets. Left: distributions of the tau probability variable P_τ for τ jets and q jets satisfying number of charged particles N_{CHA} <4. Right: efficiency for τ and q jets to satisfy N_{CHA} <4 and $P_\tau > P_\tau^{cut}$.

4.4 The $e^+e^- \to H^0A^0 \to b\bar{b}b\bar{b}$ Channel

The $e^+e^- \to H^0A^0 \to b\bar{b}b\bar{b}$ process is analyzed to measure the mass M_{A^0} and width Γ_{A^0} of the A^0 boson. These quantities are determined by measuring the invariant mass of the $b\bar{b}$ dijets from the H^0 and A^0 decays. The signature of the signal events is a final state consisting of 4 b-jets, which tend to be distributed nearly isotropically since the H^0 and A^0 are (pseudo-)scalars produced nearly at rest. The main sources of background are $e^+e^- \to Z^0Z^0$, W^+W^-, $t\bar{t}$, and inclusive $b\bar{b}b\bar{b}$ production. The Z^0Z^0 and W^+W^- production processes can result in 4-jet final states in which some of the light quark or c jets are misidentified as b jets. The $t\bar{t}$ production process can result in 4 jet final states plus a lepton, which can either be lost or accidentally assigned to one of the jets. Inclusive $b\bar{b}b\bar{b}$ production results in a 4 b-jet final state, but the production cross section for this process is small and the resulting dijet masses tend to be small. The Z^0Z^0, W^+W^- and

$t\bar{t}$ production processes tend to produce decay products in the forward and backward direction with respect to the beam axis, resulting in low transverse energy events with high thrust values (defined in [175]). They also tend to have fewer total and charged particles, and lower total energy recorded in the event. An additional powerful discriminant is provided by the variable Y_{34}, the value of the Y_{CUT} variable of the Durham jet clustering algorithm [170] above which the algorithm returns 3 jets and below which it returns 4 jets. These backgrounds can therefore be significantly suppressed with rejection factors of order 10-100 using kinematic selection criteria, which are summarized in Table 4.1. Distributions of the kinematic variables used in the selection criteria are displayed in Fig. 4.10.

Because the total background production cross section is of order 10^4 times larger than that of the signal, the kinematic suppression described above is not sufficient. Further background suppression is achieved by requiring four b jets in the event, where a b jet is required to have total number of particles N_{TOT} >10, number of charged particles N_{CHA} >5, and P_b >0.5, where P_b is the b jet probability determined by the LCFIVertex algorithm. The ability to require four b jets in the event is made possible by the excellent b tagging performance provided by the advanced vertex tracker based on thin sensors. These selection criteria result in a b jet selection efficiency of 0.79 using 'truth patrec' and 0.72 using 'full patrec,' where the neural net has not been retrained while using 'full patrec.' The rejection factor is sufficient to suppress the non b jet backgrounds.

For events passing selection, particles are grouped into four jets using the Durham algorithm, and paired into two dijets using the pairing which minimizes the difference between the masses of the two dijets $M_{jj}^{(1)}$ and $M_{jj}^{(2)}$. This procedure determines the correct pairing with an efficiency of 71%, and the signal H^0A^0 events in which the incorrect jet pairing (IJP) is chosen

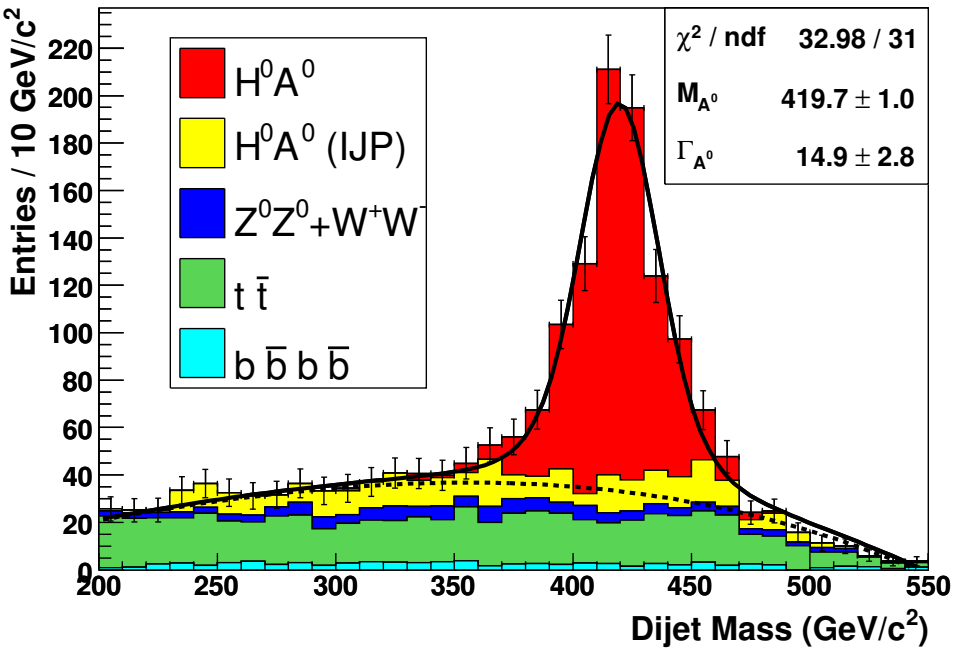

Figure 4.9: The dijet mass distribution for selected signal and background events [68]. Signal events in which the incorrect jet pairing (IJP) has been chosen are considered as a source of background. The dashed black line indicates the background fit function, the solid black line indicates the signal plus background fit functions.

are considered as a source of background. At this point the constrained kinematic fit algorithm described in Chap. 4.3.2 is performed, and the jet momenta are adjusted. Both dijets are required to satisfy 200 GeV/c^2< M_{jj} <550 GeV/c^2 and the difference between the two dijet masses is required to satisfy $|M_{jj}^{(1)} - M_{jj}^{(2)}|$ <50 GeV/c^2 in order to remove poorly reconstructed events. The efficiencies for signal and background events to pass final selection is displayed in Table 4.2.

The dijet mass distribution for events passing selection is displayed in Fig. 4.9, which contains two entries per event. A fit procedure is performed in order to extract the mass and width of the A^0 boson. The signal is described by two Breit-Wigner distributions with a fixed mass splitting of 1.4 GeV/c^2 and with the same normalization and width, convoluted with a Gaussian

resolution function. The width of the Gaussian function is fixed to the values given in Chap. 4.3.2 after applying the constrained kinematic fit algorithm. The background is described by a third order polynomial whose shape is determined by fitting to background events alone. The fit is performed with four free parameters: the signal yield, background yield, M_{A^0} and Γ_{A^0}. I find $M_{A^0} = (419.7 \pm 1.0)$ GeV/c^2 and $\Gamma_{A^0} = (14.9 \pm 2.9)$ GeV/c^2 using 'truth patrec,' where the quoted uncertainties are statistical only. Using 'full patrec' the uncertainties on M_{A^0} and Γ_{A^0} increase to 1.3 GeV/c^2 and 3.4 GeV/c^2 respectively.

4.5 The $e^+e^- \to H^0A^0 \to b\bar{b}\tau^+\tau^-$ Channel

The $e^+e^- \to H^0A^0 \to b\bar{b}\tau^+\tau^-$ process is analyzed because its rate is related to the branching fraction $BF(A^0 \to \tau^+\tau^-)$. This quantity is important to constrain other SUSY parameters related to $\Omega_\chi h^2$, as will be discussed below. The signature of this process is a final state with two b jets and two τ leptons, where the decay products are again distributed isotropically. The same backgrounds as for the $e^+e^- \to H^0A^0 \to b\bar{b}b\bar{b}$ are included and are suppressed using the kinematic selection criteria summarized in Table 4.1. For events passing this kinematic selection, the particles are grouped into four jets. Exactly two of these jets must be tagged as b jets, which are required to satisfy the same total and charged particle multiplicity requirements as above but must satisfy the tighter requirement $P_b > 0.9$. The mass of the $b\bar{b}$ dijet must satisfy 300 GeV/c$^2 < M_{bb} < 600$ GeV/c^2 and the mass of the two non-b jets must satisfy 250 GeV/c$^2 < M_{jj} < 600$ GeV/c^2. The angle θ between the two b jets and between the two non-b jets must satisfy $-0.8 < \cos\theta < 0$, and the number of charged particles with energy greater than 5 GeV that are not associated to either b jet must not exceed six. One of the two non-b jets must be tagged as a τ, where a τ is required to have less than

Table 4.1: Summary of kinematic selection criteria for the $b\bar{b}b\bar{b}$ and $b\bar{b}\tau^+\tau^-$ signal channels. The thrust and sphericity event shape variables are defined in [175]. Empty entries indicate that no requirement is placed on the given variable for the given signal channel.

Quantity	$b\bar{b}b\bar{b}$ **Channel**	$b\bar{b}\tau^+\tau^-$ **Channel**
Total event energy	E_{TOT} >700 GeV	500 GeV< E_{TOT} <1000 GeV
Total transverse energy	E_T >350 GeV	200 GeV< E_T <900 GeV
Total number of particles	N_{TOT} >80	40< N_{TOT} <180
Number of charged particles	N_{CHA} >30	15< N_{CHA} <100
Event thrust	thrust<0.9	thrust<0.85
Event sphericity		sphericity>0.1
Y_{CUT} threshold	Y_{34} >0.002	

4 energetic charged particles and must satisfy P_τ >0.8, where P_τ is the τ probability determined by the algorithm described in Chap. 4.3.4. The final step in the selection procedure is to define a variable P_{DISC} which discriminates between $b\bar{b}b\bar{b}$ and $b\bar{b}\tau^+\tau^-$ events. The variable P_{DISC} is a discriminant based on the total energy and total number of energetic charged particles not associated to either b jet, and the maximum of the two values of P_τ associated to the two non-b jets. The event is required to satisfy P_{DISC} >0.9. The final selection efficiencies for signal and background are displayed in Table 4.2 and distributions of the kinematic variables used in the selection criteria are displayed in Fig. 4.10. I find that 88 signal events and 76 background events pass selection, giving a relative statistical uncertainty of $(N_{SIG}/\sqrt{N_{SIG}+N_{BKG}})^{-1} = 0.15$ in $BF(H^0/A^0 \to \tau^+\tau^-)$.

4.6 Constraints on the Neutralino Relic Density

Assuming that the A^0 mass and width are measured with the precision determined by this analysis, and in combination with a set of particle mass and coupling measurements available at the LHC and at a 1 TeV e^+e^- collider, the dark matter relic density at the LCC-4 benchmark point can be determined to a relative uncertainty of 0.18 within the full MSSM [66]. A significant

Table 4.2: Summary of efficiencies for the $b\bar{b}b\bar{b}$ and $b\bar{b}\tau^+\tau^-$ signal channel selection. For the $H^0A^0 \to b\bar{b}b\bar{b}$ process, the first efficiency is obtained using 'truth patrec,' the second efficiency in parentheses is obtained using 'full patrec.' The difference between these two efficiencies is due to the observed decrease in b-tagging efficiency using 'full patrec.'

Process	$b\bar{b}b\bar{b}$ **Selection**	$b\bar{b}\tau^+\tau^-$ **Selection**
$H^0A^0 \to b\bar{b}b\bar{b}$	0.24±0.01 (0.17±0.01)	0
$H^0A^0 \to b\bar{b}\tau^+\tau^-$	0	0.14±0.02
$Z^0Z^0 + W^+W^-$	10^{-5}	3×10^{-8}
$t\bar{t}$	8×10^{-4}	2×10^{-4}
inclusive $b\bar{b}b\bar{b}$	4×10^{-3}	2×10^{-6}

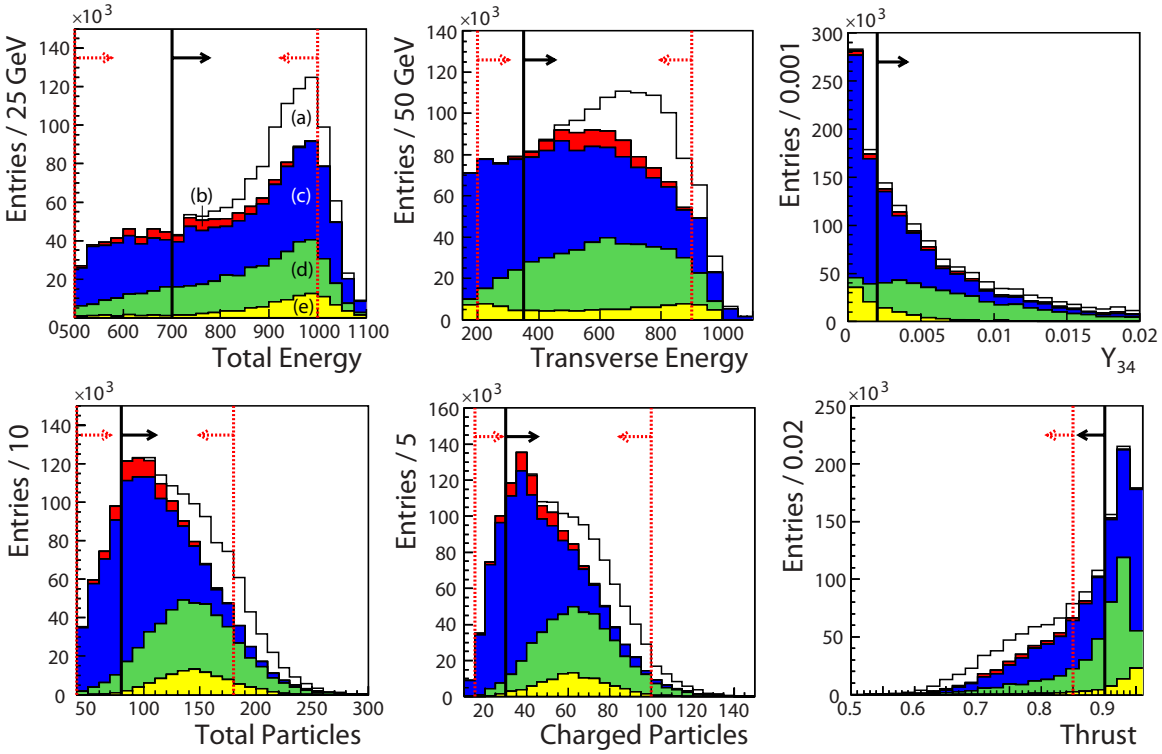

Figure 4.10: Distributions of kinematic variables for signal and background events used for signal selection. (a) White is signal $H^0A^0 \to b\bar{b}b\bar{b}$ events scaled by a factor of 100, (b) red is signal $H^0A^0 \to b\bar{b}\tau^+\tau^-$ events scaled by a factor of 100, (c) blue is W^+W^- and Z^0Z^0 events, (d) green is $t\bar{t}$ events, and (e) yellow is inclusive $b\bar{b}b\bar{b}$ events scaled by a factor of 10. The solid black (dashed red) vertical lines and arrows indicate the selection criteria for the $H^0A^0 \to b\bar{b}b\bar{b}$ ($H^0A^0 \to b\bar{b}\tau^+\tau^-$) signal channel.

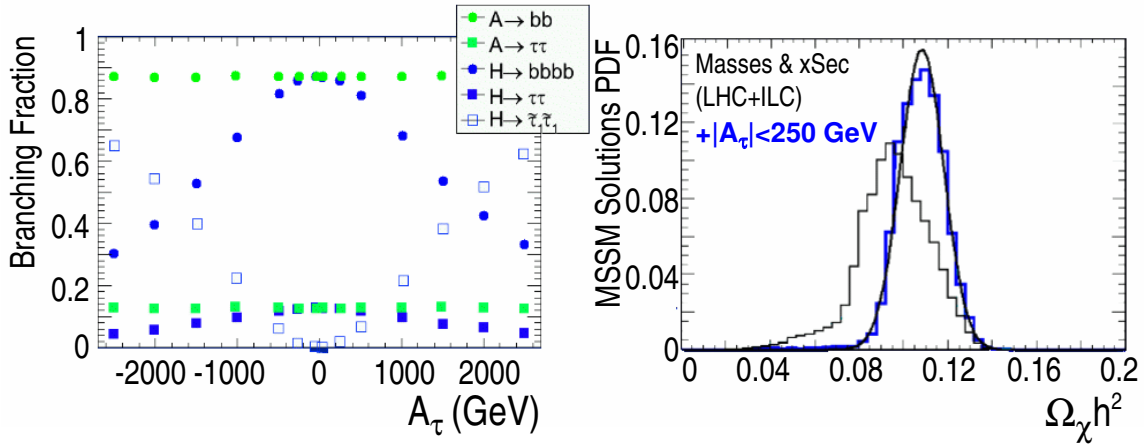

Figure 4.11: Left: dependence of the H^0 and A^0 branching fractions on the stau trilinear coupling A_τ [68] as computed using HDECAY 2.0 [176]. Right: The probability density function of $\Omega_\chi h^2$ within the full MSSM [66, 68]. The wider black histogram includes the measurements of the A^0 properties with the precision derived in this analysis plus a set of measurements available at the LHC and a future 1 TeV e^+e^- collider, and the thinner blue histogram includes the additional constraint $|A_\tau|$ <250 GeV. The Gaussian fit function has a width of 0.08.

contribution to this uncertainty is provided by MSSM scenarios in which $\Omega_\chi h^2$ is reduced by the annihilation mechanism $\chi_1^0\chi_1^0 \rightarrow H^0 \rightarrow \tilde{\tau}_1\tilde{\tau}_1$, which occurs in addition to the s-channel annihilation process via the A^0 resonance. The H^0 coupling to the $\tilde{\tau}_1$ scales as $A_\tau \frac{\cos\alpha}{\sin\beta} + \mu\frac{\sin\alpha}{\cos\beta}$, where A_τ is the stau trilinear coupling and α is a parameter which defines the mixing between the h^0 and H^0 MSSM Higgs states. This implies that at large values of $|A_\tau|$, $BF(H^0 \rightarrow \tilde{\tau}_1\tilde{\tau}_1)$ becomes sizable, leading to enhancement of the s-channel neutralino annihilation process through the H^0 resonance. In Fig. 4.11 (left), the dependence of the H^0 and A^0 branching fractions on A_τ is displayed, which shows that a measurement of $BF(H^0 \rightarrow \tilde{\tau}_1\tilde{\tau}_1)$ allows a constraint on $|A_\tau|$ to be derived. Because the $H^0 \rightarrow \tilde{\tau}_1\tilde{\tau}_1 \rightarrow \tau^+\chi_1^0\tau^-\chi_1^0$ processes leads to the same final state, $BF(H^0 \rightarrow \tilde{\tau}_1\tilde{\tau}_1)$ can be constrained using the $b\bar{b}\tau^+\tau^-$ analysis discussed above. The achievable relative uncertainty of 0.15 allows the constraint $|A_\tau| < 250$ GeV to be derived, which suppresses the tail at low $\Omega_\chi h^2$, as shown in Fig. 4.11 (right). This constraint improves the achievable relative uncertainty

on the neutralino relic density to 0.08, which is close to the current precision from the WMAP measurement.

4.7 Conclusions

This analysis presents a study of the $e^+e^- \rightarrow H^0A^0$ process simulated at a future lepton collider operating at $\sqrt{s}$=1 TeV. Full simulation and reconstruction are used to investigate a mSUGRA benchmark point at which the dark matter relic density $\Omega_\chi h^2$ is determined by the rate of neutralino annihilation via $\chi_1^0\chi_1^0 \rightarrow A^0 \rightarrow b\bar{b}/\tau^+\tau^-$. The rate of this process depends critically on the mass and width of the Supersymmetric A^0 Higgs boson, and I find that with 2 ab^{-1} of data the achievable accuracies on the A^0 mass and width are 1.0 GeV/c^2 and 2.9 GeV/c^2, respectively. I find that the branching fraction $BF(A^0 \rightarrow \tau^+\tau^-)$ can be determined with a relative uncertainty of 0.15. These measurements, in combination with a set of measurements available at the next generation of colliders, allow the dark matter relic density to be determined with a relative uncertainty of 0.08.

Chapter 5

Conclusions

In this thesis I have investigated aspects of the role of lepton colliders in probing new physics. Although data collected at hadron colliders such as the LHC is likely to lead to new physics discoveries, lepton colliders provide complementary data which is used to make precise measurements and provide sensitivity to rare processes. I have discussed two complementary strategies for probing new physics at lepton colliders, which involve searching for processes forbidden in the Standard Model in data collected at low energy, and searching for direct production of new particles at a collision energy of 1 TeV.

I have presented a search for the lepton-flavor violating decays $\Upsilon(3S) \to e\tau$ and $\Upsilon(3S) \to \mu\tau$ in a sample of $(116.7 \pm 1.2) \times 10^6$ $\Upsilon(3S)$ decays collected with the *BABAR* detector. These decays are unobservable in the Standard Model but may be observable in several beyond-the-Standard Model scenarios, and observation of these processes would therefore provide a clear signal of new physics. No statistically significant signal is found and the results are used to place the best upper limits to date on the lepton-flavor violating $\Upsilon(3S)$ decays $BF(\Upsilon(3S) \to e\tau) < 5.0 \times 10^{-6}$ and

$BF(\Upsilon(3S) \rightarrow \mu\tau) < 4.1 \times 10^{-6}$ at 90% confidence level. These results are interpreted using effective field theory in terms of constraints on the effective coupling constant $\alpha_{\ell\tau}$ and mass scale $\Lambda_{\ell\tau}$ of a generic 4-fermion $b\bar{b}\ell\tau$ contact interaction mediating the decay $\Upsilon(3S) \rightarrow \ell\tau$. In the strong coupling limit in which $\alpha_{e\tau} = \alpha_{\mu\tau} = 1$, the derived branching fraction upper limits translate to the 90% confidence level lower limits $\Lambda_{e\tau} > 1.41$ TeV and $\Lambda_{\mu\tau} > 1.47$ TeV on the mass scale of beyond-the-Standard Model physics contributing to lepton-flavor violating $\Upsilon(3S)$ decays. These results probe new physics at the TeV-scale using data collected at a collision energy of 10.35 GeV.

In order to probe the Higgs mechanism of electroweak symmetry breaking and the nature of physics beyond the SM and its relation to cosmology, it is necessary to construct a TeV-scale lepton collider and a detector capable of realizing its physics potential. I have discussed research and development efforts aimed at producing a vertex tracker capable of the required physics performance at such a collider. This includes the effort to produce thin, advanced Silicon sensors using the CMOS monolithic active pixel sensor technology. This is necessary to provide the required track extrapolation resolution and hence the required jet-flavor tagging performance. We find that thinning the sensors to 40-50 μm, which meets the material budget constraints at a future lepton collider, does not significantly degrade the performance of the sensors. These thinned sensors are used to produce a small-scale tracker prototype, which is tested using a 1.5 GeV electron beam and a 120 GeV proton beam. The results of tracking studies indicate that the tracker is capable of meeting the required impact parameter resolution specified by $\sigma_{IP} = (5 \oplus 10/p_T)$ μm, where p_T is measured in units of GeV/c. The tracker is also capable of reconstructing vertices resulting from interactions between the beam protons and a Copper target, and the longitudinal vertex resolution is found to be (260 ± 10) μm.

Finally, I have investigated the role of a TeV-scale lepton collider in understanding dark matter using simulation studies. A Supersymmetric scenario is chosen in which the dark matter is composed of neutralinos, and the neutralino relic density is determined by the rate of the process $\chi_1^0\chi_1^0 \rightarrow A^0 \rightarrow b\bar{b}/\tau^+\tau^-$. This rate depends strongly on the properties of the A^0 heavy Higgs boson. I find that with an integrated luminosity of 2 ab^{-1}, the achievable uncertainties on the A^0 mass and width are 1.0 GeV/c^2 and 2.8 GeV/c^2, respectively, and the achievable relative uncertainty on $BF(A^0 \rightarrow \tau^+\tau^-)$ is 0.15. These measurements, together with a set of measurements to be performed at the Large Hadron Collider, allow the neutralino relic density to be determined with a relative uncertainty of 0.08, comparable to the current uncertainty from the Wilkinson Microwave Anisotropy Probe. This analysis will further our understanding of dark matter by combining complementary measurements at colliders with those from cosmological observations. Comparison between the neutralino relic density and the observed dark matter density will have profound implications on our understanding of dark matter by allowing us to determine if it is composed of Supersymmetric particles.

Bibliography

[1] F. Wilczek, Rev. Mod. Phys. **71**, S85 (1999).

[2] M. Peskin and D. V. Schroeder, An Introduction to Quantum Field Theory, (1995).

[3] S. F. Novaes, arXiv:hep-ph/0001283v1 (2000).

[4] R. P. Feynman, Phys. Rev. **74**, 1430 (1948); J. Schwinger, Phys. Rev. **74**, 1439 (1948); T. Tati and S. Tomonaga, Prof. Theor. Phys. **3**, 391 (1948).

[5] C. Caso *et al.*, Eur. Phys. J. **C4**, 1 (1998).

[6] W. Lamb and R. Retherford, Phys. Rev. **72**, 241 (1947).

[7] W. Pauli, *Open Letter to Radioactive Persons*, (1930).

[8] H. Georgi, Lie Algebras in Particle Physics, (1999).

[9] S.L. Glashow, Nucl. Phys. **22**, 579 (1961); A. Salam and J.C. Ward, Phys. Lett. **13**, 168 (1964); S. Weinberg, Phys. Rev. Lett. **19**, 1264 (1967).

[10] P. W. Higgs, Phys. Rev. Lett. **12**, 132 (1964); P. W. Higgs, Phys. Rev. Lett. **13**, 508 (1964); P. W. Higgs, Phys. Rev. **145**, 1156 (1966); F. Englert and R. Brout, Phys. Rev. Lett. **13**, 321 (1964); G. S. Guralnik *et al.*, Phys. Rev. Lett. **13**, 585 (1964).

[11] F. J. Hasert *et al.* Phys. Lett. **B46**, 121 (1973).

[12] UA1 Collab., G. Arnison *et al.*, Phys. Lett. **B122**, 103 (1983); UA2 Collab., M. Banner *et al.*, Phys. Lett. **B122**, 476 (1983); UA1 Collab., G. Arnison *et al.*, Phys. Lett. **B126**, 398 (1983); UA2 Collab., P. Bagnaia *et al.*, Phys. Lett. **B129**, 130 (1983).

[13] LEP-SLC Electroweak Working Group, Phys. Rept. **427**, 257 (2006).

[14] LHC White Book, CERN/AC/93-03, (2003); LHC Conceptual Design Report, CERN/AC/95-05, (2005).

[15] M. Gell-Mann, Phys. Lett. **8**, 213 (1964); G. Zweig, CERN Report CERN-TH-401, (1964); G. Zweig, CERN Report CERN-TH-412, (1964).

[16] S. L. Glashow, J. D. Bjorken, Phys. Lett. **11**, 255 (1964).

[17] E. D. Bloom *et al.*, Phys. Rev. Lett. **23**, 935 (1969).

[18] M. Kobayashi and T. Maskawa, Prog. Theor. Phys. **49**, 652 (1973).

[19] J.-E. Augustin *et al.*, Phys. Rev. Lett. **33**, 1406 (1974).

[20] Aubert *et al.*, Phys. Rev. Lett. **33**, 1404 (1974).

[21] D. J. Gross and F. Wilczek, Phys. Rev. Lett. **30**, 1343 (1973); H. D. Politzer, Phys. Rev. Lett. **30**, 1346 (1973); D. J. Gross and F. Wilczek, Phys. Rev. **D8**, 3633 (1973); H. D. Politzer, Phys. Rep. **14**, 129 (1974).

[22] TASSO Collab., R. Brandelik *et al.*, Phys. Lett. **B86**, 243 (1979).

[23] ALEPH Collab., R. Barate *et al.*, Phys. Rept. **294**, 1 (1998).

[24] Particle Data Group, C. Amsler *et al.*, Phys. Lett. **B667**, 1 (2008).

[25] D0 Collab., S. Abachi *et al.*, Phys. Rev. Lett. **74**, 2422 (1995); CDF Collab., F. Abe *et al.*, Phys. Rev. Lett. **74**, 2626 (1995).

[26] LEP Electroweak Working Group, http://lepewwg.web.cern.ch/LEPEWWG/.

[27] M. Schmelling, Proc. of Int. Conf. of High Energy Physics (ICHEP96), MPI H-V39, (1996).

[28] NuTeV Collab., G. Zeller *et al.*, Phys. Rev.Lett. **88**, 091802 (2002).

[29] D. Treille, *The Message of the LEP Era*, (2004).

[30] S. Weinberg, Phys. Rev. **D13**, 974 (1976); S. Weinberg Phys. Rev. **D19**, 1277 (1979); E. Gildener, Phys. Rev. **D14**, 1667 (1976); L. Susskind, Phys. Rev. **D20**, 2619 (1979).

[31] U. Amaldi *et al.*, Phys. Lett. **B260**, 447 (1991); U. Amaldi *et al.*, Phys. Lett. **B281**, 374 1992.

[32] R. Davis *et al.*, Phys. Rev. Lett. **20**, 1205 (1968); Kamiokande Collab., Phys. Lett. **B335**, 237 (1994); SuperKamiokande Collab., Phys. Rev. Lett. **81**, 1562 (1998).

[33] WMAP Collab., G. Hinshaw *et al.*, Astrophys. J. Suppl. **180**, 225 (2009).

[34] A. D. Sakharov, JETP Lett. **5**, 24 (1967).

[35] S. Martin, arXiv:hep-ph/9709356v5 (2008).

[36] J. Ellis, arXiv:hep-ph/0203114v1 (2002).

[37] Y. A. Gol'fand and E. P. Likhtman, JETP Lett. **13**, 323 (1971);

[38] D. V. Volkov and V. P. Akulov, Phys. Lett. **B46**, 109 (1973).

[39] J. Wess and B. Zumino, Nucl. Phys. **B70**, 39, (1974);

[40] P. Ramond, Phys. Rev. **D3**, 2415 (1971).

[41] A. Neveu and J. H. Schwarz, Nucl. Phys. **B31**, 86 (1971).

[42] S. Dimopoulos and H. Georgi, Nucl. Phys. **B193**, 150 (1981).

[43] S. Dimopoulos, S. Raby, F. Wilczek, Phys. Rev. **D24**, 1681 (1981).

[44] K. Inonue *et al.*, Prog. Theor. Phys. **67**, 1889 (1982); R. Flores and M. Sher, Ann. Phys. **148**, 95 (1983); H. P. Nilles and M. Nusbaumer, Phys. Lett. **B145**, 73 (1984); P. Majumdar and P. Roy, Phys. Rev. **D30**, 2432 (1984).

[45] J. F. Gunion and H. E. Haber, Nucl. Phys. **B272**, 1 (1986).

[46] S. Dimopoulos and S. Raby, Nucl. Phys. **B192**, 353 (1981); E. Witten, Nucl. Phys. **B188**, 513 (1981); M. Dine *et al.*, Nucl. Phys. **B189**, 575 (1981); S. Dimopoulos and H. Georgi, Nucl. Phys. **B193**, 150 (1981); N. Sakai, Z. Phys. **C11**, 153 (1981). R. K. Kaul and P. Majumdar, Nucl. Phys. **B199**, 36 (1982).

[47] L. E. Ibanez and G. G. Ross, Phys. Lett. **B105**, 439 (1981); S. Dimopoulos *et al.*, Phys. Rev. **D24**, 1681 (1981); J. Ellis *et al.*, Phys. Lett. **B249**, 441 (1990); P. Langacker and M. Luo, Phys. Rev. **D44**, 817 (1991); J. Ellis *et al.*, Phys. Lett. **260**, 131 (1991).

[48] H. Pagels and J. R. Primack, Phys. Rev. Lett. **48**, 223 (1982); S. Weinberg, Phys. Rev. Lett. **48**, 1303 (1982); H. Goldberg, Phys. Rev. Lett. **50**, 1419 (1983); J. R. Ellis *et al.*, Phys. Lett. **B127**, 233 (1983); J. R. Ellis *et al.*, Nucl. Phys. **B238**, 453 (1984).

[49] ATLAS Collab., CERN-LHCC-99-15, ATLAS-TDR-15, (1999).

[50] CMS Collab., G. L. Bayatian *et al.*, J. Phys. **G34**, 995 (2007).

[51] American Linear Collider Working Group, T. Abe *et al.*, BNL-52627, SLAC-R-570, (2001).

[52] A. Djouadi *et al.*, International Linear Collider Reference Design Report Vol. 2, (2007).

[53] ALEPH Collab., R. Barate *et al.*, Phys. Lett. **B429**, 169 (1998).

[54] C. Bobeth, M. Misiak and J. Urban, Nucl. Phys. **B574**, 291 (2000).

[55] M. Misiak and M. Steinhauser, Nucl. Phys. **B683**, 277 (2004).

[56] A. K. Grant, Nucl. Instrum. Meth. **A408**, 21 (1998).

[57] L. Roszkowski *et al.* JHEP, 075 (2007).

[58] *BABAR* Collab., B. Aubert *et al.*, Phys. Rev. **D75**, 012008, (2007).

[59] Belle Collab., H. Yang *et al.*, Phys. Rev. Lett. **94**, 111802 (2005).

[60] *BABAR* Collab., B. Aubert *et. al*, SLAC-PUB-13480, (2008).

[61] J. Brau *et al.*, International Linear Collider Reference Design Report Vol. 1, (2007).

[62] T. Behnke *et al.*, International Linear Collider Reference Design Report Vol. 4, (2007).

[63] M. Battaglia *et al.*, Nucl. Instrum. Meth. **A579**, 675 (2007).

[64] M. Battaglia *et al.*, Nucl. Instrum. Meth. **A593**, 292 (2008).

[65] R. Turchetta *et al.*, Nucl. Instrum. Meth. **A501**, 251 (2003);

[66] E. Baltz *et al.*, Phys. Rev. **D74**, 103521 (2006).

[67] M. Battaglia *et al.*, J. Phys. **G30**, R217 (2004).

[68] M. Battaglia, B. Hooberman and N. Kelley, Phys. Rev. **D78**, 015021 (2008).

[69] R. Barbieri, L. Hall, A. Strumia, Nucl. Phys. **B445**, 219 (1995).

[70] J. R. Ellis *et al.*, Eur. Phys. J. **C14**, 319 (2000).

[71] J. R. Ellis, M. Raidal and T. Yanagida, Phys. Lett. **B581**, 9 (2004).

[72] M. Raidal *et al.*, Eur. Phys. J. **C57**, 13 (2008).

[73] G. Feinberg, Phys.Rev. **110**, 1482 (1958).

[74] S. M. Bilenky and B. Pontecorvo, Phys. Lett. **B61**, 248 (1976).

[75] J.C. Pati and A. Salam, Phys. Rev. **D10**, 275 (1974).

[76] H. Georgi and S.L. Glashow, Phys. Rev. Lett. **32**, 438 (1974).

[77] SINDRUM Collab., U. Bellgardt *et al.*, Nucl. Phys. **B299**, 1 (1988).

[78] MEGA Collab., M. L. Brooks *et al.*, Phys. Rev. Lett. **83**, 1521 (1999);

[79] P. Wintz, Proc. of Int. Conf. of High Energy Physics (ICHEP98), (1998).

[80] *BABAR* Collab., B. Aubert *et al*, Phys. Rev. Lett. **96**, 041801 (2006).

[81] *BABAR* Collab., B. Aubert *et al*, Phys. Rev. Lett. **95**, 041802 (2005).

[82] Belle Collab., Y. Miyazaki *et al.*, Phys. Lett. **B648**, 341 (2007).

[83] *BABAR* Collab., B. Aubert *et al*, Phys. Rev. Lett. **98**, 061803 (2007).

[84] Belle Collab., M. C. Chang *et al.*, Phys. Rev. **D68**, 111101, (2003).

[85] CDF Collab., F. Abe *et al.*, Phys. Rev. Lett. **81**, 5742 (1998).

[86] BNL Collab., D. Ambrose *et al.*, Phys. Rev. Lett. **81**, 5734 (1998).

[87] CLEO Collab., W. Love *et al.*, Phys. Rev. Lett. **101**, 201601 (2008).

[88] S. Nussinov, R.D. Peccei, X.M. Zhang, Phys. Rev. **D63**, 016003 (2001).

[89] Belle Collab., Y. Miyazaki *et al.*, Phys. Lett. **B660**, 154 (2008).

[90] PEP-II Conceptual Design Report, SLAC-418, (1993).

[91] P. Oddone, Annals N.Y. Acad. Sci. **578**, 237 (1989).

[92] Belle Collab., M. T. Cheng *et al*, BELLE-TDR-3-95, KEK-95-1, (1995).

[93] T. Orimoto, Ph.D. Thesis, SLAC-R-845, (2006).

[94] *BABAR* Collab., B. Aubert *et al.*, Nucl. Instrum. Meth. **A479**, 1 (2002).

[95] I. Narsky, arXiv:physics/0507143v1 [physics.data-an] (2008).

[96] Particle Data Group, S. Eidelman *et al.*, Phys. Lett. **B592**, 1 (2004); and 2005 partial update for edition 2006.

[97] S. Godfrey and J. L. Rosner, Phys. Rev. **D64**, 074011 (2001).

[98] M. B. Voloshin,Mod. Phys. Lett. **A19**, 2895 (2004).

[99] F. Wilczek, Phys. Rev. Lett. **39**, 1304 (1977).

[100] M.-A. Sanchis-Lozano, J. Phys. Soc. Jap. **76**, 044101 (2007).

[101] *BABAR* Collab., B. Aubert *et al.* Phys. Rev. Lett. **101**, 071801 (2008).

[102] B.F. Ward, S. Jadach, Z. Was, Nucl. Phys. Proc. Suppl. **116**, 73 (2003).

[103] S. Jadach, W. Placzek and B.F.L. Ward, Phys. Lett. **B390**, 298 (1997).

[104] D.J. Lange, Nucl. Instrum. Meth. Phys. Res. **A462**, 152 (2001).

[105] P. Golonka, Z. Was, Eur. Phys. J. **C45**, 97 (2006).

[106] S. Agostinelli *et al.*, Nucl. Instrum. Meth. **A506**, 250 (2003).

[107] R. J. Barlow, Nucl. Instrum. Meth. **A297**, 496 (1990).

[108] ARGUS Collab., H. Albrecht *et al.*, Phys. Lett. **B241**, 278 (1990).

[109] J.E. Gaiser, Ph.D. Thesis, SLAC-R-255, page 178 (1982).

[110] Z.K. Silagadze, Phys. Scripta **64**, 128 (2001).

[111] D. Black, T. Han, H.-J. He, M. Sher, Phys. Rev. **D66**, 053002 (2002).

[112] A. de Gouvea *et al.*, Nucl. Phys. **B188**, 303 (2009).

[113] ALEPH Collab., D. Buskulic *et al.*, Nucl. Instrum. Meth. **A360**, 481 (1995).

[114] P. Meade and M. Reece, Phys. Rev. **D74**, 015010 (2006); J. Hubisz *et al.*, Phys. Rev. **D74**, 075008 (2008); G. L. Kane *etl a.*; A. J. Barr, Phys. Lett. **B596**, 205 (2004); T. Goto *et al*, Phys. Rev. **D70**, 075016 (2004); J. M. Smillie and B. R. Webber, JHEP **10**, 69 (2005).

[115] DELPHI Collab., CERN/LEPC/83-3, DELPHI 83-66/1, (1983); DELPHI Collab., P. Abreu *et al.*, Nucl. Instrum. Meth. **A378**, 57 (1996).

[116] ATLAS Collab., CERN-LHCC-99-14, ATLAS-TDR-14, (1999).

[117] N. Sinev *et al.*, Nucl. Instrum. Meth. **A409**, 243 (1998).

[118] STAR Collab., A. Shabetai *et al.*, Eur. Phys. J. **C49**, 169 (2007). L. Greiner *et al.*, J. Instrum. **4**, P03008 (2009).

[119] *BABAR* Collab., Do. Boutigny *et al.*, SLAC-R-457, (1995).

[120] H. Spieler, Semiconductor Detector Systems, (2005).

[121] G. Lutz, Semiconductor Radiation Detectors: Device Physis, (2007).

[122] G. Deptuch, Ph.D. thesis, (2002).

[123] CMS Collab., G. L. Bayatian *et al.*, CERN-LHCC-2006-001, CMS-TDR-008-1, (2006).

[124] CMS Collab., CERN/LHCC 98-6, (1998).

[125] F. Anghinolfi *et al.*, IEEE Trans. Nucl. Sci. **NS-39**, 650 (1992).

[126] C. J. S. Damerell *et al.*, Nucl. Instrum. Meth. **A253**, 478 (1987).

[127] J. Kemmer and G. Lutz, Nucl. Instrum. Meth. **A253**, 365 (1987); J. Kemmer and G. Lutz, Nucl. Instrum. Meth. **A273**, 588, (1988); J.Kemmer *et al.*, Nucl. Instrum. Meth. **A228**, 92 (1990); J. Ulrici *et al.*, Nucl. Instrum. Meth. **A465**, 247 (2001).

[128] E. R. Fossum, IEEE Trans. on Electron Devices, Vol. 44, No. 10, 1689 (1997); B. Dierickz *et al.*, Proc. of the IEEE CCD&AIS Workshop, P1 (1997); L. J. Kozlowski *et al.*, Proc. of SPIE, vol. 3698, 388 (1999).

[129] G. Deptuch *et al.*, Nucl. Instrum. Meth. **A511**, 240 (2003); S. A. Kleinfelder *et al.*, IEEE Trans. Nucl. Sci. **NS-51/5**, 2328, (2004).

[130] G. Claus *et al.*, Nucl. Instrum. Meth. **A465**, 120 (2001). Y. Gornushkin *et al.*, Nucl. Instrum. Meth. **A478**, 311 (2002).

[131] S. Kleinfelder *et al.* Nucl. Instrum. Meth. **A565**, 132 (2006).

[132] W. Dulinski *et al.* Nucl. Instrum. Meth. **A546**, 274 (2005).

[133] Y. Gornushkin *et al.* Nucl. Instrum. Meth. **A513**, 291 (2003).

[134] G. Deptuch, Nucl. Instrum. Meth. **A543**, 537 (2005).

[135] Aptek Industries, San Just, CA 95111, USA.

[136] A. L. Robinson *et al.*, Nucl. Instrum. Meth. **A319**, 40 (1992).

[137] F. Gaede *et al.*, Proc. of Conf. for Computing in High Energy and Nuclear Physics (CHEP03), PSN TUKT001, (2003).

[138] F. Gaede, Nucl. Instrum. Meth. **A559**, 177 (2006).

[139] LCCD Homepage, http://ilcsoft.desy.de/lccd/v00-03-06/doc/html/index.html.

[140] A. Besson *et al.*, Nucl. Instrum. Meth. **A568**, 233 (2006).

[141] T. Lohse, Report DESY 105-93.

[142] E. Hartouni *et al.*, DESY-PRC-95-01, (1995).

[143] LHCb Collab., P.R. Barbosa-Marinho *et al.*, CERN-LHCC-2001-040, (2001).

[144] LEP Collabs: ALEPH, DELPHI, L3 and OPAL, Phys. Lett. **B565**, 61 (2003).

[145] M. Veltman, Acta Phys. Polon. **B8**, 475 (1977).

[146] Muon g-2 Collab., H. N. Brown *et al.*, Phys. Rev. Lett. **86**, 227 (2001).

[147] M. Battaglia, Proc. of Int. Conf. on Linear Colliders (LCWS 04), vol. 2, 951 (2004).

[148] G. Bertone *et al.*, Phys. Rept. **405**, 279 (2005).

[149] F. Zwicky, Astrophys. J. **86**, 217 (1937).

[150] L. Volders, Bull. Astro. Inst. Netherlands **14**, 323 (1959).

[151] NASA Hubble Space Telescope, N. Benitez *et al.*, (2003).

[152] A. Boriello and P. Salluci, Lect. Notes Phys. **616**, 66 (2003).

[153] X-ray: NASA/CXC/CfA M.Markevitch *et al.*; Optical: NASA/STScI; Magellan/U.Arizona D.Clowe *et al.*; Lensing Map: NASA/STScI, ESO WFI, Magellan/U.Arizona D.Clowe *et al.*, (2004).

[154] H. Hoekstra *et al*, New Astron. Rev. **46**, 767 (2002).

[155] M. C. Weisskopf *et al.*, Exper. Astron. **16**, 1 (2003).

[156] COBE Collab., G. F. Smoot *et al.*, Astrophys. J. **396**, L1-L5 (1992); COBE Collab., C. L. Bennett *et al.*, Astrophys. J. **464** L1-L4 (1996).

[157] Planck Collab., Report ESA-SCI(2005)1, (2005).

[158] C. Alcock *et al.* Astrophys. J. **486**, 697 (1997).

[159] R. Scherrer and M. Turner, Phys. Rev. **D33**, 1585 (1986).

[160] G. Belanger *et al.*, Comput. Phys. Commun. **176**, 367 (2007).

[161] T. Sjostrand *et al.*, Comput. Phys. Commun. **135**, 238 (2001).

[162] T. Ohl, Comput. Phys. Commun. **101**, 269 (1997).

[163] F. E. Paige *et al.*, arXiv:hep-ph/0312045, (2003).

[164] CompHEP Collab., E. Boos *et al.*, Nucl. Instrum. Meth. **A534**, 250 (2004).

[165] StdHep Homepage, http://cepa.fnal.gov/psm/stdhep/.

[166] G. Musat, Proc. of Int. Conf. on Linear Colliders (LCWS 04), vol. 1, 437 (2004).

[167] T. Behnke, Pramana **69**, 697 (2007).

[168] DELPHI Collab., P. A. Aarnio *et al.*, Nucl. Instrum. Meth. **A303**, 233 (1991).

[169] M. A. Thompson, AIP Conf. Proc. **896**

[170] S. Catani *et al.*, Phys. Lett. **B269**, 432 (1991).

[171] D. J. Jackson, Nucl. Instrum. Meth. **A388**, 247 (1997); R. Hawkings, LC-PHSM-2000-021-TESLA, (2000).

[172] S. R. Magill, New J. Phys. **9**, 409 (2007).

[173] DELPHI Collab., P. Abreu *et al.*, Eur. Phys. J. **C2**, 581 (1998).

[174] CMS Collab., G. Bagliesi *et al.*, J. Phys. Conf. Ser. **119**, 032005 (2008).

[175] T. Sjostrand *et al.*, J. HEP **0605**, 026 (2006).

[176] A. Djouadi *et al.*, Comput. Phys. Commun. **108**, 56 (1998).

Appendix A

Comparison of *BABAR* Data and Simulated Events

In this section comparisons of data and simulated event distributions are shown for events passing selection for the four signal channels in the 27.5 fb^{-1} $\Upsilon(3S)$ data sample. Events are displayed which pass all selection criteria except for the variable being plotted. Data is denoted by points with error bars, simulated SM background processes are denoted by histograms with solid or dotted black outlines and simulated signal processes are denoted by histograms without outlines. The signal branching fraction has been set to 10^{-3}. For those channels and distributions in which a selection requirement is used, the events removed by the requirement are covered with diagonal red lines. All momenta are measured in the CM frame and the polar angle is measured with respect to the e^+ beam axis. Good agreement between data and simulation is achieved. The legend is given in Fig. A.1.

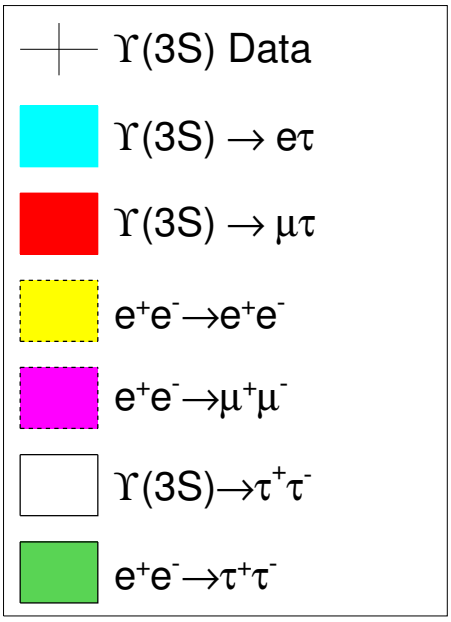

Figure A.1: The legend for data and simulated events.

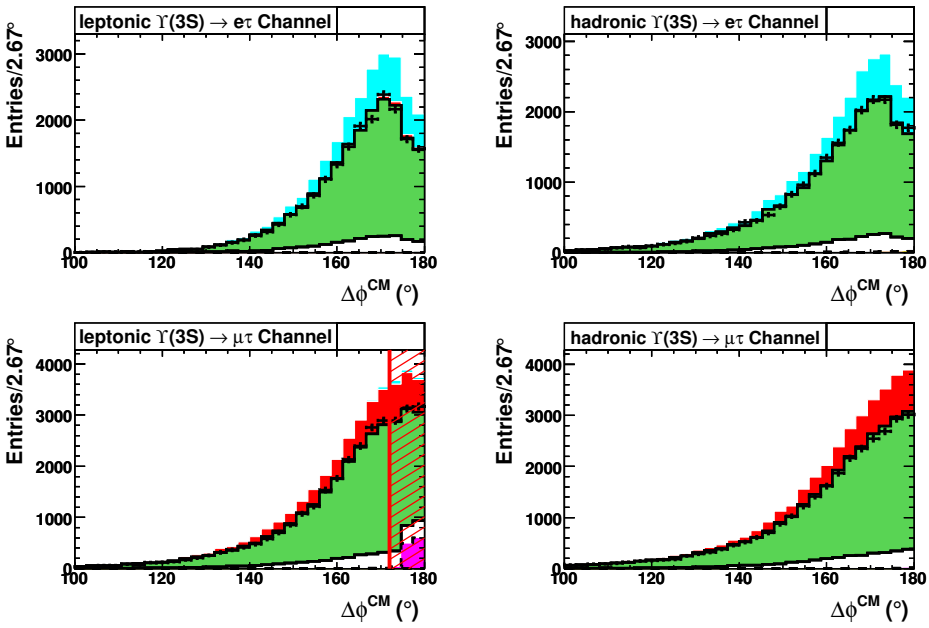

Figure A.2: Difference between the two track azimuthal angles in the CM frame.

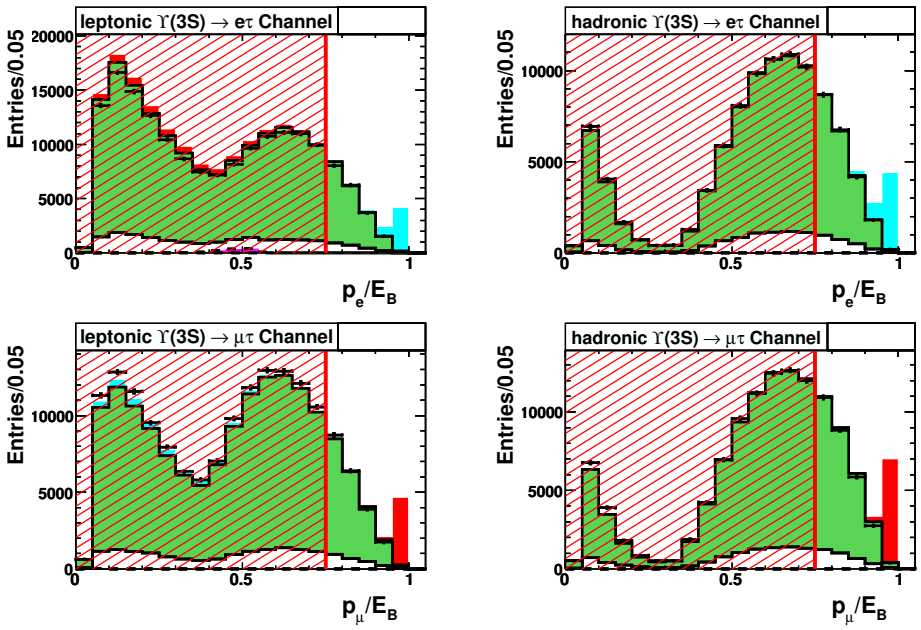

Figure A.3: Momentum of the primary lepton, normalized to the beam energy.

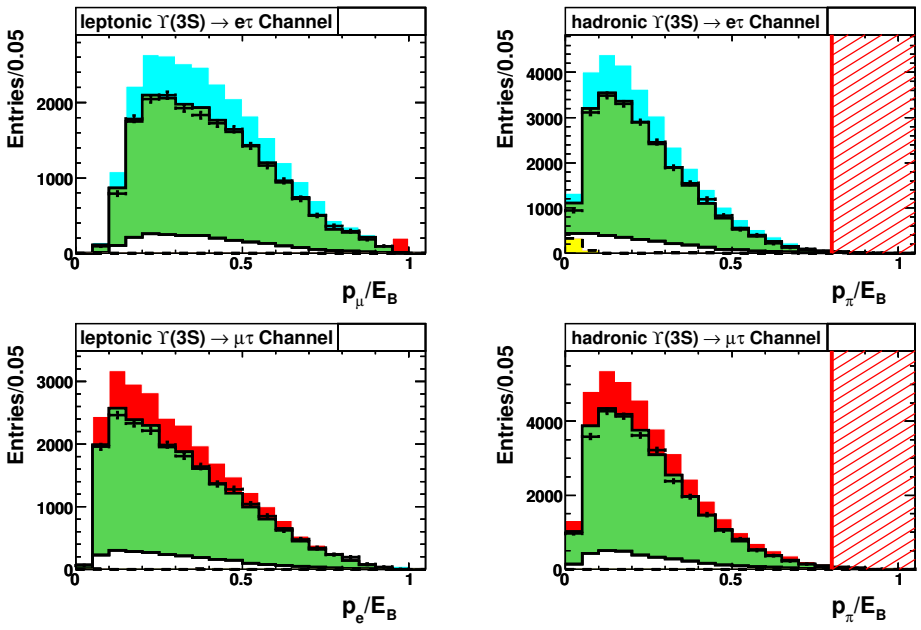

Figure A.4: Momentum of the τ-daughter, normalized to the beam energy.

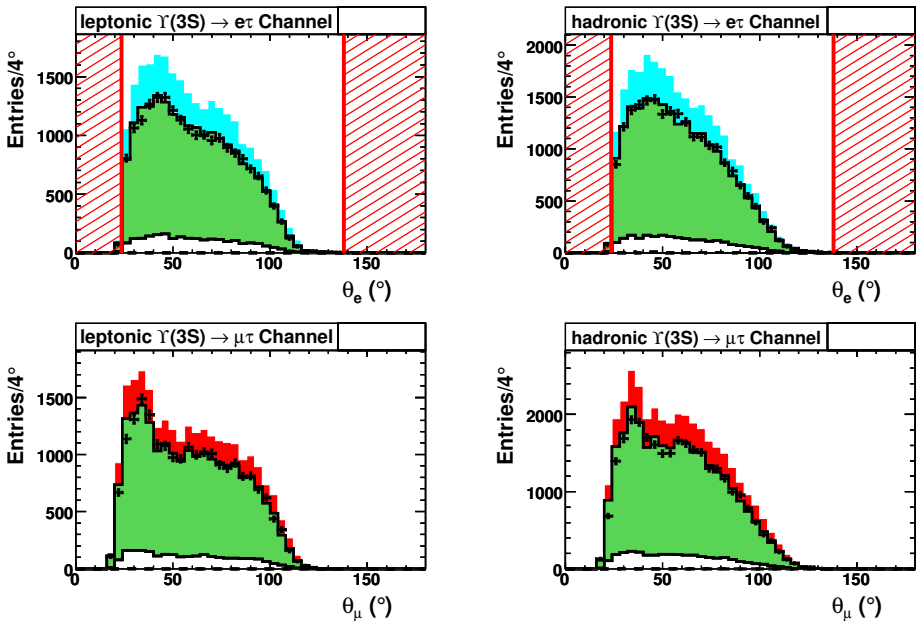

Figure A.5: Polar angle of the primary lepton in the lab frame.

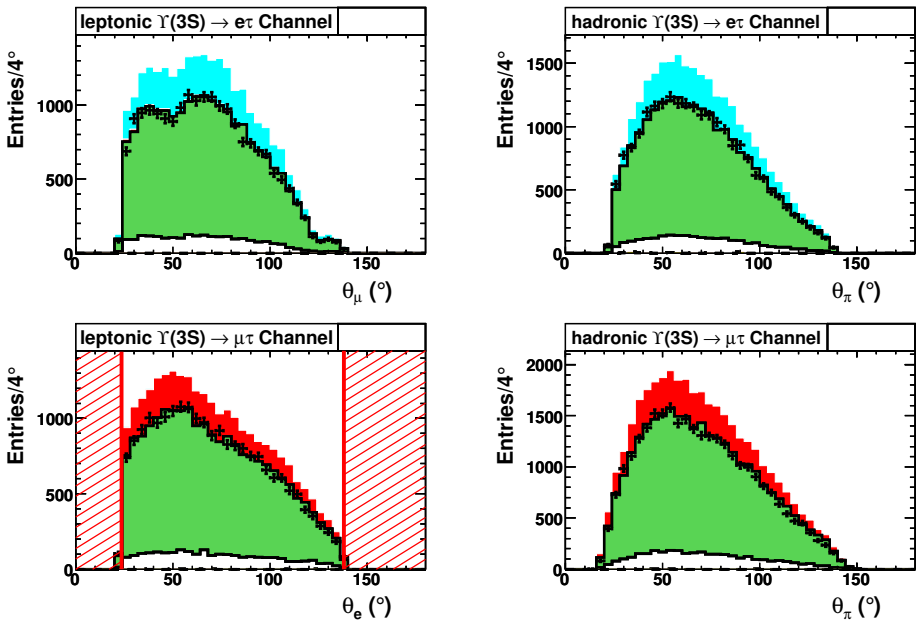

Figure A.6: Polar angle of the τ-daughter in the lab frame.

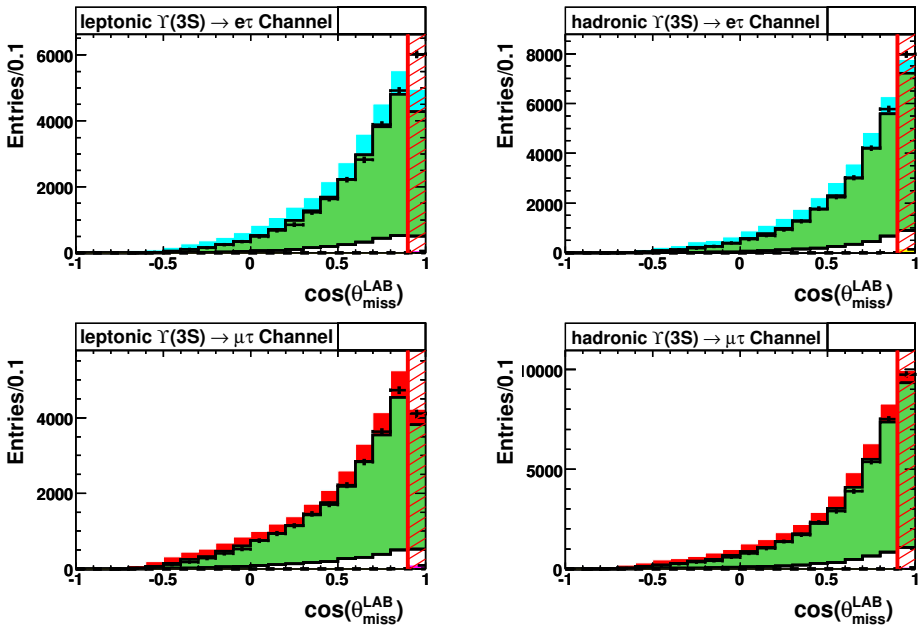

Figure A.7: Cosine of the polar angle of the missing momentum in the lab frame.

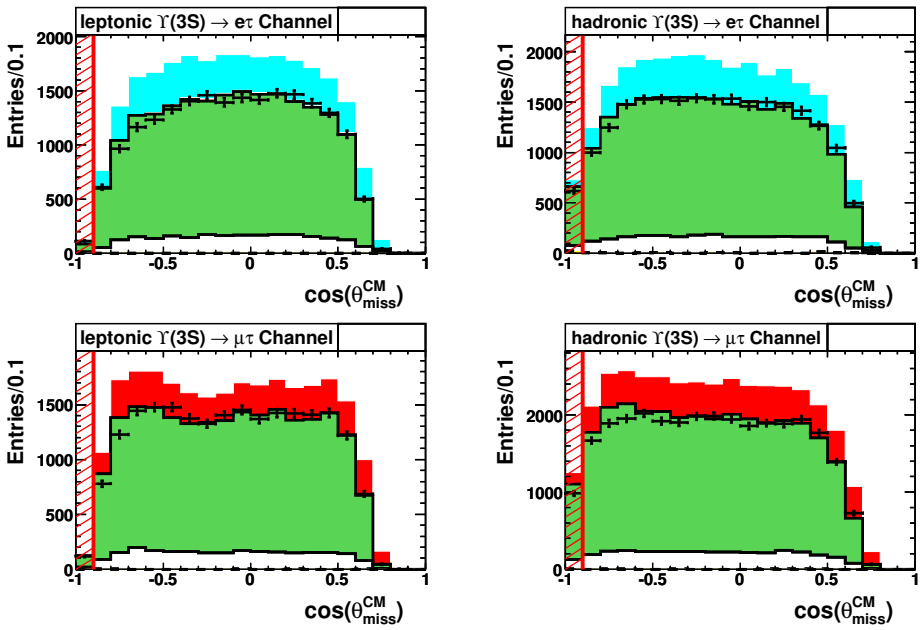

Figure A.8: Cosine of the polar angle of the missing momentum in the CM frame.

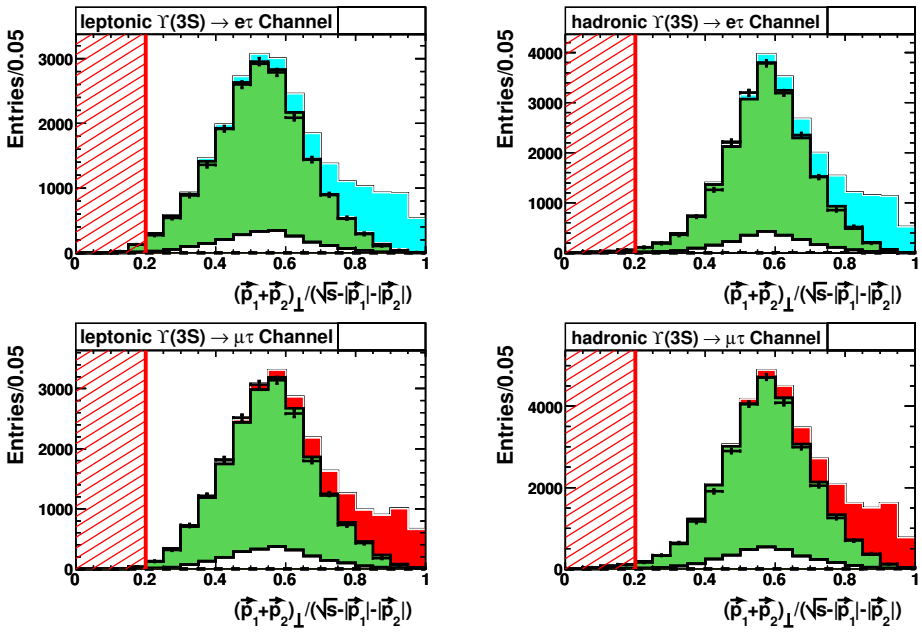

Figure A.9: The ratio $(\vec{p}_1 + \vec{p}_2)_\perp / (\sqrt{s} - |\vec{p}_1| - |\vec{p}_2|)$, where $\vec{p}_i$ are the track momenta.

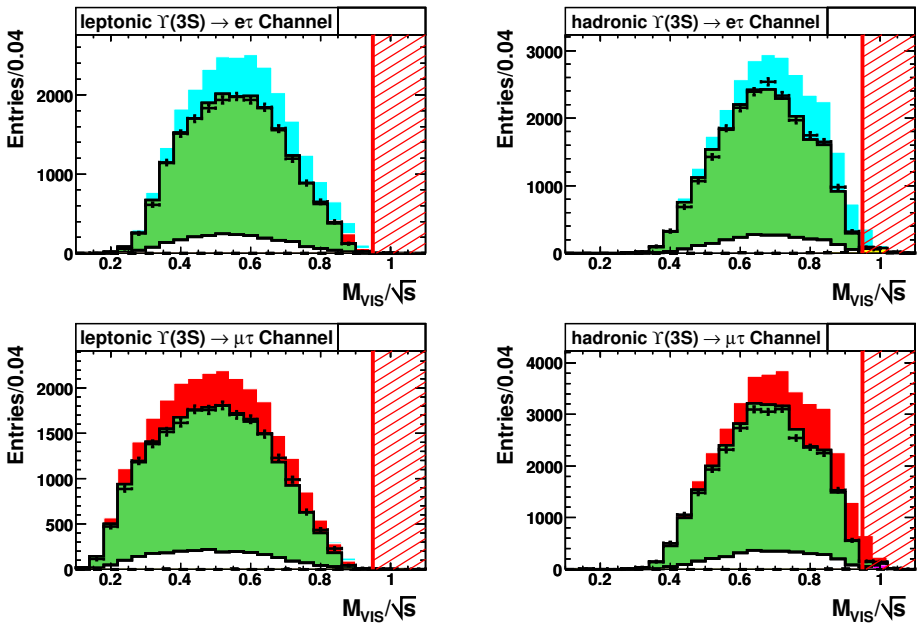

Figure A.10: Total visible energy normalized to the CM collision energy.

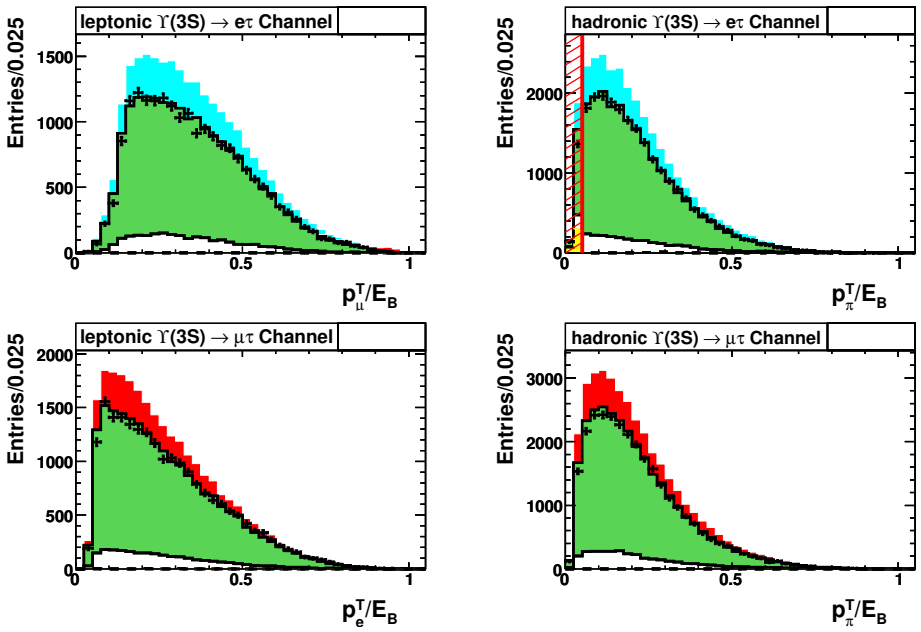

Figure A.11: Transverse momentum of the τ-daughter normalized to the beam energy.

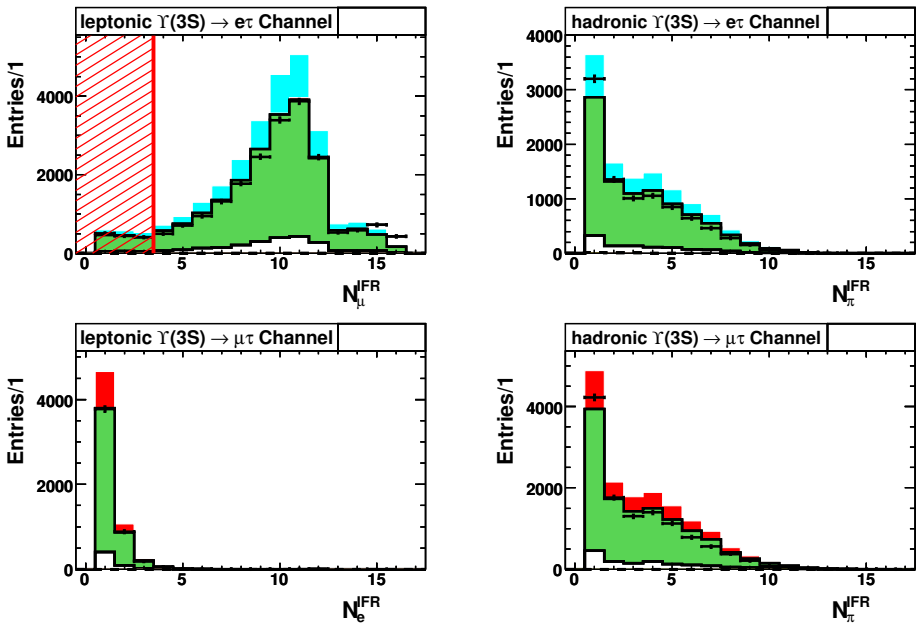

Figure A.12: Number of layers of the IFR muon system penetrated by the τ-daughter.

Appendix B

Studies of the *BABAR* Detector

Momentum Resolution

In this appendix I review the results of my study of the *BABAR* detector momentum resolution. In App. B.1 the resolution function is derived using τ-pair events simulated at the $\Upsilon(4S)$ mass. Comparison of the the momentum resolution between $\Upsilon(3S)$ and $\Upsilon(4S)$ data is presented in App. B.2, and comparison between $\Upsilon(3S)$ data and simulated events is presented in in App. B.3.

B.1 Determination of the Momentum Resolution Function

In this section, the lepton momentum resolution function is derived using simulated τ-pair events generated at the $\Upsilon(4S)$ mass. Because the momentum resolution depends on the true generated momentum $\mathrm{p_{TRUE}}$, the simulated event samples are divided into four bins defined by 0.75< $\mathrm{p_{TRUE}/E_B}$ <0.80, 0.80< $\mathrm{p_{TRUE}/E_B}$ <0.85, 0.85< $\mathrm{p_{TRUE}/E_B}$ <0.90 and 0.9< $\mathrm{p_{TRUE}/E_B}$ <0.95. To account for any possible bias in the resolution function resulting from the kinematic selection, the

fits are performed separately for τ-pair events passing selection in the four signal modes. For each signal channel and for each bin in $\mathrm{p_{TRUE}}$, a double Crystal Ball function is fitted to the distribution $(\mathrm{p_{RECO}} - \mathrm{p_{TRUE}})/\mathrm{E_B}$. Because all parameters of the resulting fit function except for the width parameter σ do not depend strongly on $\mathrm{p_{TRUE}}$, the best-fit value of these parameters averaged over the four bins of $\mathrm{p_{TRUE}}$ for a given signal channel is chosen. The double Crystal Ball function is then refitted with these parameters fixed and only the width floated, as shown in Figs. B.1, B.3, B.5 and B.7. The width parameter σ is extrapolated linearly to $\mathrm{p_{TRUE}}/\mathrm{E_B} = 0.96$, approximately 1σ to the left of the cut-off as shown in Figs. B.2, B.4, B.6 and B.8.

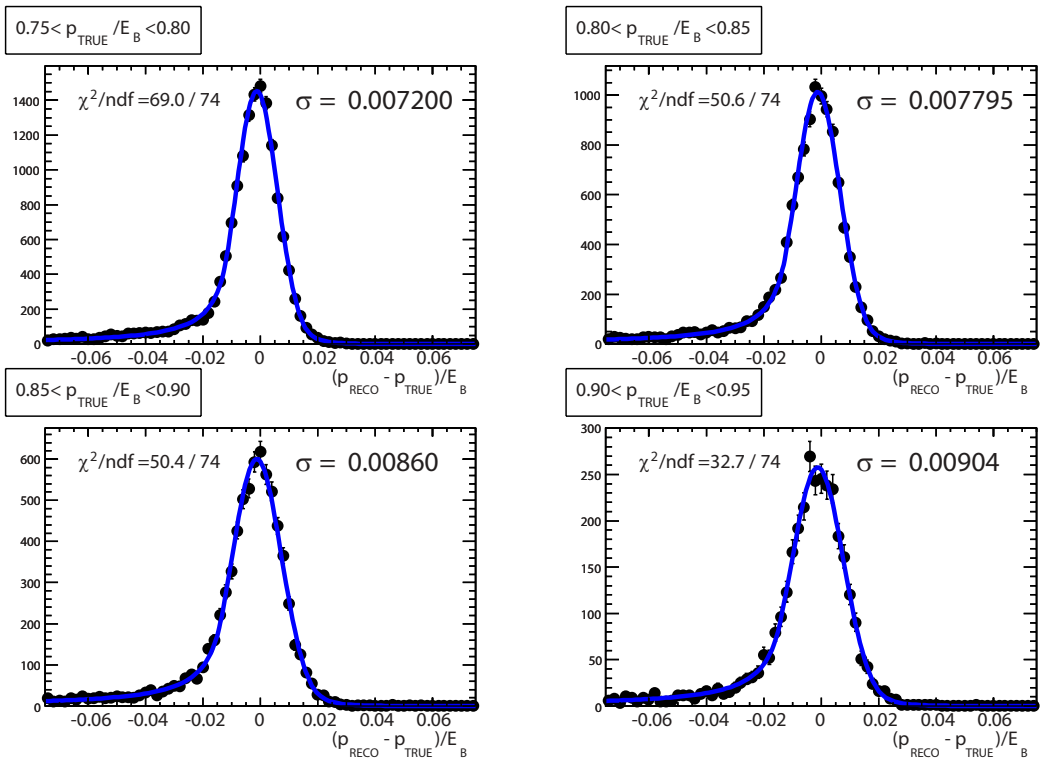

Figure B.1: Detector resolution function fit results for the leptonic $e\tau$ channel. The fits are divided into 4 bins of $\mathrm{p_{TRUE}/E_B}$. A double Crystal Ball function is fitted to the distribution $(\mathrm{p_{RECO}} - \mathrm{p_{TRUE}})/\mathrm{E_B}$ for the electrons from the τ decay for each bin of $\mathrm{p_{TRUE}/E_B}$.

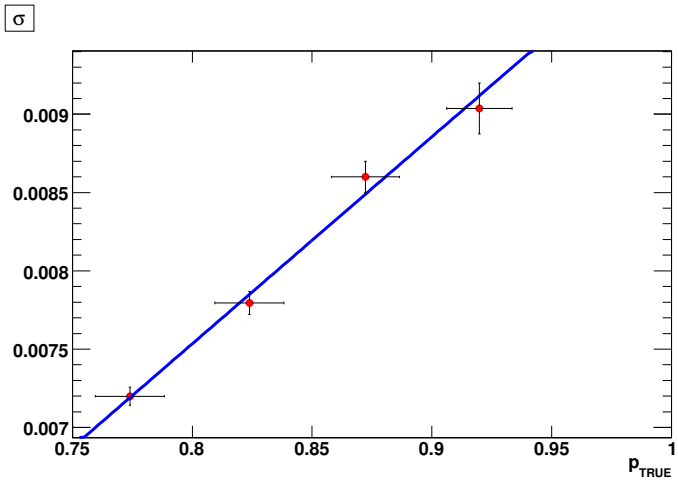

Figure B.2: Double Crystal Ball width parameter σ for the leptonic $e\tau$ channel, plotted as a function of $\mathrm{p_{TRUE}/E_B}$.

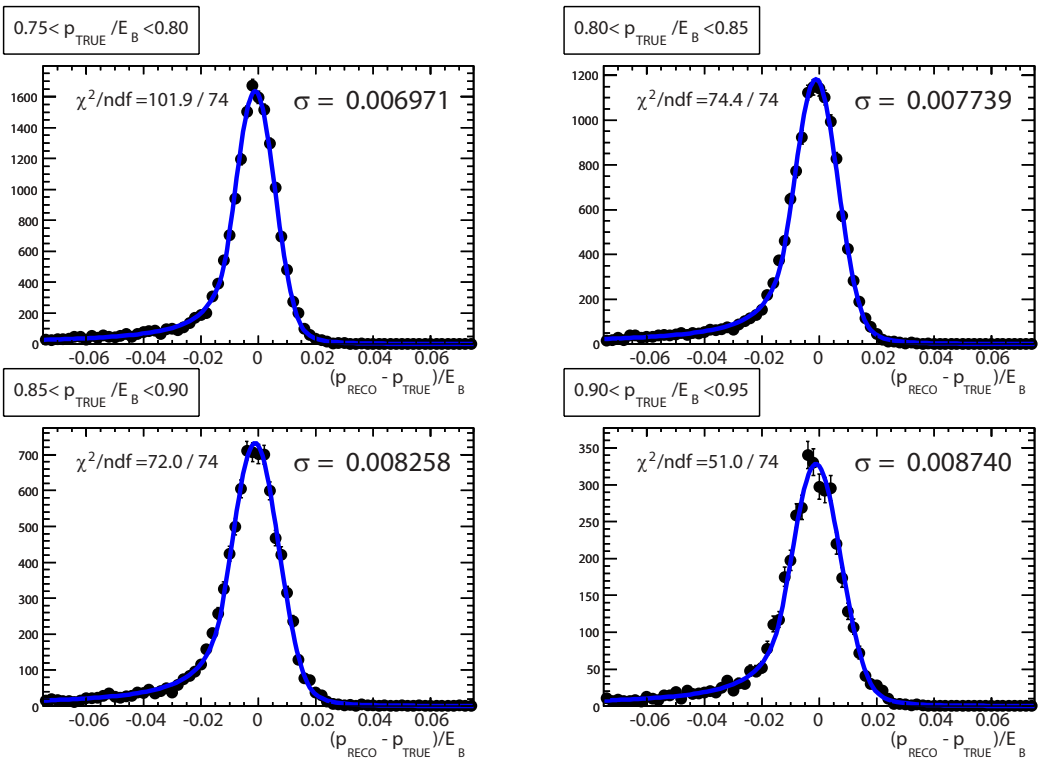

Figure B.3: Detector resolution function fit results for the hadronic $e\tau$ channel. The fits are divided into 4 bins of $\mathrm{p_{TRUE}/E_B}$. A double Crystal Ball function is fitted to the distribution $(\mathrm{p_{RECO}} - \mathrm{p_{TRUE}})/\mathrm{E_B}$ for the electrons from the τ decay for each bin of $\mathrm{p_{TRUE}/E_B}$.

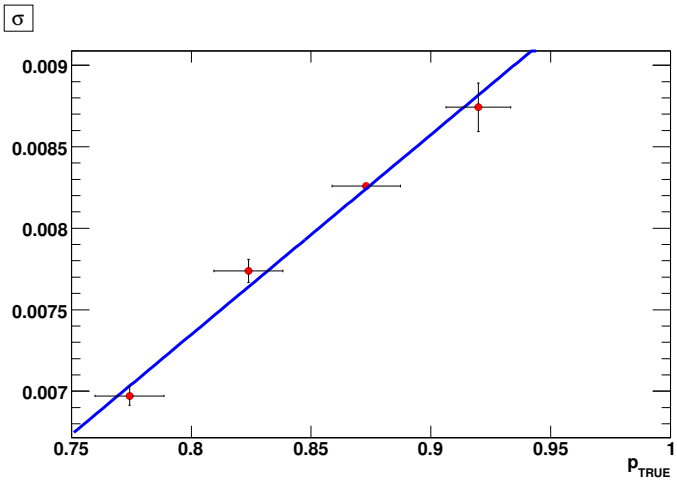

Figure B.4: Double Crystal Ball width parameter σ for the hadronic $e\tau$ channel, plotted as a function of $\mathrm{p_{TRUE}/E_B}$.

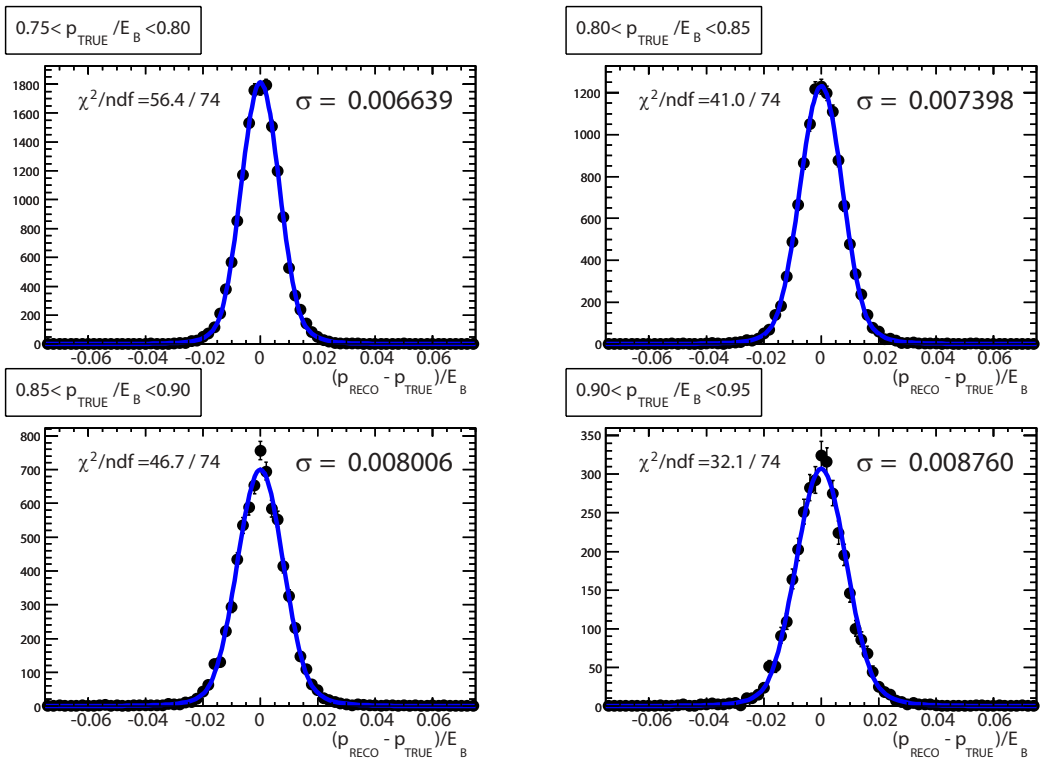

Figure B.5: Detector resolution function fit results for the leptonic $\mu\tau$ channel. The fits are divided into 4 bins of $\mathrm{p_{TRUE}/E_B}$. A double Crystal Ball function is fitted to the distribution $(\mathrm{p_{RECO}} - \mathrm{p_{TRUE}})/\mathrm{E_B}$ for the muons from the τ decay for each bin of $\mathrm{p_{TRUE}/E_B}$.

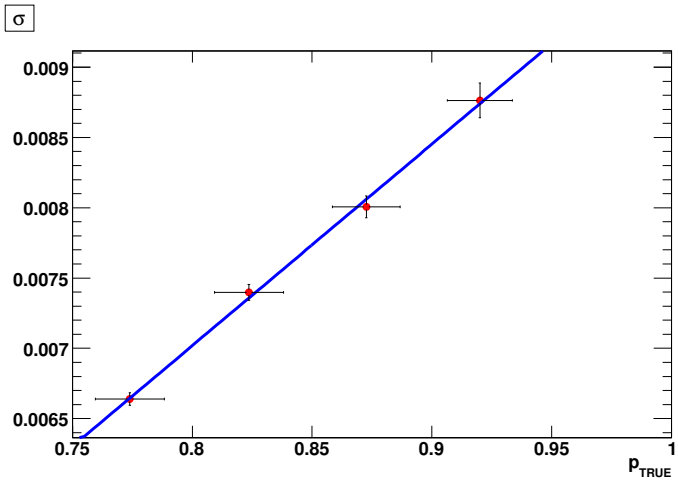

Figure B.6: Double Crystal Ball width parameter σ for the leptonic $\mu\tau$ channel, plotted as a function of $\mathrm{p_{TRUE}/E_B}$.

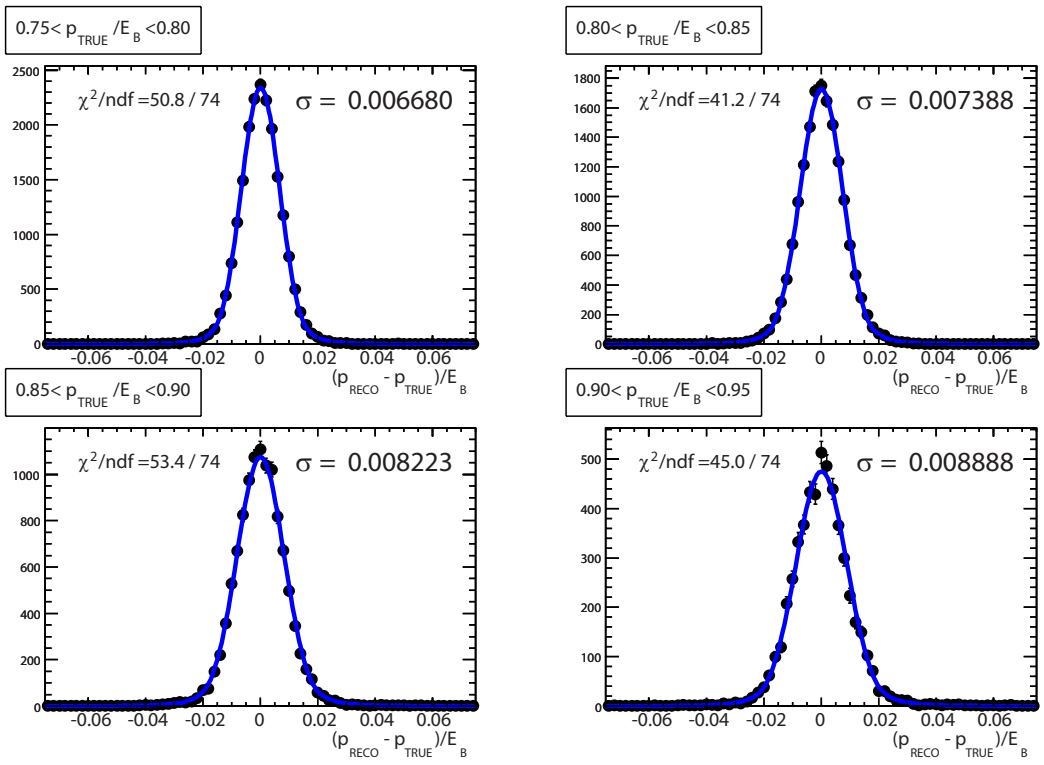

Figure B.7: Detector resolution function fit results for the hadronic $\mu\tau$ channel. The fits are divided into 4 bins of $\mathrm{p_{TRUE}/E_B}$. A double Crystal Ball function is fitted to the distribution $(\mathrm{p_{RECO}} - \mathrm{p_{TRUE}})/\mathrm{E_B}$ for the muons from the τ decay for each bin of $\mathrm{p_{TRUE}/E_B}$.

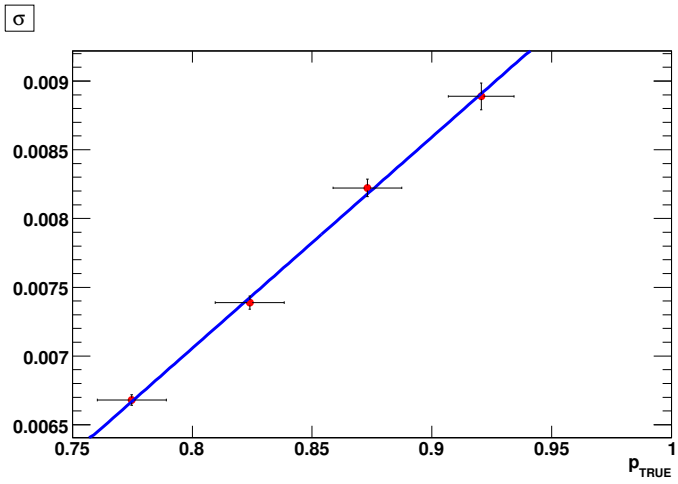

Figure B.8: Double Crystal Ball width parameter σ for the hadronic $\mu\tau$ channel, plotted as a function of $\mathrm{p_{TRUE}/E_B}$.

B.2 Comparison of Momentum Resolution Between $\Upsilon(3S)$ and $\Upsilon(4S)$ Data

To assess potential differences in the momentum resolution between $\Upsilon(3S)$ and $\Upsilon(4S)$ data, Bhabha and μ-pair control samples are compared between these two data samples. For the Bhabha sample, a PDF consisting of a triple Gaussian plus an Argus distribution is fitted to the p_e/E_B distribution for the $\Upsilon(4S)$ data sample. This PDF is then fitted to the $\Upsilon(3S)$ data sample, but with all mean parameters shifted by a common parameter 'shift' and all width parameters scaled by a common parameter 'scale'. The curvature of the Argus distribution and the triple Gaussian fraction of the total PDF are also allowed to vary between $\Upsilon(3S)$ and $\Upsilon(4S)$ data, as shown in Fig. B.9. For the μ-pair sample, a PDF consisting of a double Crystal Ball function plus two Gaussians is fitted to to the p_μ/E_B distribution for the $\Upsilon(4S)$ data sample. The same PDF is fitted to the $\Upsilon(3S)$ data sample, but with all mean parameters shifted and all width parameters scaled, as shown in Fig. B.10. The fit results are summarized in Table B.1. The detector resolution functions for electrons and muons extracted from $\Upsilon(4S)$ data are shifted and scaled by the values determined using this procedure when fitting to $\Upsilon(3S)$ data.

B.3 Comparison of Momentum Resolution Between $\Upsilon(3S)$ Data and Simulated Events

To assess potential differences in the momentum resolution between $\Upsilon(3S)$ data and simulated events, Bhabha and μ-pair control samples are compared between these two samples. Data collected 30 MeV below the $\Upsilon(3S)$ resonance (off-peak data) is used in order to exclude resonant

Table B.1: Summary of results of the comparisons of momentum resolution between $\Upsilon(3S)$ and $\Upsilon(4S)$ data and between $\Upsilon(3S)$ data and simulated events. All mean parameters of the resolution function are shifted by the parameter 'shift' and scaled by the parameter 'scale.'

	Sample	**Shift**	**Scale**
$\Upsilon(3S)$ data vs. $\Upsilon(4S)$ data	Bhabha	$(0.6 \pm 6.5) \times 10^{-5}$	1.020 ± 0.003
	μ-pair	$(0.3 \pm 6.3) \times 10^{-6}$	1.032 ± 0.006
$\Upsilon(3S)$ data vs. simulated events	Bhabha	$(0.5 \pm 5.4) \times 10^{-5}$	1.030 ± 0.014
	μ-pair	$(-3.9 \pm 0.6) \times 10^{-4}$	1.017 ± 0.009

μ-pair production. For the Bhabha sample, a PDF consisting of a double Crystal Ball function plus an Argus distribution is fitted to the simulated events. In the corresponding fit to data, the mean and Argus endpoint are shifted and the width is scaled. The Argus curvature χ and double Crystal Ball fraction of the total PDF are also allowed to vary between $\Upsilon(3S)$ data and simulated events, as shown in Fig. B.11. For the μ-pair sample, a PDF consisting of a double Crystal Ball function plus a double Gaussian is fitted to the simulated events. In the corresponding fit to data, all mean parameters are shifted and all width parameters are scaled as shown in Fig. B.12. The fit results are summarized in Table B.1. The values of the shift and scale parameters are used to assess the systematic uncertainty resulting from the discrepancies in the mean and width of the detector resolution function between data and simulation.

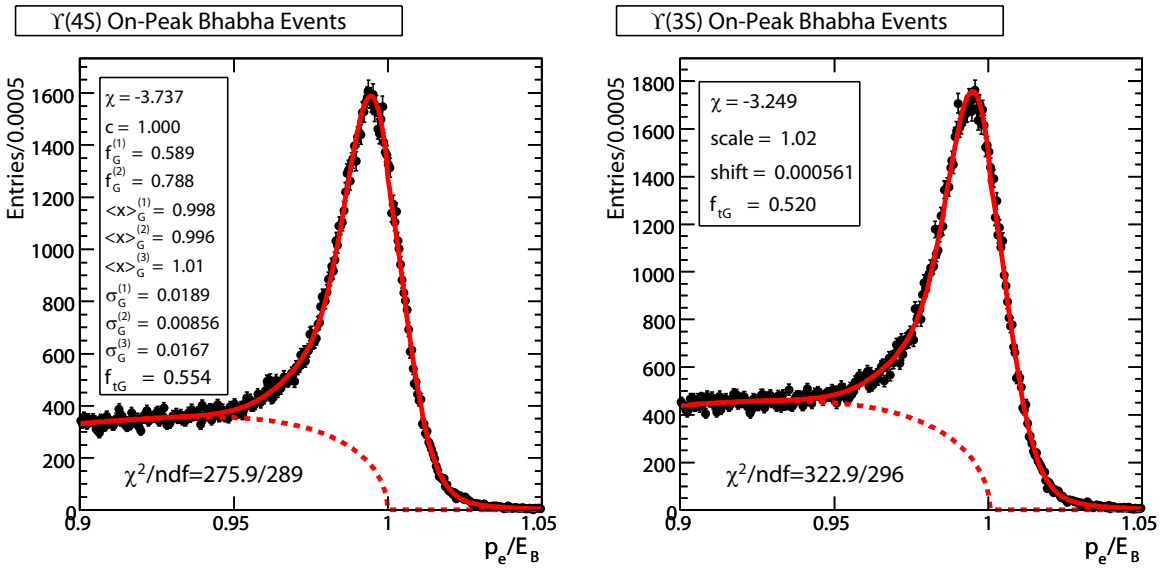

Figure B.9: Comparison of Bhabha control samples in $\Upsilon(3S)$ and $\Upsilon(4S)$ data. The fit function is an Argus distribution (dotted line) plus a triple Gaussian.

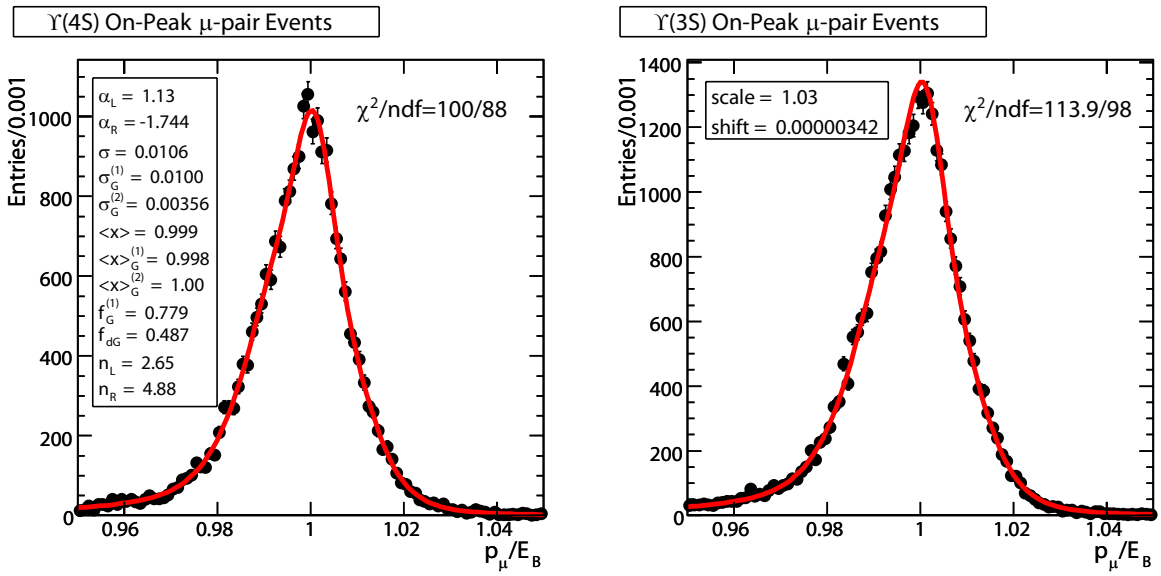

Figure B.10: Comparison of μ-pair control samples in $\Upsilon(3S)$ and $\Upsilon(4S)$ data. The fit function is a double Crystal Ball function plus two Gaussians.

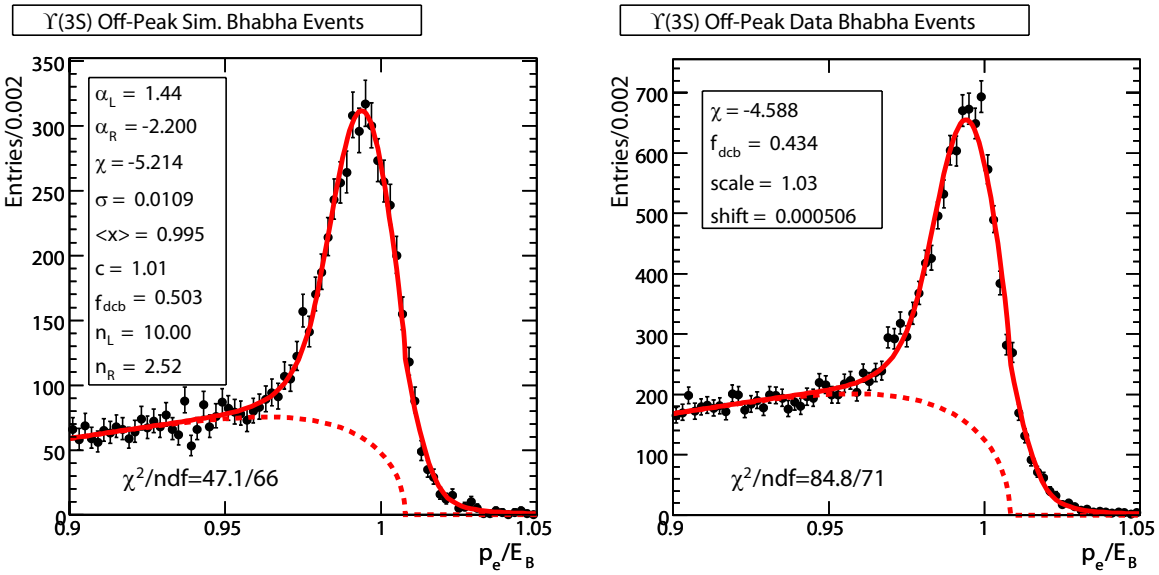

Figure B.11: Comparison of Bhabha control samples in $\Upsilon(3S)$ data and simulated events. The fit function is an Argus distribution (dotted line) plus a double Crystal Ball function.

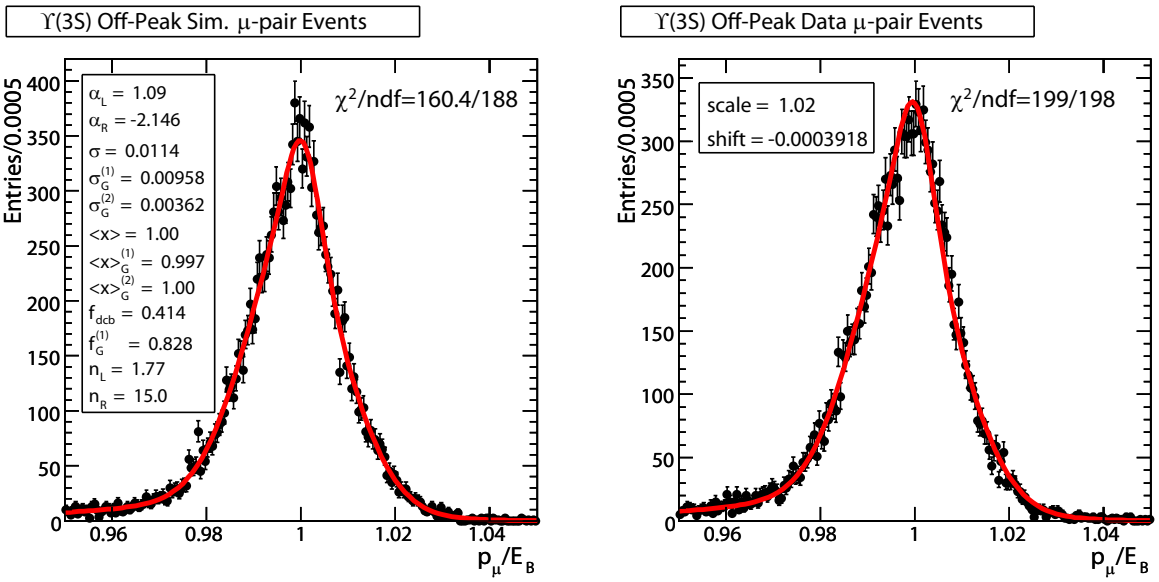

Figure B.12: Comparison of μ-pair control samples in $\Upsilon(3S)$ data and simulated events. The fit function is a double Crystal Ball function plus two Gaussians.

Appendix C

Validation of *BABAR* Fit Procedure Using Simulated Pseudo-Experiments

A large number of simulated pseudo-experiments are performed in order to further validate the fit procedure used in the *BABAR* analysis. For each of the four signal channels, the peaking background yield is extracted from the fit to the full $\Upsilon(4S)$ data sample and scaled to the $\Upsilon(3S)$ data sample by the ratio of integrated luminosities times the $1/s$ scaling factor $(10.58\ \text{GeV}/10.35\ \text{GeV})^2$. The τ-pair background yield is determined by counting the number of events in each channel of $\Upsilon(3S)$ data and subtracting off the expected peaking background contribution. To determine the shape of the τ-pair background PDF, x_{MAX} is fixed to the value extracted from the fit to the full $\Upsilon(4S)$ data sample, while the polynomial shape parameters c_2 and c_3 are determined by fitting to $\Upsilon(3S)$ data over the sideband region defined by 0.75$<\ p_1/E_B\ <$0.95. Background samples are generated from the background PDFs with Poisson-smeared expected yields for each $\Upsilon(3S)$ signal channel. A Poisson-smeared number of simulated signal events is added from the sim-

ulated x distributions of the four signal channels, with the mean of the generated signal yield $\mathrm{N_{GEN}} = 0, 5, 10, 15, 20$. The fit is performed while floating the signal, τ-pair background and peaking background yields, as well as the two polynomial shape parameters, the same parameters that are floated in the fit to $\Upsilon(3S)$ data. The extracted signal yield, error and pull (the extracted signal yield minus the generated signal yield divided by the signal yield uncertainty) are determined and the procedure is repeated 1000 times for each channel and value of $\mathrm{N_{GEN}}$. The resulting pull distributions of the extracted signal yield are shown in Figs. C.1, C.3, C.5 and C.7. The mean and sigma of a Gaussian fitted to these pull distributions are plotted as a function of $\mathrm{N_{GEN}}$ in Figs. C.2, C.4, C.6, C.8.

For an idealized fit procedure, the mean of the Gaussian fit to the pull distribution should be zero and the width should be one. In this study small deviations from zero in the mean of the Gaussian of of order $\pm 10\%$ are observed. The sign and magnitude of this bias varies between channel and as the generated signal yield is varied. Deviations from one in the width of the Gaussian, typically of order +5-10%, are also observed. The biases and deviations from unit width are small enough that the resulting systematic uncertainty does not significantly affect the sensitivity, so bias correction is not be applied. The systematic error due to potential bias in the fit procedure is discussed in Chap. 2.11.

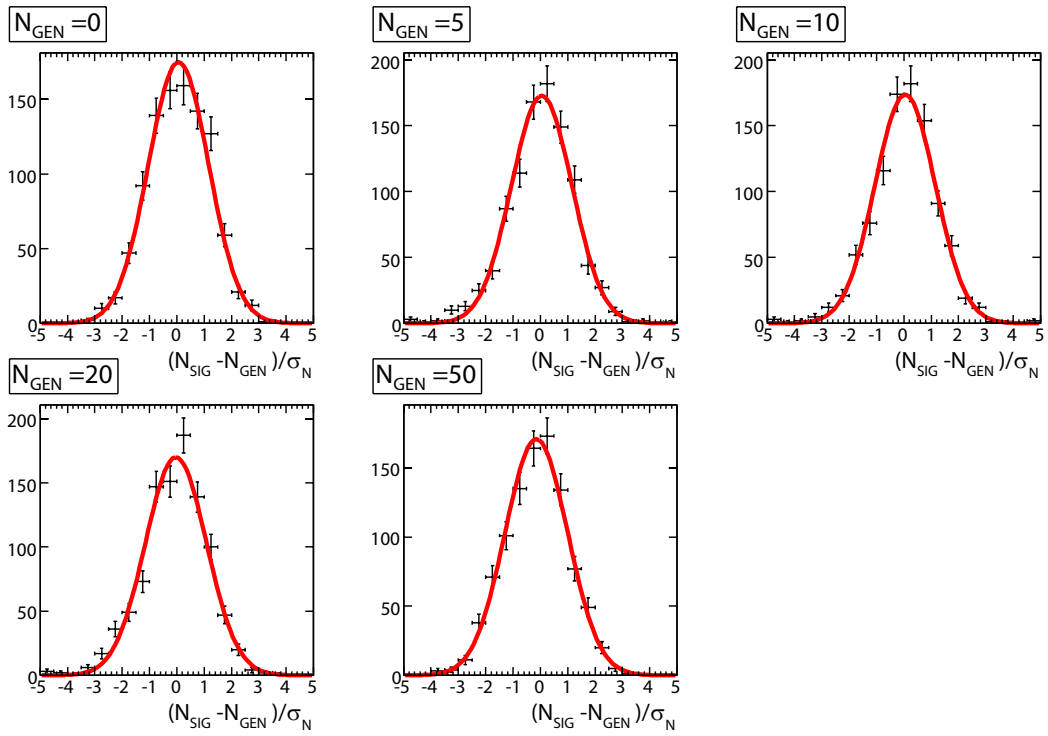

Figure C.1: Pull distributions for the leptonic $e\tau$ channel. $\mathrm{N_{SIG}}$ is the signal yield extracted by the fit and σ_{N} is the signal yield uncertainty. $\mathrm{N_{GEN}}$ is the mean number of simulated signal events added to the simulated background sample.

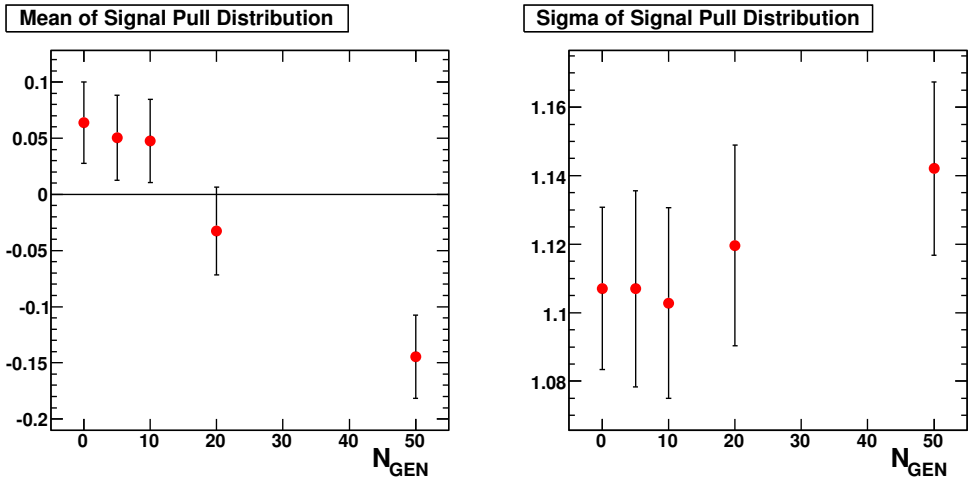

Figure C.2: The mean and sigma of a Gaussian fitted to the pull distributions for the leptonic $e\tau$ channel as a function of the mean generated signal yield $\mathrm{N_{GEN}}$.

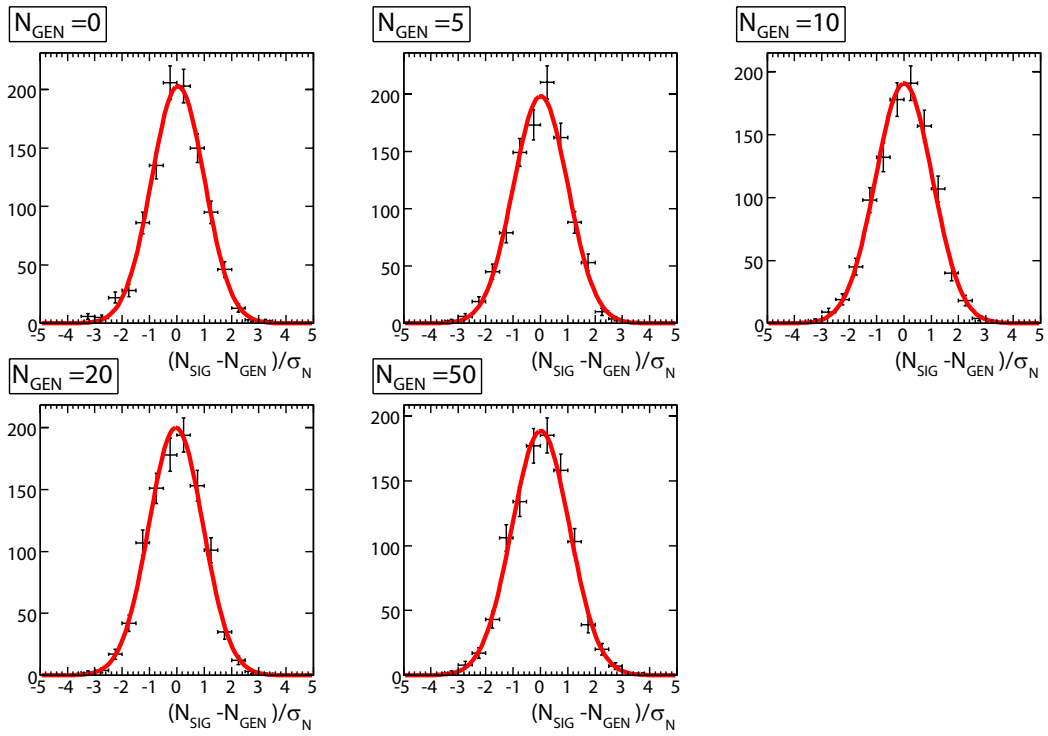

Figure C.3: Pull distributions for the hadronic $e\tau$ channel. $\mathrm{N_{SIG}}$ is the signal yield extracted by the fit and σ_{N} is the signal yield uncertainty. $\mathrm{N_{GEN}}$ is the mean number of simulated signal events added to the simulated background sample.

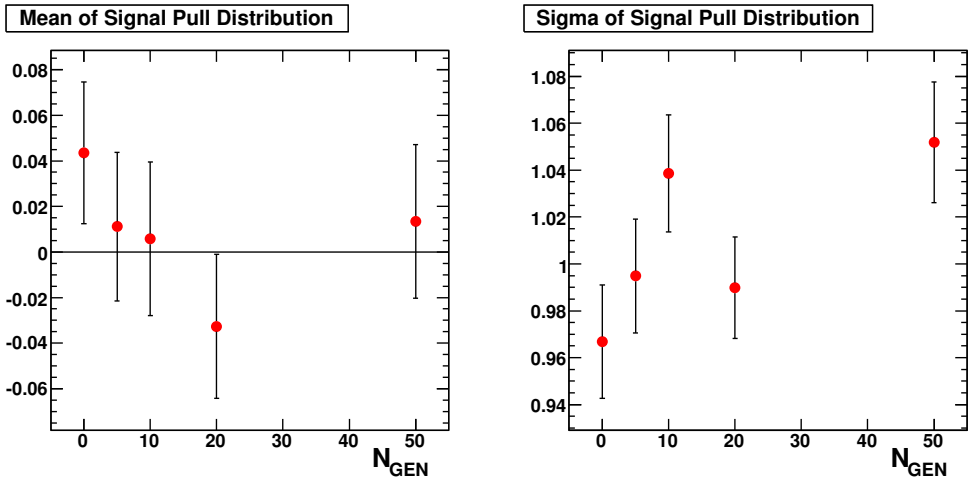

Figure C.4: The mean and sigma of a Gaussian fitted to the pull distributions for the hadronic $e\tau$ channel as a function of the mean generated signal yield $\mathrm{N_{GEN}}$.

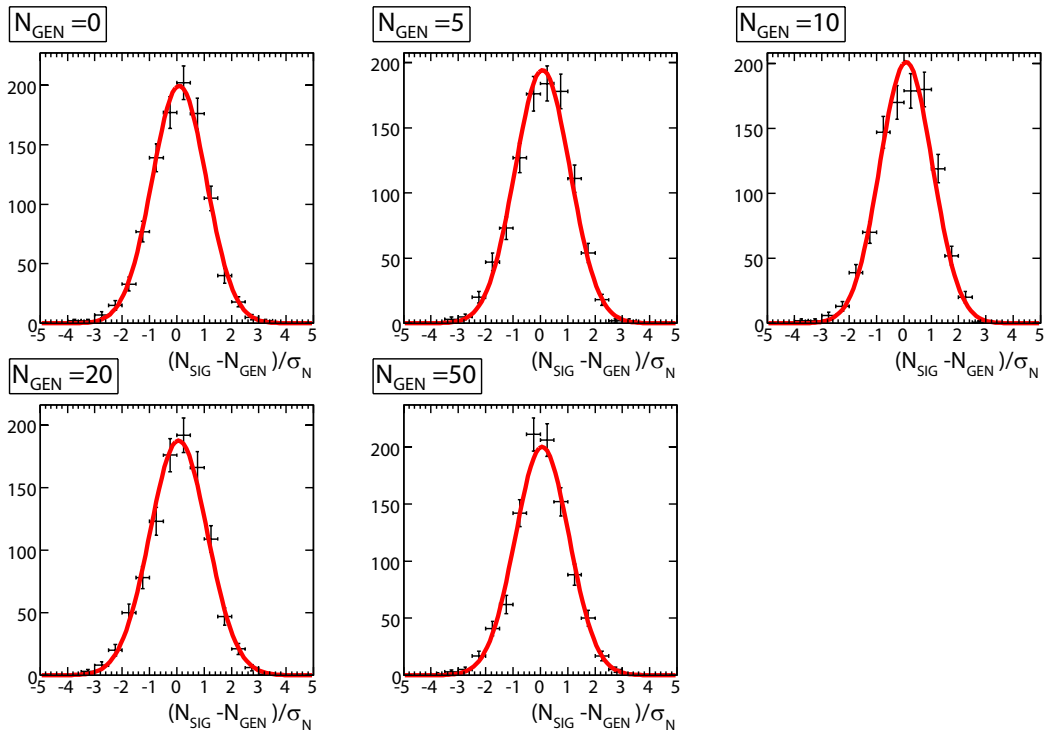

Figure C.5: Pull distributions for the leptonic $\mu\tau$ channel. $\mathrm{N_{SIG}}$ is the signal yield extracted by the fit and σ_{N} is the signal yield uncertainty. $\mathrm{N_{GEN}}$ is the mean number of simulated signal events added to the simulated background sample.

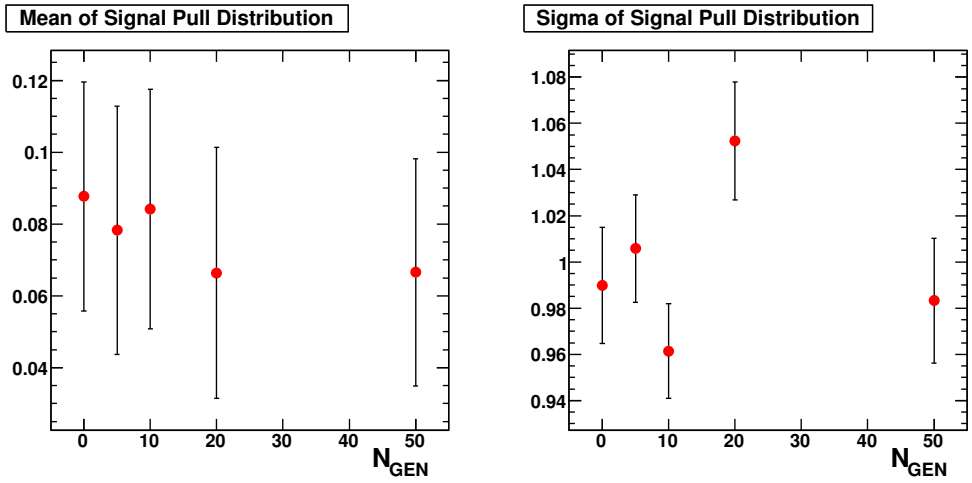

Figure C.6: The mean and sigma of a Gaussian fitted to the pull distributions for the leptonic $\mu\tau$ channel as a function of the mean generated signal yield $\mathrm{N_{GEN}}$.

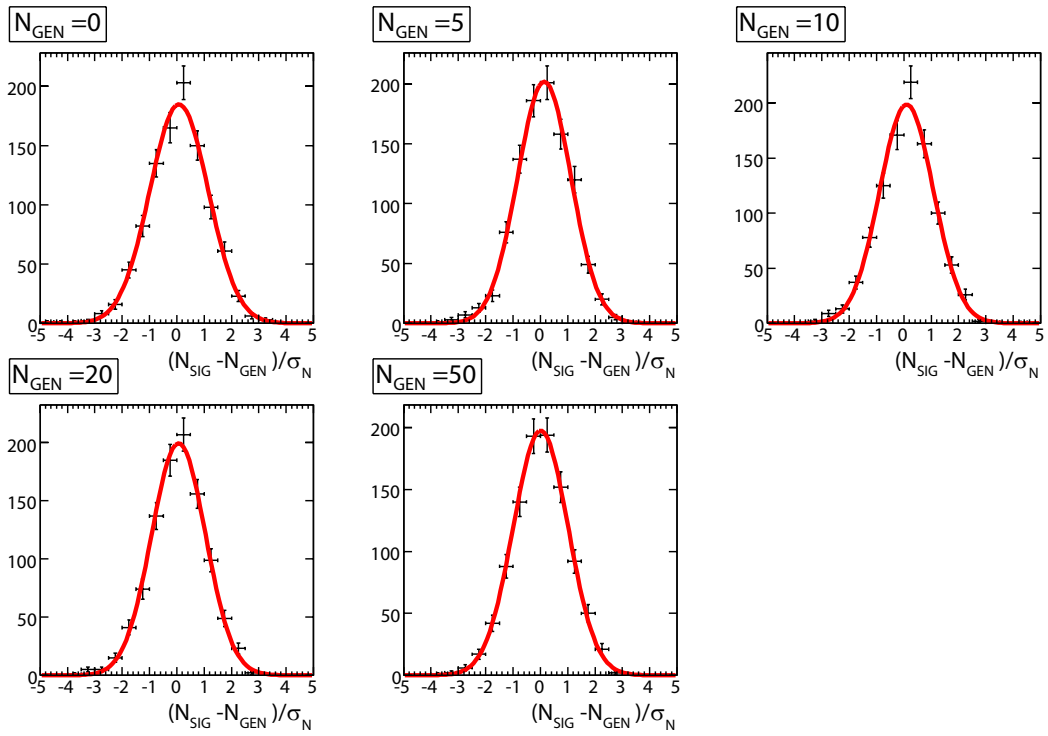

Figure C.7: Pull distributions for the hadronic $\mu\tau$ channel. $\mathrm{N_{SIG}}$ is the signal yield extracted by the fit and σ_{N} is the signal yield uncertainty. $\mathrm{N_{GEN}}$ is the mean number of simulated signal events added to the simulated background sample.

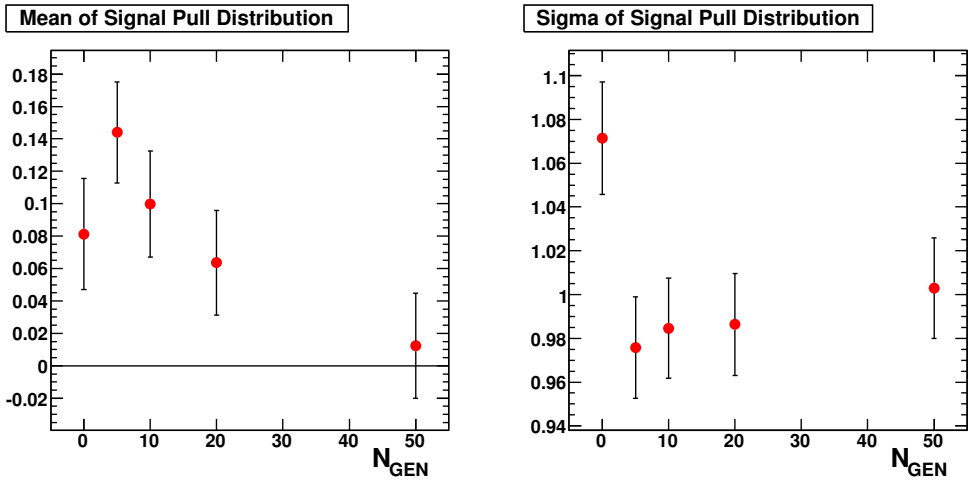

Figure C.8: The mean and sigma of a Gaussian fitted to the pull distributions for the hadronic $\mu\tau$ channel as a function of the mean generated signal yield $\mathrm{N_{GEN}}$.